UNIVERSITY OF SÃO PAULO
SÃO CARLOS SCHOOL OF ENGINEERING
DEPARTMENT OF STRUCTURAL ENGINEERING

DAVID LEONARDO NASCIMENTO DE FIGUEIREDO AMORIM

On the lumped damage mechanics for nonlinear structural analyses: new developments and applications

São Carlos
2016

DAVID LEONARDO NASCIMENTO DE FIGUEIREDO AMORIM

On the lumped damage mechanics for nonlinear structural analyses: new developments and applications

CORRECTED VERSION

The original version is in the São Carlos School of Engineering

Thesis presented to the Engineering School of São Carlos, University of São Paulo, as one of the requisites for obtaining the degree of Doctor in Sciences, Structural Engineering.

Concentration area: Structures

Advisor: Prof. Tit. Sergio Persival Baroncini Proença

São Carlos

2016

Amorim, David Leonardo Nascimento de Figueiredo
A524o On the lumped damage mechanics for nonlinear structural analyses: new developments and applications / David Leonardo Nascimento de Figueiredo Amorim; orientador Sergio Persival Baroncini Proença. São Carlos, 2016.

Tese (Doutorado) - Programa de Pós-Graduação em Engenharia de Estruturas -- Escola de Engenharia de São Carlos da Universidade de São Paulo, 2016.

1. Lumped damage mechanics. 2. Reinforced concrete. 3. Quasi-brittle materials. 4. High cycle fatigue. 5. Localisation. I. Título.

FOLHA DE JULGAMENTO

Candidato: Engenheiro **DAVID LEONARDO NASCIMENTO DE FIGUEIREDO AMORIM.**

Título da tese: "Sobre a teoria do dano concentrado para análise não linear de estruturas: novos desenvolvimentos e aplicações".

Data da defesa: 22/03/2016

Comissão Julgadora:	**Resultado:**
Prof. Associado **Márcio Roberto Silva Corrêa (Orientador designado)** (Escola de Engenharia de São Carlos/EESC)	APROVADO
Prof. Dr. **Julio Flórez-López** (Universidade de Los Andes)	APROVADO
Prof. Dr. **Osvaldo Luís Manzoli** (Universidade Estadual Paulista "Júlio de Mesquita Filho"/UNESP - Bauru)	APROVADO
Prof. Dr. **José Luiz Antunes de Oliveira e Sousa** (Universidade Estadual de Campinas/UNICAMP)	Aprovado
Prof. Dr. **Eduardo de Moraes Rego Fairbairn** (Universidade Federal do Rio de Janeiro/UFRJ)	APROVADO

Coordenador do Programa de Pós-Graduação em Engenheira Civil (Engenharia de Estruturas):
Prof. Titular **Humberto Breves Coda**

Presidente da Comissão de Pós-Graduação:
Prof. Associado **Paulo Sergio Lima Segantine**

To my mother, Neide, to my grandmother, Neide, to my uncle, João Pedro, and to my brother, Alfredo.

À minha mãe, Neide, à minha avó, Neide, ao meu tio, João Pedro, e ao meu irmão, Alfredo.

ACKNOWLEDGEMENTS

I thank God for everything in my life.

I thank my family for all support and education invested in me, especially to my grandmother, my mother, my uncle and my brother, to whom I also dedicate this work.

I thank my girlfriend Camila for the companionship and attention, making this journey less tough.

I thank my friends who were part of the six years I lived in São Carlos: Adauri Niero, Alberto Douglas, Alexandre Cardoso, Alessandra Kyoko, Ayrton Ferreira, Carolina Ramírez, Danieli Tanno, Davi Gadelha, Dorival Piedade, Ellen Kellen, Enio Mesacasa, Érica Kimura, Fabio Carlos, Fabio Rocha, Fernando Vecchio, Gabriel Rocha, Gisele Martins, Guilherme Barbosa, Higor Argolo, Igor Cotta, Irene Pimentel, Ivie Emi, Jesus Garcia, Ketson Roberto, Larissa Miranda, Leonardo Marcolin, Lorenzo Lube, Manoel Dênis, Marcela Filizola, Marcela Kataoka, Matheus Fernandes, Nayara Falanca, Olivia da Costa, Patrícia Rocha, Priscila Camiloti, Rafael Marques, Rodrigo Almeida, Rodrigo Barros, Rodrigo Enami, Rodrigo Soares, Socorro Sampaio, Suzana Valverde, Thiago Santos, Valdeir Galindo, Vinícius Correia, Vinícius Rocha, Vítor Rafael, Wagner Santiago and Wagner Silva.

I thank my friends from Maceió, who made that my homeland has never been so far. I especially thank my childhood friends for the life-time friendship and for all days we faced rain and sun just to see a CSA's football match. I also thank my friends from UFAL (Federal University of Alagoas), for the friendship since the graduate course.

Many people want a good advisor, I have two! I thank my advisor, Professor Sergio Proença, for the friendship, for all time dedicated to me and for the always pertinent advices. I especially thank my *moral co-advisor*, Professor Julio Flórez-López, for the friendship, patience and dedication. His name should be in the cover of this work, but the university bureaucracy did not allow it.

I thank Professors Masayoshi Nakashima and Masahiro Kurata for inviting me to visit the Kyoto University and for the amazing experience I had in Japan.

I thank: Akiko Suzuki, Diana, Francesca, Ikumi Hamashima, Kaede Minegishi, Kostas, Liusheng He, Miho Sato, Hiromichi Nishino, Hiroyuki Inamasu, Ryousuke Nishi, Takuma Togo, Yongtao Bai and Yunbiao Luo, for the good moments I had in Japan.

I acknowledge CAPES (Coordenação de Aperfeiçoamento de Pessoal de Nível Superior) for the financial support.

AGRADECIMENTOS

Agradeço a Deus por tudo em minha vida.

Agradeço à minha família por todo o suporte e educação investidos em mim, em especial à minha avó, minha mãe, meu tio e meu irmão, aos quais também dedico este trabalho.

Agradeço à Camila por todo o companheirismo e atenção, fazendo com que esta jornada fosse menos dura.

Agradeço, pela convivência, aos amigos que fizeram parte dos seis anos que vivi em São Carlos: Adauri Niero, Alberto Douglas, Alexandre Cardoso, Alessandra Kyoko, Ayrton Ferreira, Carolina Ramírez, Danieli Tanno, Davi Gadelha, Dorival Piedade, Ellen Kellen, Enio Mesacasa, Érica Kimura, Fabio Carlos, Fabio Rocha, Fernando Vecchio, Gabriel Rocha, Gisele Martins, Guilherme Barbosa, Higor Argolo, Igor Cotta, Irene Pimentel, Ivie Emi, Jesus Garcia, Ketson Roberto, Larissa Miranda, Leonardo Marcolin, Lorenzo Lube, Manoel Dênis, Marcela Filizola, Marcela Kataoka, Matheus Fernandes, Nayara Falanca, Olivia da Costa, Patrícia Rocha, Priscila Camiloti, Rafael Marques, Rodrigo Almeida, Rodrigo Barros, Rodrigo Enami, Rodrigo Soares, Socorro Sampaio, Suzana Valverde, Thiago Santos, Valdeir Galindo, Vinícius Correia, Vinícius Rocha, Vítor Rafael, Wagner Santiago e Wagner Silva.

Agradeço aos amigos de Maceió, que fizeram com que minha terra natal nunca estivesse tão longe. Agradeço especialmente aos meus amigos de infância, pela convivência e por todos os dias que enfrentamos chuva e sol só para ver o CSA jogar. Também agradeço aos amigos da UFAL, pela amizade que dura desde a graduação.

Muitos querem ter um bom orientador, eu tenho dois! Agradeço ao meu orientador, Professor Sergio Proença, pela amizade, por todo tempo dedicado a mim e pelos conselhos sempre pertinentes. Agradeço especialmente ao meu *coorientador moral*, Professor Julio Flórez-López, pela amizade, paciência e dedicação. Seu nome também deveria estar na capa deste trabalho, mas infelizmente a burocracia da universidade não permitiu.

Agradeço aos Professores Masayoshi Nakashima e Masahiro Kurata pelo convite para visitar a Universidade de Quioto e pela incrível experiência que tive no Japão.

Agradeço a: Akiko Suzuki, Diana, Francesca, Ikumi Hamashima, Kaede Minegishi, Kostas, Liusheng He, Miho Sato, Hiromichi Nishino, Hiroyuki Inamasu, Ryousuke Nishi, Takuma Togo, Yongtao Bai e Yunbiao Luo, pelos bons momentos quando estive no Japão.

Agradeço a CAPES (Coordenação de Aperfeiçoamento de Pessoal de Nível Superior) pelo suporte financeiro.

Se avexe não...
Amanhã pode acontecer tudo
Inclusive nada

José Accioly Cavalcante Neto

ABSTRACT

AMORIM, D. L. N. F. **On the lumped damage mechanics for nonlinear structural analyses: new developments and applications**. 2016. 193 p. Thesis (Doctorate) – São Carlos School of Engineering, University of São Paulo, São Carlos, 2016.

The accurate description of the nonlinear structural behaviour is an important issue in engineering science. Usually, classic nonlinear theories, such as fracture and damage mechanics, applied to finite element programmes are used to fulfil that purpose. Classic fracture mechanics describes the structural deterioration process by a few discrete cracks. This theory presents good precision for structures with simple geometries, few cracks and homogeneous materials. Classic damage mechanics measures the deterioration process by an internal variable called damage. This theory has been successful in the description of several deterioration mechanisms in continuum media. Despite their accuracy, classic fracture and damage mechanics present some drawbacks. Firstly, regarding civil engineering problems, both theories are not suitable for some practical applications. Secondly, fracture mechanics demands the consideration of initial cracks to begin the analysis. Lastly, classic damage models may present an issue known as localisation, what essentially leads to ill-posed problems and mesh-dependent numerical algorithms. Alternatively, a recent theory, called lumped damage mechanics, was proposed in order to achieve good accuracy in actual engineering problems. Such theory applies key concepts from fracture and damage mechanics in plastic hinges. In the light of the foregoing, the main goal of this thesis is the extension of the lumped damage mechanics framework to analyse different engineering problems. So far, lumped damage mechanics was characterised as a simplified methodology to analyse reinforced concrete frames under seismic and monotonic loadings; even with a few contributions on the analysis of local buckling in metallic structures. Therefore, this work extends the lumped damage mechanics framework to analyse reinforced concrete arches, unreinforced concrete structures, high cycle fatigue and continuum problems. The application examples show the accuracy of the proposed methodologies.

Keywords: Lumped damage mechanics. Reinforced concrete. Quasi-brittle materials. High cycle fatigue. Localisation.

RESUMO

AMORIM, D. L. N. F. **Sobre a teoria do dano concentrado para análise não linear de estruturas: novos desenvolvimentos e aplicações**. 2016. 193 p. Tese (Doutorado) – Escola de Engenharia de São Carlos, Universidade de São Paulo, São Carlos, 2016.

A descrição acurada do comportamento não linear de estruturas é um problema importante na engenharia. Usualmente, teorias não lineares clássicas, tais como as mecânicas da fratura e do dano, aplicadas a programas de elementos finitos são utilizadas a fim de cumprir aquele propósito. A mecânica da fratura clássica descreve o processo de deterioração estrutural por meio de um pequeno número de fissuras discretas. Esta teoria apresenta boa precisão para estruturas com geometrias simples, poucas fissuras e materiais homogêneos. A mecânica do dano clássica tem sido exitosa na descrição de diversos mecanismos de deterioração em meios contínuos. Apesar de precisas, as abordagens clássicas em fratura e dano apresentam alguns entraves. Primeiramente, tratando-se de problemas da engenharia civil, ambas teorias não são adequadas para aplicações práticas. Em segundo lugar, os modelos clássicos de fratura demandam a consideração de fissuras iniciais para iniciar a análise. Por fim, os modelos clássicos de dano podem apresentar um problema conhecido como localização, o que essencialmente implica em problemas mal colocados e algoritmos com dependência de malha. Alternativamente, uma teoria recente, chamada teoria do dano concentrado, foi proposta a fim de obter boa precisão em problemas reais de engenharia. Tal teoria aplica conceitos-chave das mecânicas da fratura e do dano em rótulas plásticas. À luz do exposto, o principal objetivo desta tese é a extensão da teoria do dano concentrado para analisar diferente problemas da engenharia. Até então, a teoria do dano concentrado era caracterizada como uma metodologia simplificada para analisar pórticos de concreto armado sob solicitações monotônicas ou sísmicas; mesmo com algumas poucas contribuições na análise de instabilidade local em estruturas metálicas. Desta forma, este trabalho estende a teoria do dano concentrado a fim de analisar arcos de concreto armado, estruturas de concreto simples, fadiga de alto ciclo e problemas contínuos. Os exemplos de aplicação mostram a acurácia das metodologias propostas.

Palavras-chave: Teoria do dano concentrado. Concreto armado, Materiais quase-frágeis. Fadiga de alto ciclo. Localização.

LIST OF ABBREVIATIONS AND ACRONYMS

CMT	Constant Moment Triangle
FM	Fracture Mechanics
FPZ	Fracture Process Zone
LDM	Lumped Damage Mechanics
LDMH	Lumped Damage Model with Hysteresis
LFFM	Lumped Fatigue and Fracture Mechanics
RVE	Representative Volume Element
SCF	Stress Concentration Factor
SIF	Stress Intensity Factor
XLDM	Extended Lumped Damage Mechanics

LIST OF SYMBOLS

$M(x)$	Bending moment in a cross section x of the frame member
E	Young's modulus
I	Inertia moment of the cross section
$w(x)$	Transversal displacement
$N(x)$	Axial force in a cross section x of the frame member
A	Area of the cross section
$u(x)$	Longitudinal displacement
ϕ_i	Flexural rotation of the node i of the frame member b
ϕ_j	Flexural rotation of the node j of the frame member b
δ	Chord elongation of the frame member b
m_i	Bending moment at the node i of the frame member b
m_j	Bending moment at the node j of the frame member b
n_b	Axial force across the frame member b
L	Deformed length
L_0	Initial length
$\{\boldsymbol{u}\}_i$	Generalised displacements of the node i
u_i	Displacement at the X-axis direction
w_i	Displacement at the Z-axis direction
θ_i	Total rotation of the node i with respect to initial configuration
XZ	Global axes
$\{\mathbf{q}\}_b$	Matrix of the generalised nodal displacements of a member b
$\{\mathbf{U}\}$	Matrix of the generalised nodal displacements of the structure
$\{\boldsymbol{\phi}\}_b$	Matrix of generalised deformations
$x_L z_L$	Local axes
α_b^0	Initial orientation angle of a frame member b
L_b^0	Initial length of a frame member b
α_b	Current orientation angle of a frame member b
L_b	Current length of a frame member b
$\{\mathbf{q}^L\}_b$	Matrix of the generalised displacements in local coordinates
u_i^L	Displacement at the x_L-axis direction

w_i^L	Displacement at the z_L-axis direction
θ_i^L	Total rotation of the node i with respect to initial configuration
$[\mathbf{T}]_b$	Axes transformation matrix
$[\mathbf{B}(\mathbf{q}^L)]_b$	Kinematic transformation matrix of the member b in the local coordinate system
$[\mathbf{B}(\mathbf{q})]_b$	Kinematic transformation matrix of the member b in the global coordinate system
$[\mathbf{B}^0]_b$	Kinematic transformation matrix of the member b in its initial configuration
$[\mathbf{B}_E(\mathbf{U})]_b$	Enlarged kinematic transformation matrix in current configuration
$[\mathbf{B}_E^0]_b$	Enlarged kinematic transformation matrix in initial configuration
$\mathcal{W}_{def}^*$	Virtual deformation work
$\mathcal{W}_{ext}^*$	Virtual external work of the applied forces
$\{\mathbf{P}\}$	Matrix of generalised nodal external forces
$\{\mathbf{U}^*\}$	Virtual global nodal displacements
$\{\mathbf{M}\}_b$	Matrix of generalised stresses of a frame member b
$M_b(x_b)$	Bending moment distribution along the element
$Q_b(x_b)$	Applied distributed load
$w_b(x_b)$	Deflections along the element b
$u_b(x_b)$	Longitudinal displacements along the element b
EI_b	Flexural rigidity of the element b
AE_b	Axial rigidity of the element b
$\mathbb{C}_1$ to $\mathbb{C}_4$	Integration constants
ϕ_i^0	Flexural rotation of the node i of the frame member b
ϕ_j^0	Flexural rotation of the node j of the frame member b
p_0	Uniformly distributed transverse load
$[\mathbf{F_0}]_b$	Flexibility matrix of the frame member b
$\{\boldsymbol{\phi}^{\mathbf{0}}\}_b$	Matrix of initial deformations
$[\mathbf{E_0}]_b$	Elasticity matrix of the frame member b
$\{\mathbf{M}^{\mathbf{0}}\}_b$	Matrix of initial stresses
a	Crack length
$\mathrm{E_T}$	Total energy
U	Deformation or strain energy

$\mathcal{W}_{ext}$	External work
$\mathrm{E_S}$	Necessary energy for the formation of new crack surfaces
G^a	Energy release rate
R^a	Cracking resistance
U_0	Deformation energy for a plate without crack
σ_0	Applied tension
Γ_S	Elastic surface energy of the material
a_{cr}	Critical crack half-length
K_I	Stress intensity factor (mode I)
K_{II}	Stress intensity factor (mode II)
K_{III}	Stress intensity factor (mode III)
ν	Poisson's ratio
K_C	Critical stress intensity factor
σ_C	Critical value for the applied stress
$\vec{\boldsymbol{n}}$	Cross section orientation in the RVE
S	Total area of the cross section $\vec{\boldsymbol{n}}$
S_D	Area of the micro-cracks, micro-voids or other defects, in the cross section $\vec{\boldsymbol{n}}$
$\tilde{S}$	Effective area of the cross section $\vec{\boldsymbol{n}}$
$\omega_{\vec{\boldsymbol{n}}}$	Local damage in the cross section $\vec{\boldsymbol{n}}$
ω	Isotropic damage in the RVE
$\tilde{\sigma}$	Effective stress in the RVE
ε	Total strain
ε^e	Elastic strain
ε^p	Plastic strain
ε^d	Damage strains
ω_u	Ultimate damage
G^ω	Energy release rate of a damaged RVE
R^ω	Damage resistance function
U^*	Complementary energy
$\{\boldsymbol{\phi^e}\}_b$	Matrix of generalised deformations of the elastic beam-column
$\{\boldsymbol{\phi^d}\}_b$	Damage deformation matrix
$\{\boldsymbol{\phi^p}\}_b$	Matrix of plastic deformations

ϕ_i^p, ϕ_j^p	Plastic rotations at the inelastic hinges i and j (respectively)
d_i, d_j	Damage variables at the inelastic hinges i and j (respectively)
$[\mathbf{C}(\mathbf{D})]_b$	Matrix of additional flexibility due to concrete cracking
$[\mathbf{F}(\mathbf{D})]_b$	Flexibility matrix of a damaged frame member
$[\mathbf{E}(\mathbf{D})]_b$	Elasticity matrix of a damaged frame member
G_i^d, G_j^d	Damage driving moments of the inelastic hinges i and j (respectively)
R_i^d, R_j^d	Crack resistance functions of the inelastic hinges
t	Total deflection of the beam-column pseudo-joint
$\mathfrak{E}(d)$	Specimen stiffness due to damage d
$\mathfrak{E}_0$	Specimen stiffness while undamaged
t_p	Plastic deflection of the beam-column pseudo-joint
R_{0_i}	Initial crack resistance at a hinge i
q_i	Hardening parameter at a hinge i
f_i	Yield function at a hinge i
c_i	Kinematic hardening parameter at a hinge i
M_{y_i}	Yield moment
M_{cr}	First cracking moment
M_u	Ultimate moment
d_u	Ultimate damage
M_p	Plastic moment
d_p	Plastic damage
ϕ_u^p	Ultimate plastic rotation
$\{\mathbf{L}\}$	Residual force vector
$\{\mathbf{Q}\}_b$	Matrix of internal forces at global coordinates
R_b	Radius of the arch element b
ψ_b	Arc angle of the arch element b
β_b	Angle between the axes Z and z_L
(X_C, Z_C)	Coordinates of the circle centre
$\{\mathbf{Q}^L\}_b$	Matrix of internal forces at local coordinates
$\{\mathbf{Q_0}\}_b$	Matrix of initial forces at global coordinates
$\{\mathbf{Q_0^L}\}_b$	Matrix of initial forces at local coordinates

$\{\mathbf{Q_0}_E\}_b$	Enlarged matrix of initial forces
U_b	Strain energy of an arch element b
$M(\theta)$	Bending moment at a section located at an angle θ
$N(\theta)$	Axial force at a section located at an angle θ
$[\mathbf{F_0^f}]_b$	Flexural flexibility matrix
$[\mathbf{F_0^a}]_b$	Axial flexibility matrix
$\{\mathbf{D}\}^T$	Damage variables matrix
d_a	Axial damage
$\dot{\mathcal{W}}_p$	Plastic power
θ_i^p	Plastic rotation at an inelastic hinge i
θ_j^p	Plastic rotation at an inelastic hinge j
Δ_i^p	Plastic elongation at an inelastic hinge i
Δ_j^p	Plastic elongation at an inelastic hinge j
δ^p	Generalised plastic elongation
μ	Decaying tendency of the quasi-brittle response
q_{un}	Hardening parameter for unreinforced concrete
W( )	Lambert W function
COD_i	Crack opening displacement at an inelastic hinge i
h	Cross section total height
$\tilde{h}$	Cross section effective height
$\widetilde{I_b}$	Effective inertia moment
G_f	Fracture energy
H_f	Fracture quantity proportional to G_f
Λ	Crack surface
C	Compliance of the inelastic hinge
$\tilde{A}$	Effective area of the cross section
γ	Parameter characterising the cross section geometry
b	Base of the cross section
P	Applied force
$\mathfrak{F}$	Correction factor
λ	Arbitrary constant

N	Cycle
$\{\mathbf{q}(\mathrm{N})\}_b$	Matrix of nodal displacements of a member b at a cycle N
$\{\boldsymbol{\phi}(\mathrm{N})\}_b$	Matrix of generalised deformations of a member b at a cycle N
$\{\mathbf{M}(\mathrm{N})\}_b$	Matrix of generalised stresses of a member b at a cycle N
$\{\mathbf{D}(\mathrm{N})\}$	Damage matrix of a member b at a cycle N
$\left[\mathbf{F}\left(\mathbf{D}(\mathrm{N})\right)\right]_b$	Flexibility matrix of a damaged member b at a cycle N
G_a^d	Axial damage driving moment
$\{\mathbf{P}(\mathrm{N})\}$	Cyclic applied load
$\mathrm{C_P}$, $\mathrm{n_P}$	Material parameters of the Paris law
σ_{cr}, ε_{cr}, ε_u	Material parameters for one-dimensional damage models
m_{cr}, ϕ_u	Material parameters for a flexural lumped damage model
$\{\mathbf{q}\}_t$	Matrix of nodal generalised displacements of the CMT element
w_i, w_j, w_k	Deflections of the nodes i, j and k of the CMT element
θ_a, θ_b, θ_c	Normal slopes at the sides ij, jk and ki of the CMT element
$w(x,y)$	Deflection of the CMT element
$z(x,y)$	Rigid-body deflection of the CMT element
$w^r(x,y)$	Relative deflection of the CMT element
$\{\boldsymbol{\phi}\}_t$	Matrix of generalised deformations of the CMT element
ϕ_a, ϕ_b, ϕ_c	Flexural rotations at the sides ij, jk and ki of the CMT element
$[\mathbf{B}^0]_t$	Kinematic transformation matrix of the CMT element
L_{ij}, L_{jk}, L_{ki}	Lengths of the sides of the CMT element
$\{\boldsymbol{\chi}\}_t$	Matrix of curvatures of the CMT element
$[\mathbf{T}]_t$	Transformation matrix of the CMT element
m_{xx}, m_{yy}, m_{xy}	Specific constant moments of the CMT element
$\{\boldsymbol{\beta}\}_t$	Specific bending moment matrix of the CMT element
m_a, m_b, m_c	Normal specific bending moments at the sides of the CMT element
$\{\mathbf{M}\}_t$	Generalised stress matrix of the CMT element
M_{ij}, M_{jk}, M_{ki}	Generalised stresses
$\{\mathbf{Q}\}_t$	Nodal forces of the CMT element

$[\mathbf{D}]_t$	Flexural rigidity matrix
D	Bending stiffness of the plate
U_f	Strain energy of the CMT element
$[\mathbf{F_0}]_t$	Flexibility matrix of the CMT element
$\{\boldsymbol{\phi}^{\boldsymbol{d}}\}_t$	Matrix of generalised damage deformations of the CMT element
$\phi_a^d, \phi_b^d, \phi_c^d$	Generalised damage deformations
$\{\boldsymbol{\phi}^{\boldsymbol{e}}\}_t$	Matrix of elastic deformations of the CMT element
δ^e	Elastic elongation
δ^d	Elongation of the localisation band
δ_u	Ultimate elongation of the localisation band
$\{\boldsymbol{\varepsilon}\}_b$	Strain matrix
$\{\boldsymbol{\sigma}\}_b$	Stress matrix
$[\mathbf{K}]_b$	Stiffness matrix
$[\mathbf{b}]_b, [\mathbf{b}']_b$	Conventional compatibility matrix
$[\mathbf{H}]$	Matrix of elastic coefficients
$\{\boldsymbol{\delta}\}_b$	Matrix of generalised deformations
$\delta_{ij}, \delta_{ik}, \delta_{il}, \delta_{jk}, \delta_{kl}$	Total elongations of the equivalent truss
$[\mathbf{T}]_b, [\mathbf{T}']_b$	Transformation matrix
$\{\boldsymbol{\delta}^{\boldsymbol{d}}\}_b$	Matrix of generalised damage deformations
$\epsilon_{\blacksquare *}$	Thickness of the band at the node ■ in the $*$ direction
$\{\boldsymbol{\delta}^{\boldsymbol{e}}\}_b$	Matrix of elastic deformations

SUMMARY

1 INTRODUCTION

The analysis and prediction of nonlinear structural behaviour is an important issue for engineers and researchers. Nonlinear theories were proposed in order to achieve an accurate description of the structural behaviour. Among classic nonlinear theories, three options are emphasised: theory of plasticity, fracture mechanics and damage mechanics.

Theory of plasticity is probably the most known nonlinear framework. In this theory, local plastic strains are responsible to account for the deterioration process.

Classic fracture mechanics is a powerful tool to analyse propagation of a small number of cracks in continuum media. Differently from plasticity, in fracture mechanics a small number of discrete cracks characterises the deterioration process. The crack propagation is taken into account by energy principles. This approach shows remarkable success for structures with simple geometries, few cracks and homogeneous materials.

Classic damage mechanics is the most recent great theory to describe the processes of deterioration and structural failure. The fundamental idea is quite simple: the introduction of an internal variable that characterises the material deterioration. This variable, called damage, usually takes values between zero and one. Damage is introduced in the behaviour laws also using simple concepts: an effective stress combined to a strain equivalence hypothesis. This theory has been successful in the description of several deterioration mechanisms in continuum media.

Usually, the structural modelling is carried out using finite elements. For several engineering applications, frame members are sufficient to analyse structural behaviour. Thus, during the 20^{th} century, several engineers and researchers proposed models based on plasticity to analyse frame structures.

Alternatively, a recent nonlinear theory, called Lumped Damage Mechanics (LDM), was introduced in the early nineties in order to achieve more realistic results of frame structures. LDM applies some key concepts from fracture and damage mechanics in plastic hinges. Therefore, LDM models usually present suitable results for practical problems. It is noteworthy that the great majority of LDM models were developed to analyse reinforced concrete structures under monotonic or seismic loadings.

On the other hand, in some specific cases, structures should be modelled as continuum media. This consideration demands two-dimensional or even three-dimensional finite element

analyses. As previously mentioned, the three emphasised classic theories (theory of plasticity, fracture and damage mechanics) applied in finite element programmes can describe the nonlinear structural behaviour.

However, all aforementioned classic theories present some drawbacks. For instance, fracture mechanics demands the consideration of initial cracks to begin the analysis. This characteristic is not always suitable for practical applications. Another important drawback, which is clearly observed in classic plasticity and damage models, is a phenomenon called localisation. Note that localisation is a common term for physical and mathematical evidences. From the physical point of view, localisation denotes the formation of, for instance, shear bands with strain discontinuities; in other words, localisation is a physical phenomenon experimentally observed. From the mathematical point of view, localisation is a term used to refer to the mathematical drawbacks of classic damage or plasticity models, such as the loss of ellipticity that leads to ill-posed problems and mesh-dependent numerical algorithms. The failure of the classic damage mechanics in describing localisation bands marked the end of this stage of the theory.

Therefore, modern damage mechanics was developed to circumvent this issue with two basic ideas: a modification in the damage evolutions laws by weight functions (nonlocal models) and the introduction of suitable kinematics (strain or displacement discontinuities) to take into account the damage localisation. In common, both ideas seek one main objective: the development of models that lead to objective numerical results. For a detailed review on modern damage models see, e.g., Comi (1996), Peerlings et al. (1996), Manzoli, Oliver and Cervera (1998), Comi and Rizzi (2000), Comi and Perego (2001), Bažant and Jirásek (2002), Desmorat, Gatuingt and Ragueneau (2007), Richard and Ragueneau (2013) and references therein. Some of those models were specifically developed to analyse concrete structures. Bažant and Lin (1988) was one of the very first model to consider a nonlocal model for concrete. Note that Comi and Perego (2001) presented a remarkable local damage approach considering a fracture energy regularisation. Regarding nonlocal models, Desmorat, Gatuingt and Ragueneau (2007) proposed a three-dimensional nonlocal damage model with induced damage anisotropy. Richard and Ragueneau (2013) proposed a nonlocal damage model for structures subjected to cyclic loadings, where crack closure is also considered.

In the light of the foregoing, despite their accuracy and importance, the aforementioned theories (theory of plasticity, fracture and damage mechanics) present drawbacks or limitations in terms of computational costs or structural modelling that may

difficult their use for some engineering applications. Alternatively, LDM presents itself as an interesting tool for the modelling of structural behaviour.

Therefore, the objective of this thesis is to describe, numerically, the nonlinear structural behaviour by means of LDM. To reach this objective, the LDM framework must be extended. In this sense, this thesis is organised as follows.

Chapter 2 presents a review in LDM for frame structures, where a historic overview and the main concepts of fracture and damage mechanics are briefly highlighted in order to present the LDM theory for reinforced concrete frames. Note that, so far, all developments in LDM were presented to straight frames.

Therefore, chapter 3 depicts the first original contribution of this thesis: LDM model for reinforced concrete arches. This is an important advance, once some structures are composed by arches. Chapter 3 also presents the second original development of this thesis: LDM model for quasi-brittle structures. This model was used to analyse unreinforced concrete beams, a tunnel lining and masonry arches, showing the capability of the LDM approach.

Chapter 4 illustrates the use of LDM to analyse high cycle fatigue problems. Such advance is the third original development of this thesis. At this point, some concepts of fracture mechanics, such as stress intensity factors, are easily applied in LDM framework. This new approach allows for a simple and accurate solution of high cycle fatigue problems.

Finally, chapter 5 opens a new research frontier: the extension of the LDM framework to continuum media. In this thesis, bending and tensile plates were used to illustrate the capability and accuracy of this new LDM approach. So far, LDM was usually taken as a simplified methodology to analyse frame structures. Note that, for the analysed examples, the extended LDM shows objectivity (refinement- or size-independence). Such observation may characterise LDM as a new general theory to analyse the nonlinear structural behaviour.

2 LUMPED DAMAGE MECHANICS FOR FRAME STRUCTURES

2.1 Preamble

Several civil engineering structures, such as buildings, bridges, cranes and electrical towers, are usually analysed as frames. Thus, the frame analysis is one of the most important themes in structural engineering. However, many textbooks that broach the frame analysis present solely linear elastic approaches.

Some researchers and engineers presented simplified methodologies in order to characterise nonlinear phenomena in frames. Since most of those models where developed during the second half of the 20th century, they were based the concept of plastic hinges. On what follows, some of the main contributions in the field of the simplified methodologies are briefly reviewed.

The very first inelastic beam model intending to analyse the inelastic earthquake response of tall buildings was proposed by Clough, Benuska and Wilson (1965). In such model the inelastic deformations are concentrated in plastic hinges at the edges of the beam element and the stiffness degradation is accounted for by a perfectly plastic rule.

Concerning the behaviour of reinforced concrete structures, an important step into a more realistic modelling was given by Takeda, Sozen and Nielsen (1970), where a tri-linear force-deflection curve was proposed based on experimental observations using an earthquake simulator. This model accounts for concrete cracking, steel yielding and stiffness degradation under cyclic load reversals by means of a specific set of rules.

Riva and Cohn (1990) proposed a method which combines a moment-rotation constitutive model with a relatively simple structural model, considering the effect of lumped plasticity. As a general condition, for certain load level the distributions of moment and curvature of the structure are determined in a way to satisfy equilibrium, constitutive and compatibility relations.

Mulas and Filippou (1990) proposed an analytical approach to analyse the nonlinear behaviour of reinforced concrete frames under seismic loading. Mulas and Filippou (1990) also discussed the modelling of elements and the development of efficient numerical techniques to analyse nonlinear dynamics.

Later works also applied concepts from fracture (BROEK, 1984) and continuum damage mechanics (LEMAITRE; CHABOCHE, 1985) in plastic hinges. Some of these simplified methodologies are briefly reviewed on what follows.

Flórez-López (1993, 1995) and Cipollina, López-Inojosa and Flórez-López (1995) proposed a methodology which considers lumped dissipation mechanisms to analyse the behaviour of reinforced concrete structures. In this procedure it can be proved (with some matrix manipulation) that the elastic equations are the same of the direct stiffness method, now written using Powell's (1969) notation. In such model the concrete cracking, steel yielding and stiffness degradation induced by reversal cyclic loading are accounted for using the Griffith criterion (damage evolution law) and a kinematic hardening law. Perdomo, Ramírez and Flórez-López (1999) generalised such method by considering variable axial forces along the frame member; and the equations of such model were rewritten in terms of flexibility.

Another generalisation of the model proposed by Flórez-López (1993, 1995) was presented by Álvares (1999), where a criterion of bending moment transmission between the nodes of the same element is proposed, based on the direct stiffness method. Alva (2004) and Alva and El Debs (2010) proposed a modification of the model presented by Álvares (1999) by means of a penalising factor on the damage evolution law in order to achieve a more accurate reproduction of experimental responses.

According to Perera et al. (2000), models based on Griffith criterion are not capable of reproduce with good precision the collapse of structures under seismic actions. Thereby, Perera et al. (2000) proposed a lumped damage model which considers the accumulated fatigue, based on the formulation presented by Perdomo, Ramírez and Flórez-López (1999). Later, Kaewkulchai and Williamson (2004) proposed a model to analyse progressive collapse. Such model is based on the frame element proposed by Kim (1995).

Faleiro, Oller and Barbat (2010) proposed a model based on the formulation presented by Flórez-López (1993, 1995) and Cipollina, López-Inojosa and Flórez-López (1995), where modifications were proposed on yield and damage laws. Santoro and Kunnath (2013) proposed a beam element based on the formulation presented by Perdomo Ramírez and Flórez-López (1999), although some modifications on yield function and damage evolution laws were also proposed.

Toi and Hasegawa (2011) proposed a lumped dissipation model where an inelastic hinge can appear anywhere along a Bernoulli-Euler finite beam element. The formation of the inelastic hinge is based on some criteria which are valid solely for Bernoulli-Euler cubic

elements with two integration points. According to Toi and Hasegawa (2011), this lumped dissipation model is mesh-independent.

None of the aforementioned approaches is capable to reproduce the hysteresis phenomena in an unloading-reloading procedure. Thus, Araújo (2007) and Araújo and Proença (2008) proposed a formulation so-called lumped dissipation model with hysteresis (LDMH). This model is a generalisation of the formulation proposed by Flórez-López (1993, 1995) with some concepts introduced by Alva (2004).

Recently, Flórez-López and Proença (2013) presented a lumped plasticity model for arches. Such model is based on the elastic formulation presented by Palaninathan and Chandrasekharan (1985), being adopted the Powell's notation and the plastic hinge concept.

Summarising, it is noteworthy that several researchers around the world developed frame models to study inelastic phenomena. Several frame models adopted the concept of plastic hinges, and some of those introduced concepts of fracture and continuum damage mechanics. Such models are usually based on the pioneer works of Flórez-López (1993, 1995) and Cipollina, López-Inojosa and Flórez-López (1995), which originated a new branch of structural analysis called *Lumped Damage Mechanics*. This general interest shows the importance of this theme for engineering applications.

The term *Lumped Damage Mechanics* was firstly coined by Marante and Flórez-López (2003) to characterise the nonlinear modelling of frame structures using concepts of fracture and continuum damage mechanics with the idea of plastic hinges. Flórez-López, Marante and Picón (2015) published the first book about lumped damage mechanics (LDM).

2.2 Theory of structures for planar frames

2.2.1 An introduction to Powell's notation

Until early sixties linear elastic structures were usually studied through the well-established force and displacement methods. Powell aimed for a new set of equations in an attempt to achieve a standardisation for a theory including geometric nonlinear effects in elastic structures.

To reach this objective, Powell proposed a theoretical formulation assuming small strains and large displacements. The new formulation was originally applied on frames, therefore involving both flexural effects and axial strain effects. However, Powell ensured that this methodology could be extended to other finite elements, such as the elements for plate bending, plane and three-dimensional stress.

In this theory, the frame structure is understood as composed by rigid joints linked by deformable structural (frame) members. It is also assumed that members are initially straight and external forces are applied only at the joints.

From now on, due to the further developments of this thesis, Powell's notation is presented only for linear elastic frame members. The structural behaviour of the frame members are deduced considering the Euler-Bernoulli flexure theory:

$$M(x) = EI\frac{d^2w}{dx^2} \tag{2.1}$$

$$N(x) = AE\frac{du}{dx} \tag{2.2}$$

where $M(x)$ and $N(x)$ are, respectively, the bending moment and axial force distributions along the element, E is the Young's modulus, I is the inertia moment of the cross section, A is the area of the cross section, w is the transverse displacement and u is the longitudinal displacement. Note that in the original development (POWELL, 1969) eq.(2.2) also presents a quadratic term $AE/2\,(dw/dx)^2$ in order to introduce the effects of large displacements.

According to the proposed development, the deformations and rigid body displacements of the element must be separated. Consider a frame member deformed without rigid body displacements (see Figure 2.1a). In such configuration, the member presents generalised deformations (ϕ_i, ϕ_j, δ) which are, respectively, two flexural rotations and a chord elongation. Combined to such deformations, there are generalised stresses (m_i, m_j, n_b), respectively, two bending moments and an axial force.

The unique definition of the kinematics of each element in terms of the member generalised deformations implies a unique solution for the behaviour of the complete structure in terms of joints generalised displacements. Therefore, the objective turns into the correct representation of axial and transverse displacements at any point of the element in terms of the generalised deformations.

The longitudinal $u(x)$ and transversal $w(x)$ displacements are represented by linear and cubic polynomials, respectively. Considering the supports in Figure 2.1b and assuming that the difference between the deformed (L) and initial (L_0) lengths are negligible, the equations for longitudinal and transversal displacements along the member and the correspondent boundary conditions are written as follows:

$$u(0) = 0 \qquad u(L) = \delta$$
$$u(x) = \frac{x}{L}\delta \tag{2.3}$$

$$w(0) = w(L) = 0 \qquad -\left.\frac{dw}{dx}\right|_{x=0} = \phi_i \qquad -\left.\frac{dw}{dx}\right|_{x=L} = \phi_j$$
$$w(x) = \left(-\frac{x^3}{L^2} + \frac{2x^2}{L} - x\right)\phi_i + \left(-\frac{x^3}{L^2} + \frac{x^2}{L}\right)\phi_j \tag{2.4}$$

Both equations for longitudinal $u(x)$ and transversal $w(x)$ displacements, parameterised by the generalised deformations, depict the deformed shape of the frame member shown in Figure 2.1b.

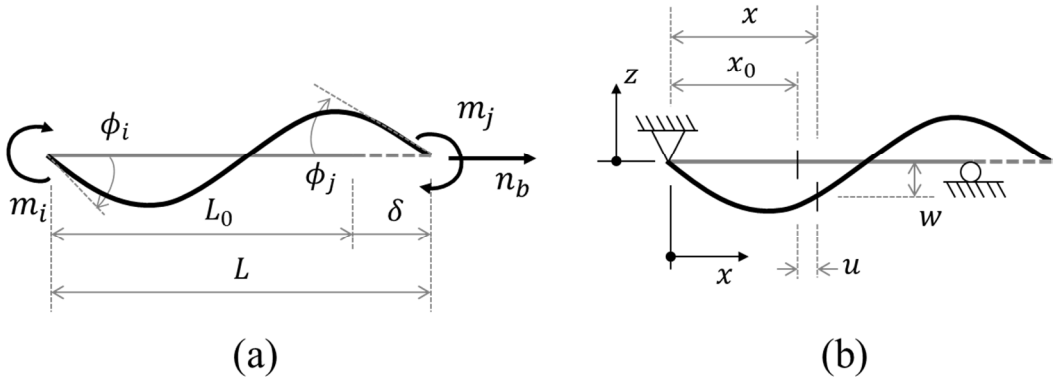

Figure 2.1 – (a) Member actions and deformations and (b) displacements of differential element (POWELL, 1969).

Then, using equations (2.1) and (2.2) the distributions of bending moments and axial forces along the element are given by the following equations:

$$M(x) = EI\left[\left(-\frac{6x}{L^2} + \frac{4}{L}\right)\phi_i + \left(-\frac{6x}{L^2} + \frac{2}{L}\right)\phi_j\right] \tag{2.5}$$

$$N(x) = AE\frac{\delta}{L} \tag{2.6}$$

On what follows, Powell's notation is employed in its reduced form to linear elastic frames, in order to introduce the concepts of lumped damage mechanics (FLÓREZ-LÓPEZ; MARANTE; PICÓN, 2015).

2.2.2 Kinematics of plane frames

Consider a planar frame structure composed by m members connected by n nodes (Figure 2.2a). The matrix of generalised displacements of the node i is denoted as:

$$\{\boldsymbol{u}\}_i = \{u_i \quad w_i \quad \theta_i\}^T \tag{2.7}$$

where u_i and w_i are the displacements at the directions of the global axes: X and Z, respectively, and θ_i is the total rotation of the node with respect to initial configuration; the superscript T means transpose. Then the matrix of the generalised nodal displacements of a member b between the nodes i and j is denoted by:

$$\{\mathbf{q}\}_b = \left\{\{\boldsymbol{u}\}_i^T \quad \{\boldsymbol{u}\}_j^T\right\}^T = \{u_i \quad w_i \quad \theta_i \quad u_j \quad w_j \quad \theta_j\}^T \tag{2.8}$$

The generalised nodal displacement matrix of the structure is given by gathering the generalised displacements of all nodes:

$$\{\mathbf{U}\} = \{\{\boldsymbol{u}\}_1^T \quad \{\boldsymbol{u}\}_2^T \quad \ldots \quad \{\boldsymbol{u}\}_{\mathrm{n}}^T\}^T = \{u_1 \quad w_1 \quad \theta_1 \quad u_2 \quad \ldots \quad u_{\mathrm{n}} \quad w_{\mathrm{n}} \quad \theta_{\mathrm{n}}\}^T \tag{2.9}$$

Note that the generalised nodal displacement matrix describes only components of the nodal rigid body movement i.e. there is no explicit information about the elastic behaviour and shape modification of the structure. To describe element deformations, a second set of variables, called generalised deformations, is needed. As previously introduced, the generalised deformation matrix of a member b, between nodes i and j, is denoted by $\{\boldsymbol{\phi}\}_b = \{\phi_i \quad \phi_j \quad \delta\}^T$, where ϕ_i and ϕ_j are the relative rotations of the cross sections i and j with respect to the chord $i-j$, respectively, and δ is the chord elongation (see Figure 2.2b).

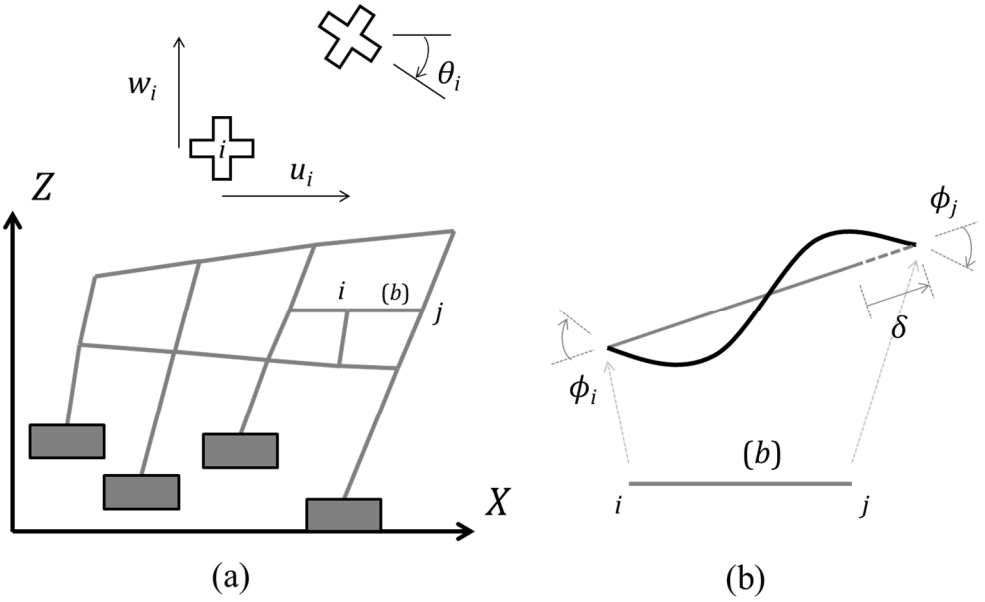

Figure 2.2 – (a) Planar frame structure and generalised displacements of node i; (b) generalised deformations of a member b between nodes i and j.

If the frame member b suffers solely rigid body movement, the generalised deformation matrix $\{\boldsymbol{\phi}\}_b$ is nil. If there is shape modification of the member, the generalised deformations indicate the new shape of the member. The possible shape changes according to the given signs of each rotation component is depicted in Figure 2.3. The terms ϕ_i and ϕ_j specify the flexural behaviour of the member b i.e. if ϕ_i and ϕ_j present same sign, the frame member b shows an 'S-like' deformed shape (Figure 2.3a); if ϕ_i and ϕ_j present different signs, the frame member b shows a 'C-like' deformed shape (Figure 2.3b). Positive or negative sign of the term δ indicates if the member b is stretched or shortened from its original length, respectively.

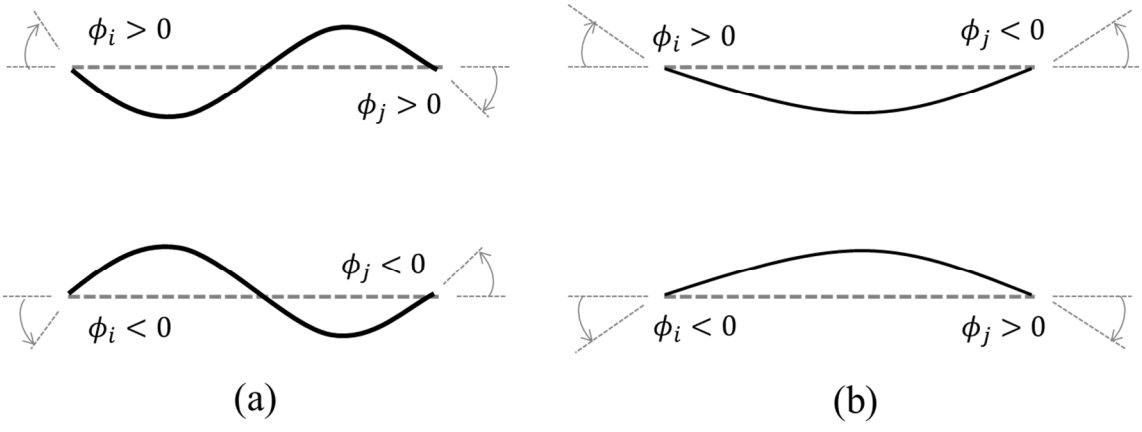

Figure 2.3 – Deformed shapes of a frame member b due to generalised deformations ϕ_i and ϕ_j.

The generalised deformations can be obtained from the generalised displacements by means of geometrical considerations. For instance, consider a frame member b connected to nodes i and j as depicted in Figure 2.4. In such figure, the frame member is presented in its initial configuration. Note that in Figure 2.4 both global (XZ) and local $(x_L z_L)$ axes are shown. For a frame member, the local axes are such that present the origin at the node i and the x_L-axis direction coincides with the chord $i-j$ of the member. The member in its initial configuration forms an angle α_b^0 with the horizontal and presents L_b^0 as chord length. After nodal movements, the angle and the cord length change, being described by the generalised displacements of the member i.e. $\alpha_b = \alpha_b(\{\mathbf{q}\}_b)$, $L_b = L_b(\{\mathbf{q}\}_b)$.

The generalised displacements can also be attached to the local coordinate axes (Figure 2.4): $\{\mathbf{q}^L\}_b^T = \{u_i^L \quad w_i^L \quad \theta_i^L \quad u_j^L \quad w_j^L \quad \theta_j^L\}$. Both global $\{\mathbf{q}\}_b$ and local $\{\mathbf{q}^L\}_b$ generalised displacement matrices are geometrically related as follows:

$$\begin{aligned}
u_i^L &= u_i \cos\alpha_b + w_i \sin\alpha_b \\
w_i^L &= -u_i \sin\alpha_b + w_i \cos\alpha_b \\
\theta_i^L &= \theta_i \\
u_j^L &= u_j \cos\alpha_b + w_j \sin\alpha_b \\
w_j^L &= -u_j \sin\alpha_b + w_j \cos\alpha_b \\
\theta_j^L &= \theta_j
\end{aligned} \tag{2.10}$$

Eq.(2.10) can be rewritten in matrix form:

$$\{\mathbf{q}^L\}_b = [\mathbf{T}]_b\{\mathbf{q}\}_b \qquad \therefore\ [\mathbf{T}]_b = \begin{bmatrix} \cos\alpha_b & \sin\alpha_b & 0 & 0 & 0 & 0 \\ -\sin\alpha_b & \cos\alpha_b & 0 & 0 & 0 & 0 \\ 0 & 0 & 1 & 0 & 0 & 0 \\ 0 & 0 & 0 & \cos\alpha_b & \sin\alpha_b & 0 \\ 0 & 0 & 0 & -\sin\alpha_b & \cos\alpha_b & 0 \\ 0 & 0 & 0 & 0 & 0 & 1 \end{bmatrix} \tag{2.11}$$

where $[\mathbf{T}]_b$ is the axes transformation matrix.

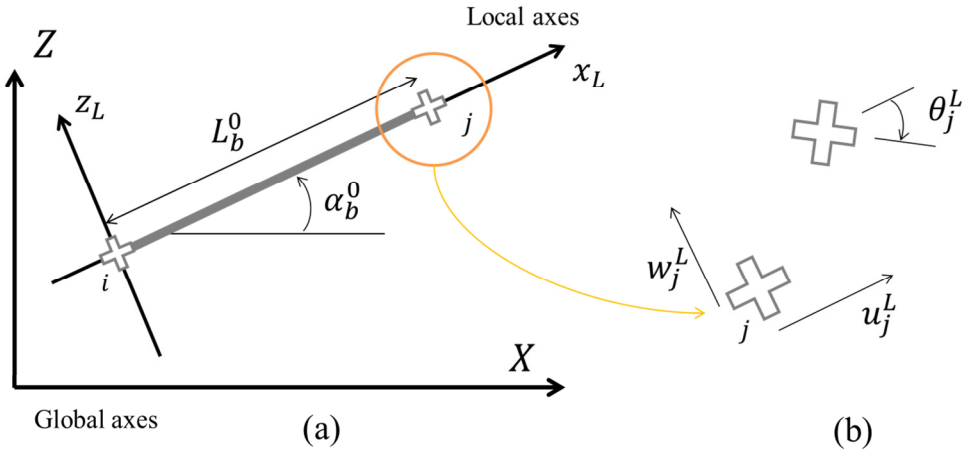

Figure 2.4 – (a) Local coordinates for a frame member b and (b) generalised displacements in the local coordinate axes.

The relationship between generalised displacements and generalised deformations can be easily deduced from the local coordinate system (Figure 2.5). For each infinitesimal generalised displacement applied at a node, i or j, the frame member presents an specific deformed configuration, given by increments of generalised deformations.

Consider a horizontal infinitesimal displacement du_i^L applied at node i (Figure 2.5a). Such infinitesimal displacement only reduces the member length i.e.

$$d\phi_i = 0 \qquad d\phi_j = 0 \qquad d\delta = -du_i^L \tag{2.12}$$

By applying a vertical infinitesimal displacement dw_i^L at the node i (Figure 2.5b), increments of relative rotations of the member's cross sections i and j are obtained, but there are no cord elongation:

$$d\phi_i = -\frac{dw_i^L}{L_b} \qquad d\phi_j = -\frac{dw_i^L}{L_b} \qquad d\delta = 0 \tag{2.13}$$

An infinitesimal rotation $d\theta_i^L$ (Figure 2.5c) results only on an increment of relative rotation of the member's cross section i:

$$d\phi_i = d\theta_i^L \qquad d\phi_j = 0 \qquad d\delta = 0 \tag{2.14}$$

Analogously, the same procedure is applied to node j (Figure 2.5d-f) resulting on the following relations:

$$d\phi_i = 0 \qquad d\phi_j = 0 \qquad d\delta = du_j^L \tag{2.15}$$

$$d\phi_i = \frac{dw_j^L}{L_b} \qquad d\phi_j = \frac{dw_j^L}{L_b} \qquad d\delta = 0 \tag{2.16}$$

$$d\phi_i = 0 \qquad d\phi_j = d\theta_j^L \qquad d\delta = 0 \tag{2.17}$$

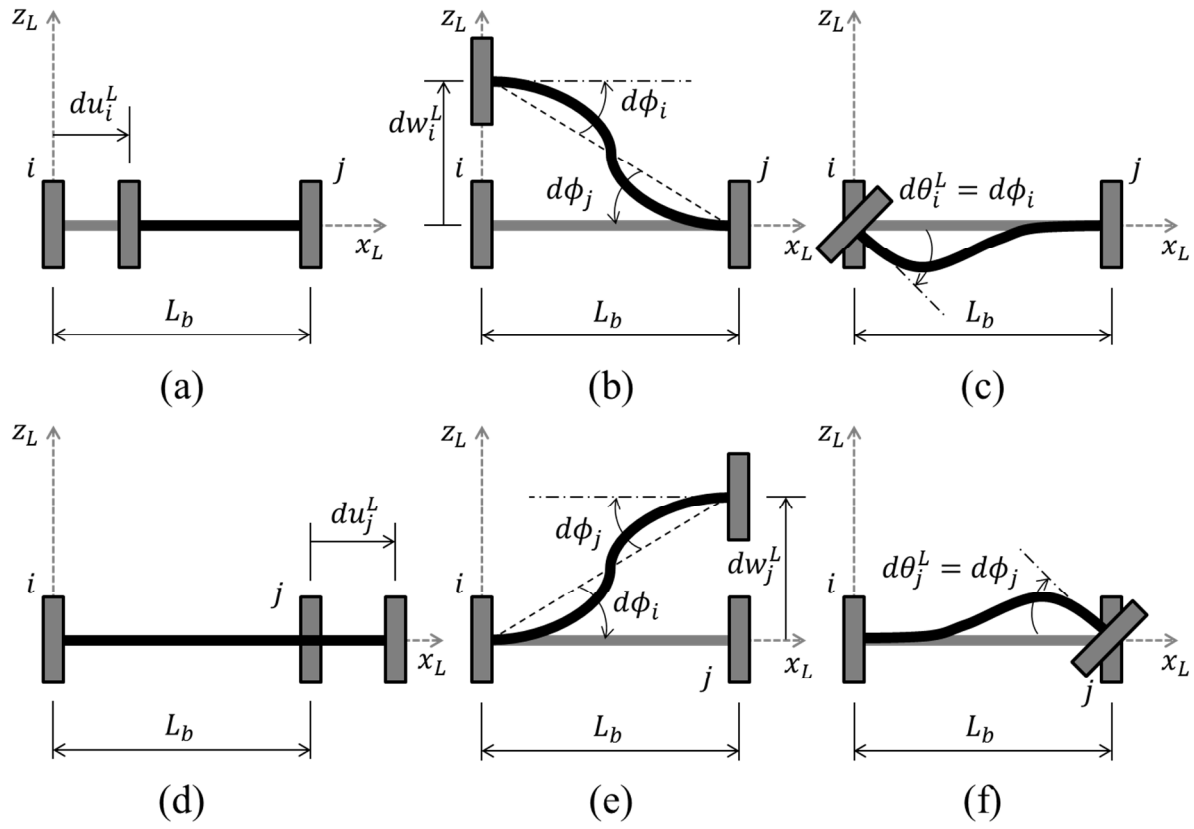

Figure 2.5 – Increment of generalised deformations of a frame member b due to infinitesimal generalised displacements at the nodes i and j.

Now, considering all infinitesimal displacements at the same time, the increments of generalised deformations are:

$$\begin{cases} d\phi_i = -\dfrac{dw_i^L}{L_b} + d\theta_i^L + \dfrac{dw_j^L}{L_b} \\ d\phi_j = -\dfrac{dw_i^L}{L_b} + \dfrac{dw_j^L}{L_b} + d\theta_j^L \\ d\delta = -du_i^L + du_j^L \end{cases} \quad \Rightarrow \quad \{d\boldsymbol{\phi}\}_b = [\mathbf{B}(\mathbf{q}^L)]_b \{d\mathbf{q}^L\}_b \tag{2.18}$$

$$\therefore \quad [\mathbf{B}(\mathbf{q}^L)]_b = \begin{bmatrix} 0 & -\dfrac{1}{L_b} & 1 & 0 & \dfrac{1}{L_b} & 0 \\ 0 & -\dfrac{1}{L_b} & 0 & 0 & \dfrac{1}{L_b} & 1 \\ -1 & 0 & 0 & 1 & 0 & 0 \end{bmatrix}$$

where $[\mathbf{B}(\mathbf{q}^L)]_b$ is the kinematic transformation matrix of the member b in the local coordinate system. The substitution of eq.(2.10) in eq.(2.18) results:

$$\{d\boldsymbol{\phi}\}_b = [\mathbf{B}(\mathbf{q}^L)]_b [\mathbf{T}]_b \{d\mathbf{q}\}_b = [\mathbf{B}(\mathbf{q})]_b \{d\mathbf{q}\}_b$$

$$\therefore \quad [\mathbf{B}(\mathbf{q})]_b = \begin{bmatrix} \dfrac{\sin\alpha_b}{L_b} & -\dfrac{\cos\alpha_b}{L_b} & 1 & -\dfrac{\sin\alpha_b}{L_b} & \dfrac{\cos\alpha_b}{L_b} & 0 \\ \dfrac{\sin\alpha_b}{L_b} & -\dfrac{\cos\alpha_b}{L_b} & 0 & -\dfrac{\sin\alpha_b}{L_b} & \dfrac{\cos\alpha_b}{L_b} & 1 \\ -\cos\alpha_b & \sin\alpha_b & 0 & \cos\alpha_b & \sin\alpha_b & 0 \end{bmatrix} \tag{2.19}$$

where $[\mathbf{B}(\mathbf{q})]_b$ is the kinematic transformation matrix of the member b. Note that eq.(2.19) is valid for the nonlinear case, where the effects of geometric nonlinearity are taken into account. However, when such effects can be neglected (because structures are usually very rigid) the kinematic equation can be expressed as:

$$\alpha_b \cong \alpha_b^0 \qquad L_b \cong L_b^0 \qquad \{\boldsymbol{\phi}\}_b \cong [\mathbf{B}^0]_b \{\mathbf{q}\}_b \tag{2.20}$$

where $[\mathbf{B}^0]_b$ is the kinematic transformation matrix referred to the initial configuration of the structure.

The kinematic equation can also be expressed in terms of the displacement matrix of the structure:

$$\{d\boldsymbol{\phi}\}_b = [\mathbf{B}_E(\mathbf{U})]_b\{d\mathbf{U}\}$$
or
$$\{\boldsymbol{\phi}\}_b \cong [\mathbf{B}_E^0]_b\{\mathbf{U}\} \tag{2.21}$$

where $[\mathbf{B}_E(\mathbf{U})]_b$ (or $[\mathbf{B}_E^0]_b$) is denoted enlarged transformation matrix and it is built by adding columns of zeros in the positions of nodes that do not belong to the member, i.e.

$$[\mathbf{B}_E(\mathbf{U})]_b = \begin{matrix} \\ \\ \\ \downarrow \\ u_1 \end{matrix} \begin{matrix} \\ \\ \\ \downarrow \\ w_1 \end{matrix} \begin{matrix} \\ \\ \\ \\ \dots \end{matrix} \begin{matrix} \\ \\ \\ \downarrow \\ u_i \end{matrix} \begin{matrix} \\ \\ \\ \downarrow \\ w_i \end{matrix} \begin{matrix} \\ \\ \\ \downarrow \\ \theta_i \end{matrix} \begin{matrix} \\ \\ \\ \downarrow \\ u_{i+1} \end{matrix} \begin{matrix} \\ \\ \\ \\ \dots \end{matrix} \begin{matrix} \\ \\ \\ \downarrow \\ u_j \end{matrix} \begin{matrix} \\ \\ \\ \downarrow \\ w_j \end{matrix} \begin{matrix} \\ \\ \\ \downarrow \\ \theta_j \end{matrix} \begin{matrix} \\ \\ \\ \\ \dots \end{matrix} \begin{matrix} \\ \\ \\ \downarrow \\ \theta_{\mathrm{n}} \end{matrix}$$
$$= \begin{bmatrix} 0 & 0 & \dots & \frac{\sin\alpha_b}{L_b} & -\frac{\cos\alpha_b}{L_b} & 1 & 0 & \dots & -\frac{\sin\alpha_b}{L_b} & \frac{\cos\alpha_b}{L_b} & 0 & \dots & 0 \\ 0 & 0 & \dots & \frac{\sin\alpha_b}{L_b} & -\frac{\cos\alpha_b}{L_b} & 0 & 0 & \dots & -\frac{\sin\alpha_b}{L_b} & \frac{\cos\alpha_b}{L_b} & 1 & \dots & 0 \\ 0 & 0 & \dots & -\cos\alpha_b & \sin\alpha_b & 0 & 0 & \dots & \cos\alpha_b & \sin\alpha_b & 0 & \dots & 0 \end{bmatrix} \tag{2.22}$$

2.2.3 Statics of plane frames

Applying the principle of virtual work, the static equilibrium of a structure can be described by the following equation:

$$\mathcal{W}_{def}^* = \mathcal{W}_{ext}^* \tag{2.23}$$

where $\mathcal{W}_{def}^*$ is the deformation work, $\mathcal{W}_{ext}^*$ is the external work of the applied forces, and the superscript * means virtual.

Now, consider a general frame structure as the one depicted on Figure 2.6a. Note that there are applied forces and moments concentrated at nodes and distributed loads on loading members (blue arrows in Figure 2.6a). As usual in structural analysis, distributed loading on members can be substituted by equivalent forces, which are applied on nodes. Therefore, all external loads can be gathered in a matrix of generalised nodal external forces:

$$\{\mathbf{P}\} = \{P_{u1} \quad P_{w1} \quad P_{\theta 1} \quad P_{u2} \quad \dots \quad P_{ui} \quad P_{wi} \quad P_{\theta i} \quad \dots \quad P_{w\mathrm{n}} \quad P_{\theta\mathrm{n}}\}^T \tag{2.24}$$

Note that for each generalised force component there are two indexes: the first one is related to the global reference direction i.e. u for horizontal force, w for vertical force and θ for bending moment; and the second one is related to the node i.e. $1,2,\dots,i,j,\dots$ n.

Then, being $\{\mathbf{U}^*\}$ the matrix of the virtual global nodal displacements, the external virtual work is defined as:

$$\mathcal{W}^*_{ext} = \{\mathbf{U}^*\}^T\{\mathbf{P}\} \tag{2.25}$$

In order to obtain the expression of the deformation work for a frame element, the generalised stress matrix $\{\mathbf{M}\}_b^T = \{m_i, m_j, n_b\}$ of a member b is immediately introduced. In such matrix m_i and m_j are the bending moments at the member ends and n_b the axial force (see Figure 2.6b). Thus, considering the conjugated generalised deformation matrix $\{\boldsymbol{\phi}^*\}_b$, the expression of the deformation work results:

$$\mathcal{W}^*_{def} = \sum_{b=1}^{\mathrm{m}} \{\boldsymbol{\phi}^*\}_b^T\{\mathbf{M}\}_b \tag{2.26}$$

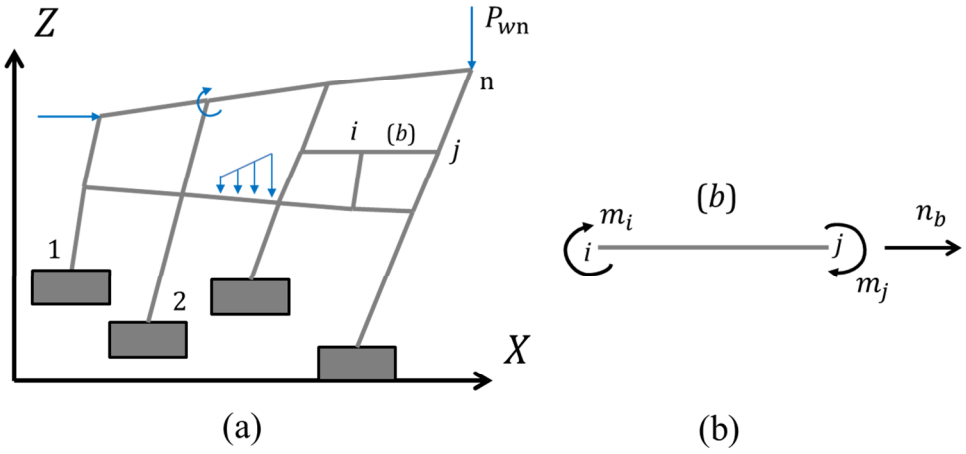

Figure 2.6 – (a) External forces on a frame structure and (b) generalised stresses in a frame member.

The equilibrium equation is obtained by substituting (2.25) and (2.26) int (2.23):

$$\sum_{b=1}^{\mathrm{m}} \{\boldsymbol{\phi}^*\}_b^T \{\mathbf{M}\}_b = \{\mathbf{U}^*\}^T \{\mathbf{P}\} \quad \Rightarrow \quad \sum_{b=1}^{\mathrm{m}} \{\mathbf{U}^*\}^T [\mathbf{B}_E^0]_b^T \{\mathbf{M}\}_b = \{\mathbf{U}^*\}^T \{\mathbf{P}\} \quad \forall \{\mathbf{U}^*\}$$
$$\sum_{b=1}^{\mathrm{m}} [\mathbf{B}_E^0]_b^T \{\mathbf{M}\}_b = \{\mathbf{P}\} \tag{2.27}$$

2.2.4 Constitutive relations for linear elasticity

So far, kinematic and equilibrium relations for frame members were obtained using Powell's notation. In order to complete the set of equations, the constitutive relations must be deduced. Such formulation is hereby based on the theory of Euler-Bernoulli beams.

Consider a frame member as the one depicted in Figure 2.7a. By equilibrium conditions and the kinematics of Euler-Bernoulli beams, the following equations are obtained:

$$\frac{d^2 M_b(x_b)}{dx_b^2} = Q_b(x_b) \qquad \frac{d^2 w_b(x_b)}{dx_b^2} = \frac{M_b(x_b)}{EI_b} \qquad n_b = EA_b \frac{du_b(x_b)}{dx_b} \tag{2.28}$$

where $M_b(x_b)$ is the bending moment distribution along the element, $Q_b(x_b)$ is the applied distributed load, $w_b(x_b)$ is the deflection, $u_b(x_b)$ is the longitudinal displacement, n_b is the axial force, and EI_b and AE_b are, respectively, the flexural (Young's modulus multiplied by the inertia moment of the cross section) and axial (Young's modulus multiplied by the area of the cross section) rigidities. The hypothesis that the bending and axial effects are uncoupled is adopted.

By solving the first ordinary differential equation of (2.28) results:

$$M_b(x) = \int_0^x \int_0^x Q_b(x_b)\, dx_b\, dx_b + \mathbb{C}_1 x + \mathbb{C}_2 \tag{2.29}$$

Considering the bending moments m_i and m_j at the ends of the frame member, i.e. $M_b(0) = m_i$ and $M_b(L_b) = -m_j$, the integration constants $\mathbb{C}_1$ and $\mathbb{C}_2$ can be found.

By using the solution obtained in (2.29) in the second ordinary differential equation in (2.28), the general solution for the deflection is then achieved:

$$w_b(x) = \int_0^x \int_0^x \int_0^x \int_0^x Q_b(x_b)\, dx_b\, dx_b\, dx_b dx_b + \mathbb{C}_1 \frac{x^3}{6} + \mathbb{C}_2 \frac{x^2}{2} + \mathbb{C}_3 x + \mathbb{C}_4 \tag{2.30}$$

where the constants $\mathbb{C}_3$ and $\mathbb{C}_4$ are obtained through the boundary conditions $w_b(0) = 0$ and $w_b(L_b) = 0$ (Figure 2.7b).

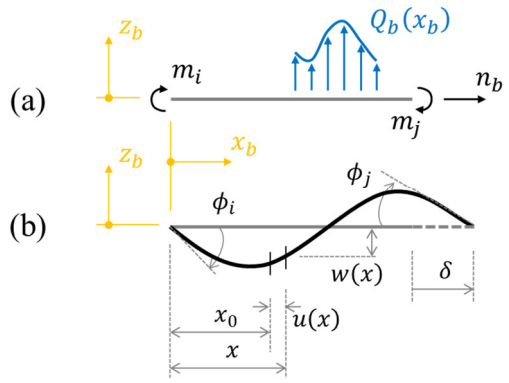

Figure 2.7 – Forces and deflections on an element b in local coordinate axes.

Now, the generalised deformations can be calculated through the deflection equation i.e.

$$\begin{aligned} -\left.\frac{dw_b}{dx}\right|_{x=0} &= \phi_i = \frac{L_b}{3EI_b} m_i - \frac{L_b}{6EI_b} m_j + \phi_i^0 \\ -\left.\frac{dw_b}{dx}\right|_{x=L_b} &= \phi_i = -\frac{L_b}{6EI_b} m_i + \frac{L_b}{3EI_b} m_j + \phi_j^0 \end{aligned} \tag{2.31}$$

where ϕ_i^0 and ϕ_j^0 are, respectively, the terms of the generalised deformations ϕ_i and ϕ_i that do not depend on the generalised stresses m_i and m_j.

Considering the common case of uniformly distributed transverse load, as depicted in Figure 2.8, the terms ϕ_i^0 and ϕ_j^0 are:

$$\phi_i^0 = \frac{p_0 L_b^3}{24EI_b} \qquad \phi_j^0 = -\frac{p_0 L_b^3}{24EI_b} \tag{2.32}$$

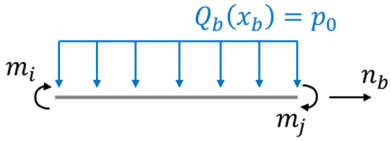

Figure 2.8 – Forces on an element b in local coordinate axes.

The solution of the third ordinary differential equation in (2.28) with the boundary conditions $u_b(0) = 0$ and $u_b(L_b) = \delta$ lies:

$$n_b = \frac{EA_b}{L_b}\delta \tag{2.33}$$

Finally, by rearranging the equations (2.31) and (2.33) the constitutive relations can be expressed as:

$$\{\boldsymbol{\phi}\}_b = [\mathbf{F_0}]_b\{\mathbf{M}\}_b + \{\boldsymbol{\phi}^{\mathbf{0}}\}_b \tag{2.34}$$

where $[\mathbf{F_0}]_b$ is the flexibility matrix of the frame member b

$$[\mathbf{F_0}]_b = \begin{bmatrix} \frac{L_b}{3EI_b} & -\frac{L_b}{6EI_b} & 0 \\ -\frac{L_b}{6EI_b} & \frac{L_b}{3EI_b} & 0 \\ 0 & 0 & \frac{L_b}{AE_b} \end{bmatrix} \tag{2.35}$$

and $\{\boldsymbol{\phi}^{\mathbf{0}}\}_b = \begin{Bmatrix} \phi_i^0 & \phi_j^0 & 0 \end{Bmatrix}^T$ is denoted matrix of initial deformations.

Alternatively, the constitutive relations can be expressed as:

$$\{\mathbf{M}\}_b = [\mathbf{E_0}]_b\{\boldsymbol{\phi}\}_b + \{\mathbf{M}^{\mathbf{0}}\}_b \tag{2.36}$$

where $[\mathbf{E_0}]_b$ is the elasticity matrix:

$$[\mathbf{E_0}]_b = \begin{bmatrix} \frac{4EI_b}{L_b} & \frac{2EI_b}{L_b} & 0 \\ \frac{2EI_b}{L_b} & \frac{4EI_b}{L_b} & 0 \\ 0 & 0 & \frac{AE_b}{L_b} \end{bmatrix} \tag{2.37}$$

and $\{\mathbf{M^0}\}_b = -[\mathbf{E_0}]_b\{\boldsymbol{\phi^0}\}_b$ is denoted matrix of initial stresses.

2.3 Fracture and continuum damage mechanics revisited

In this section some of the main concepts of fracture and continuum damage mechanics are broached. The objective here is to present hypotheses and assumptions from both theories that can characterise the behaviour of materials and structures.

2.3.1 Basics on fracture mechanics

During the 20th century, several accidents occur due to crack nucleation and propagation, especially in warships (Figure 2.9) and aeroplanes. Initially, many studies were devoted to achieve fracture criteria based on applied forces. However, those studies could not explain that, for the same structure such as warships, some structures fail and some do not fail.

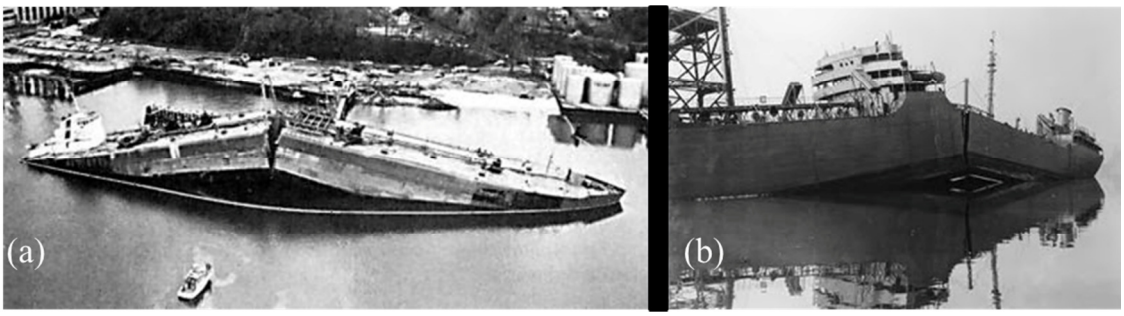

Figure 2.9 – Warships catastrophic failure: (a) Liberty and (b) SS Schenectady; both in 1943.
[Images from: Ferreira (2013)]

After several tests, engineers and researchers realised the fracture process starts in regions with geometrical notches and rivet connection holes due to stress concentration. This phenomenon was neglected by the regulation codes at that time, despite the works presented by Kirsch (1898), Kosolov (1909) and Inglis (1913), where problems of tensile plates with circular and elliptic holes were solved (Figure 2.10), among others.

Nevertheless, those studies do not explain the crack propagation. Note that if a crack is considered as a flat ellipse by the minor axis tending to zero, the stress concentration factor (SCF) tends to infinity. This observation shows that fracture criteria based on applied forces are inefficient.

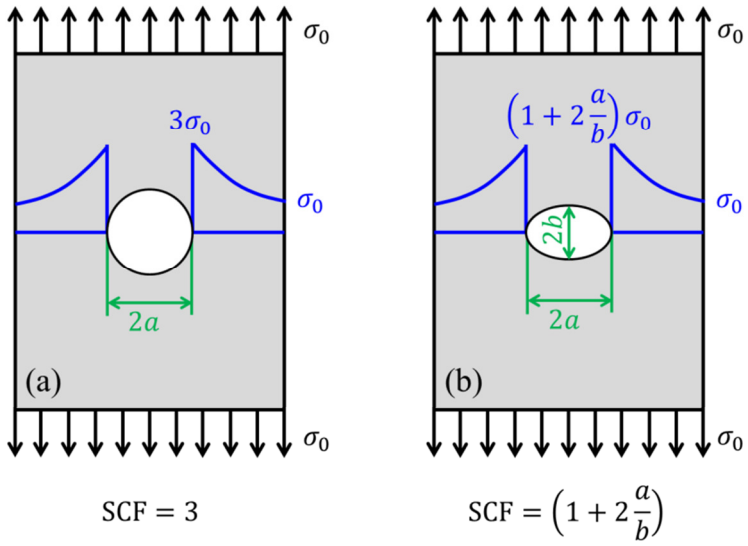

Figure 2.10 – Stress concentration for tensile plates with (a) circular and (b) elliptic holes.

Based on previous works, Griffith (1921, 1924) proposed to quantify the fracture process by energy criteria (see Gdoutos (2005) for a detailed historic perspective of Griffith's work). Using the thermodynamics of irreversible processes, Griffith (1921, 1924) proposed an energy balance taking into account the crack length $2a$ (or crack surface, considering unitary width).

Neglecting thermal actions, the total energy $\mathrm{E_T}$ for a mechanical problem is:

$$\mathrm{E_T} = U - \mathcal{W}_{ext} + \mathrm{E_S} \tag{2.38}$$

where U is the deformation energy, $\mathcal{W}_{ext}$ is the external work and $\mathrm{E_S}$ is the necessary energy for the formation of new crack surfaces.

The Griffith's energy balance results:

$$\frac{\partial \mathrm{E_T}}{\partial a} = 0 \quad \Rightarrow \quad -\frac{\partial (U - \mathcal{W}_{ext})}{\partial a} = \frac{\partial \mathrm{E_S}}{\partial a} \tag{2.39}$$

Where the left branch of the minimisation is the so-called energy release rate G^a and the right branch is the cracking resistance R^a i.e.

$$G^a = -\frac{\partial(U - \mathcal{W}_{ext})}{\partial a}$$
$$R^a = \frac{\partial \mathrm{E_S}}{\partial a} \tag{2.40}$$

Now, the propagation threshold can be understood as an equilibrium point. In other words, there is crack growth if the energy release rate is equal to the cracking resistance ($G^a = R^a$). For the sake of simplicity, an academic example is now presented (GRIFFITH, 1921, 1924): consider an infinity tensile plate with a degenerated elliptic hole (similar to the one in Figure 2.10b). Considering the case of plane stress, the potential energy is given by:

$$\mathrm{E_T} = U - \mathcal{W}_{ext} + \mathrm{E_S} = U_0 - \frac{\pi\sigma_0^2}{E}a^2 + 2(2\Gamma_S a) \tag{2.41}$$

where U_0 is the deformation energy for a plate without crack, E is the Young's modulus, σ_0 is the applied tension and Γ_S is the elastic surface energy of the material.

Note that the potential energy, in terms of the crack length, is expressed by a parabolic function. Therefore, by simple graphical observations (Figure 2.11) it can be affirmed that if the crack length is smaller than a critical value i.e. $a < a_{cr}$ (Figure 2.11a) any increase of crack length da requires an increase of energy. On the other hand, if the crack length is greater or equal to a critical value i.e. $a \geq a_{cr}$ (Figure 2.11b) any increase of crack length da results on lower values of energy. As a result, there is a crack critical length that ensures crack propagation with constant load (σ_0 in this case).

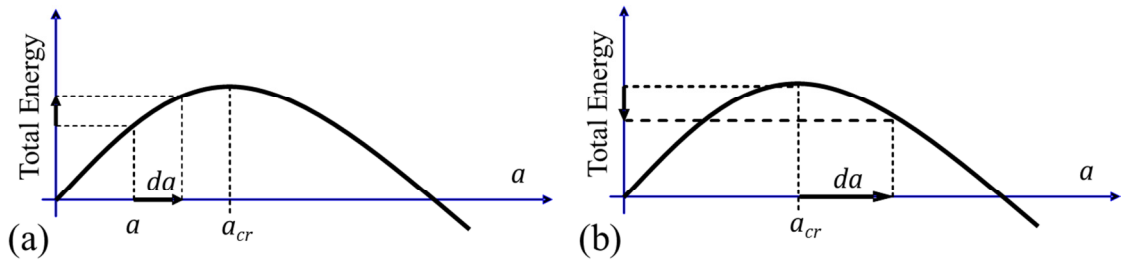

Figure 2.11 – Total energy vs crack length for an infinity tensile plate with a degenerated elliptic hole.

The crack propagation condition $G^a = R^a$ is then expressed as:

$$-\frac{\partial}{\partial a}\left[U_0 - \frac{\pi\sigma_0^2}{E}a^2\right] = \frac{\partial}{\partial a}[2(2\Gamma_S a)]$$
$$2\frac{\pi\sigma_0^2}{E}a = 4\Gamma_S \tag{2.42}$$

Such instability condition can be rewritten as:

$$\sigma_0\sqrt{a} = \sqrt{\frac{2E\Gamma_S}{\pi}} \tag{2.43}$$

Note that the value $\sqrt{2E\Gamma_S/\pi}$ presents only constant coefficients, which can be characterised as a material parameter. Then, the previous equation shows that the crack will grow solely if the product $\sigma_0\sqrt{a}$ reaches such material parameter. It is noteworthy that this result was experimentally verified by Griffith (1921, 1924) for glass plates.

The works developed by Griffith were the genesis of what is now called fracture mechanics (see Broek (1984) for a review).

Despite the efficacy of the energy balance, obtaining such relation is a challenging task. Therefore, Irwin (1957) proposed a new quantity so-called stress intensity factor (SIF). The adoption of SIF intends to overcome the SCF for fracture analysis, allowing an accurate description of the stress state near the crack tip.

For a crack, any behaviour can be expressed by the combination of three modes (Figure 2.12): opening (mode I), in-plane shear (mode II) and out-of-plane shear (mode III). There is a SIF for each mode (K_I, K_{II}, K_{III}). So, the energy release rate can be expressed by the stress intensity factors:

$$G^a = \frac{1}{E}\left(K_I^2 + K_{II}^2 + \frac{K_{III}^2}{1+\nu}\right) \qquad \text{for plane stress}$$
$$G^a = \frac{(1-\nu)^2}{E}\left(K_I^2 + K_{II}^2 + \frac{K_{III}^2}{1-\nu}\right) \qquad \text{for plane strain} \tag{2.44}$$

where ν is the Poisson's ration.

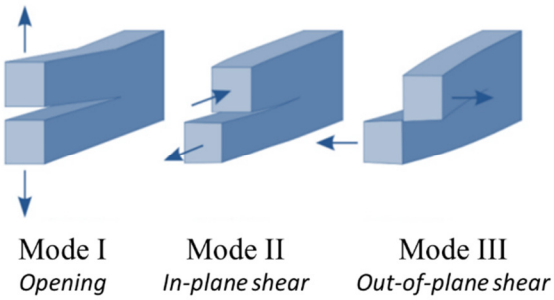

Figure 2.12 – Fracture modes.

For the Griffith fundamental problem, only mode I is active. Then, considering plane stress, the energy release rate can be expressed as:

$$G^a = \frac{K_I^2}{E} \tag{2.45}$$

Therefore, the stress intensity factor is now expressed by the applied stress:

$$2\frac{\pi\sigma_0^2}{E}a = \frac{K_I^2}{E} \quad \Rightarrow \quad K_I = \sigma_0\sqrt{2\pi a} \tag{2.46}$$

Thus, the instability condition occurs for critical values of SIF, i.e. $K_C = \sigma_C\sqrt{2\pi a}$, where σ_C is the critical value for the applied stress.

2.3.2 Basics on continuum damage mechanics

For some problems, the inelastic phenomena occur due to diffuse distribution of micro-cracks or other micro-defects that affect material integrity. A pioneer work regarding material integrity was proposed by Kachanov (1958) and later developed by Rabotnov (1968). Afterwards, Lemaitre and Chaboche (1985) used the thermodynamics of irreversible processes to formulate, in a formal manner, the so-called continuum damage mechanics.

Continuum damage mechanics is based on the introduction of an internal variable that measures micro-defects density, such as micro-cracks and micro-voids. Such micro-defects are too small to be considered as discrete cracks and though not small enough to be neglected. The quantification of micro-defects cannot be done in the structural scale (macroscale). Thus,

the representative volume element (RVE) is introduced (Figure 2.13). The RVE is a portion of a material represented in mesoscale, which allows the micro-defects quantification.

Consider an arbitrary cross section $\vec{\boldsymbol{n}}$ of the RVE, being S the total area and S_D the area of the micro-cracks, micro-voids or other defects (Figure 2.13a). Then, the effective area $\tilde{S}$ is given by:

$$\tilde{S} = S - S_D \tag{2.47}$$

The mechanical resistance loss at an arbitrary cross section $\vec{\boldsymbol{n}}$ is, by definition, the local damage $\omega_{\vec{\boldsymbol{n}}}$ (LEMAITRE; CHABOCHE, 1985), measured as (Figure 2.13b):

$$\omega_{\vec{\boldsymbol{n}}} = \frac{S_D}{S} \tag{2.48}$$

Observe that the damage variable $\omega_{\vec{\boldsymbol{n}}}$ lies between zero and one. If $\omega_{\vec{\boldsymbol{n}}} = 0$ the micro-defects are negligible or do not exist; if $\omega_{\vec{\boldsymbol{n}}} = 1$ the cross section $\vec{\boldsymbol{n}}$ is totally damaged, resulting that the RVE breaks in two parts.

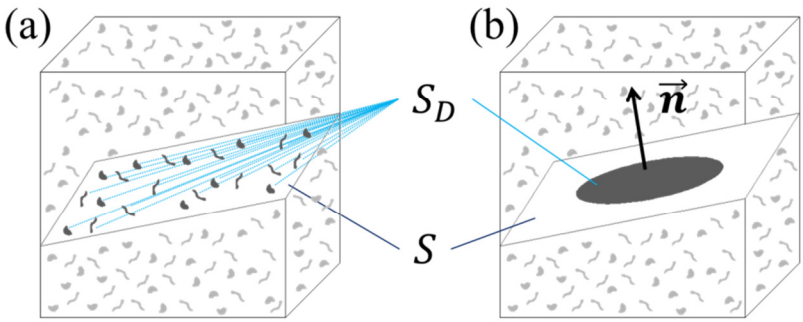

Figure 2.13 – Representative volume element (RVE).

For the sake of simplicity, henceforward the hypothesis of isotropic damage is adopted, i.e.

$$\omega_{\vec{\boldsymbol{n}}} = \omega \qquad \forall\, \vec{\boldsymbol{n}} \tag{2.49}$$

Considering a uniaxial case, if there is an applied force on an undamaged RVE the resistance force is the product between the Cauchy stress and the cross section area i.e. σS. If micro-cracks nucleate and propagate in the RVE the resistance force can be calculated in a similar way; however, since the cross section presents now an effective area $\tilde{S}$ smaller than the total area, the Cauchy stress in the resistance force is then replaced by an effective stress i.e. $\tilde{\sigma}\tilde{S}$. Therefore, by the equality $\sigma S = \tilde{\sigma}\tilde{S}$ the effective stress is obtained:

$$\tilde{\sigma} = \frac{\sigma S}{\tilde{S}} = \frac{\sigma S}{S - S_D} \quad \Rightarrow \quad \tilde{\sigma} = \frac{\sigma}{1 - \omega} \tag{2.50}$$

Note that $\tilde{\sigma} \geq \sigma$ i.e. $\omega = 0 \Rightarrow \tilde{\sigma} \to \sigma$ (Figure 2.14a) and $\omega \to 1 \Rightarrow \tilde{\sigma} \to \infty$ (Figure 2.14b). Considering this observation, Lemaitre and Chaboche (1985) proposed the so-called hypothesis of strain equivalence, which dictates that the deformation behaviour presented by the material is solely affected by damage in the form of effective stress (Figure 2.15):

$$\tilde{\sigma} = E\varepsilon^e \;\; \Rightarrow \;\; \sigma = (1 - \omega)E(\varepsilon - \varepsilon^p) \tag{2.51}$$

where E is the Young's modulus, ε is the total strain, ε^e is the elastic strain and ε^p is the plastic strain.

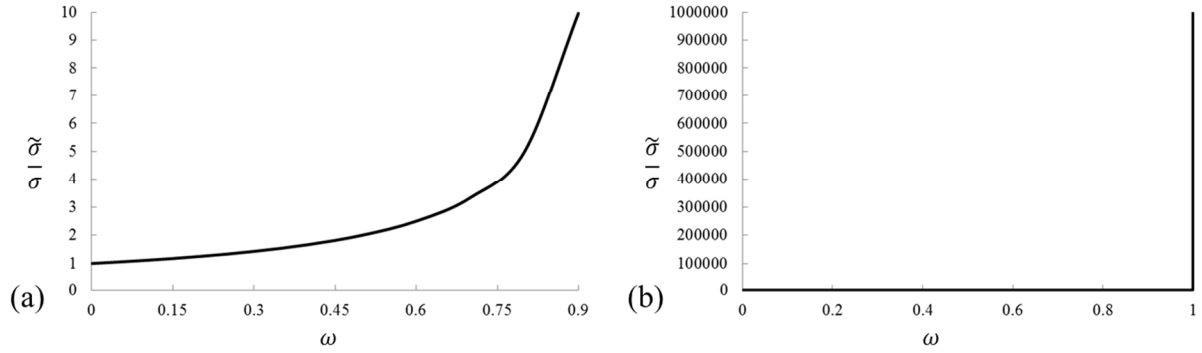

Figure 2.14 – Relation between the effective and Cauchy stress with damage variable ω in the following intervals: (a) $[0.0,0.9]$ and (b) $[0.0,1.0)$.

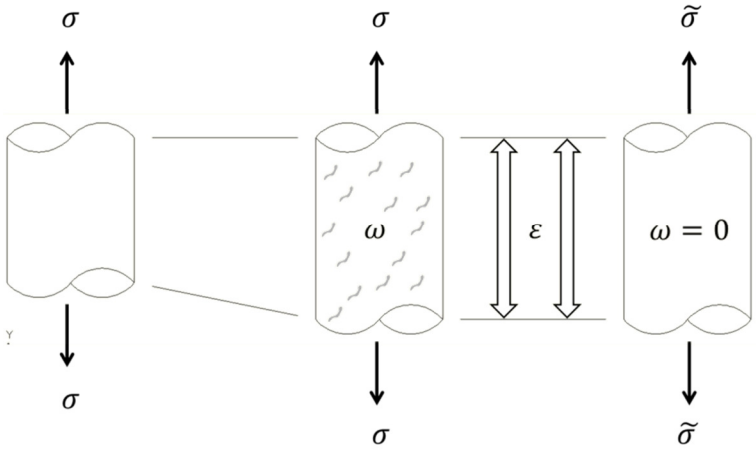

Figure 2.15 – Hypothesis of strain equivalence.

Through the hypothesis of strain equivalence, Hooke's law (2.51) can be expressed as:

$$\varepsilon - \varepsilon^p = \frac{\sigma}{(1-\omega)E} = \frac{1}{E}\sigma + \frac{\omega}{(1-\omega)E}\sigma \qquad \therefore \begin{cases} \varepsilon^e = \dfrac{1}{E}\sigma \\ \varepsilon^d = \dfrac{\omega}{(1-\omega)E}\sigma \end{cases} \tag{2.52}$$

where the total strain is now understood as a sum between elastic, damage and plastic strains i.e. $\varepsilon = \varepsilon^e + \varepsilon^d + \varepsilon^p$. Obviously, if $\omega = 0 \Rightarrow \varepsilon^d = 0$ otherwise $\varepsilon^d \neq 0$ (for a certain value of σ).

By mathematical definition, the damage variable may reach values near to one; however, physically, materials collapse with lower values of damage. Therewith, here the term ultimate damage ω_u is adopted for such values of damage. According to Lemaitre and Chaboche (1985), materials usually present ω_u around 0.5 to 0.9.

Now, consider a generalised Griffith criterion (MARIGO, 1985) applied to continuum damage mechanics:

$$G^\omega - R^\omega \leq 0 \tag{2.53}$$

where G^ω is the energy release rate of a damaged RVE and R^ω is the "damage resistance function" (FLÓREZ-LÓPEZ; MARANTE; PICÓN, 2015). The energy release rate can be expressed as:

$$G^{\omega} = -\frac{\partial U}{\partial \omega} = \frac{\partial U^{*}}{\partial \omega} \tag{2.54}$$

being U the strain energy and U^{*} the complementary energy, given by:

$$\begin{aligned} U &= \frac{1}{2}\sigma\varepsilon = \frac{1}{2}(1-\omega)E\varepsilon^{2} \\ U^{*} &= \frac{1}{2}\sigma\varepsilon = \frac{1}{2}\frac{\sigma^{2}}{(1-\omega)E} \end{aligned} \tag{2.55}$$

Finally, the energy release rate of a damaged RVE can be written in terms of stiffness or flexibility i.e.

$$G^{\omega} = \frac{1}{2}E\varepsilon^{2} = \frac{1}{2}\frac{\sigma^{2}}{(1-\omega)^{2}E} \tag{2.56}$$

2.4 Lumped damage mechanics for reinforced concrete frames

Nowadays, fracture and continuum damage mechanics are not often used in practical applications of civil engineering, but with limited use in specific fields. For civil engineering, such procedures are not suitable for practical purposes. On the other hand, the concepts behind both theories are strongly supported by thermodynamics. Then, the main idea presented by Flórez-López (1993, 1995) was the modelling of reinforced concrete structures using the concepts of fracture and continuum damage mechanics coupled with the concept of plastic hinge.

Such model was the basis of several studies around the world, with several applications to reinforced concrete buildings, bridges and arches, for plane (see e.g. Cippolina, López-Inojosa and Flórez-López (1995), Liu and Liu (2004), Araújo and Proença (2008), Faleiro, Oller and Barbat (2010), Alva and El Debs (2010), Toi and Hasegawa (2011), Perdomo et al. (2013), Santoro and Kunnath (2013), Amorim, Proença and Flórez-López (2013), and some of the references therein) or three-dimensional frames (MARANTE; FLÓREZ-LÓPEZ, 2003), crack propagation in steel beams under ultra-low cycle fatigue (BAI et al., 2016), tunnel linings and masonry arches (AMORIM; PROENÇA; FLÓREZ-LÓPEZ,

2014a, 2014b). All these developments are gathered in a new branch of structural mechanics which is called lumped damage mechanics (LDM).

Once this chapter is intended to present a review, the LDM for reinforced concrete (RC) frames is now presented.

2.4.1 Constitutive relations for inelastic frames

The nonlinear modelling of RC structures with LDM is carried out by assuming that the inelastic phenomena are concentrated at hinges, located at the ends of the elastic frame member. In other words, the frame element is considered as an assemblage of a linear elastic beam-column with two inelastic hinges at the edges (Figure 2.16a).

Considering the hypothesis of strain equivalence, the generalised deformations (Figure 2.16b) can be described as eq.(2.52):

$$\{\boldsymbol{\phi}\}_b = \{\boldsymbol{\phi}^{\boldsymbol{e}}\}_b + \left\{\boldsymbol{\phi}^{\boldsymbol{d}}\right\}_b + \{\boldsymbol{\phi}^{\boldsymbol{p}}\}_b \tag{2.57}$$

where $\{\boldsymbol{\phi}^{\boldsymbol{e}}\}_b$ is the matrix of generalised deformations of the elastic beam-column, $\left\{\boldsymbol{\phi}^{\boldsymbol{d}}\right\}_b$ is the damage deformation matrix and $\{\boldsymbol{\phi}^{\boldsymbol{p}}\}_b$ is the matrix of plastic deformations.

The elastic generalised deformations are described by eq.(2.34), conveniently rewritten here:

$$\{\boldsymbol{\phi}^{\boldsymbol{e}}\}_b = [\mathbf{F_0}]_b\{\mathbf{M}\}_b + \{\boldsymbol{\phi}^{\mathbf{0}}\}_b \tag{2.58}$$

being $[\mathbf{F_0}]_b$ the elastic flexibility matrix of the slender frame member, $\{\mathbf{M}\}_b$ the matrix of generalised stresses (Figure 2.16c) and $\{\boldsymbol{\phi}^{\mathbf{0}}\}_b$ the matrix of initial deformations.

The plastic deformations are related to reinforcement yielding. Usually, plastic elongations are neglected for reinforced concrete structures. Therefore, the matrix of plastic deformations contains solely the plastic rotations of the hinges i.e.

$$\{\boldsymbol{\phi}^{\boldsymbol{p}}\}_b = \begin{Bmatrix} \phi_i^p \\ \phi_j^p \\ 0 \end{Bmatrix} \tag{2.59}$$

The concrete cracking is accounted for by damage variables at the hinges (d_i, d_j). As the continuum damage variable (ω), the ones from lumped damage mechanics (d_i, d_j) lie between zero and one and quantify the loss of (flexural) integrity at the hinges.

Revisiting the hypothesis of strain equivalence (2.52), the damage deformations can be expressed as:

$$\{\boldsymbol{\phi}^{\boldsymbol{d}}\}_b = [\mathbf{C}(\mathbf{D})]_b\{\mathbf{M}\}_b \qquad \therefore [\mathbf{C}(\mathbf{D})]_b = \begin{bmatrix} \dfrac{L_b d_i}{3EI_b(1-d_i)} & 0 & 0 \\ 0 & \dfrac{L_b d_j}{3EI_b(1-d_j)} & 0 \\ 0 & 0 & 0 \end{bmatrix} \tag{2.60}$$

where $[\mathbf{C}(\mathbf{D})]_b$ is a matrix of additional flexibility due to concrete cracking. Note that if $d_i = 0$ and $d_j = 0$ the matrix $[\mathbf{C}(\mathbf{D})]_b$ is nil i.e. there is no concrete cracking; on the other hand, if $d_i \to 1$ and $d_j \to 1$ the inelastic hinges present the behaviour of perfect hinges, found in textbooks of structural analysis, which means that the concrete cracking is extremely severe.

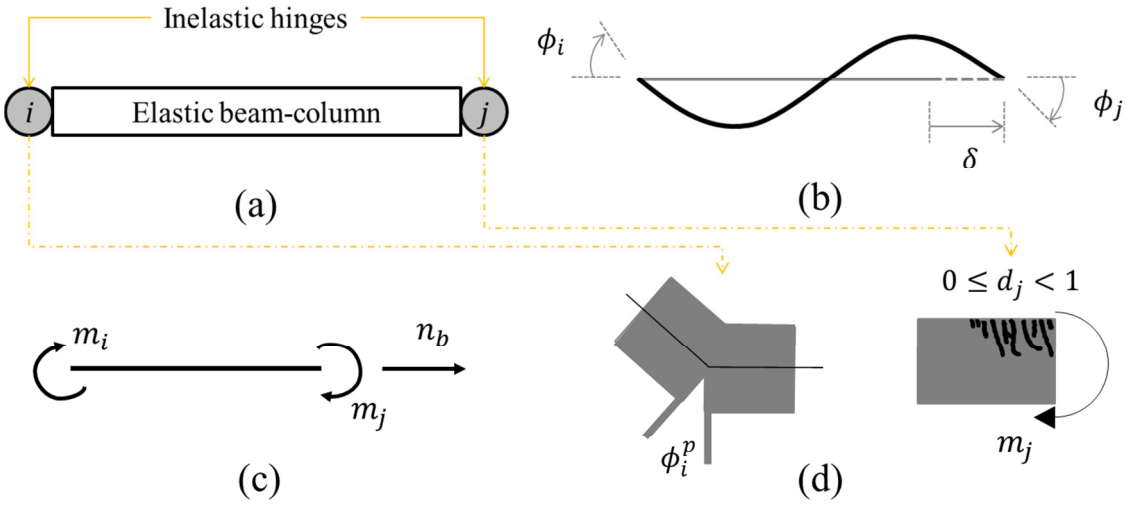

Figure 2.16 – Lumped damage mechanics for RC frames: (a) inelastic hinges, (b) generalised deformations, (c) generalised stresses and (d) inelastic phenomena

By substituting (2.58) and (2.60) in (2.57), the constitutive relation results:

$$\{\boldsymbol{\phi} - \boldsymbol{\phi}^{\boldsymbol{p}}\}_b = [\mathbf{F}(\mathbf{D})]_b\{\mathbf{M}\}_b + \{\boldsymbol{\phi}^{\mathbf{0}}\}_b \tag{2.61}$$

where

$$[\mathbf{F(D)}]_b = [\mathbf{F_0}]_b + [\mathbf{C(D)}]_b = \begin{bmatrix} \frac{L_b}{3EI_b(1-d_i)} & -\frac{L_b}{6EI_b} & 0 \\ -\frac{L_b}{6EI_b} & \frac{L_b}{3EI_b(1-d_j)} & 0 \\ 0 & 0 & \frac{L_b}{AE_b} \end{bmatrix} \tag{2.62}$$

is the flexibility matrix of a damaged frame member.

The constitutive relation can also be expressed in terms of stiffness i.e.

$$\{\mathbf{M}\}_b = [\mathbf{E(D)}]_b\{\boldsymbol{\phi} - \boldsymbol{\phi}^{\boldsymbol{p}}\}_b + \{\mathbf{M^0(D)}\}_b \tag{2.63}$$

where $[\mathbf{E(D)}]_b = [\mathbf{F(D)}]_b^{-1}$ is the elasticity matrix of a damaged frame member

$$[\mathbf{E(D)}]_b = k_f \begin{bmatrix} 12(1-d_i) & 6(1-d_i)(1-d_j) & 0 \\ 6(1-d_i)(1-d_j) & 12(1-d_j) & 0 \\ 0 & 0 & \frac{AE_b}{k_f L_b} \end{bmatrix} \tag{2.64}$$

$$\therefore k_f = \frac{1}{3-(1-d_i)(1-d_j)}\frac{EI_b}{L_b}$$

and $\{\mathbf{M^0(D)}\}_b = -[\mathbf{E(D)}]_b\{\boldsymbol{\phi}^{\mathbf{0}}\}_b$.

2.4.2 Generalised Griffith criterion for an inelastic hinge

Previously, a generalisation of the Griffith criterion was presented for a simple uniaxial case using continuum damage mechanics. Now, a generalised Griffith criterion is presented for the aforementioned inelastic hinges.

Consider a damaged frame member as the one presented in Figure 2.16a. The complementary energy of such member is given by:

$$U^* = \frac{1}{2}\{\mathbf{M}\}_b^T\{\boldsymbol{\phi} - \boldsymbol{\phi}^{\boldsymbol{p}}\}_b = \frac{1}{2}\{\mathbf{M}\}_b^T[\mathbf{F}(\mathbf{D})]_b\{\mathbf{M}\}_b + \frac{1}{2}\{\mathbf{M}\}_b^T\{\boldsymbol{\phi}^{\mathbf{0}}\}_b \tag{2.65}$$

Then, the energy release rates of hinges i and j are expressed in terms of damage variables. Therefore, those quantities are now called "damage driving moments" (FLÓREZ-LÓPEZ; MARANTE; PICÓN, 2015) and expressed as:

$$\begin{aligned} G_i^d &= \frac{\partial U^*}{\partial d_i} = \frac{F_{11}^0 m_i^2}{2(1-d_i)^2} = \frac{L_b m_i^2}{6EI_b(1-d_i)^2} \\ G_j^d &= \frac{\partial U^*}{\partial d_j} = \frac{F_{22}^0 m_j^2}{2\left(1-d_j\right)^2} = \frac{L_b m_j^2}{6EI_b\left(1-d_j\right)^2} \end{aligned} \tag{2.66}$$

Since the damage evolution is based on Griffith criterion, the damage evolution laws for both hinges are given by:

$$\begin{cases} \Delta d_i = 0 \quad \text{if} \quad G_i^d < R_i^d \\ G_i^d = R_i^d \quad \text{if} \quad \Delta d_i > 0 \end{cases} \\ \begin{cases} \Delta d_j = 0 \quad \text{if} \quad G_j^d < R_j^d \\ G_j^d = R_j^d \quad \text{if} \quad \Delta d_j > 0 \end{cases} \tag{2.67}$$

where the terms R_i^d and R_j^d are the crack resistance functions of the inelastic hinges.

The crack resistance functions were obtained through experimental observations (FLÓREZ-LÓPEZ; MARANTE; PICÓN, 2015). Note that for materials modelled using fracture mechanics, such as the glass plates tested by Griffith (1921, 1924), the experimental measurement of the crack resistance function is directly related to the crack length. On the other hand, for RC frames modelled with inelastic hinges, the measurement of the quantity and lengths of cracks is pointless. Therefore, a variable named damage describes the loss of flexural rigidity due concrete cracking. Such variable can be measured by a mono-sign cyclic test (FLÓREZ-LÓPEZ; MARANTE; PICÓN, 2015). In order to represent a beam-column joint on a frame structure subjected to bending, an RC specimen, as the one depicted in Figure 2.17, was experimentally studied (FLÓREZ-LÓPEZ; MARANTE; PICÓN, 2015).

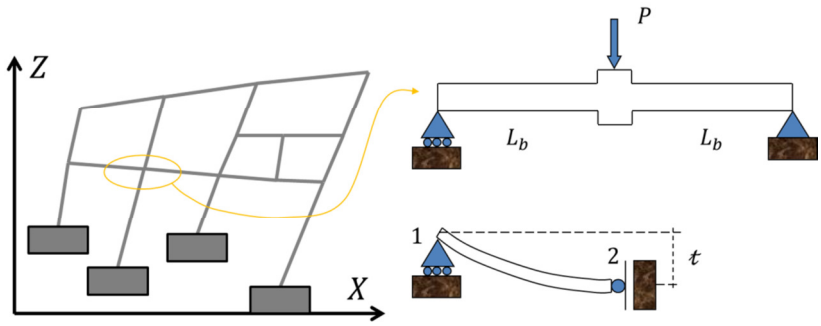

Figure 2.17 – Experimental test for crack propagation in RC elements due to bending: test set-up.
[After Flórez-López, Marante and Picón (2015)]

Considering the frame member assumed to be half of the specimen, located between nodes 1 and 2, the constitutive relation is:

$$\phi_2 - \phi_2^p = -\frac{L_b}{6EI_b}m_1 + \frac{L_b}{3EI_b(1-d_2)}m_2 \tag{2.68}$$

From the equilibrium relations, the bending moments result:

$$m_1 = 0 \qquad m_2 = \frac{PL_b}{2} \tag{2.69}$$

where P is the applied force.

Finally, the kinematic equation for this problem is:

$$\phi_2 = \frac{t}{L_b} \tag{2.70}$$

where t is the total deflection of the beam-column pseudo-joint.

The substitution of (2.69) and (2.70) in (2.68) results:

$$P = \mathfrak{E}(d)\left(t - t_p\right) \qquad \therefore \begin{cases} d = d_2 \\ \mathfrak{E}(d) = \mathfrak{E}_0(1-d) = \dfrac{6EI_b}{L_b}(1-d) \\ t_p = \phi_2^p L_b \end{cases} \tag{2.71}$$

Note that the quantity $\mathfrak{E}(d)$ is measured through an unloading-reloading process in the specimen (Figure 2.18). The value $\mathfrak{E}(d)$ quantifies a slope that crosses the point where the elastic unloading starts and the abscissa-axis for $t = t_p$ (Figure 2.18). Thus, the value $\mathfrak{E}_0$ represents the specimen while undamaged. Now, the damage variable can be experimentally calculated:

$$d = 1 - \frac{\mathfrak{E}(d)}{\mathfrak{E}_0} \tag{2.72}$$

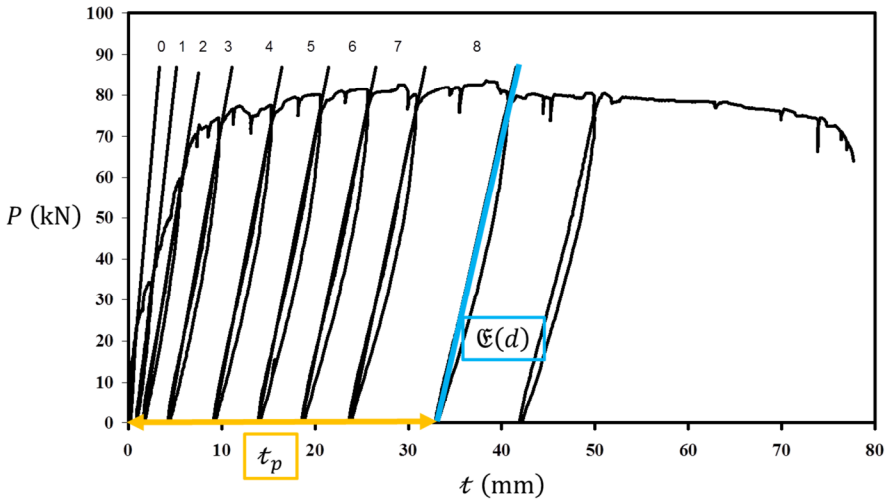

Figure 2.18 – Graphical representation of damage measurement.
[After Flórez-López, Marante and Picón (2015)]

During the test, the specimen presents concrete cracking as depicted in Figure 2.19.

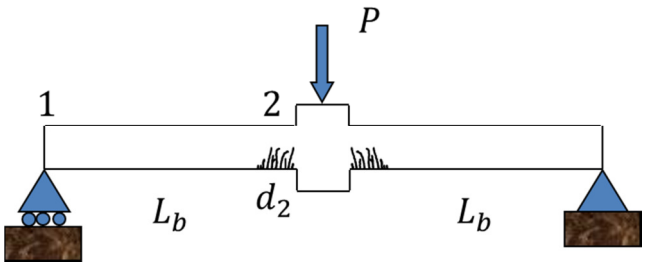

Figure 2.19 – Concrete cracking.

With experimental measurements, a graph for damage d (2.72) in terms of the energy release rate G^d (2.67) is plotted (Figure 2.20). Once the energy release rates G^d are computed while damage evolves, according to the generalised Griffith criterion, previously presented,

for such conditions G^d is equal to the crack resistance function (R^d). Therefore, the mathematical expression that describes the experimental data with good accuracy is given by (FLÓREZ-LÓPEZ; MARANTE; PICÓN, 2015):

$$R^d(d) = R_0 + q\frac{\ln(1-d)}{1-d} \tag{2.73}$$

where R_0 and q are parameters that depend on specimen characteristics.

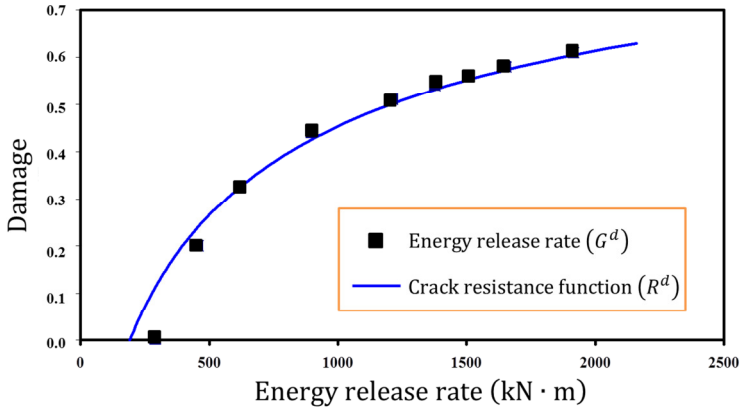

Figure 2.20 – Damage as a function of energy release rate.
[After Cipollina, López-Inojosa and Flórez-López (1995)]

In order to complete the modelling of RC frames, nonlinear behaviour of the reinforcement must be studied. With some algebraic manipulation, the constitutive relation of the test specimen (2.68) can be rewritten as:

$$\phi_2^p = \frac{t}{L_b} - \frac{L_b}{3EI_b(1-d_2)}m_2 \tag{2.74}$$

Thus, the plastic rotation of the cracked section can be graphed (Figure 2.21) using the bending moment and damage variable, both experimentally acquired.

Once most of lumped damage models were proposed to analyse RC structures under seismic conditions, the yield function of an inelastic hinge i is described by kinematic hardening:

$$f_i = \left| \frac{m_i}{1 - d_i} - c_i \phi_i^p \right| - M_{y_i} \leq 0 \tag{2.75}$$

where c_i and M_{y_i} are parameters that depend on specimen characteristics. Therefore, the plastic deformation evolution laws for a frame member b are:

$$\begin{cases} \Delta\phi_i^p = 0 \quad \text{if} \quad f_i < 0 \\ f_i = 0 \quad \text{if} \quad \Delta\phi_i^p \neq 0 \end{cases} \qquad \begin{cases} \Delta\phi_j^p = 0 \quad \text{if} \quad f_j < 0 \\ f_j = 0 \quad \text{if} \quad \Delta\phi_j^p \neq 0 \end{cases} \qquad \therefore f_j = \left| \frac{m_j}{1 - d_j} - c_j \phi_j^p \right| - M_{y_j} \leq 0 \tag{2.76}$$

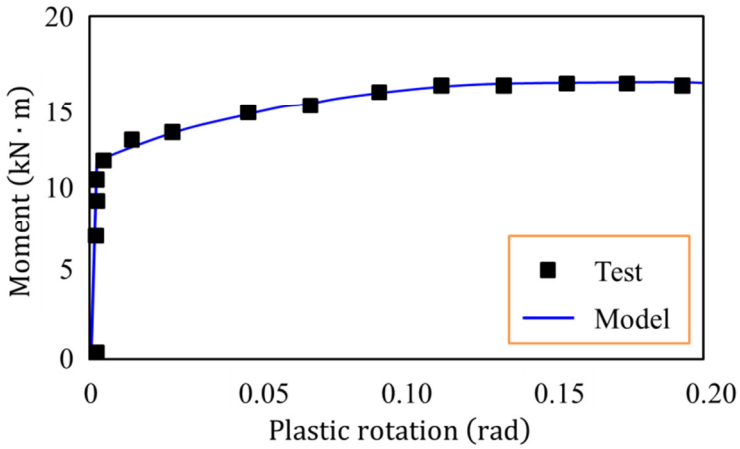

Figure 2.21 – Generalised stress as a function of plastic deformation.
[After Cipollina, López-Inojosa and Flórez-López (1995)]

So far, for each inelastic hinge, four parameters where introduced in order to describe the structural behaviour of RC frames. Regarding the aforementioned RC specimen, such parameters were obtained by means of experimental observations. However, for any RC frame, those parameters can be accurately obtained through the classic theory of reinforced concrete. Since there are four parameters to determine, other four known quantities are needed.

Regarding concrete cracking, from the generalised Griffith criterion the following relation is obtained:

$$G^d = R^d \quad \Rightarrow \quad \frac{F^0 m^2}{2(1-d)^2} = R_0 + q \frac{\ln(1-d)}{1-d} \tag{2.77}$$

Note that such equation relates moment and damage (Figure 2.22). According to the classic theory of reinforced concrete, if the moment reaches a value called first cracking moment M_{cr} (see Appendix A) cracks nucleate. At this point there is no damage, then the initial crack resistance R_0 is obtained:

$$\frac{F^0 M_{cr}^2}{2} = R_0 \tag{2.78}$$

From the classic theory of reinforced concrete it is well-known that the first cracking moment depends on the axial force on the element, then, R_0 is also a function of the axial force.

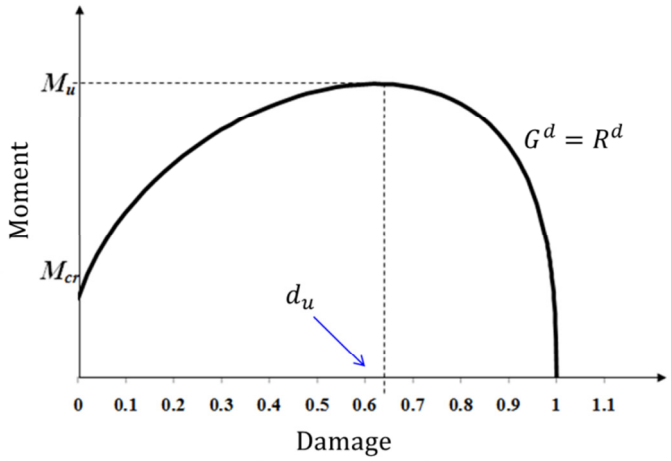

Figure 2.22 – Moment as a function of damage, as stated in the generalised Griffith criterion.

The maximum value of bending moment, called ultimate moment (M_u), occur at a specific value of damage (Figure 2.22). Such value is called ultimate damage (d_u), which occurs in the maximum condition i.e.

$$\frac{\partial m}{\partial d} = 0 \quad \Rightarrow \quad 2(1-d_u)R_0 + q[\ln(1-d_u)+1] = 0 \tag{2.79}$$

If $d = d_u \Rightarrow m = M_u$ and substituting the value of R_0 in (2.77) results:

$$\frac{F^0 M_u^2}{2(1-d_u)^2} = \frac{F^0 M_{cr}^2}{2} + q\frac{\ln(1-d_u)}{1-d_u} \tag{2.80}$$

The equations (2.79) and (2.80) are a nonlinear system, which once solved gives the values of the hardening parameter (q) and ultimate damage (d_u). Note that the ultimate damage (d_u) usually takes a value from 0.6 to 0.65, and the hardening parameter (q) also depends on the axial force.

Since the reinforcement only yields when cracks are already propagating, it is reasonable to consider the plastic moment M_p larger than the first cracking moment (M_{cr}). As for the ultimate moment, the plastic moment is directly related to a damage value, called plastic damage (d_p). Such value (d_p) represents the cracking density when the reinforcement starts yielding. Then, if $d = d_p \Rightarrow m = M_p$ (2.77) results:

$$\frac{F^0 M_p^2}{2\left(1-d_p\right)^2} = R_0 + q\frac{\ln\left(1-d_p\right)}{1-d_p} \tag{2.81}$$

At this point the yield function is nil and there is no plastic rotation yet i.e. $\phi^p = 0$. Thus, the parameter M_y results:

$$M_y = \frac{M_p}{1-d_p} \tag{2.82}$$

The yield function is also nil when moment reaches its ultimate value, resulting:

$$c = \frac{1}{\phi_u^p}\left(\frac{M_u}{1-d_u} - M_y\right) = \frac{1}{\phi_u^p}\left(\frac{M_u}{1-d_u} - \frac{M_p}{1-d_p}\right) \tag{2.83}$$

where ϕ_u^p is the ultimate plastic rotation (see Appendix A).

The equations (2.81) to (2.83) compose a system in which the parameters c, M_y and d_p are the solution. The value d_p usually lies between 0.3 and 0.4.

2.5 Numerical implementation

Uzcategui (2012) originally developed the finite element programme used in this thesis. The numerical implementation was made in two levels: global and local. The global level gathers the set of routines which solve the equilibrium equations. The local level

presents a routine that contains the finite element, being responsible for the structural behaviour.

Consider the equilibrium equation (2.27), conveniently rewritten:

$$\{\mathbf{L}\} = \sum_{b=1}^{\mathrm{m}} [\mathbf{B}_E^0]_b^T \{\mathbf{M}\}_b - \{\mathbf{P}\} = \{\mathbf{0}\} \tag{2.84}$$

Equation (2.84) establishes that the resolution is only obtained when the residual force vector $\{\mathbf{L}\}$, defined as the difference between the internal and external forces, is null.

A finite element programme (UZCATEGUI, 2012) is here composed of a set of routines that process the user input, generate the structure calculation process step-by-step and provide the analysis results in tabulated or graphical form. At each calculation step, the programme solves numerically the problem defined by the matrix equation (2.84) accounting for the boundary conditions. These conditions are defined by known displacement values in regions where the forces are unknown and *vice-versa*.

The finite element is fundamentally inserted in the routine that calculates the internal forces $\{\mathbf{Q}\}_b = [\mathbf{B}_E^0]_b^T \{\mathbf{M}\}_b$ from displacements. The computational procedure that expands the matrices of internal forces and combines them in the matrix of residual forces is the well-known assemblage algorithm.

The frame element is then defined by the kinematic equation (2.21), which allows the strain calculation from displacements, by the elastic (2.61), damage (2.67) and plasticity (2.75)-(2.76) laws, which provide the generalised stresses and internal variables from strains and, finally, by the equilibrium equation $\{\mathbf{Q}\}_b = [\mathbf{B}_E^0]_b^T \{\mathbf{M}\}_b$, which returns the internal forces from stresses.

The system of global equilibrium equations of the structure is, in general, nonlinear. Therefore such system must be solved by linearization of the problem with some iterative method to correct the solution estimative, being the Newton's method or any of its variants usually employed. In this case, due to the linearization, it is also necessary the calculation of tangent stiffness matrix, or Jacobian, of internal forces: $[\partial \mathbf{Q}(\mathbf{U})/\partial \mathbf{U}]_b$.

Note that the constitutive model, represented by the set of equations (2.61), (2.67), (2.75)-(2.76) is also nonlinear. Therefore, it is necessary the use of Newton's method combined with a predictor and corrector strategy in local character. It is noteworthy that an especial characteristic of this type of local problem is that the convergence conditions vary

significantly with the damage i.e. as higher the damage value to be calculated as smaller is the increment size. Furthermore, loading increases are usually followed by damage concentration on few hinges. That is why the classical procedure, which involves calculations of both global and local equilibrium problems, is not efficient. In this case, it is preferable to use different steps of calculation on each element (AVÓN, 2002). Figure 2.23 shows a possible local algorithm based on this idea. It is noteworthy that the following developments are based on this algorithm.

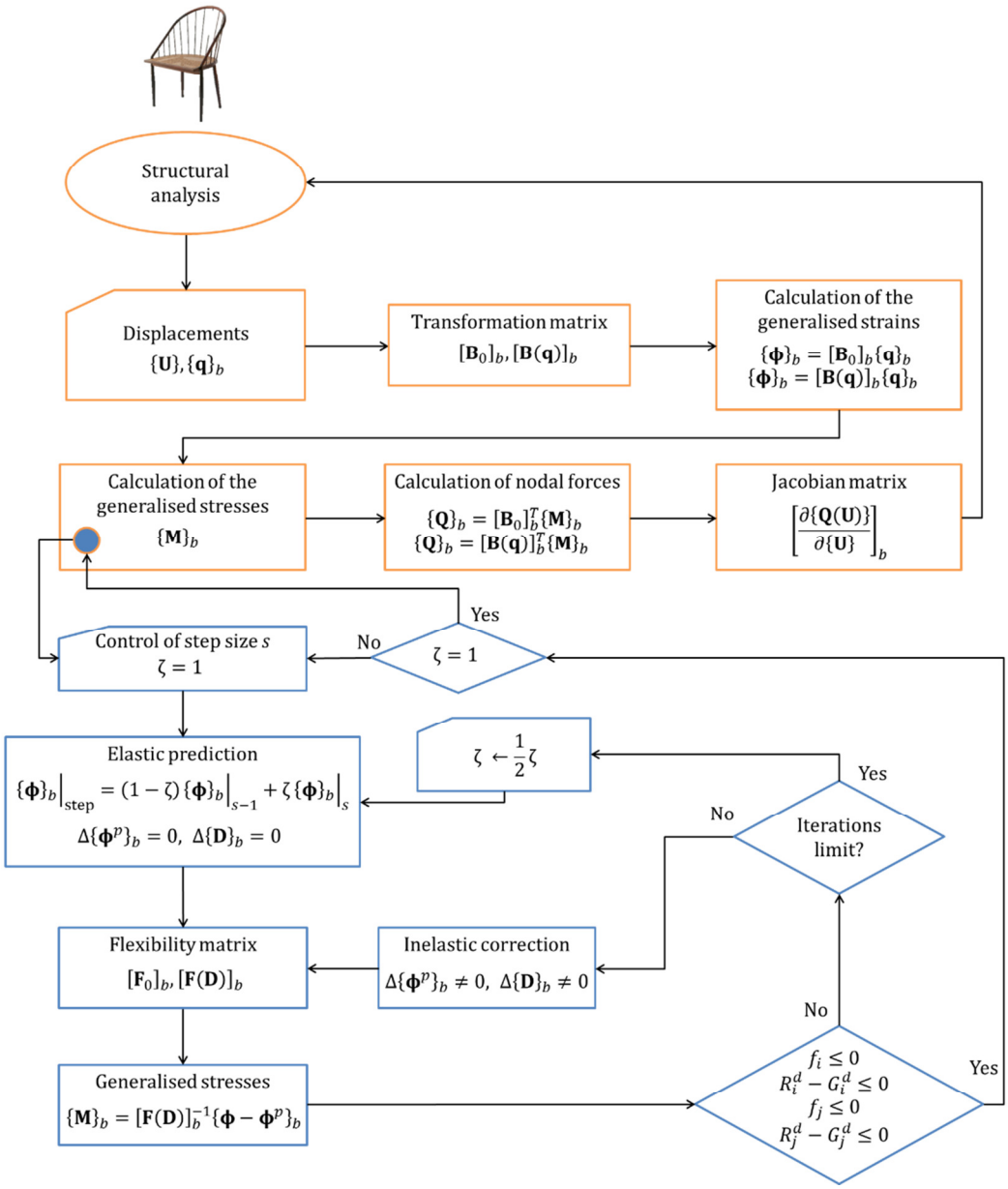

Figure 2.23 – Multistep algorithm.

3 LUMPED DAMAGE MECHANICS FOR ARCHES

The lumped damage models presented in this chapter are original developments of this thesis, being already published in Amorim, Proença and Flórez-López (2013, 2014a, 2014b). These procedures are based on the lumped plasticity model proposed by Flórez-López and Proença (2013), where the elastic formulation was firstly presented by Palaninathan and Chandrasekharan (1985).

3.1 Statics and kinematics of arches

Consider the frame illustrated in Figure 3.1 where an arch element b, between the nodes i and j, is highlighted. Such element is characterised by a radius (R_b) and an angle (ψ_b). Two coordinate systems are defined: global (X, Z) and local (x_L, z_L). The angle between the axes Z and z_L is called β_b. The angles ψ_b and β_b may be expressed as:

$$\cos\beta_b = \frac{Z_i - Z_C}{R_b}$$
$$\cos(\psi_b + \beta_b) = \frac{Z_j - Z_C}{R_b} \tag{3.1}$$

being (X_C, Z_C) coordinates of the circle centre which contains the arch element, and (X_i, Z_i) and (X_j, Z_j) the global coordinates of nodes i and j, respectively.

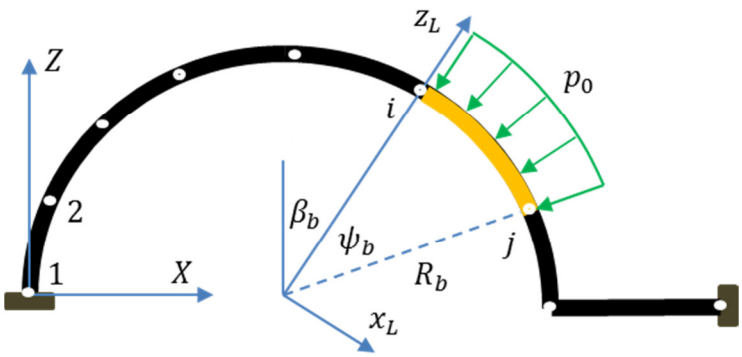

Figure 3.1 – Structure with a circular arch.

Three sets of static variables are introduced: the nodal forces matrix in global coordinates $\{\mathbf{Q}\}_b = \{Q_{ui} \quad Q_{wi} \quad Q_{\theta i} \quad Q_{uj} \quad Q_{wj} \quad Q_{\theta j}\}^T$ (Figure 3.2a), the nodal forces matrix in local coordinates $\{\mathbf{Q}^L\}_b = \{Q^L_{ui} \quad Q^L_{wi} \quad Q^L_{\theta i} \quad Q^L_{uj} \quad Q^L_{wj} \quad Q^L_{\theta j}\}^T$ (Figure 3.2b) and the generalised stress matrix $\{\mathbf{M}\}_b = \{m_i \quad m_j \quad n_i\}^T$ (Figure 3.2c). The nodal forces and generalised stress matrices are related by the equilibrium equations:

$$\begin{aligned} &\{\mathbf{Q}^L\}_b = [\mathbf{B}(\mathbf{q}^L)]_b^T\{\mathbf{M}\}_b - \{\mathbf{Q}_\mathbf{0}^L\}_b \\ &\{\mathbf{Q}\}_b = [\mathbf{B}(\mathbf{q})]_b^T\{\mathbf{M}\}_b - \{\mathbf{Q}_\mathbf{0}\}_b \\ &\quad \therefore [\mathbf{B}(\mathbf{q})]_b = [\mathbf{B}(\mathbf{q}^L)]_b[\mathbf{T}]_b^T \end{aligned} \tag{3.2}$$

where $[\mathbf{B}(\mathbf{q}^L)]_b$ and $[\mathbf{B}(\mathbf{q})]_b$ are the kinematic transformation matrices in local and global coordinates, respectively. The term $[\mathbf{T}]_b$ is the usual geometric transformation matrix which relates the nodal forces matrices of the two reference systems: $\{\mathbf{Q}\}_b = [\mathbf{T}]_b\{\mathbf{Q}^L\}_b$. Note that $\{\mathbf{Q}_\mathbf{0}\}_b$ and $\{\mathbf{Q}_\mathbf{0}^L\}_b$ are called matrices of initial forces at global and local coordinates, respectively. For the sake of simplicity, in this thesis, such matrices are deduced only for uniformly radial load p_0 (Figure 3.1):

$$\{\mathbf{Q}_\mathbf{0}\}_b = [\mathbf{T}]_b\{\mathbf{Q}_\mathbf{0}^L\}_b = [\mathbf{T}]_b\left\{0 \quad \frac{p_0R_b(\cos\psi_b - 1)}{\sin\psi_b} \quad 0 \quad 0 \quad \frac{p_0R(\cos\psi_b - 1)}{\sin\psi_b} \quad 0\right\}^T \tag{3.3}$$

being $[\mathbf{B}(\mathbf{q}^L)]_b$ and $[\mathbf{T}]_b$ given as follows:

$$[\mathbf{B}(\mathbf{q}^L)]_b = \begin{bmatrix} 0 & -\dfrac{1}{R_b\sin\psi_b} & 1 & -\dfrac{1}{R_b} & \dfrac{\cos\psi_b}{R\sin\psi_b} & 0 \\ 0 & -\dfrac{1}{R_b\sin\psi_b} & 0 & -\dfrac{1}{R_b} & \dfrac{\cos\psi_b}{R\sin\psi_b} & 1 \\ 1 & \dfrac{-1+\cos\psi_b}{\sin\psi_b} & 0 & -1 & \dfrac{-1+\cos\psi_b}{\sin\psi_b} & 0 \end{bmatrix} \tag{3.4}$$

$$[\mathbf{T}]_b = \begin{bmatrix} \cos\beta_b & \sin\beta_b & 0 & 0 & 0 & 0 \\ -\sin\beta_b & \cos\beta_b & 0 & 0 & 0 & 0 \\ 0 & 0 & 1 & 0 & 0 & 0 \\ 0 & 0 & 0 & \cos(\psi_b+\beta_b) & \sin(\psi_b+\beta_b) & 0 \\ 0 & 0 & 0 & -\sin(\psi_b+\beta_b) & \cos(\psi_b+\beta_b) & 0 \\ 0 & 0 & 0 & 0 & 0 & 1 \end{bmatrix} \tag{3.5}$$

Note that $[\mathbf{B}(\mathbf{q}^L)]_b$ is easily obtained by equilibrium relations between $\{\mathbf{Q}^L\}_b$ (Figure 3.2b) and $\{\mathbf{M}\}_b$ (Figure 3.2c), once it is assumed no distributed loads ($p_0 = 0$).

By assuming small displacement regime, the equilibrium becomes:

$$\sum_{b=1}^{\mathrm{m}} \{\mathbf{Q}\}_b = \{\mathbf{P}\} \quad \Rightarrow \quad \sum_{b=1}^{\mathrm{m}} [\mathbf{B}_E^0]_b^T \{\mathbf{M}\}_b = \{\mathbf{P}\} + \sum_{b=1}^{\mathrm{m}} \left\{\mathbf{Q_0}_E\right\}_b \tag{3.6}$$

where the $[\mathbf{B}_E^0]_b$ and $\left\{\mathbf{Q_0}_E\right\}_b$ are expanded matrices as the ones presented for straight frames.

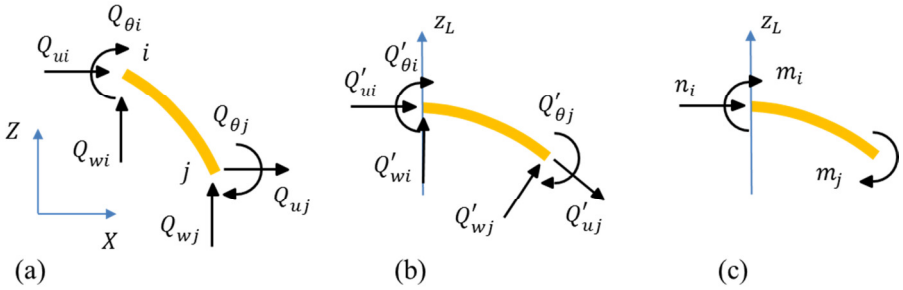

Figure 3.2 – Static variables: (a) internal forces in global and (b) local coordinates, and (c) generalised stresses.

The right-hand part of the matrix equilibrium equation (3.6) includes two terms of external forces: the ones applied on the nodes and those resulting from the distributed forces on the element. Therefore, the virtual work equation ensuing from (3.6) is:

$$\{\mathbf{U}^*\}^T \sum_{b=1}^{\mathrm{m}} [\mathbf{B}_E^0]_b^T \{\mathbf{M}\}_b = \{\mathbf{U}^*\}^T \left(\{\mathbf{P}\} + \sum_{b=1}^{\mathrm{m}} \left\{\mathbf{Q_0}_E\right\}_b \right)$$

or

$$\sum_{b=1}^{\mathrm{m}} \{\boldsymbol{\phi}^*\}_b^T \{\mathbf{M}\}_b = \{\mathbf{U}^*\}^T \left(\{\mathbf{P}\} + \sum_{b=1}^{\mathrm{m}} \left\{\mathbf{Q_0}_E\right\}_b \right) \tag{3.7}$$

The term inside the parentheses in (3.7) is the general external forces. The left-hand term of (3.7) represents the virtual work of generalised stresses and the right-hand the external virtual work. Thus, being $\{\boldsymbol{\phi}\}_b = \{\phi_i \quad \phi_j \quad \delta_i\}^T$ the matrix of generalised deformations, the kinematic equation results:

$$\{\boldsymbol{\phi}\}_b = [\mathbf{B}_E^0]_b\{\mathbf{U}\} \tag{3.8}$$

3.2 Constitutive relations for arches

3.2.1 Linear elastic arches

Regarding only linear elasticity and assuming the Euler-Bernoulli beam theory ($R_b/h > 10$), the strain energy of an arch element b is:

$$U_b = \int_0^{\psi_b} \left(\frac{M(\theta)^2}{2EI_b} + \frac{N(\theta)^2}{2AE_b}\right) R_b d\theta \tag{3.9}$$

where EI_b and AE_b are the conventional bending and axial stiffness, $M(\theta)$ and $N(\theta)$ are the bending moment and axial force at a section located at an angle θ (Figure 3.3):

$$\begin{aligned} M(\theta) &= m_i + n_i R_b(1-\cos\theta) - \frac{m_i + m_j + n_i R_b(1-\cos\psi_b)}{\sin\psi_b}\sin\theta \\ &\quad + p_0 R_b^2 \frac{\sin\theta - \sin\theta\cos\psi_b - \sin\psi_b + \sin\psi_b\cos\theta}{\sin\psi_b} \\ N(\theta) &= \frac{m_i + m_j + n_i R_b(1-\cos\psi_b)}{R_b\sin\psi_b}\sin\theta + n_i\cos\theta \\ &\quad - p_0 R_b \frac{\sin\theta - \sin\theta\cos\psi_b - \sin\psi_b + \sin\psi_b\cos\theta}{\sin\psi_b} \end{aligned} \tag{3.10}$$

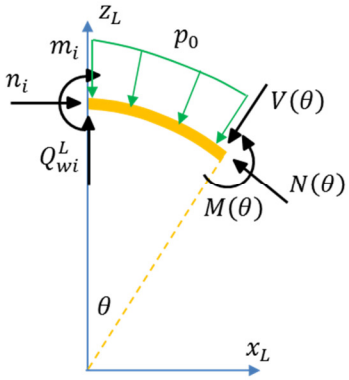

Figure 3.3 – Shear force, axial force and bending moment at a section of the elastic component.

The elastic deformations are obtained through the Castigliano's Theorem:

$$\phi_i^e = \frac{\partial U_b}{\partial m_i} \qquad \phi_j^e = \frac{\partial U_b}{\partial m_j} \qquad \delta_i^e = \frac{\partial U_b}{\partial n_i} \tag{3.11}$$

In matrix notation, such deformations can be written as:

$$\{\boldsymbol{\phi}^e\}_b = [\mathbf{F_0}]_b\{\mathbf{M}\}_b + \{\boldsymbol{\phi}^{\mathbf{0}}\}_b \tag{3.12}$$

where $[\mathbf{F_0}]_b$ is the elastic flexibility matrix:

$$[\mathbf{F_0}]_b = \begin{bmatrix} F_{11}^0 & F_{12}^0 & F_{13}^0 \\ F_{12}^0 & F_{22}^0 & F_{23}^0 \\ F_{13}^0 & F_{23}^0 & F_{33}^0 \end{bmatrix} = \begin{bmatrix} \dfrac{\partial^2 U_b}{\partial m_i \partial m_i} & \dfrac{\partial^2 U_b}{\partial m_i \partial m_j} & \dfrac{\partial^2 U_b}{\partial m_i \partial n_i} \\ \dfrac{\partial^2 U_b}{\partial m_j \partial m_i} & \dfrac{\partial^2 U_b}{\partial m_j \partial m_j} & \dfrac{\partial^2 U_b}{\partial m_j \partial n_i} \\ \dfrac{\partial^2 U_b}{\partial n_i \partial m_i} & \dfrac{\partial^2 U_b}{\partial n_i \partial m_j} & \dfrac{\partial^2 U_b}{\partial n_i \partial n_i} \end{bmatrix} \tag{3.13}$$

and $\{\boldsymbol{\phi}^{\mathbf{0}}\}_b$ is the initial deformation matrix produced by the distributed forces on the arch element:

$$\begin{aligned} \phi_i^0 &= \frac{p_0 R_b}{2} \frac{(5R_b^2 AE_b \sin\psi_b + EI_b \sin\psi_b - 2R_b^2 AE_b \psi_b \cos\psi_b - 3R_b^2 AE_b \psi_b - EI_b \psi_b)}{EI_b(\cos\psi_b + 1)AE_b} \\ \phi_j^0 &= \frac{1}{2} \frac{p_0 R_b (R_b^2 AE_b \sin\psi_b - R_b^2 AE_b \psi_b + EI_b \sin\psi_b + EI_b \psi_b)}{EI_b(\cos\psi_b + 1)AE_b} \\ \delta^0 &= \frac{p_0 R_b^2 (EI_b \sin\psi_b + 3R_b^2 AE_b \sin\psi_b - R^2 AE_b \psi_b \cos\psi_b - EI_b \psi_b - 2R^2 AE_b \psi_b)}{EI_b(\cos\psi_b + 1)AE_b} \end{aligned} \tag{3.14}$$

Since U_b is expressed by flexural and axial terms, the flexibility matrix can be understood as a sum between two parts: flexural $\left[\mathbf{F_0^f}\right]_b$ and axial $[\mathbf{F_0^a}]_b$ flexibility matrices i.e.

$$[\mathbf{F_0}]_b = \left[\mathbf{F_0^f}\right]_b + [\mathbf{F_0^a}]_b \tag{3.15}$$

where

$$
\begin{aligned}
F_{11}^{f} &= \frac{R_b(-8\sin\psi_b + 6\psi_b - 4\psi_b(\cos\psi_b)^2 + 6\cos\psi_b\sin\psi_b)}{4EI_b(\sin\psi_b)^2} \\
F_{12}^{f} &= \frac{R_b(-4\sin\psi_b + 2\psi_b - 2\cos\psi_b\sin\psi_b)}{4EI_b(\sin\psi_b)^2} \\
F_{13}^{f} &= \frac{R_b^2(10\cos\psi_b\sin\psi_b + 6\psi_b - 2\psi_b\cos\psi_b - 4\psi_b(\cos\psi_b)^2 - 10\sin\psi_b)}{4EI_b(\sin\psi_b)^2} \\
F_{22}^{f} &= \frac{R_b(2\psi_b - 2\cos\psi_b\sin\psi_b)}{4EI_b(\sin\psi_b)^2} \\
F_{23}^{f} &= \frac{R_b^2(-2\sin\psi_b - 2\psi_b\cos\psi_b + 2\psi_b + 2\cos\psi_b\sin\psi_b)}{4EI_b(\sin\psi_b)^2} \\
F_{33}^{f} &= \frac{R_b^3(-12\sin\psi_b + 12\sin\psi_b\cos\psi_b - 4\psi_b(\cos\psi_b)^2 - 4\psi_b\cos\psi_b + 8\psi_b)}{4EI_b(\sin\psi_b)^2}
\end{aligned}
\tag{3.16}
$$

and

$$
\begin{aligned}
F_{11}^{a} &= \frac{2\psi_b - 2\cos\psi_b\sin\psi_b}{4R_bAE_b(\sin\psi_b)^2} \\
F_{12}^{a} &= \frac{2\psi_b - 2\cos\psi_b\sin\psi_b}{4R_bAE_b(\sin\psi_b)^2} \\
F_{13}^{a} &= \frac{2\sin\psi_b + 2\psi_b - 2\cos\psi_b\sin\psi_b - 2\psi_b\cos\psi_b}{4AE_b(\sin\psi_b)^2} \\
F_{22}^{a} &= \frac{2\psi_b - 2\cos\psi_b\sin\psi_b}{4R_bAE_b(\sin\psi_b)^2} \\
F_{23}^{a} &= \frac{2\sin\psi_b + 2\psi_b - 2\cos\psi_b\sin\psi_b - 2\psi_b\cos\psi_b}{4AE_b(\sin\psi_b)^2} \\
F_{33}^{a} &= R_b\frac{4\sin\psi_b - 4\sin\psi_b\cos\psi_b - 4\psi_b\cos\psi_b + 4\psi_b}{4AE_b(\sin\psi_b)^2}
\end{aligned}
\tag{3.17}
$$

Geometrically, an arch segment can be degenerated to a straight line segment considering an infinite radius. Then, if $R_b \to \infty$ the angle ψ_b tends to zero, $R_b \sin\psi_b$ tends to the length of the element L_b and β_b becomes its orientation. Thus, the arch frame member can be degenerated to a straight frame member:

$$\lim_{R_b\to\infty}[\mathbf{B^0}]_b = \begin{bmatrix} \frac{\sin\beta_b}{L_b} & -\frac{\cos\beta_b}{L_b} & 1 & -\frac{\sin\beta_b}{L_b} & \frac{\cos\beta_b}{L_b} & 0 \\ \frac{\sin\beta_b}{L_b} & -\frac{\cos\beta_b}{L_b} & 0 & -\frac{\sin\beta_b}{L_b} & \frac{\cos\beta_b}{L_b} & 1 \\ -\cos\beta_b & -\sin\beta_b & 0 & \cos\beta_b & \sin\beta_b & 0 \end{bmatrix}$$

$$\lim_{R_b\to\infty}\{\mathbf{Q_0}\}_b = \frac{p_0 L_b}{2}\{\sin\beta_b \quad -\cos\beta_b \quad 0 \quad \sin\beta_b \quad -\cos\beta_b \quad 0\}^T$$

$$\lim_{R_b\to\infty}[\mathbf{F_0}]_b = \begin{bmatrix} \frac{L_b}{3EI_b} & -\frac{L_b}{6EI_b} & 0 \\ -\frac{L_b}{6EI_b} & \frac{L_b}{3EI_b} & 0 \\ 0 & 0 & \frac{L_b}{AE_b} \end{bmatrix} \quad \therefore \begin{cases} \lim_{R_b\to\infty}[\mathbf{F_0^f}]_b = \begin{bmatrix} \frac{L_b}{3EI_b} & -\frac{L_b}{6EI_b} & 0 \\ -\frac{L_b}{6EI_b} & \frac{L_b}{3EI_b} & 0 \\ 0 & 0 & 0 \end{bmatrix} \\ \lim_{R_b\to\infty}[\mathbf{F_0^a}]_b = \begin{bmatrix} 0 & 0 & 0 \\ 0 & 0 & 0 \\ 0 & 0 & \frac{L_b}{AE_b} \end{bmatrix} \end{cases} \tag{3.18}$$

$$\lim_{R_b\to\infty}\{\boldsymbol{\phi_0}\}_b = \frac{p_0 L_b^3}{24EI_b}\{1 \quad -1 \quad 0\}$$

Now, considering only a linear elastic straight frame element, the stiffness matrix of such element, given by: $\lim_{R_b\to\infty}[\mathbf{B^0}]_b^T[\mathbf{F_0}]_b^{-1}[\mathbf{B^0}]_b$, is identical to the one presented in textbooks of structural analysis of the so-called *direct stiffness method*.

3.2.2 Reinforced concrete arches

Analogously to straight frames, the arch member can be used to analyse RC structures. The finite element is composed by an assemblage of an elastic arch member and inelastic hinges located at its edges, as presented in Figure 3.4.

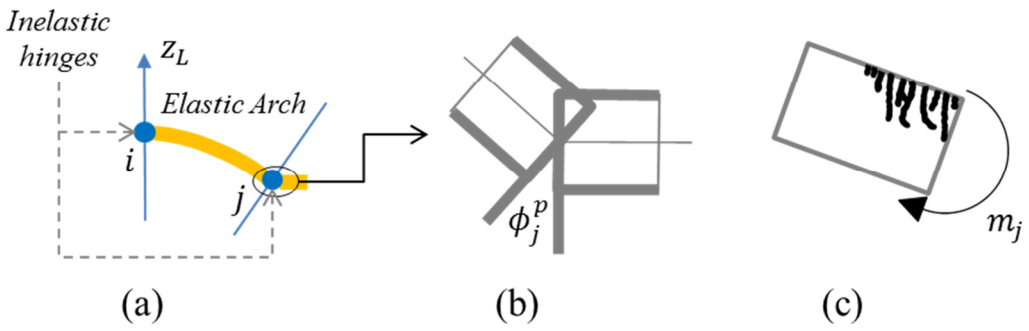

Figure 3.4 – An arched frame element with two inelastic hinges.

Again, consider that the generalised deformations $\{\boldsymbol{\phi}\}_b$ are described as a composition of an elastic part $\{\boldsymbol{\phi}^{\boldsymbol{e}}\}_b = [\mathbf{F_0}]_b\{\mathbf{M}\}_b + \{\boldsymbol{\phi_0}\}_b$, a part due to damage $\{\boldsymbol{\phi}^{\boldsymbol{d}}\}_b = [\mathbf{C(D)}]_b\{\mathbf{M}\}_b$ and a plastic part $\{\boldsymbol{\phi}^{\boldsymbol{p}}\}_b$:

$$\{\boldsymbol{\phi}\}_b = \{\boldsymbol{\phi}^{\boldsymbol{e}}\}_b + \{\boldsymbol{\phi}^{\boldsymbol{d}}\}_b + \{\boldsymbol{\phi}^{\boldsymbol{p}}\}_b \tag{3.19}$$

being $\{\mathbf{D}\}^T = \{d_i \quad d_j \quad d_a\}$ the damage variables matrix, which includes now bending damage variables (d_i and d_j) and an axial damage parameter d_a (see Figure 3.5), $[\mathbf{F_0}]$ the elastic flexibility matrix (previously presented) and $[\mathbf{C(D)}]$ the flexibility matrix on the hinges, given by:

$$[\mathbf{C(D)}]_b = \begin{bmatrix} \frac{d_i}{(1-d_i)}F_{11}^f & 0 & 0 \\ 0 & \frac{d_j}{(1-d_j)}F_{22}^f & 0 \\ 0 & 0 & \frac{d_a}{(1-d_a)}F_{33}^a \end{bmatrix} \tag{3.20}$$

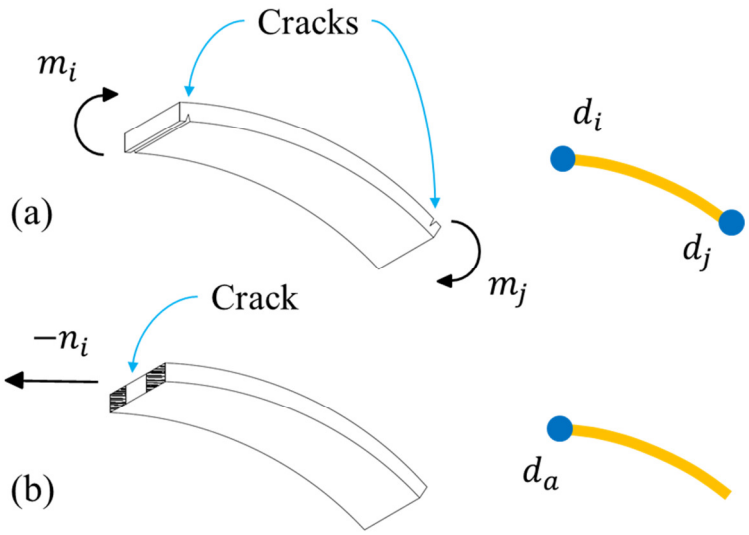

Figure 3.5 – Representation of bending damage and axial damage

Substituting the relations that characterise $\{\boldsymbol{\phi}^{\boldsymbol{e}}\}_b$ and $\{\boldsymbol{\phi}^{\boldsymbol{d}}\}_b$ in the eq.(3.19), the constitutive law is expressed as:

$$\{\boldsymbol{\phi} - \boldsymbol{\phi^p}\}_b = [\mathbf{F(D)}]_b\{\mathbf{M}\}_b + \{\boldsymbol{\phi_0}\}_b \tag{3.21}$$

being $\{\boldsymbol{\phi_0}\}_b$ the matrix of generalised initial deformations (previously presented) and $[\mathbf{F(D)}]_b = [\mathbf{F_0}]_b + [\mathbf{C(D)}]_b$ the damaged flexibility matrix:

$$[\mathbf{F(D)}]_b = \begin{bmatrix} \frac{1}{1-d_i}F_{11}^f + F_{11}^a & F_{12}^0 & F_{13}^0 \\ F_{12}^0 & \frac{1}{1-d_j}F_{22}^f + F_{22}^a & F_{23}^0 \\ F_{13}^0 & F_{23}^0 & F_{33}^f + \frac{1}{1-d_a}F_{33}^a \end{bmatrix} \tag{3.22}$$

Inelastic hinges may experience plastic rotations and permanent elongations as shown in Figure 3.6. The plastic power $\dot{\mathcal{W}}_p$ is therefore:

$$\dot{\mathcal{W}}_p = M(0)\dot{\theta}_i^p - N(0)\dot{\Delta}_i^p + M(\psi_b)\dot{\theta}_j^p - N(\psi_b)\dot{\Delta}_j^p \tag{3.23}$$

where θ_i^p and θ_j^p are plastic rotations and Δ_i^p and Δ_j^p are plastic elongations at the inelastic hinges i and j (see Figure 3.6); $M(0)$ and $N(0)$ are the bending moment and axial force on hinge i, respectively, and, analogously, $M(\psi_b)$ and $N(\psi_b)$ are the bending moment and axial force on hinge j, respectively.

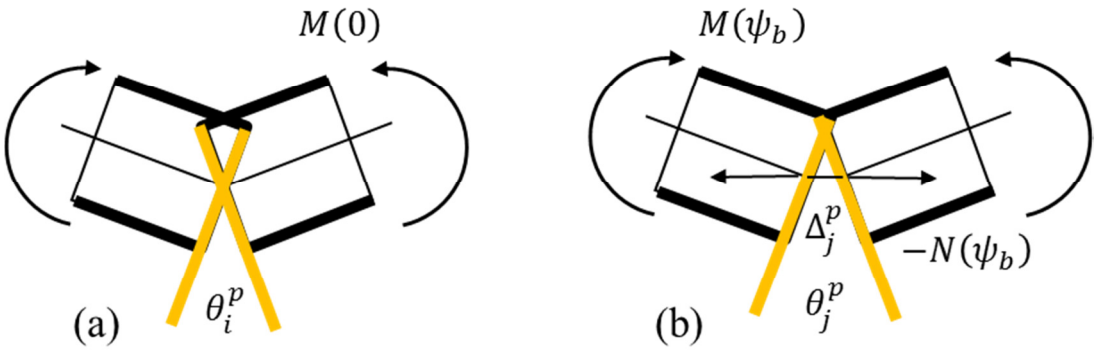

Figure 3.6 – Plastic rotations and elongations.

On the other hand, the plastic power $\dot{\mathcal{W}}_p$ can also be expressed in terms of the generalised plastic deformations $\{\boldsymbol{\phi^p}\} = \{\phi_i^p, \phi_j^p, \delta^p\}^T$ i.e.

$$\dot{\mathcal{W}}_p = m_i\dot{\phi}_i^p + m_j\dot{\phi}_j^p + n\dot{\delta}^p = M(0)\dot{\theta}_i^p - N(0)\dot{\Delta}_i^p + M(\psi_b)\dot{\theta}_j^p - N(\psi_b)\dot{\Delta}_j^p \tag{3.24}$$

Afterwards, using both relations of (3.10) results in the following equations:

$$\begin{aligned} N(0) &= n_i \\ N(\psi_b) &= \frac{m_i + n_i R_b + m_j}{R_b} \\ M(0) &= m_i \\ M(\psi_b) &= -m_j \end{aligned} \tag{3.25}$$

Thus,

$$\begin{aligned} \phi_i^p &= \theta_i^p - \frac{\Delta_j^p}{R_b} \\ \phi_j^p &= -\theta_j^p - \frac{\Delta_j^p}{R_b} \\ \delta^p &= -\left(\Delta_i^p + \Delta_j^p\right) \end{aligned} \tag{3.26}$$

So, neglecting the plastic elongations Δ_i^p and Δ_j^p the generalised deformations become: $\phi_i^p = \theta_i^p$, $\phi_j^p = -\theta_j^p$ and $\delta^p = 0$. Then, the generalised plastic deformations matrix results:

$$\{\boldsymbol{\phi}^{\boldsymbol{p}}\}^T = \left\{\phi_i^p, \phi_j^p, 0\right\} \tag{3.27}$$

being ϕ_i^p and ϕ_j^p now understood as plastic rotations of the inelastic hinges.

3.2.2.1 Evolution of internal variables

The evolution law of the generalised plastic deformations are exactly as the ones for straight frames:

$$\begin{cases}\Delta\phi_i^p = 0 \quad \text{if} \quad f_i < 0 \\ f_i = 0 \quad \text{if} \quad \Delta\phi_i^p \neq 0\end{cases} \qquad \therefore f_i = \left|\frac{m_i}{1-d_i} - c_i\phi_i^p\right| - M_{y_i} \leq 0$$
$$\begin{cases}\Delta\phi_j^p = 0 \quad \text{if} \quad f_j < 0 \\ f_j = 0 \quad \text{if} \quad \Delta\phi_j^p \neq 0\end{cases} \qquad \therefore f_j = \left|\frac{m_j}{1-d_j} - c_j\phi_j^p\right| - M_{y_j} \leq 0 \tag{3.28}$$

Neglecting the axial damage parameter, the damage evolution laws for RC arches are given by:

$$\begin{cases}\Delta d_i = 0 \quad \text{if} \quad G_i^d < R_i^d \\ G_i^d = R_i^d \quad \text{if} \quad \Delta d_i > 0\end{cases} \quad \therefore G_i^d = \frac{F_{11}^f m_i^2}{2(1-d_i)^2} \qquad R_i^d(d_i) = R_{0_i} + q_i\frac{\ln(1-d_i)}{1-d_i}$$
$$\begin{cases}\Delta d_j = 0 \quad \text{if} \quad G_j^d < R_j^d \\ G_j^d = R_j^d \quad \text{if} \quad \Delta d_j > 0\end{cases} \quad \therefore G_j^d = \frac{F_{22}^f m_j^2}{2\left(1-d_j\right)^2} \qquad R_j^d(d_i) = R_{0_j} + q_j\frac{\ln\left(1-d_j\right)}{1-d_j} \tag{3.29}$$

3.2.2.2 Practical applications

Since the lumped damage model for RC arches is an original development of this thesis, validation examples are needed. Now, three examples are discussed in order to present the accuracy of the proposed model.

The first validation example consists on a test carried out by Caratelli et al. (2011). In such work, a precast RC tunnel segment was tested (Figure 3.7). Note that such tunnel lining was actually built between Italy and Austria (CARATELLI et al., 2011).

The specimen considered by Caratelli et al. (2011) present thickness, length and width equal to 200 mm, 3640 mm and 1500 mm, respectively (Figure 3.7). The concrete presents average cubic compressive strength of 50 MPa, 8 mm rebars were used as longitudinal reinforcement and open stirrups were used as splitting reinforcement (Figure 3.7).

Regarding the symmetry of the problem, the RC segment was represented by two arch elements as shown in Figure 3.7. Through the classic RC theory, the interaction diagrams (Figure 3.8) are obtained (see Appendix A).

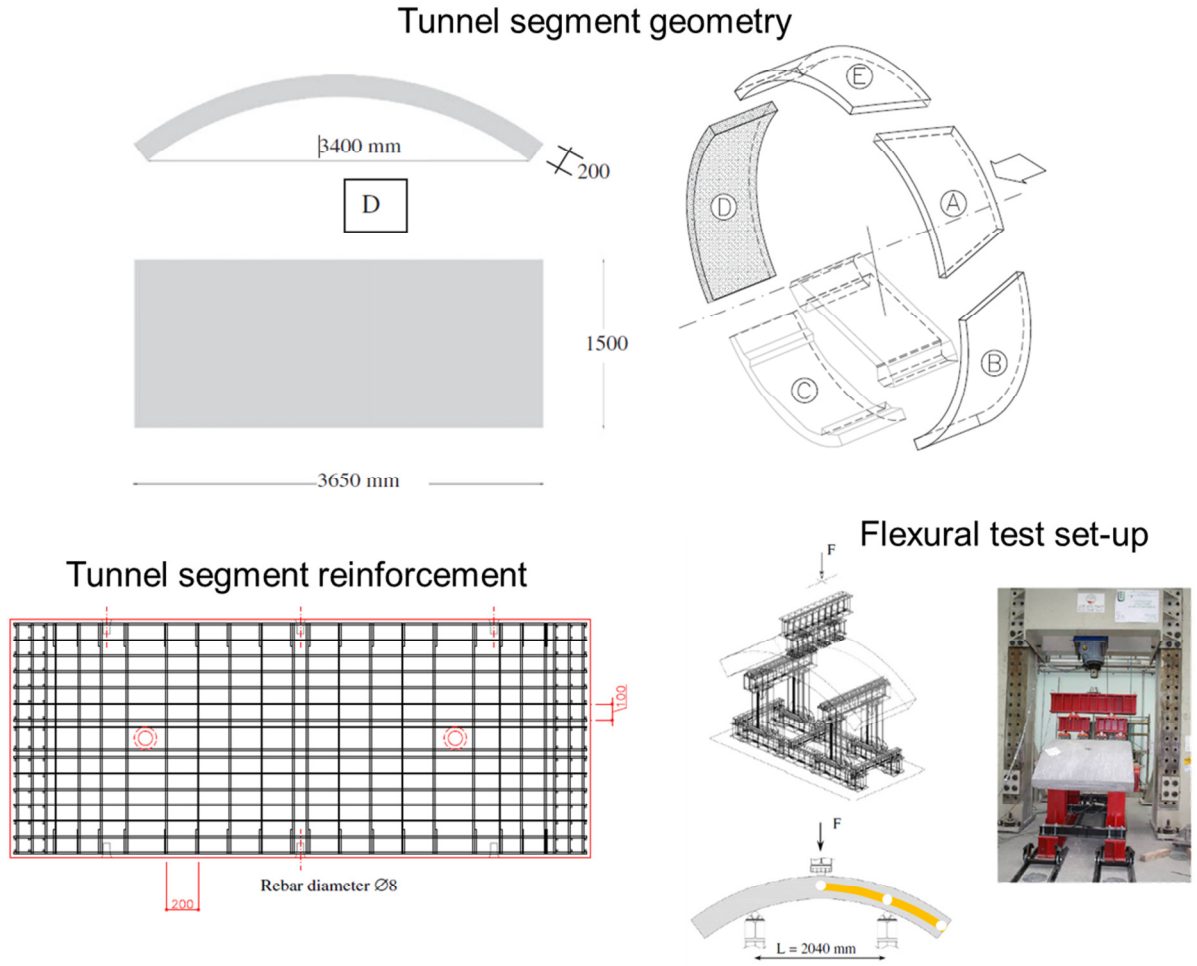

Figure 3.7 – Specimen characterisation and test set-up. [After Caratelli et al. (2011)]

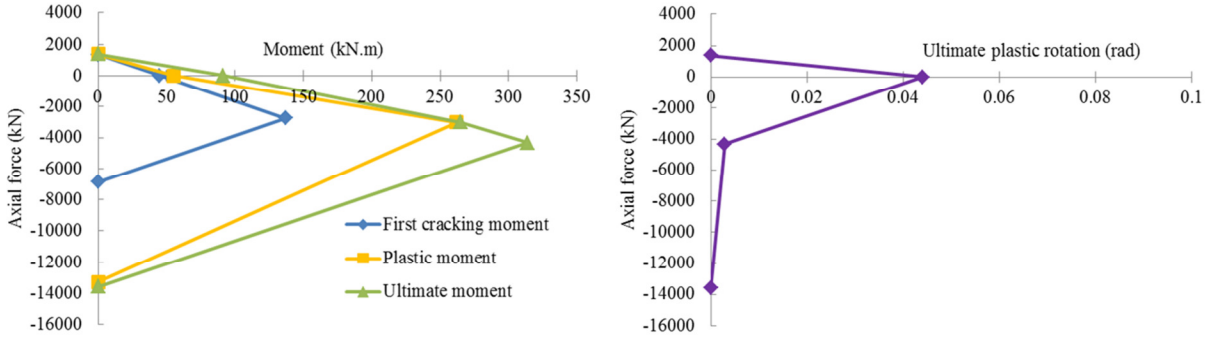

Figure 3.8 – Interaction diagrams.

Thus, since the axial force along the specimen is negligible, $M_{cr} = 45100\ \text{kN} \cdot \text{mm}$, $M_p = 55000\ \text{kN} \cdot \text{mm}$ and $M_u = 91600\ \text{kN} \cdot \text{mm}$ were taken from the interaction diagrams as the first cracking, plastic and ultimate moment, respectively. The ultimate plastic rotation is $\phi_u^p = 0.0441\ \text{rad}$ (see Appendix A) was taken with the same idea (negligible axial force).

Figure 3.9 presents the comparison between numerical and experimental (CARATELLI et al., 2011) responses on the top of the specimen. Note that the numerical solution is well fitted to the experimental result.

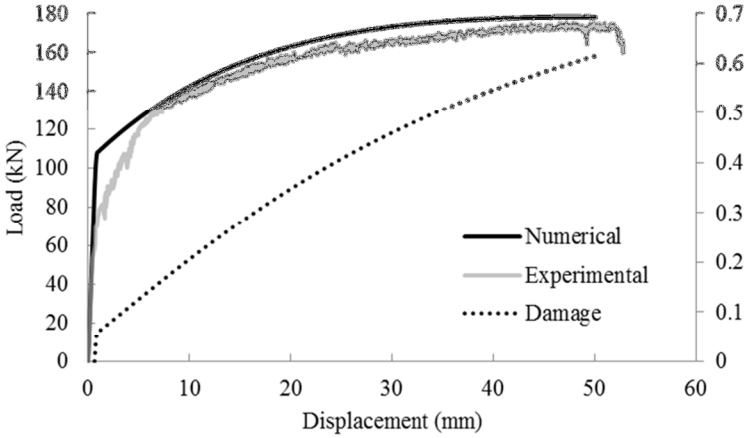

Figure 3.9 – Comparison between experimental and numerical solutions.

The main gap between numerical and experimental responses is observed for displacements smaller than 10 mm. This occurs due to diffuse cracking in concrete, which is predominant at that point. Afterwards, the inelastic phenomena concentrate at the loaded point, resulting in a well-fitted numerical response.

Considering again the initial stage of the test, the diffuse cracking occurs in the region between the supports (or from the loaded point to one support, due to the problem symmetry). In the numerical analysis, only one finite element represents this region. Therefore, it might be pointed out that the adopted mesh is favourable for the analysed problem, since there is no inelastic hinges between the loaded point and the support. Obviously, the adoption of two elements (Figure 3.10a) is a result of the practical purposes of this approach. However, another analysis with four elements is carried out (Figure 3.10b) to evaluate the accuracy of the numerical model. This new mesh (Figure 3.10b) presents a node in the region with diffuse cracking i.e. now an inelastic hinge can nucleate in the region with diffuse cracking. In Figure 3.10c presents a comparison between experimental and numerical analyses.

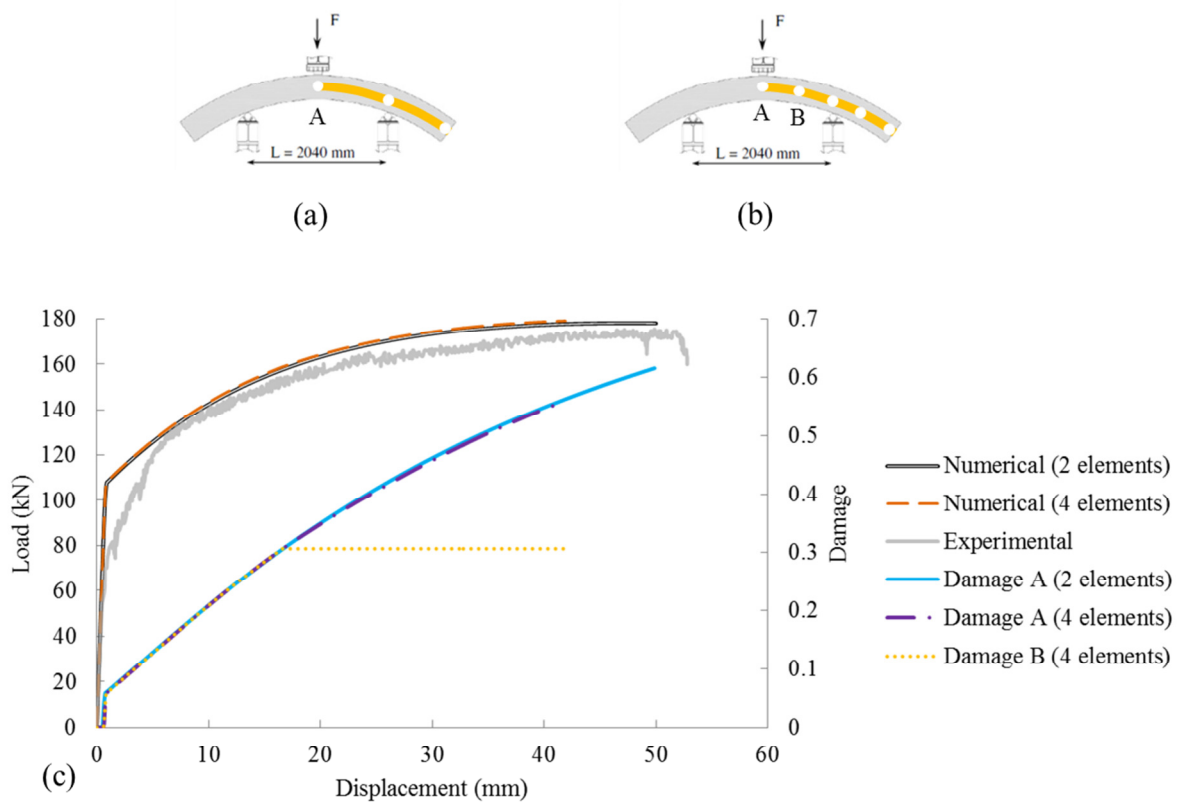

Figure 3.10 – Tunnel segment analysis: adopted meshes with (a) two and (b) four elements, and experimental and numerical responses.

Note that the numerical analyses (Figure 3.10c) are practically coincident. In the mesh with two elements, the cracking process is entirely lumped at the hinge A. On the other hand, in the mesh with four elements the hinges A and B account for the diffuse cracking. Despite this characteristic, when the diffuse cracking is no longer determinant to the mechanical behaviour, the damage evolution at hinge B stopped completely. At this point, damage at hinge A continues to evolve, ensuring the same global behaviour observed in the mesh with only two elements. This result shows the accuracy of the LDM approach, where the quantity of inelastic hinges seems to be irrelevant to characterise the structural behaviour.

The second validation example consists in the numerical simulation of a test carried out by Nishikawa (2003). The specimen under consideration was similar to the one of the previous example but the loading was applied in two points of the segment (see Figure 3.11a). The specimen was represented using two arch elements as shown in the Figure 3.11b.

The comparison between test and model is presented in Figure 3.12. This time, the parameters for the simulation were not computed but identified from the experimental results because of lack of pertinent information:

$$EI_b = 0.3014284 \times 10^{10}\ \text{kN} \cdot \text{mm}^2$$
$$AE_b = 0.1092 \times 10^{7}\ \text{kN}$$
$$R_b = 1409\ \text{mm}$$
$$M_{cr} = 1786\ \text{kN} \cdot \text{mm} \quad (3.30)$$
$$M_p = 12952\ \text{kN} \cdot \text{mm}$$
$$M_u = 17722\ \text{kN} \cdot \text{mm}$$
$$\phi_u^p = 0.02137\ \text{rad}$$

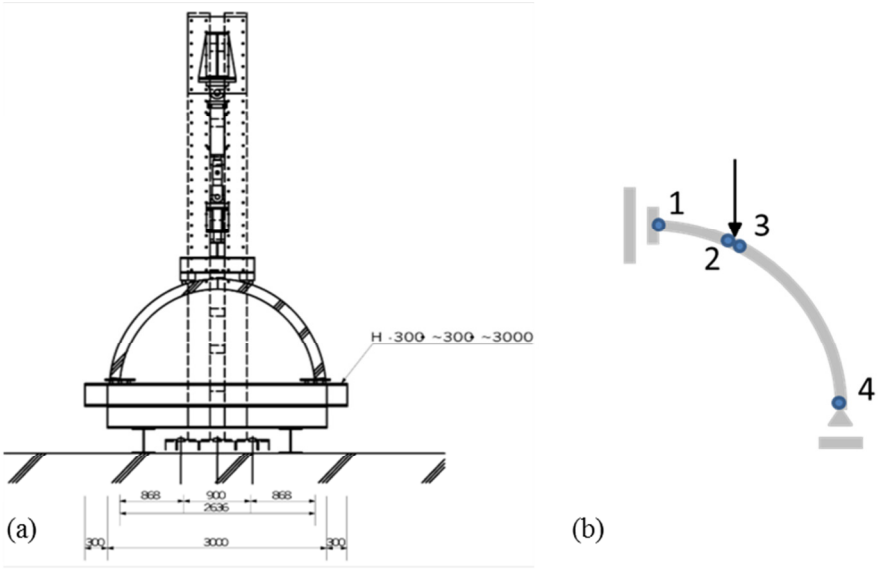

Figure 3.11 – (a) Test by Nishikawa (2003) and (b) problem idealisation.

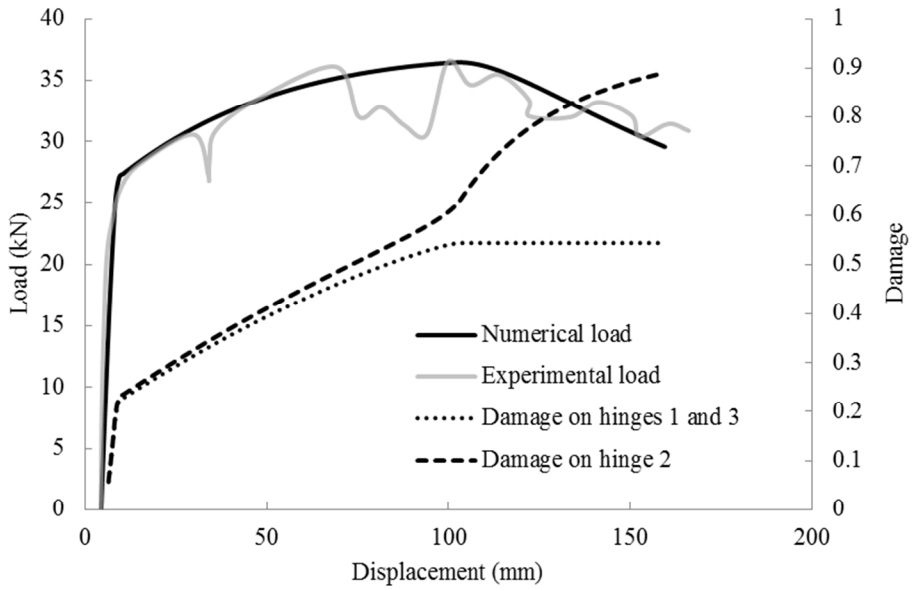

Figure 3.12 – Displacement vs. force and displacement vs. damage in the test by Nishikawa (2003).

Figure 3.13 shows the bending moment distribution at four different stages of the loading; in the horizontal axis the position of the cross-sections is represented by its angle with respect to the axis of symmetry of the arch; bending moments at the internal cross sections were computed using (3.10). Figure 3.14 indicates the deformed configurations and the damage as well as plastic rotations of the hinges. Figure 3.13a and Figure 3.14a correspond to the initiation of cracking at hinges 1 and 2. Up to this stage, the behaviour of the arch is elastic; note that the maximum bending moments are equal to the first cracking moment of the cross-section. Figure 3.13b and Figure 3.14b correspond to the initiation of yielding of the longitudinal reinforcement, hence appearance of plastic rotations. At this stage, damage has evolved in hinges 1, 2 and 3 reaching values of 0.20; the resulting damage rotations of the hinges and are indicated in Figure 3.14b. Physically, those damage rotations are the consequence of the crack opening displacements of the set of fissures that are assumed concentrated in the plastic hinge zone. Moments on the hinges at this stage are equal to the yield moment of the cross section.

Figure 3.13c and Figure 3.14c correspond to the maximum force reached during the simulation. Therefore bending moments are equal to the ultimate moments of the cross-section. At this stage, damage as well as plastic rotations are present in the inelastic hinges; their values are indicated in Figure 3.14c. The state of the arch at the end of the simulation is represented in Figure 3.13d and Figure 3.14d.

The model captures correctly the softening phase of the behaviour. Damage localisation was observed in the simulation. In the hardening stage, damage evolves in the inelastic hinges 1, 2 and 3; subsequently, damage evolution stops in hinges 1 and 3 while energy dissipation concentrates only on hinge 2. This damage localisation can also be observed in the bending distributions of Figure 3.13c-d as well as in the damage rotations indicated in Figure 3.14c-d. Note that the values of the damage rotations at hinge 1 decreased between stages c and d but augmented in hinge 2. Plastic rotation, on the other hand, remained constant in hinge 1 but continued increasing at hinge 2.

Due to the lack of pertinent information, the damage localisation in the experiment may be not occurred at the same point of the numerical solution. Nevertheless, note that the entire process of damage localisation was captured by the finite element programme without human intervention. The automatic choice for the hinge 2 is easily explained by the LDM equations. Firstly, observe that hinge 2 belongs to the left element and hinge 3 belongs to the right one. In arch elements, the terms F_{11}^{f} and F_{22}^{f} of the flexibility matrix are different. The

term F_{22}^f dictates the damage evolution in hinge 2 and the term F_{11}^f has the same function in hinge 3. Since the radius R_b and the flexural rigidity EI_b are constant for both elements, considering the arc angles of each element the flexibility terms are: $F_{22}^f \cong 0.11R_b/EI_b$ for hinge 2 and $F_{11}^f \cong 0.33R_b/EI_b$ for hinge 3. Therefore, hinge 2 concentrates damage.

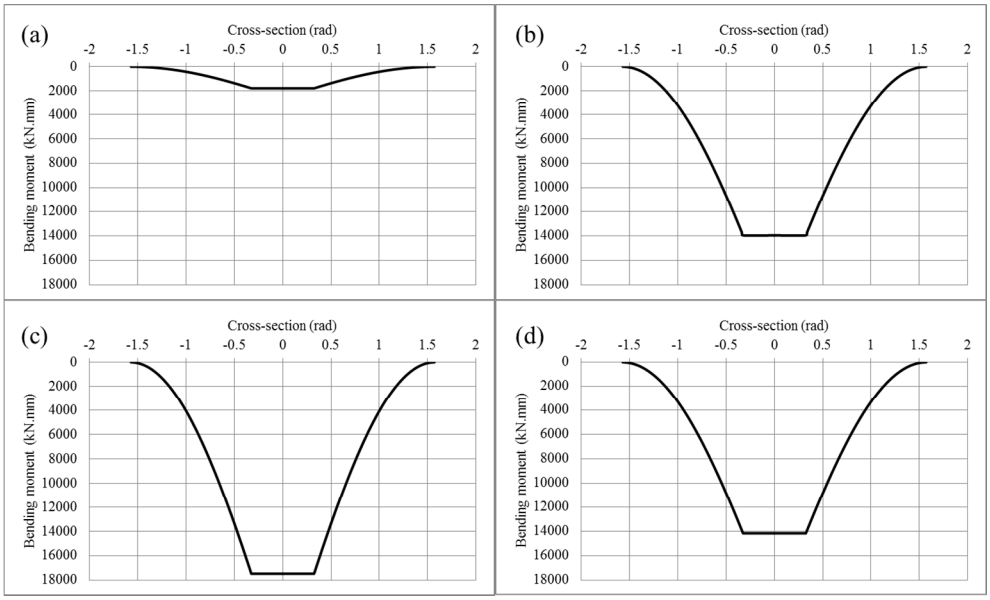

Figure 3.13 – Bending moment distribution (a) crack initiation (b) plasticity initiation (c) ultimate force (d) final analysis.

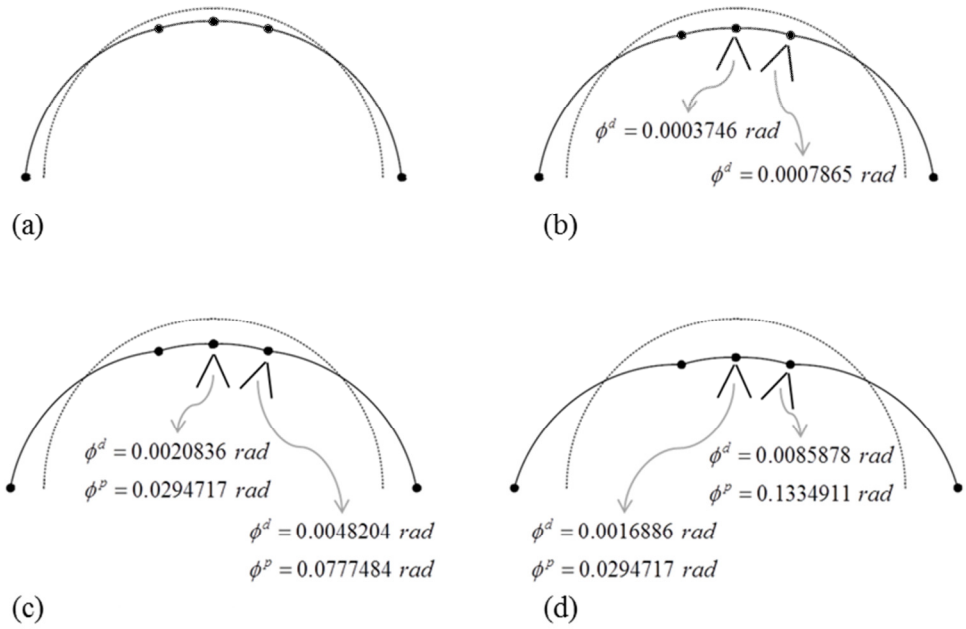

Figure 3.14 – Deformed configurations of the arch (a) crack initiation (b) plasticity initiation (c) ultimate force (d) final analysis.

The third examples addresses to a circular tube, tested by Silva (2011). The circular tube was made out of reinforced concrete (Figure 3.15c). The test set-up is depicted in Figure 3.15a. Taking advantage of the double symmetry of the problem, only one element was used to model the quarter circumference (Figure 3.15b). For the numerical analysis, $EI = 7.986 \times 10^8\ \text{kN} \cdot \text{mm}^2$, $AE = 1584000\ \text{kN}$, $\text{M}_{\text{cr}} = 7516.7\ \text{kN} \cdot \text{mm}$, $\text{M}_{\text{p}} = 9166.7\ \text{kN} \cdot \text{mm}$, $\text{M}_{\text{u}} = 28625\ \text{kN} \cdot \text{mm}$, $\phi_u^p = 0.0113$ were adopted as model parameters.

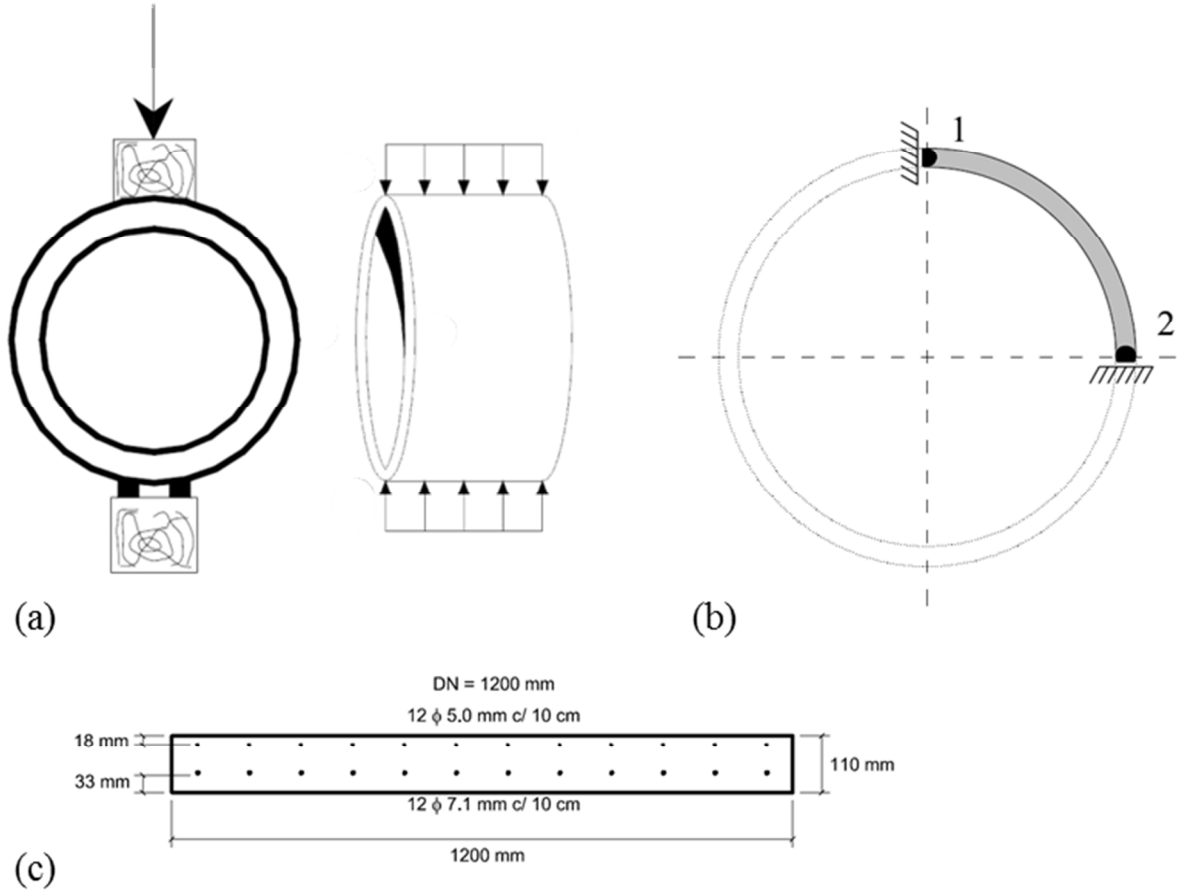

Figure 3.15 – (a) Set-up of a test on a reinforced concrete tube (SILVA, 2011); (b) Adopted mesh; (c) Tube cross section.

Figure 3.16 shows the comparison between the numerical simulation and the experimental response in a graph of displacement vs. force. One can see clearly the good correspondence between experimental and numerical results.

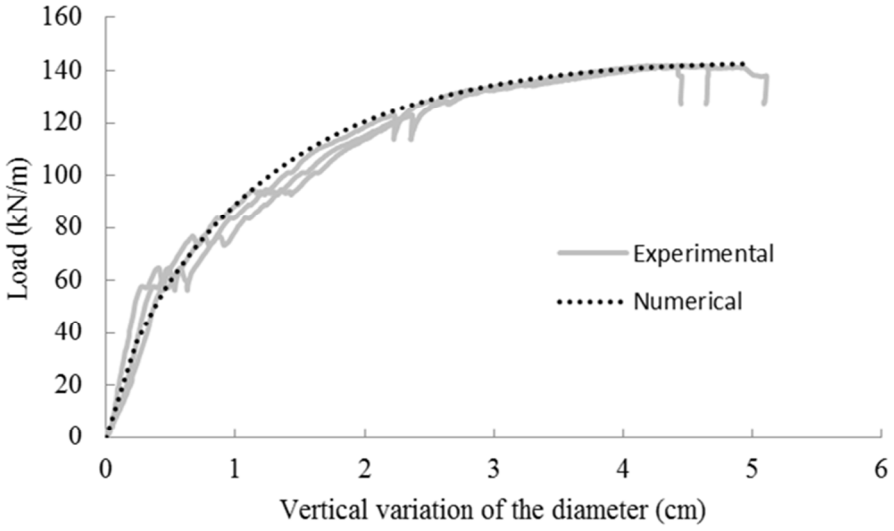

Figure 3.16 – Displacement vs. load.

3.2.3 Quasi-brittle structures

Now, a lumped damage model is proposed to analyse structures made of quasi-brittle materials, such as unreinforced concrete. The main difference from the aforementioned models is related to the meaning and the evolution laws of the internal variables.

The inelastic phenomena on RC structures are quantified via two internal variables: plastic deformation and damage. The plastic deformation variable describes the yielding of the reinforcement and the damage variable is related to the concrete cracking.

However, for unreinforced concrete structures (or any quasi-brittle structures), plastic deformations can be neglected $\{\boldsymbol{\phi}^{\boldsymbol{p}}\}_b = \{\mathbf{0}\}$ but the damage variable is still related to crack propagation. Then, the constitutive relation is given by:

$$\{\boldsymbol{\phi}\}_b = [\mathbf{F(D)}]_b\{\mathbf{M}\}_b + \{\boldsymbol{\phi_0}\}_b \tag{3.31}$$

3.2.3.1 Evolution of internal variables

The damage evolution law is again proposed by a generalised Griffith criterion:

$$\begin{cases} \Delta d_i = 0 \quad \text{if} \quad G_i^d < R_i^d \\ G_i^d = R_i^d \quad \text{if} \quad \Delta d_i > 0 \end{cases} \quad \therefore G_i^d = \frac{F_{11}^f m_i^2}{2(1-d_i)^2}$$
$$\begin{cases} \Delta d_j = 0 \quad \text{if} \quad G_j^d < R_j^d \\ G_j^d = R_j^d \quad \text{if} \quad \Delta d_j > 0 \end{cases} \quad \therefore G_j^d = \frac{F_{22}^f m_j^2}{2\left(1-d_j\right)^2} \tag{3.32}$$

where the crack resistance function $R^d(d)$ must be defined and, again, the axial damage d_a is neglected.

Immediately, an intuitive adoption to this type of structure is to assume a perfectly brittle behaviour:

$$R^d(d) = R_0 \tag{3.33}$$

Such adoption can present some issues as, for instance, the numerical response may not be representative due to the perfectly brittle behaviour and the model might present numerical instabilities.

An enhanced alternative is to consider that the quasi-brittle behaviour is described by an exponential function (Figure 3.17) such as:

$$m = M_{cr} \exp\left(-\mu(\phi - \phi_{cr})\right) \tag{3.34}$$

where M_{cr} is the first cracking moment, $\phi_{cr} = F^0 M_{cr}$ is the first cracking rotation and μ is a parameter that characterises the decaying tendency of the exponential branch (Figure 3.17).

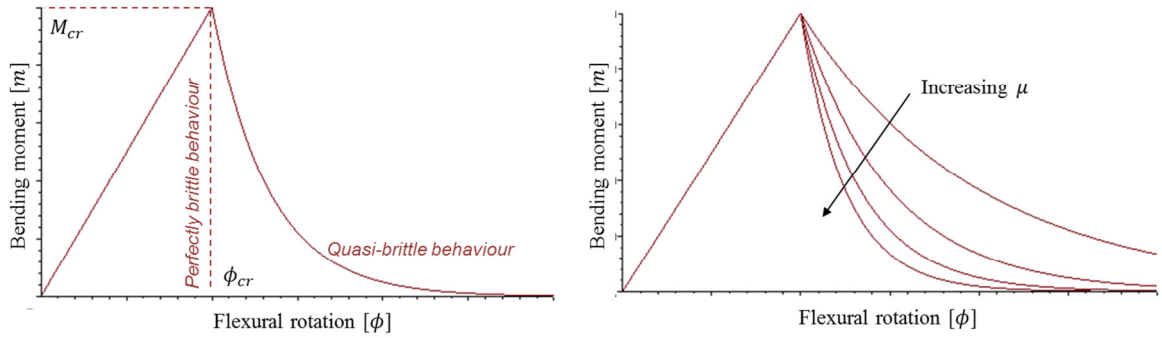

Figure 3.17 – Quasi-brittle behaviour.

Using a deformation equivalence hypothesis, the quasi-brittle behaviour can also be expressed by an elasticity relation i.e.

$$m = (1 - d)\frac{1}{F^0}\phi \tag{3.35}$$

Finally, by the generalised Griffith criterion:

$$\frac{m^2 F^0}{2(1-d)^2} = R^d(d) \tag{3.36}$$

where $R^d(d)$ is the new crack resistance function.

By solving the system composed by equations (3.34), (3.35) and (3.36), and adopting $q_{un} = \mu M_{cr} F^0 \exp(\mu M_{cr} F^0)$ as a model parameter, the new crack resistance function is:

$$R^d(d) = \frac{M_{cr}^2 F^0}{2} \mathrm{W}\left(\frac{q_{un}}{1-d}\right)^2 \mathrm{W}(q_{un})^{-2} = R_0 \mathrm{W}\left(\frac{q_{un}}{1-d}\right)^2 \mathrm{W}(q_{un})^{-2} \tag{3.37}$$

where W( ) is the Lambert W function (see Corless et al. (1996) for a detailed discussion). Note the presence of the element flexibility F^0 in the definition of the model parameter q_{un}, therefore, q_{un} depends on the element length.

The Lambert W function, also named as omega function or product function, is the transcendental function that solves the equation $y \exp(y) = x$ i.e. if $y = \mathrm{W}(x)$ then the equation $y \exp(y) = x$ is solved. The Lambert W function can be univocally defined as a real function in the interval $(-\exp(-1), \infty)$.

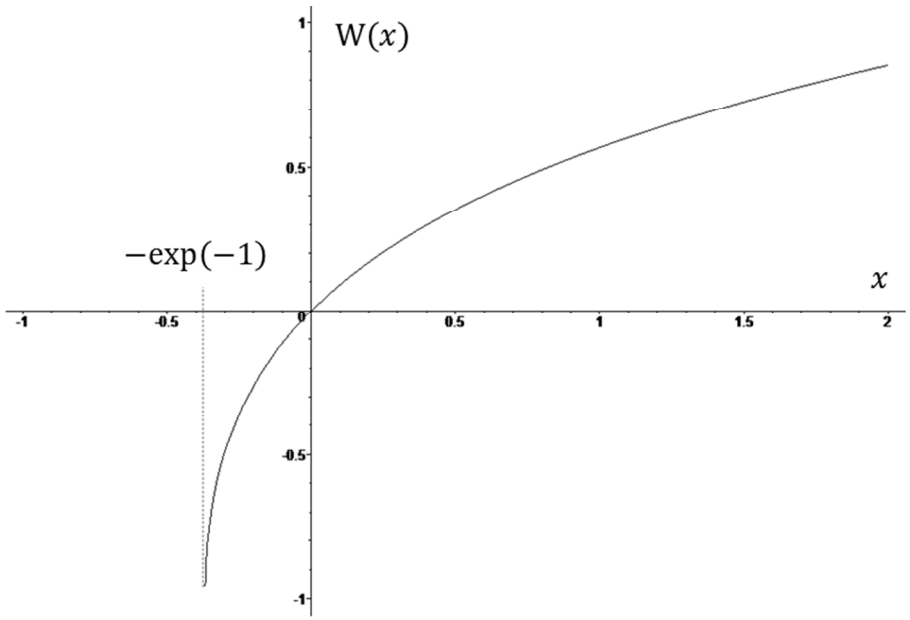

Figure 3.18 – Univocal definition of the Lambert W function.

Figure 3.19 presents a comparison between the three crack-resistance functions previously presented (logarithmic hardening – for RC structures –, perfectly brittle, and Lambert hardening).

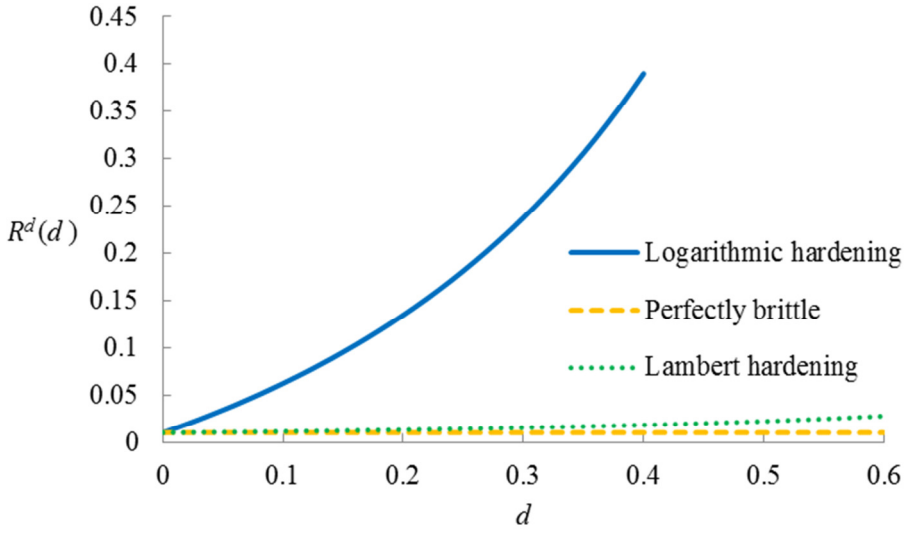

Figure 3.19 – Crack-resistance functions ($R_0 = 0.01$) for reinforced concrete ($q = -0.45$), unreinforced concrete ($q_{un} = 1.21$) and perfectly brittle behaviour.

Note that the Lambert hardening is a general relationship for brittle and quasi-brittle behaviours. In other words, if: $q_{un} \to \infty \Rightarrow \mathrm{W}\left(q_{un}/(1-d)\right)^2 \mathrm{W}(q_{un})^{-2} \to 1$ i.e. if the model parameter q_{un} tends to infinite, the Lambert hardening tends to assume a perfectly brittle behaviour.

3.2.3.2 Crack opening displacement as a function of the damage in an inelastic hinge

Differently from RC structures, when an inelastic hinge activates in an unreinforced concrete structure there is predominance of a crack that should propagate up to the collapse of the cross section. Considering this particular behaviour, the crack opening displacement (COD), or crack mouth opening displacement, can be estimated by the activated inelastic hinge.

This information may be useful in practical applications, where the COD can be correlated to a decision making about structural retrofitting and maintenance. According to Shi (2009), the diagnostics of structures such as tunnels, dams and bridges, among others, is obtained by using crack analysis.

Therefore, a methodology to estimate COD in unreinforced concrete structures (or any quasi-brittle structures) is here proposed. In a structure, consider a region with a cracked cross section (Figure 3.20a). In such cross section the resisting height $\tilde{h}$ is smaller than the total height (h) due to the crack length. Thus, by LDM, the crack is described by a damage variable, resulting in a damage rotation of the inelastic hinge ϕ_i^d (Figure 3.20b). Being l the distance between the crack mouth and the neutral axis, the COD can be calculated as:

$$\mathrm{COD}_i \cong \phi_i^d l = \phi_i^d \left(h - \frac{\tilde{h}}{2} \right) \tag{3.38}$$

Between the quantities that are necessary to estimate COD, note that the resisting, or effective, height $\tilde{h}$ is still uncalculated.

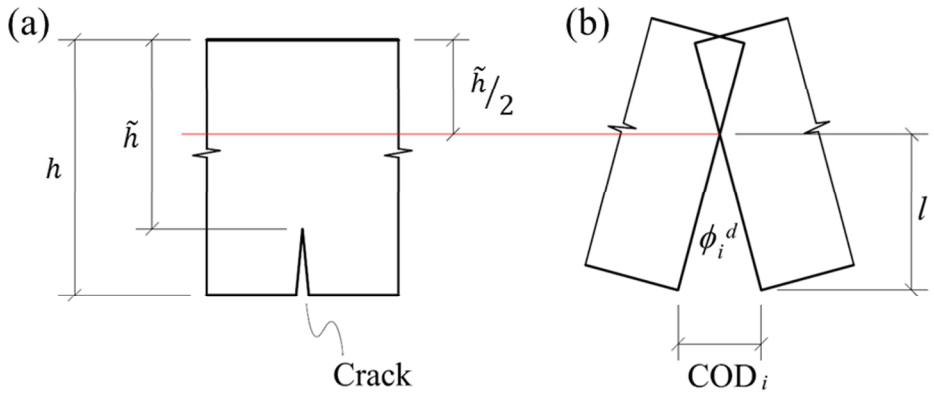

Figure 3.20 – Estimation of COD.

Now, the main assumption is that the inertia is directly affected by damage. In this sense, in an inelastic hinge i, there is an effective inertia that may be approximated by the following relation:

$$\tilde{I_b} \cong I_b(1 - d_i) \tag{3.39}$$

thus

$$\frac{b\tilde{h}^3}{12} \cong \frac{bh^3}{12}(1 - d_i) \tag{3.40}$$

Therefore, the effective height is defined in terms of the total height and the damage variable:

$$\tilde{h} = h\sqrt[3]{1-d_i} \tag{3.41}$$

Finally, COD is given as:

$$\mathrm{COD}_i \cong \phi_i^d h\left(1 - \frac{\sqrt[3]{1-d_i}}{2}\right) \tag{3.42}$$

3.2.3.3 Parametric analysis

So far, the model parameter q_{un} was defined as $q_{un} = \mu M_{cr} F^0 \exp(\mu M_{cr} F^0)$ i.e. q_{un} is related to the decaying tendency of the quasi-brittle response (μ). Since a simplified estimation of COD is possible by the proposed LDM approach, the model parameter q_{un} can be expressed in terms of fracture energy G_f (Figure 3.21a). The fracture energy G_f is obtained by integration of $\sigma - \mathrm{COD}$ relation.

For an inelastic hinge, the $\sigma - \mathrm{COD}$ relation depends on the bending moment (m), the damage rotation (ϕ^d) and the function of the crack length (a) in terms of the damage variable. The simplified COD expression (3.38) is given by the product between the damage rotation (ϕ^d) and the distance from the neutral axis to the crack mouth (l). Note that the quantity l depends on the relation between the crack length and the damage variable. Then, since COD is proportional to ϕ^d and l is based on simplified assumptions, so far, an alternative is to use $m - \phi^d$ relation instead of $\sigma - \mathrm{COD}$ (Figure 3.21b). Now, the integration of the $m - \phi^d$ relation gives a quantity H_f proportional to the fracture energy ($H_f \propto G_f$). This proportionality depends on the relation between $m - \phi^d$ and $\sigma - \mathrm{COD}$ expressions.

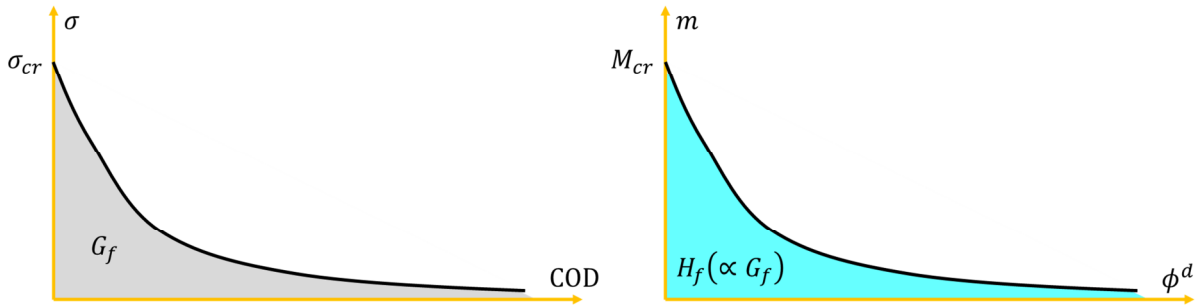

(a) (b)

Figure 3.21 – Parametric analysis based on fracture energy.

The $m-\phi^d$ relation is a result of the generalised Griffith criterion:

$$\frac{m^2F^0}{2(1-d)^2}=\frac{M_{cr}^2F^0}{2}\mathrm{W}\left(\frac{q_{un}}{1-d}\right)^2\mathrm{W}(q_{un})^{-2}$$
$$m=M_{cr}(1-d)\frac{\mathrm{W}\left(\frac{q_{un}}{1-d}\right)}{\mathrm{W}(q_{un})}\qquad\therefore d=\frac{\phi^d}{F^0m+\phi^d} \tag{3.43}$$

The fracture quantity H_f is obtained by:

$$H_f=\int_0^\infty m(\phi^d)d\phi^d=\frac{1}{2}\frac{M_{cr}^2F^0[\mathrm{W}(q_{un})+2]}{\mathrm{W}(q_{un})} \tag{3.44}$$

Therefore, q_{un} is expressed as:

$$q_{un}=\frac{2M_{cr}^2F^0}{2H_f-M_{cr}^2F^0}\exp\left(\frac{2M_{cr}^2F^0}{2H_f-M_{cr}^2F^0}\right)$$
or
$$\frac{2M_{cr}^2F^0}{2H_f-M_{cr}^2F^0}=\mathrm{W}(q_{un})=\mu F^0M_{cr} \tag{3.45}$$

Note that the fracture quantity H_f is inversely proportional to μ i.e. it is also possible to express μ in terms of the fracture energy (G_f).

In order to analyse the influence of H_f in the numerical solution, an unreinforced concrete cantilever beam (see Figure 3.22) is evaluated. Two meshes, with one and two

elements, are used to analyse this problem (Figure 3.22). For the sake of simplicity, an arbitrary value of H_f is adopted (Figure 3.22). Therefore, the parameter q_{un} presents a value for each mesh (Figure 3.22). Figure 3.23 presents the comparison between the numerical solutions.

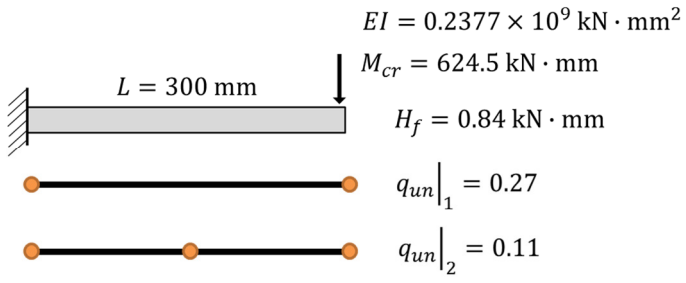

Figure 3.22 – Unreinforced cantilever beam: problem geometry and adopted meshes.

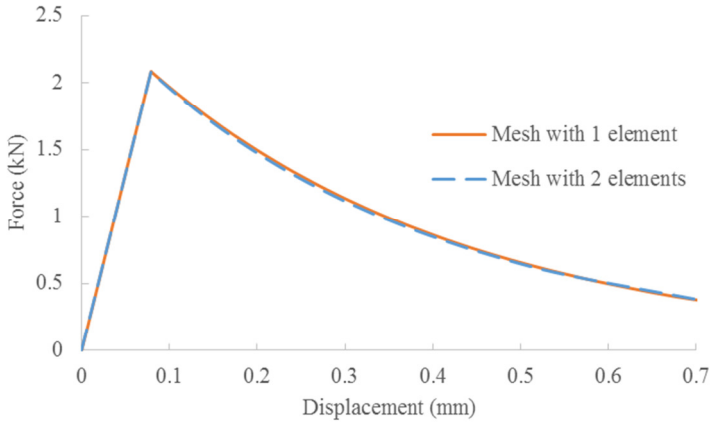

Figure 3.23 – Comparison between numerical solutions.

Note that the numerical responses are practically coincident. Such characteristic is due to the adoption of the fracture quantity (H_f). For real problems, if H_f is obtained by the fracture energy (G_f), the numerical analysis should reproduce a unique solution. It is noteworthy that, in the case with two elements, the mid-span hinge does not activate.

On what follows, due to the lack of pertinent information about H_f the model parameter q_{un} is obtained by experimental observations of decaying tendency of the quasi-brittle response (μ).

3.2.3.4 Practical applications

In order to continue the validation process of this proposed lumped damage model, four examples where studied. In such examples, the LDM response is compared with experimental and/or classic fracture mechanics responses.

The first example addresses to an unreinforced concrete beam subjected to bending (Figure 3.24a), tested by Shi et al. (2001). They also presented numerical modelling using finite elements and classic fracture mechanics (Figure 3.24b).

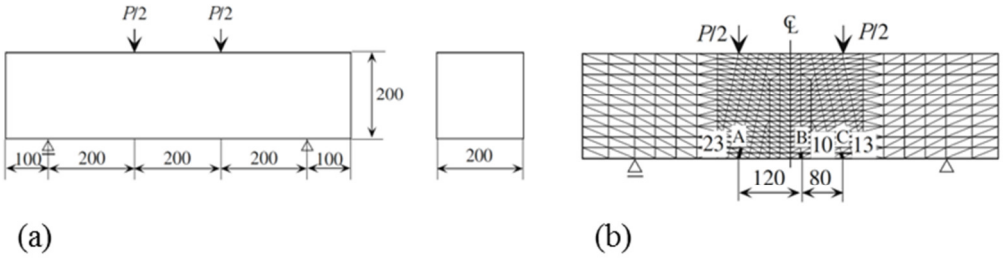

Figure 3.24 – Fracture test on an unreinforced concrete beam (dimensions in mm): (a) test geometry (Shi et al., 2001) and (b) finite element mesh for fracture analysis (Shi et al., 2001).

Shi et al. (2001) carried out six simulations, considering different positions and lengths of cracks. According to Shi et al. (2001), the best simulation with fracture mechanics considers asymmetric crack propagation, since the experimental behaviour presents a main crack under the left point of applied force.

Note that even if the structure is symmetric, the experimental result was not. Numerically, this response can be obtained by including a slightly larger crack in the fracture mechanics (FM) analysis (see Figure 3.24b) or a smaller crack resistance in the LDM one.

A mesh with five elements was used in the LDM simulation (Figure 3.25a). Figure 3.25b shows the comparison between FM, LDM and experimental responses in a displacement vs. load graph. Figure 3.26 depicts the COD vs. load responses for FM and LDM analyses.

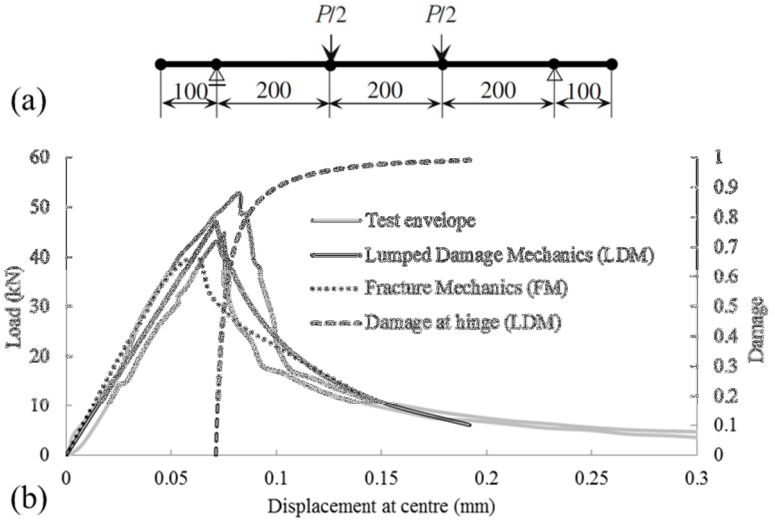

Figure 3.25 – Fracture test on an unreinforced concrete beam: (a) Mesh for the LDM analysis (dimensions in mm) and (b) displacement vs. force. LDM analysis with $M_{cr} = 4705$ kN · mm, $EI = 0.22 \times 10^{10}$ kN · mm and $q_{un} = 0.20$; experimental and Fracture Mechanics (FM) results from Shi et al. (2001).

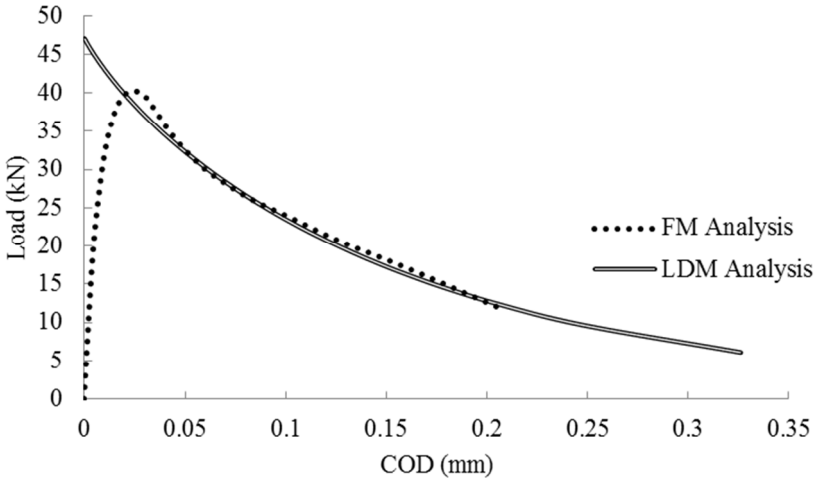

Figure 3.26 – Force vs. Crack opening displacement, fracture mechanics results (SHI et al., 2001) and LDM approach.

Regarding Figure 3.25b, the LDM response is quite fitted to the FM and the experimental ones. An excellent agreement is also observed in the COD estimation, where there is only a numerical confrontation i.e. FM vs. LDM.

The second example also addresses to an unreinforced concrete beam, which was tested by Hamad, Owen and Hussein (2013). The test scheme is presented in Figure 3.27 (HAMAD; OWEN; HUSSEIN, 2013).

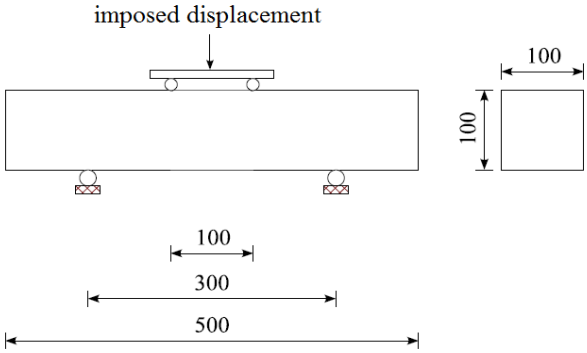

Figure 3.27 – Fracture test scheme used by Hamad et al. (2013); dimensions in mm.

According to Hamad, Owen and Hussein (2013), due to physical imperfections of the specimen, an asymmetric response was observed, being the main crack positioned at 136 mm of the left support (Figure 3.28), instead of appearing at the mid-span of the prism (150 mm of the left support). Therefore, to perform the best simulation it is convenient to set a node/hinge precisely at 136 mm from the left support. Then, the LDM mesh contains six elements (Figure 3.29).

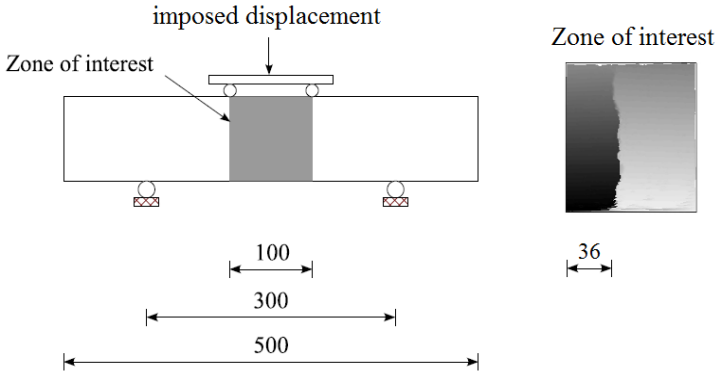

Figure 3.28 – Region with maximum bending moment and crack pattern HAMAD; OWEN; HUSSEIN, 2013); dimensions in mm.

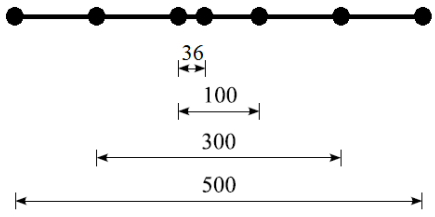

Figure 3.29 – LDM mesh (dimensions in mm).

In this example, the LDM is compared solely with experimental responses. Figure 3.30 presents comparisons between LDM and experimental responses.

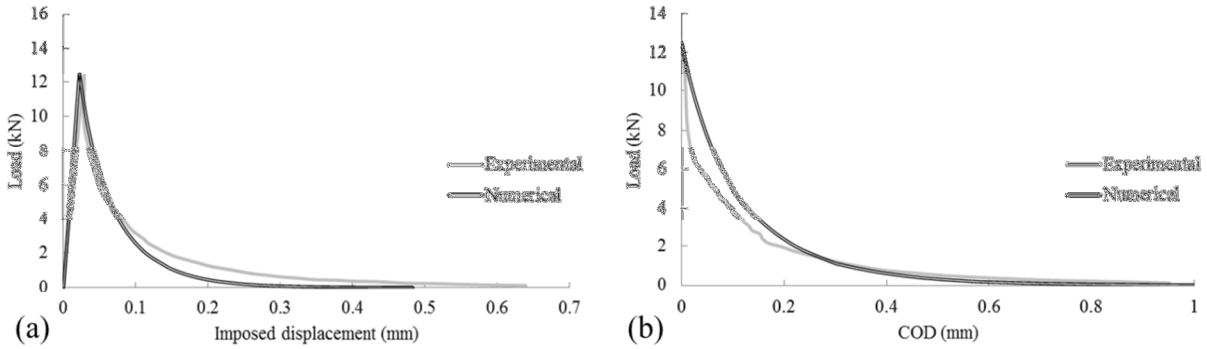

Figure 3.30 – Fracture test on an unreinforced concrete beam (HAMAD; OWEN; HUSSEIN, 2013): (a) displacement vs. load and (b) COD vs. load graphs. Parameters for LDM analysis: $M_{cr} = 625.4$ kN · mm, $EI = 0.2377 \times 10^9$ kN · mm^2 and $q_{un} = 0.027$.

Both comparisons depicted in Figure 3.30 show the good accuracy of the hereby presented procedure. Regarding COD (Figure 3.30b), in correspondence to the crack nucleation the numerical response indicates a smooth decrease of load. However, the experimental behaviour depicts a more abrupt decrease. According to Hamad, Owen and Hussein (2013), in this test the COD becomes visible to the naked eye when the value of 0.15 mm is reached. At this point, the numerical simulation is already quite close to the experimental behaviour. Beyond 0.2 mm of COD, the numerical and experimental responses are really close. According to Hamad, Owen and Hussein (2013), the prism failure was reached when the value of COD was 1.0 mm. At this point, in the numerical model the hinge presents damage value equal to 0.999994, characterising failure.

Differently from the previous beam examples, the third example consists on an experimental test of a tunnel lining, carried out by Abo, Tanaka and Yoshida (2000). The specimen geometry and test set-up are depicted in Figure 3.31.

Again, an analysis of the structure using fracture mechanics concepts in combination with the FEM was described in Shi et al. (2001) and is used as reference for the simplified analysis based on LDM. Note that the experimental results are available only for the hardening phase of the behaviour, thus only the fracture mechanics results can be used as a reference for the LDM approach.

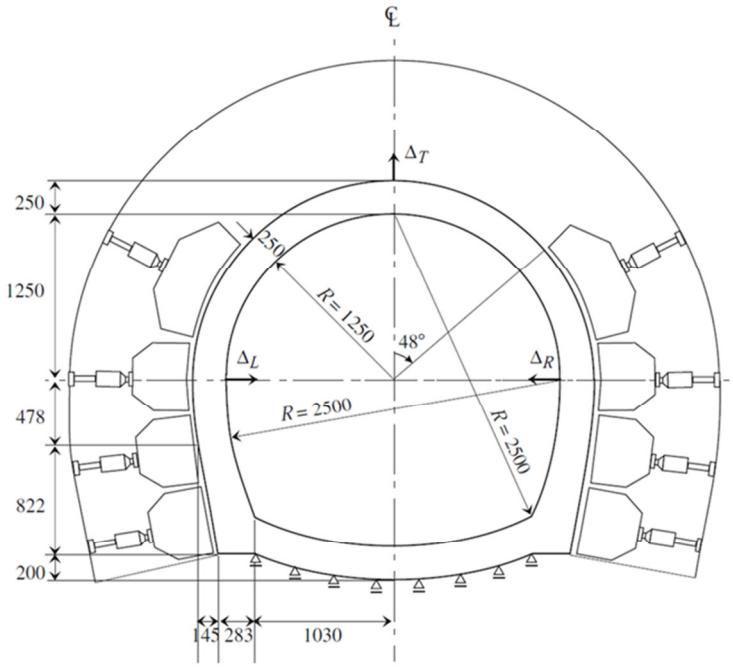

Figure 3.31 – Unreinforced concrete tunnel lining: specimen geometry and test set-up (ABO; TANAKA; YOSHIDA, 2000; SHI et al., 2001).

The finite element (SHI et al., 2001) and the LDM meshes are shown in Figure 3.32. It is noteworthy that the LDM mesh presents only four elements. The comparison between the experimental results and both numerical simulations is presented in Figure 3.33, in the form of curves of displacement vs. force. The parameters used in the LDM simulation are the following: $EI_b = 0.234375 \times 10^8\ \text{kN} \cdot \text{mm}^2$, $q_{un} = 1.87$, $M_{cr} = 24.6\ \text{kN} \cdot \text{mm}$ and $AE_b = 4500\ \text{kN}$.

The damage evolution is represented in Figure 3.34a, where it can be noted that crack propagation starts at the inelastic hinges in the point C of Figure 3.32; however, the main damage occurs at the inelastic hinges at B. Damage at point A does not evolve. In Figure 3.33, it can be noted the elastic stage represented by the straight line that starts at the origin; followed by a second curve, still close to a straight line of smaller slope, representing a global hardening phase yet. This modification of slope is due to the appearance of the first inelastic hinges at point C. The softening part of the behaviour initiates after the formation of the inelastic hinges at point B.

The COD evolution as a function of the load in both points is presented at Figure 3.34b. In the LDM analysis, crack evolution starts only after the moment on the hinge reaches the value of the cracking one; in the FE analysis this is a continuous process that initiates at a lower rate during the hardening phase of the analysis and accelerates during the final part.

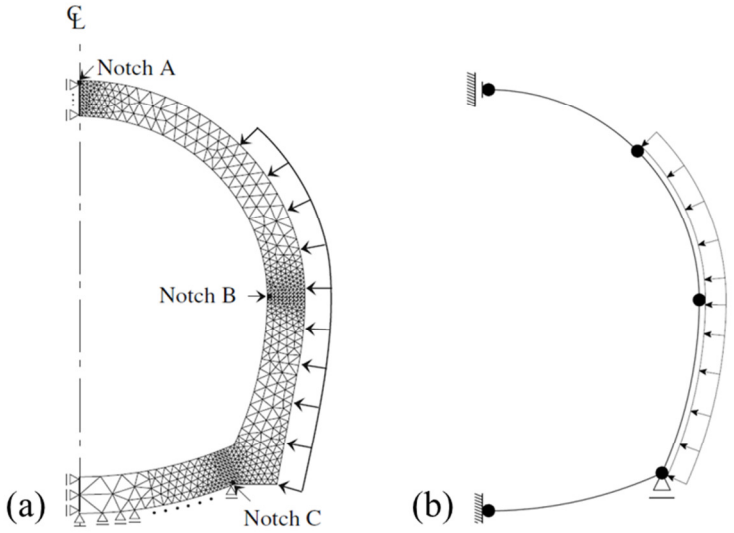

Figure 3.32 – Numerical analyses: (a) finite element mesh (SHI et al., 2001) and (b) LDM mesh.

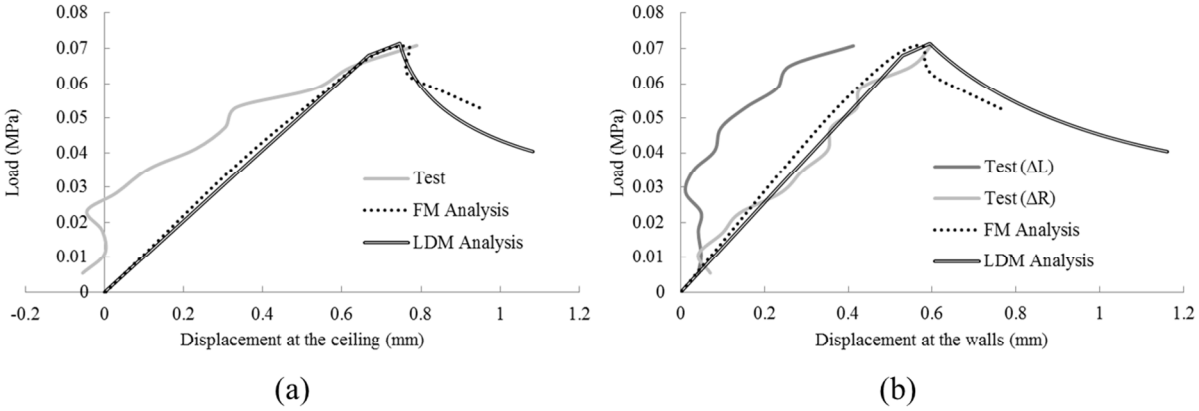

Figure 3.33 – Displacement vs. load; experimental and fracture mechanics (FM) analyses from, respectively, Abo, Tanaka and Yoshida (2000) and Shi et al. (2001).

Figure 3.35 shows the evolution of the bending moment distribution in the lining. These diagrams were computed using eq.(3.10) and values of $\{\mathbf{M}\}_b$ obtained during the analysis. Three different stages were chosen: the last elastic one that corresponds to the first hinge occurrence (Figure 3.35a), the second hinge occurrence (Figure 3.35b) and the end of the analysis (Figure 3.35c). Note that indeed, the first cracking moment value was reached at the point C in Figure 3.35a. In Figure 3.35b it can be noticed that the bending moment decreases in that area since the corresponding hinge enters in the softening stage; moments in the rest of the lining are higher. In the last figure, it can be observed a general reduction of the bending moments except in the zone close to point A. Also note that the bending moment

distribution in Figure 3.35a corresponds to the exact elastic solution of the problem; even if only four elements were used in the simulation of the lining.

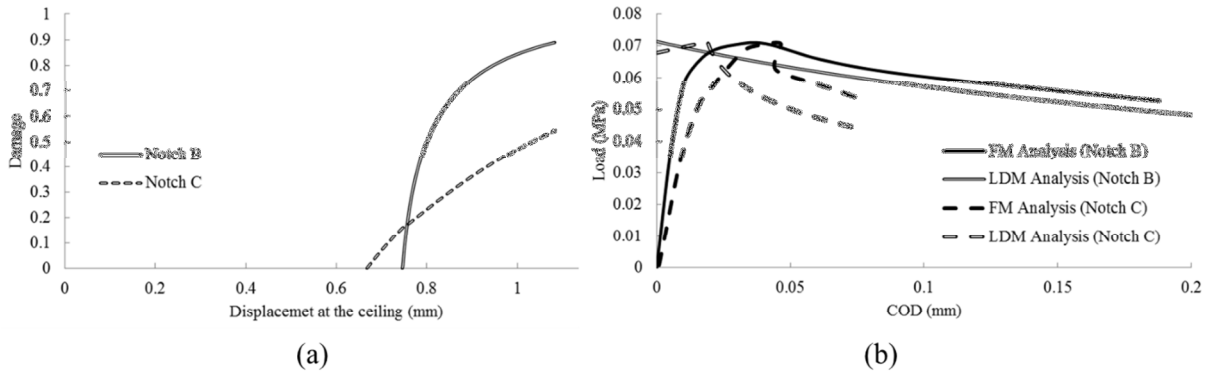

Figure 3.34 – (a) Damage evolution and (b) COD vs. load (FM analysis from Shi et al. (2001)).

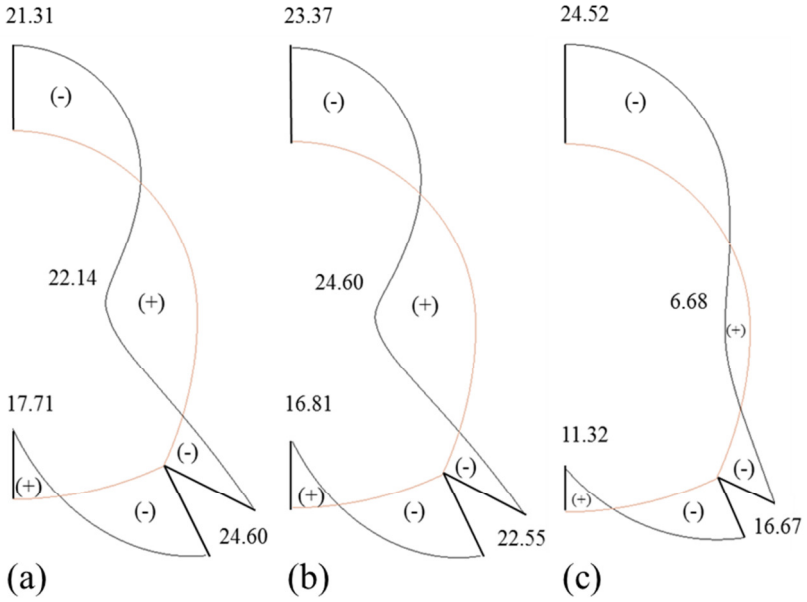

Figure 3.35 – Bending moment distribution: (a) first hinge occurrence, (b) second hinge occurrence and (c) end of the analysis.

Finally, Figure 3.36 shows the deformed configurations at the end of the analyses using both, the FM approach and the LDM result. The two configurations are quite similar. The LDM analysis does not capture the small crack propagation at the notch A. Note that in the FM analysis ‘‘the growth of crack A stops as the maximum load is obtained […] and remains inactive until structural failure’’ (SHI et al., 2001, p. 1090).

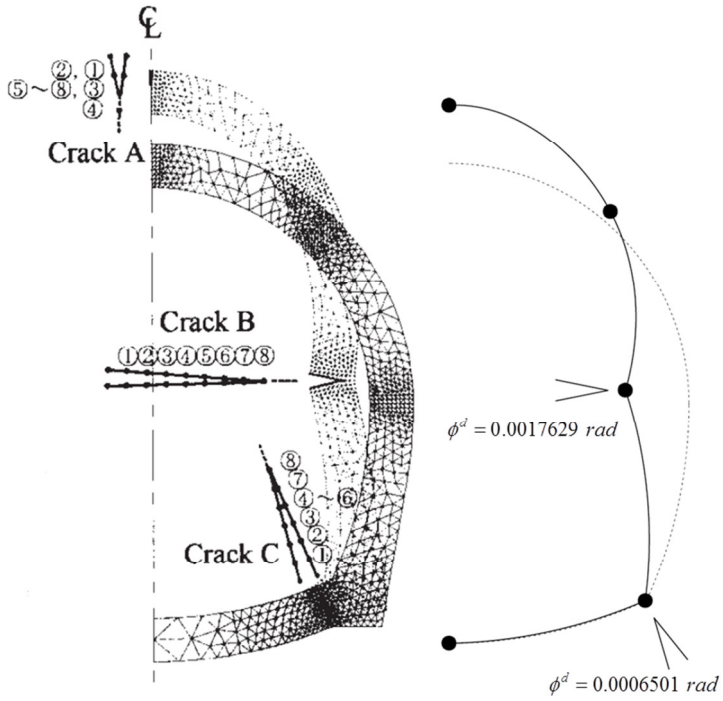

Figure 3.36 – Final deformed configuration in the FE (SHI et al., 2001) and LDM analyses.

Since this proposed model is intended to analyse any quasi-brittle structures, the next example addresses to an unreinforced masonry arch. Unreinforced masonry arches are commonly studied in order to reproduce the structural behaviour of western historic buildings.

Note that masonry arches can be analysed with the proposed lumped damage model considering that the only inelastic phenomenon is the cracking of mortar joints. Such hypothesis may fail in some cases; however, the objective of this Thesis was not to develop a specific lumped damage model for masonry structures. Nevertheless, the proposed model presents suitable results for the analysed problem.

The fourth example consists in two masonry arches tested by Basilio (2007), with approximately 1462 mm of span (L) (Figure 3.37a). At failure, both arches presented a four-hinge mechanism as depicted in Figure 3.37b, which is usual for the adopted configuration. Note that the hinges appear in sequence (H1-H2-H3-H4). For the numerical analysis, nodes were positioned where the bending moment distribution presented maximum absolute values, leading to a mesh with four elements (Figure 3.37b). Note that this arch presents a brittle behaviour (Figure 3.38), such characteristic can be numerically achieved by excluding the Lambert term of the cracking resistant function or by considering an arbitrarily large value for q_{un}. The second alternative was chosen for the numerical analysis because the exclusion of the Lambert term can present numerical instabilities and no sequential hinge formation is obtained. Then, Figure 3.38 shows the graph of force vs. displacement for the experimental

(BASILIO, 2007) and numerical responses. The parameters used in the numerical analysis ($EI_b = 0.75 \times 10^7$ kN · mm^2, $M_{cr} = 150$ kN · mm, $AE_b = 36000$ kN) were obtained by the material characterisation presented by Basilio (2007).

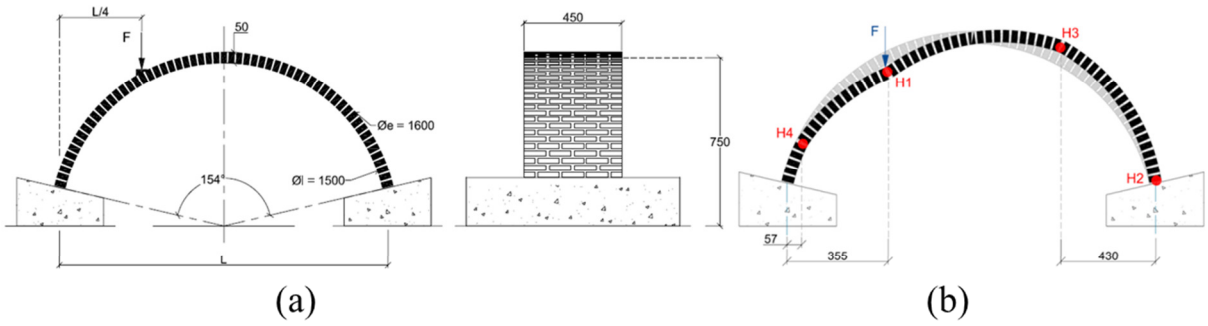

Figure 3.37 – Masonry arch (BASILIO, 2007): (a) geometry (dimensions in mm) and (b) failure mechanism.

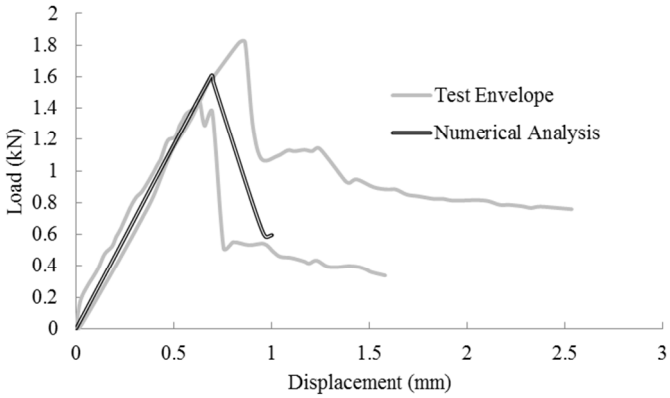

Figure 3.38 – Comparison between experimental (BASILIO, 2007) and numerical responses.

Note that the numerical response is satisfactorily fitted to the experimental envelope (BASILIO, 2007). In this analysis, the sequential hinge formation was not completed. The formation of the first hinge (Figure 3.39a) occurred in the peak of the numerical response; and the model lost numerical stability after the formation of the second hinge (Figure 3.39b).

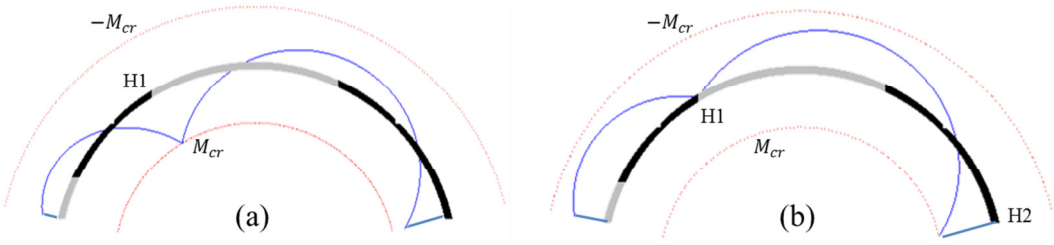

Figure 3.39 – Bending moment diagrams.

3.3 Remarks

The proposed lumped damage models for arches present suitable approximations and characterise an extension of the LDM framework. For RC modelling, it was shown that the proposed model presents accurate solutions using classic RC theory to estimate the model parameters. For quasi-brittle modelling, the accuracy observed in unreinforced concrete structures and masonry arches illustrate the versatility of such model. However, some considerations about the parameter the Lambert hardening coefficient q_{un} are necessary.

Regarding the unreinforced concrete examples presented here, the Lambert hardening coefficient q_{un} was considered as a regularisation parameter rather than a model constant. This coefficient was chosen so that a convergent solution, where the absolute value of the pre- and post-peak slopes are approximately the same (in the plots of displacement vs. force), is found. An engineer working on a real project can follow the same procedure. However, a study considering this constant as a model parameter and including an extensive experimental analysis would be very useful if this LDM procedure ever reaches some acceptance within the engineering community.

Regarding the analysed masonry arch, a brittle behaviour was reached by the adoption of a very large q_{un} value. It is noteworthy that a perfectly brittle analysis was carried out ($R^d(d) = R_0$), resulting in only one hinge formation. The total behaviour of the real arches was not acquired by the LDM analysis in such example perhaps because of the model limitation to analyse such type of structure. According to the experimental observations made by Basilio (2007), at some joints the masonry arches underwent slipping instead of cracking (or crack propagation in mode II instead of mode I, in fracture mechanics terms). Therefore, an expansion in the proposed model may overcome this issue.

4 LUMPED FATIGUE AND FRACTURE MECHANICS

In the examples presented so far, it was shown that the modelling of the complete evolution of failure using LDM of a complex structure is simple and accurate. Therefore, the analysis of a structure as the offshore platform in Figure 4.1a can be achieved with procedures based in LDM, ensuring good precision and low computer costs. Note that structures as an offshore platform (Figure 4.1a) usually collapse due to high cycle fatigue.

The analysis of a complete complex structure under high cycle fatigue using classic approaches, as continuum damage mechanics or fracture mechanics, is out of the question. It is not only a matter of computer costs, which are still determinant; the most important aspect is that data input and transformation of numerical results in engineering decisions are essentially human activities, not automatable procedures. Despite computer costs are becoming a less important factor day by day, human effort is certainly not.

Regarding classic techniques, a common procedure to analyse high cycle fatigue in complex systems consists in following a multi-scale scheme. Firstly, the global or large-scale versions of the structures are analysed with relatively simple models, for instance a linear elastic one. The vulnerable zones of the structure are then identified. Next, refined analyses of reduced structural parts with smaller geometrical complexities containing the vulnerable zones are simulated using more and more sophisticated models. Sometimes, simulations of the propagation of a crack in a sub-set of a sub-set of the total structure are the final small-scale analyses (see Figure 4.1b).

The goal of this chapter is to propose a formulation, based on LDM, adapted to the global analysis of complex structural systems that require studies of crack propagation. It is expected that the models might be used in the first, global, stages of the multi-scale studies of aerospace and offshore structures, or other industrial facilities. The potential advantages are significant. For instance, the global analysis could describe stress redistributions in the complete structure due to crack propagation in some of its components, which is not possible with elastic or elastic-plastic models. Also the connections among the different levels of the multi-scale analysis may be much more meaningful since all of them would be based on the same fundamental principles. Finally, the reliability studies that require thousands of analysis could be carried out for the entire structure and consider crack propagation in all the components at the same time.

Therefore, in this chapter the application of fatigue and fracture mechanics in inelastic hinges is presented. The modelling of high cycle fatigue using LDM is an original development of this thesis and it is here also called as Lumped Fatigue and Fracture Mechanics (LFFM).

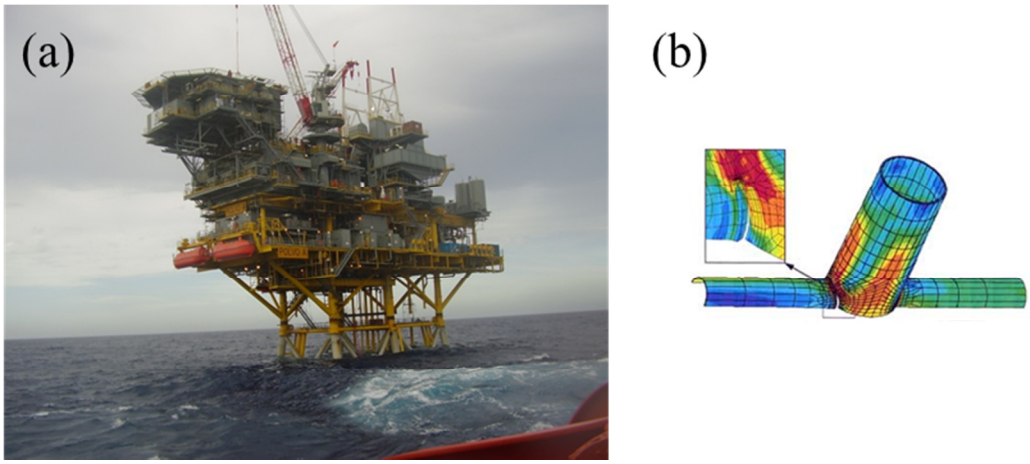

Figure 4.1 – (a) Offshore structure (TECHCON, 2015) and (b) crack propagation in a metallic joint (TWI-Global, 2013).

4.1 Modelling of single crack evolution through LDM

4.1.1 Stress intensity factor of an inelastic hinge subjected to bending moment

In RC components, damage takes the form of multiple cracks in the plastic hinge zone. However, in some other important applications, for instance low cycle fatigue in steel beams (BAI et al., 2016), high cycle fatigue or unreinforced concrete under monotonic loadings (AMORIM; PROENÇA; FLÓREZ-LÓPEZ, 2014a), it is assumed that damage is associated to only a single significant crack. Additionally, in the two last cases, plastic rotations can be negligible.

Now, the problem of fracture mechanics, i.e. the propagation analysis of countable cracks, is dealt with the tools of LDM. In this case, the damage parameter can be considered as a dimensionless measure of the crack surface as it will be shown on what follows.

The stress intensity factors K_I can be computed from the energy release rate G^a through the well-known expression:

$$K_I = \sqrt{EG^a} \tag{4.1}$$

Note that the energy release rate G^a differs from the damage driving moments G_i^d or G_j^d since in the former case it is computed as the derivative of the complementary energy with respect to the crack surface Λ and the latter are derivatives with respect to the damage variables. However, both kinds of variables are closely related. As aforementioned, the damage rotation of an inelastic hinge i is:

$$\phi_i^d = C m_i \qquad \therefore C = \frac{d_i F_{ii}^f}{1 - d_i} \tag{4.2}$$

where C is the compliance of the inelastic hinge. Therefore, the energy release rate of an inelastic hinge i can be computed as:

$$G_i^a = \frac{1}{2}\frac{dC}{d\Lambda} m_i^2 = \frac{1}{2}\frac{\partial C}{\partial d}\frac{\partial d}{\partial \Lambda} m_i^2 = G_i^d \frac{\partial d}{\partial \Lambda} \tag{4.3}$$

Thus, in order to calculate the energy release rate, it is needed to introduce a relationship between damage and crack surface i.e. $d = d(\Lambda)$. This expression must fulfill at least the following conditions:

$$d(0) = 0 \qquad d(A) = 1 \qquad \left.\frac{\partial d}{\partial \Lambda}\right|_{\Lambda=0} = 0 \tag{4.4}$$

where A is the cross section area. Note that the first and second conditions in (4.4) are quite obvious: the first one implies that if there is no crack surface the damage variable is nil; analogously, the second condition states that if the crack surface is equal to the cross section area the damage variable is equal to one. The third condition in (4.4) addresses to the stress intensity factor. According to eq. (4.1) and (4.3), the stress intensity factor depends on the product between the damage driving moment G^d and the derivative of the damage variable with respect to the crack surface. While the crack surface is nil the stress intensity factor must be nil, therefore the quantity that ensures this condition is the derivative of the damage variable with respect to the crack surface.

For rectangular cross sections, by multiplying both terms of the eq. (3.41) by the cross section basis (b), and being h and $\tilde{h}$ the total and effective heights of the cross section,

$A = bh$ and $\tilde{A} = b\tilde{h}$ the total and effective cross section areas and $\Lambda = A - \tilde{A}$ the crack surface, the following expression is then obtained (AMORIM; PROENÇA; FLÓREZ-LÓPEZ, 2014a):

$$d(\Lambda) = 1 - \left(1 - \frac{\Lambda}{A}\right)^3 \tag{4.5}$$

Such expression was successfully extended to H shaped cross-sections in Bai et al. (2016) as:

$$d(\Lambda) = 1 - \left(1 - \frac{\Lambda}{A}\right)^\gamma \tag{4.6}$$

where γ is a parameter characterising the cross section geometry. However, the previous expressions for $d(\Lambda)$ cannot be used for the computation of stress intensity factors since they fail to fulfil the last condition of eq. (4.4); i.e. the derivative of the damage with respect to the crack surface is not zero when there is no crack. The simplest empiric modification of eq. (4.6) that satisfies all these conditions consists in multiplying the second part of (4.6) by a linear function:

$$d(\Lambda) = \frac{\Lambda}{A} - \frac{\Lambda}{A}\left(1 - \frac{\Lambda}{A}\right)^\gamma \tag{4.7}$$

Since the relation (4.7) is semi-empiric, a validation analysis is necessary. Consider a cantilever beam as the one presented in Figure 4.2a. If a crack with length a is considered in the restrained edge, the force-deflection of this beam is:

$$P = \mathfrak{E}(a)t \tag{4.8}$$

where $\mathfrak{E}(a)$ is the beam stiffness.

Therefore, considering a mesh with 3000 four-node quadrilateral elements and a unitary imposed displacement ($t = 1$), the reaction P is exactly the beam stiffness $\mathfrak{E}(a)$ with respect to the crack length (a). This is a fracture mechanics approach.

The lumped damage mechanics solution is the direct consideration of the relation (4.7). Then, a force-deflection relation is:

$$\begin{aligned} \phi &= \frac{L}{3EI(1-d)}m \\ \frac{t}{L} &= \frac{L}{3EI(1-d)}PL \\ P &= \frac{3EI(1-d)}{L^3}t \qquad \therefore d(a) = \frac{a}{h} - \frac{a}{h}\left(1-\frac{a}{h}\right)^3 \\ P &= \mathfrak{E}(a)t \end{aligned} \tag{4.9}$$

The numerical confrontation is given in Figure 4.2b.

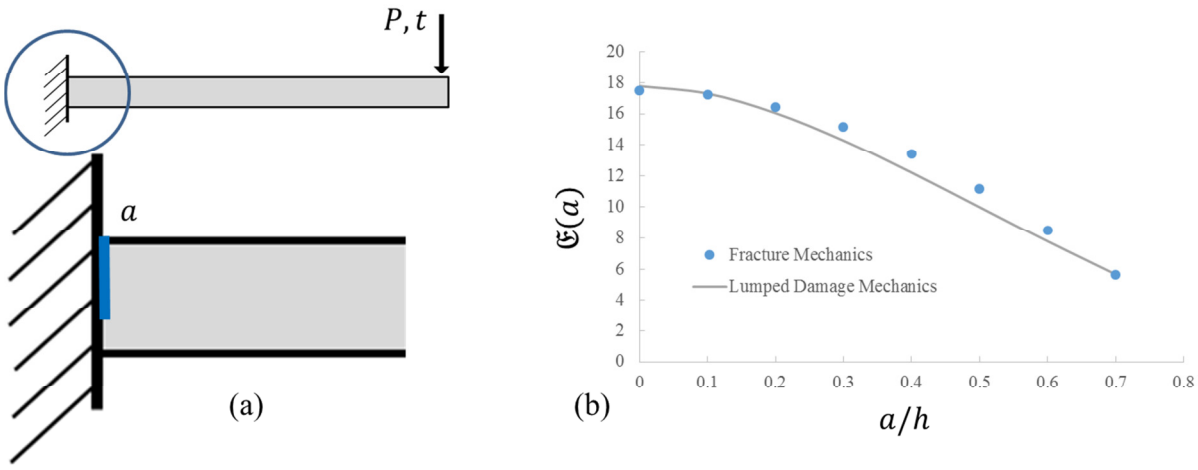

Figure 4.2 – Numerical evaluation of the damage-crack length/surface relation.

Note that Figure 4.2b shows the good accuracy of the relation (4.7). Therefore, this new equation is an interesting alternative for further developments.

Figure 4.3 shows the comparison between the values of dimensionless K_I (i.e. $K_I b\sqrt{h}/P$ where b and h are base and height of the cross section, respectively, and P is the applied force) computed with fracture mechanics (FM), as presented in Anderson (2005), and LDM for a three-point bending test; the latter was computed using equations (4.1), (4.3) and (4.7) with $\gamma = 3$ (rectangular cross sections). The beam was represented using two elements, which signifies that the cracked section was substituted by two inelastic hinges located at the same point; thus, the total energy release rate is the sum of the two contributions. Figure 4.3a presents the results of an analysis with an element that has an aspect ratio (L/h) of 5; it is 6 in Figure 4.3b and 8 in Figure 4.3c.

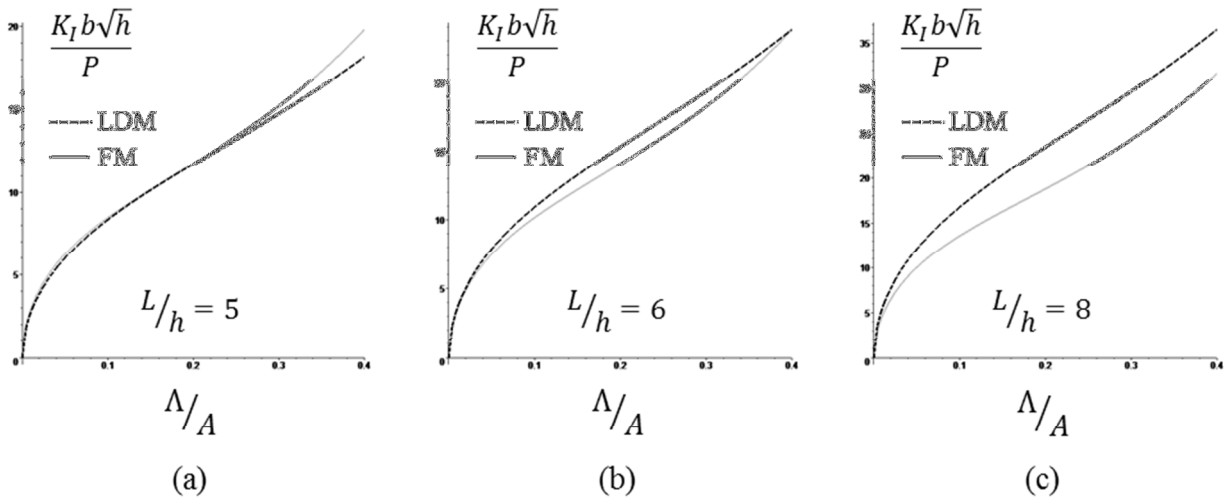

Figure 4.3 – Comparison between LDM and FM for the determination of K_I in a three-point bending specimen ($\gamma = 3$): (a) $L/h = 5$, (b) $L/h = 6$ and (c) $L/h = 8$.

The precision of the computation can be significantly increased by adding a correction factor ($\mathfrak{F}$), which depends on the aspect ratio (L/h), to eq. (4.3):

$$G_i^a = \mathfrak{F} G_i^d \frac{\partial d}{\partial \Lambda} \qquad \therefore \mathfrak{F} = \lambda \frac{h}{L} \tag{4.10}$$

where λ is a constant. Figure 4.4 shows the values of K_I (dimensionless K_I i.e. $K_I b\sqrt{h}/P$) between FM and LDM after correction.

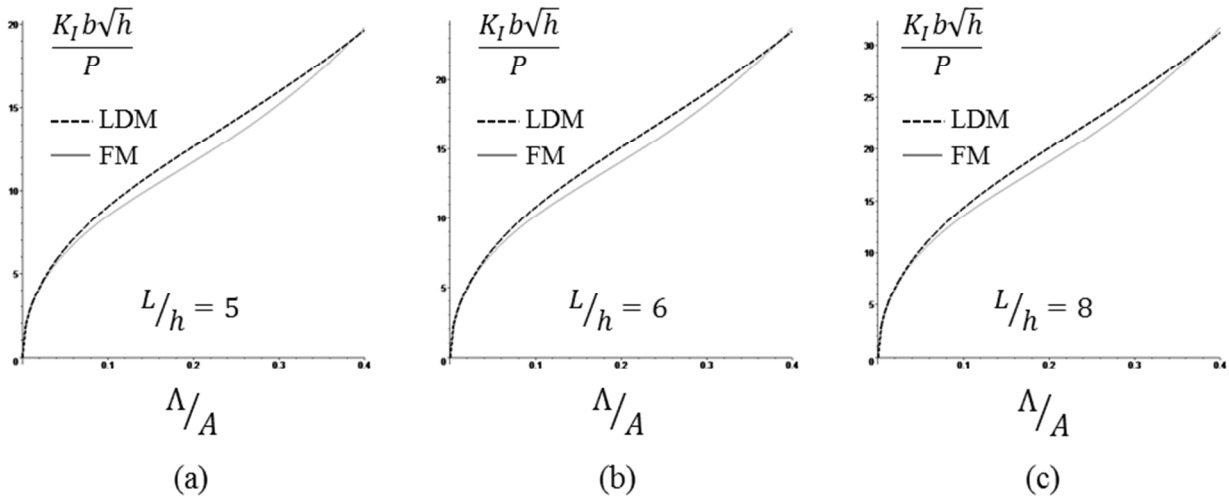

Figure 4.4 – Comparison between LDM and FM for the determination of K_I in a three-point bending specimen ($\gamma = 3, \lambda = 5.85$): (a) $L/h = 5$, (b) $L/h = 6$ and (c) $L/h = 8$.

4.1.2 Stress intensity factor of an inelastic hinge subjected to axial forces

In the previous development, the hinge was subjected only to bending. However, in some important applications the dominant effects are the result of axial forces or at least a combination of both. Now, the same procedure is followed to obtain stress intensity factors of a bar with a crack in the middle section. The damage elongation of the hinge δ^d is now defined as:

$$\delta^d = CN \qquad \therefore C = \frac{d\, F_{33}^a}{1-d} \tag{4.11}$$

Then, the energy release rate is computed again as:

$$G^a = \frac{1}{2}\mathfrak{F}\frac{\partial C}{\partial d}\frac{\partial d}{\partial \Lambda}n^2 = \mathfrak{F}G^d\frac{\partial d}{\partial \Lambda} \qquad \therefore \mathfrak{F} = \lambda\frac{h}{L} \tag{4.12}$$

Figure 4.5 shows the comparison between the values of stress intensity factor using (4.12) and fracture mechanics values given by the conventional equations i.e. bar with finite height b and width h, and a crack in the middle (ANDERSON, 2005).

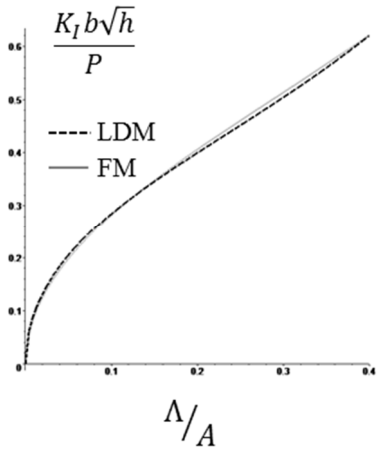

Figure 4.5 – Comparison between LDM and FM for the determination of K_I in a bar with a central crack subjected to axial forces P ($\gamma = 3$, $\lambda = 0.15$)

4.1.3 Crack opening displacement as a function of the lumped damage

As discussed in subsection 3.2.3, the crack opening displacement (COD) is again estimated. Now, since the relation between the damage variable and the crack length/surface

is changed due to the estimative of the stress intensity factor, a new estimation of COD is then required. For the same value of damage, the crack length/surface in (4.7) evolves differently from (4.5). Therefore, the evolution of the effective height $\tilde{h}$ is also different.

Consider again the LDM representation of a single crack presented in Figure 4.6. As previously presented in subsection 3.2.3, the COD is given in terms of the damage rotation, i.e. $\mathrm{COD}_i \cong \phi_i^d l$. Regarding the aforementioned differences, the previous equation for COD estimation is now rewritten in terms of the crack length (a):

$$\mathrm{COD}_i \cong \phi_i^d l = \phi_i^d \left(h - \frac{\tilde{h}}{2}\right) = \frac{1}{2}(h + a)\phi_i^d \tag{4.13}$$

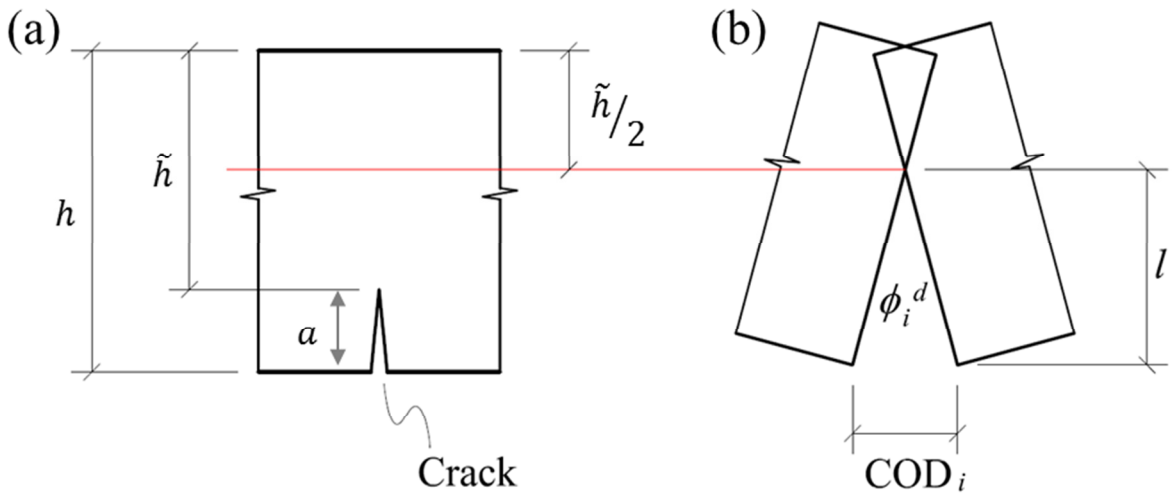

Figure 4.6 – Crack opening displacement: (a) Physical crack; (b) Inelastic hinge.

Since a new COD estimation is here proposed, the unreinforced concrete examples under monotonic load are revisited in order to compare the COD estimation between LDM, fracture mechanics (FM) and experimental observations.

The examples are: simply supported beams presented by Shi et al. (2001) and Hamad, Owen and Hussein (2013), and the tunnel lining presented by Shi et al. (2001). The description of such examples is depicted in item 3.2.3.4. Note that the new COD estimation also presents good accuracy (Figure 4.7) regarding the references (fracture mechanics or experimental observations). Therefore, the empirical modification of the COD estimation, which was necessary to fulfil the conditions to describe the stress intensity factor by LDM, still leads to accurate results.

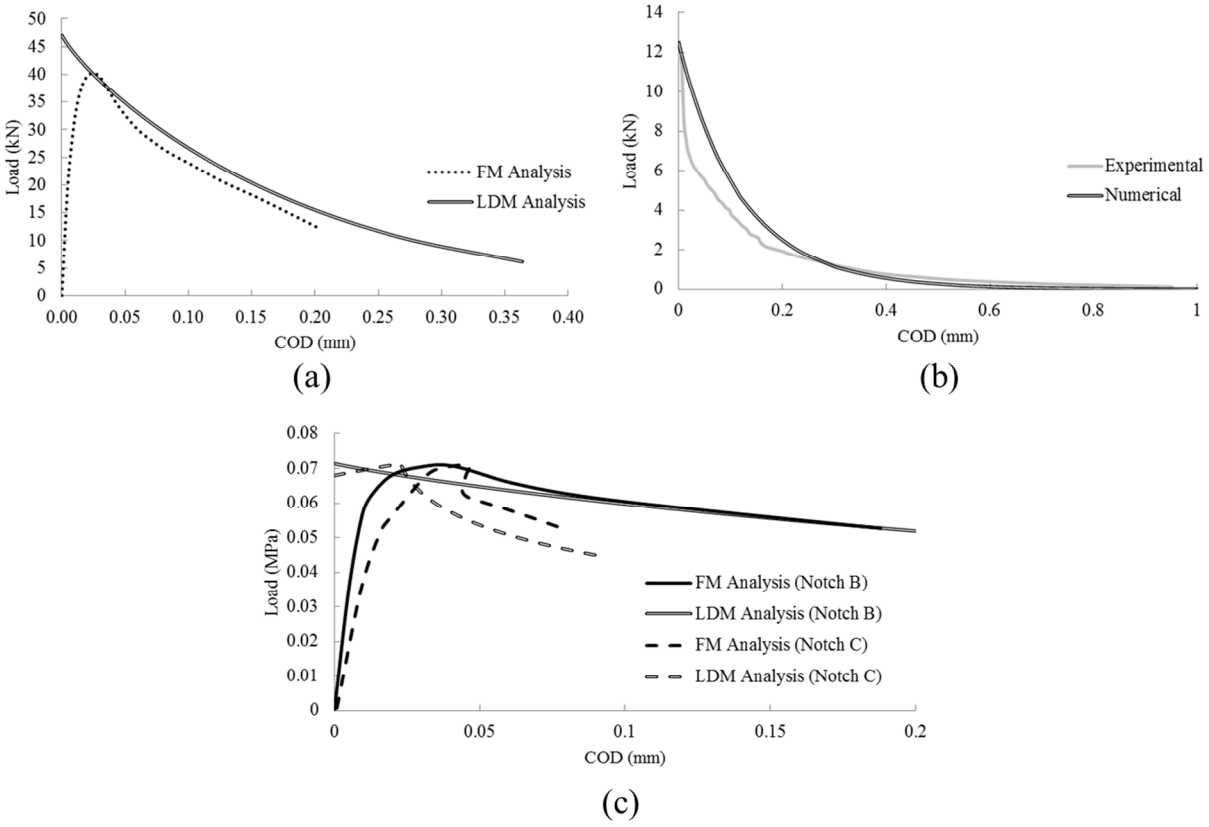

Figure 4.7 – Empirical COD estimation for unreinforced concrete structures under monotonic loads: simply supported beams presented by (a) Shi et al. (2001) and (b) Hamad, Owen and Hussein (2013), and (c) the tunnel lining presented by Shi et al. (2001). Fracture mechanics (FM) and experimental results from, respectively, Shi et al. (2001) and Hamad, Owen and Hussein (2013).

4.2 Finite elements for high cycle fatigue

Any model for high cycle fatigue based on stress intensity factors, energy release rates or generalized energy release rates (damage driving moments) can now be included in the LDM framework. In this section, an alternative procedure to the rainflow or other cycle-counting algorithms is proposed.

Consider a structure subjected to high cycle fatigue loadings. Such structure may be composed by straight and circular frame bars. Note that both element types present the same quantity of degrees of freedom (see chapters 2 and 3). For high cycle fatigue problems, it is considered that each node presents six degrees of freedom, which are the maximum and minimum displacements and rotations per cycle. Thus, the matrix of nodal displacements of a member b at a cycle N $\{\mathbf{q}(\mathrm{N})\}_b$ is:

$$\{\mathbf{q}(\mathrm{N})\}_b^T = \\ = \{u_i^{\max} \quad w_i^{\max} \quad \theta_i^{\max} \quad u_j^{\max} \quad w_j^{\max} \quad \theta_j^{\max} \quad u_i^{\min} \quad w_i^{\min} \quad \theta_i^{\min} \quad u_j^{\min} \quad w_j^{\min} \quad \theta_j^{\min}\} \tag{4.14}$$

The matrices of generalised deformations and stresses are expanded in the same way for straight frames:

$$\begin{aligned} \{\boldsymbol{\phi}(\mathrm{N})\}_b^T &= \{\phi_i^{\max} \quad \phi_j^{\max} \quad \delta^{\max} \quad \phi_i^{\min} \quad \phi_j^{\min} \quad \delta^{\min}\} \\ \{\mathbf{M}(\mathrm{N})\}_b^T &= \{m_i^{\max} \quad m_j^{\max} \quad n_b^{\max} \quad m_i^{\min} \quad m_j^{\min} \quad n_b^{\min}\} \end{aligned} \tag{4.15}$$

and circular arches:

$$\begin{aligned} \{\boldsymbol{\phi}(\mathrm{N})\}_b^T &= \{\phi_i^{\max} \quad \phi_j^{\max} \quad \delta_i^{\max} \quad \phi_i^{\min} \quad \phi_j^{\min} \quad \delta_i^{\min}\} \\ \{\mathbf{M}(\mathrm{N})\}_b^T &= \{m_i^{\max} \quad m_j^{\max} \quad n_i^{\max} \quad m_i^{\min} \quad m_j^{\min} \quad n_i^{\min}\} \end{aligned} \tag{4.16}$$

On the other hand, the variation of damage or crack surface during a cycle is neglected; therefore the damage matrix is: $\{\mathbf{D}(\mathrm{N})\} = \{d_i \quad d_j \quad d_a\}^T$. Boundary conditions and external loads on the structure can be described by histories of maximum and minimum displacements and nodal forces respectively. Each time increment, measured in terms of cycles, can include dozens, hundreds or even thousands of cycles.

The elasticity law is given by the same matrix equation previously presented, neglecting plastic rotations and expanding the flexibility matrix accordingly:

$$\begin{aligned} \{\boldsymbol{\phi}(\mathrm{N})\}_b &= \begin{bmatrix} \left[\mathbf{F}\left(\mathbf{D}(\mathrm{N})\right)\right]_b & [\mathbf{0}] \\ [\mathbf{0}] & \left[\mathbf{F}\left(\mathbf{D}(\mathrm{N})\right)\right]_b \end{bmatrix} \{\mathbf{M}(\mathrm{N})\}_b \\ \therefore \left[\mathbf{F}\left(\mathbf{D}(\mathrm{N})\right)\right]_b &= \begin{bmatrix} \frac{1}{1-d_i} F_{11}^f + F_{11}^a & F_{12}^0 & F_{13}^0 \\ F_{12}^0 & \frac{1}{1-d_j} F_{22}^f + F_{22}^a & F_{23}^0 \\ F_{13}^0 & F_{23}^0 & F_{33}^f + \frac{1}{1-d_a} F_{33}^a \end{bmatrix} \end{aligned} \tag{4.17}$$

Therefore, the corresponding damage driving moments are:

$$G_i^d = \frac{m_i^2 F_{11}^f}{2(1-d_i)^2} \qquad G_j^d = \frac{m_j^2 F_{22}^f}{2\left(1-d_j\right)^2} \qquad G_a^d = \frac{n^2\, F_{33}^a}{2(1-d_a)^2} \tag{4.18}$$

The kinematics and equilibrium equations are extended analogously:

$$\begin{gathered}\{\boldsymbol{\phi}(\mathrm{N})\}_b = \begin{bmatrix}[\mathbf{B^0}]_b & [\mathbf{0}] \\ [\mathbf{0}] & [\mathbf{B^0}]_b\end{bmatrix}\{\mathbf{q}(\mathrm{N})\}_b \\ \sum_{b=1}^{\mathrm{m}} \begin{bmatrix}[\mathbf{B}_E^0]_b^T & [\mathbf{0}] \\ [\mathbf{0}] & [\mathbf{B}_E^0]_b^T\end{bmatrix}\{\mathbf{M}(\mathrm{N})\}_b = \{\mathbf{P}(\mathrm{N})\}\end{gathered} \tag{4.19}$$

where $\{\mathbf{P}(\mathrm{N})\}$ is the matrix of cyclic applied loads.

Finally, as damage evolution law, the simplest of all high cycle fatigue laws might be used:

$$\frac{d\Lambda_i}{d\mathrm{N}} = \frac{\partial \Lambda_i}{\partial d_i}\frac{\partial d_i}{\partial \mathrm{N}} = h\mathrm{C_P}\left(K_i^{\max} - K_i^{\min}\right)^{\mathrm{n_P}} \qquad d(\Lambda_i) = \frac{\Lambda_i}{A} - \frac{\Lambda_i}{A}\left(1 - \frac{\Lambda_i}{A}\right)^{\gamma} \tag{4.20}$$

where $\mathrm{C_P}$ and $\mathrm{n_P}$ are the material parameters of the Paris law (PARIS et al., 1961; PARIS ERDOGAN, 1963). The stress intensity factors $K_i^{\max}$ and $K_i^{\min}$ are computed as previously indicated (K_I).

4.3 Fatigue in three-point bending test

This example is the numerical simulation of a test reported in Andreaus and Baragatti (2009) using the finite element proposed in the previous section. This is an aluminium beam with square cross-section $b = h = 20$ mm and $L = 300$ mm as the total span. The beam was represented using only one finite element (taking into account the symmetry of the problem) as shown in Figure 4.8a. The loading is characterised by constant maximum and minimum vertical forces (1600kN and 250kN) on the node 1 of the structure; i.e. the forces corresponding to the degrees of freedom 2 and 8 of the structure are imposed and are constant. Figure 4.8b and Figure 4.8c, respectively, show the evolution of the stiffness and crack length with the number of cycles for both, experiment and numerical analyses. The value of the beam inertia EI was identified to match the initial stiffness value of the curve in the Figure 4.8b. The initial value of damage $\mathrm{d_1}(\Lambda_0) = 0.00713125$ for the hinge in node 1 (node with

applied forces) was computed with the initial crack length reported in Andreaus and Baragatti (2009) ($\Lambda_0/b = 1$ mm) using eq. (4.7). For the simulation no correction factor was considered; i.e. the eq. (4.3) was used. Note the good agreement between test and analysis in both curves after updating.

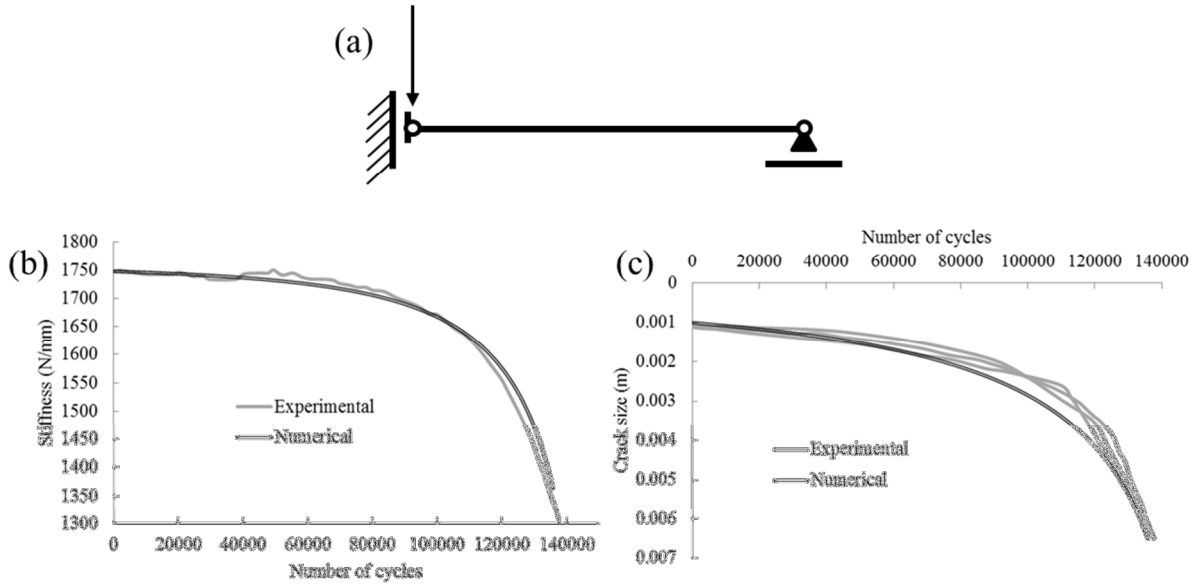

Figure 4.8 – Fatigue in a three-point bending test: (a) FE mesh, (b) Number of Cycles vs. Stiffness and (c) Number of cycles vs. crack extension. $\mathrm{EI_b} = 990\ \mathrm{N \cdot m^2}$, $\mathrm{C_P} = 0.306 \times 10^{-12}\ \mathrm{m/cycle/MPa \cdot m^{1/2}}$, $\mathrm{n_P} = 3.73$.

4.4 Fatigue in a frame structure

This example is an academic case. The purpose of this analysis is to show the capacity of the procedure to simulate crack propagation due to high cycle fatigue in complex structures. The frame structure of Figure 4.9 was divided in fourteen elements. A cycle force varying between 354 kN and 2268 kN was applied at the left upper node of the mesh.

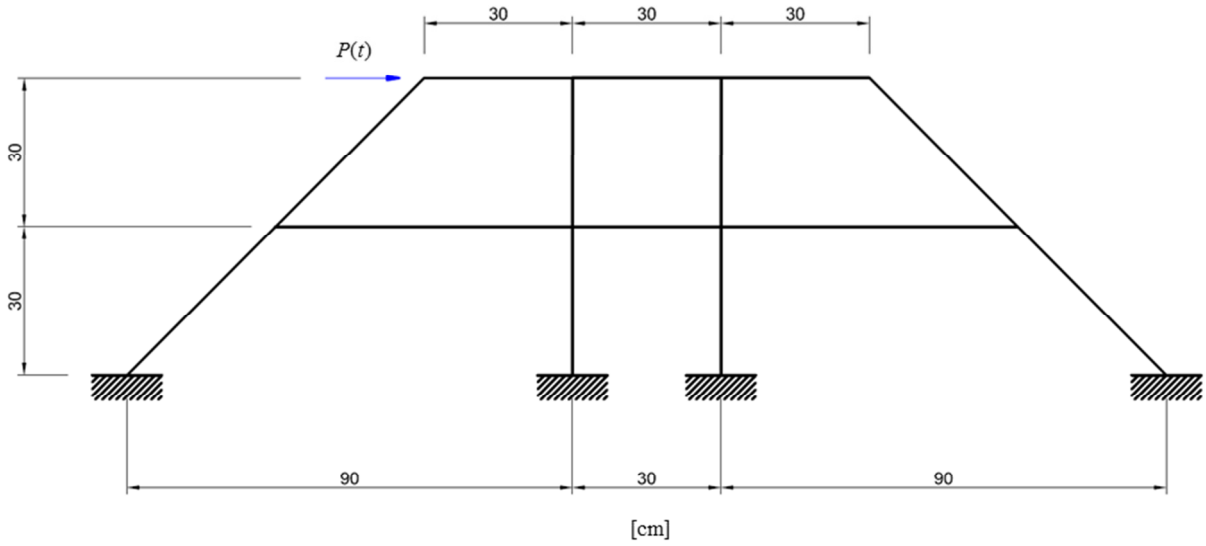

Figure 4.9 – Frame structure subjected to high cycle fatigue.

This structure was analysed using again the high cycle fatigue finite element, proposed in the previous section. The final state of damage is presented in Figure 4.10. Damage evolution is depicted in Figure 4.11a. Figure 4.11b shows the crack length and crack growth ratio histories for the two most dangerous hinges: h24 and h27.

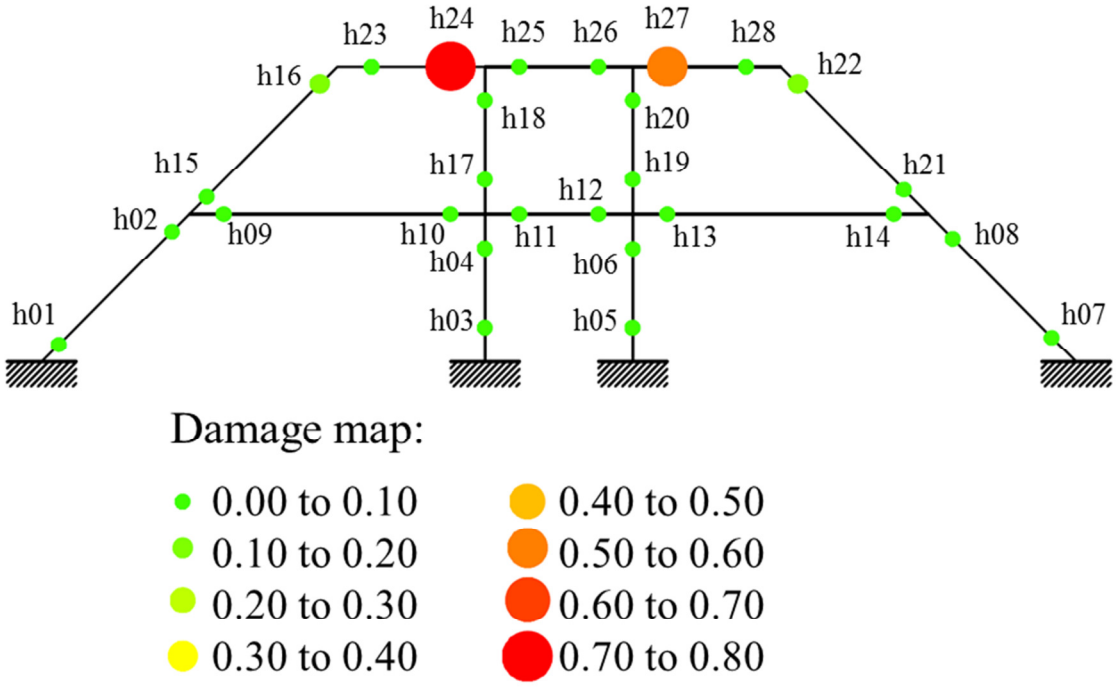

Figure 4.10 – Final state of damage.

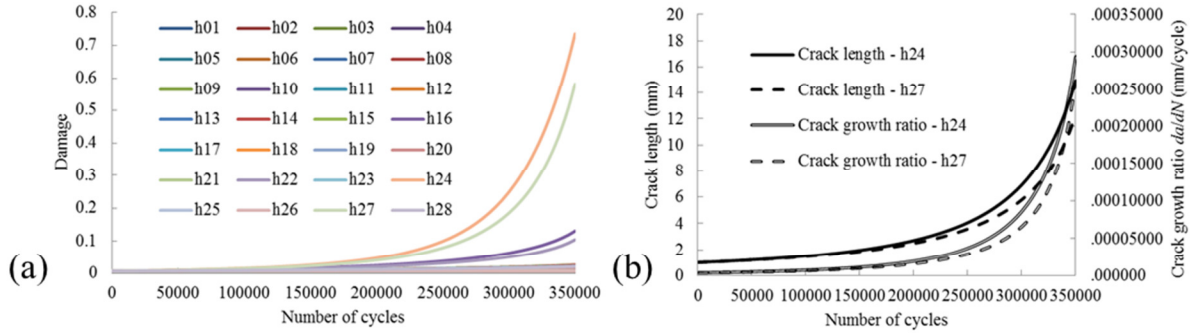

Figure 4.11 – (a) Damage evolution, (b) Crack length and growth ratio evolution.

Finally, the initial and final bending moment diagrams are presented, respectively, in Figure 4.12a and Figure 4.12b. Note the significant variation redistribution of bending moments due to the fatigue process. Even if the maximum and minimum values per cycle of external forces are constant, the local loadings on the structural components are certainly not. In h24 the variation of the bending moment was about 55% of the initial value.

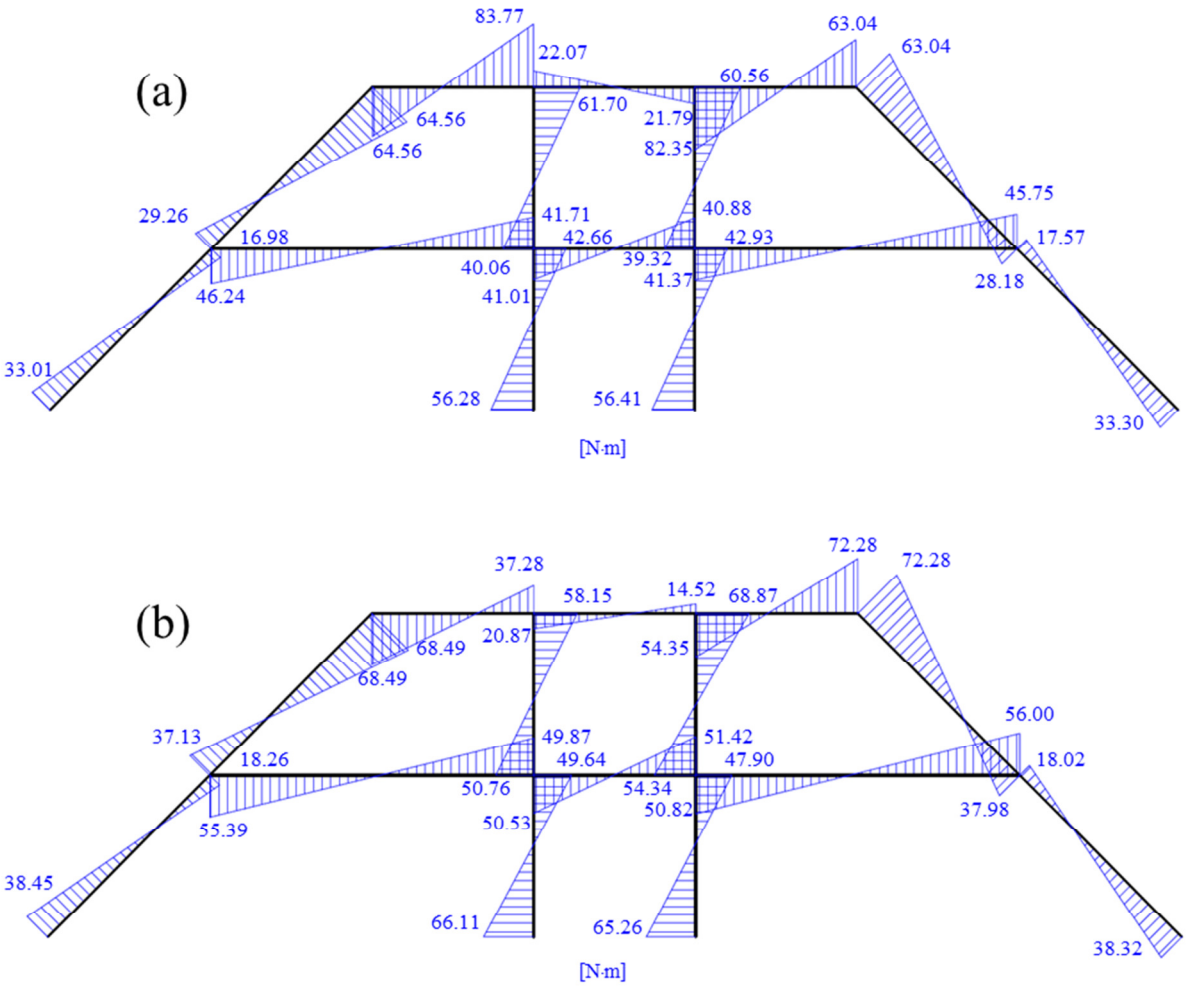

Figure 4.12 – Bending moment diagrams: (a) initial distribution and (b) final distribution.

4.5 Fatigue in an aeroplane fuselage panel

The last example represents a fuselage component subjected to fatigue due to the process of pressurisation and depressurisation that was tested in laboratory (AHMED et al., 2007). The experimental set up was represented as shown in Figure 4.13.

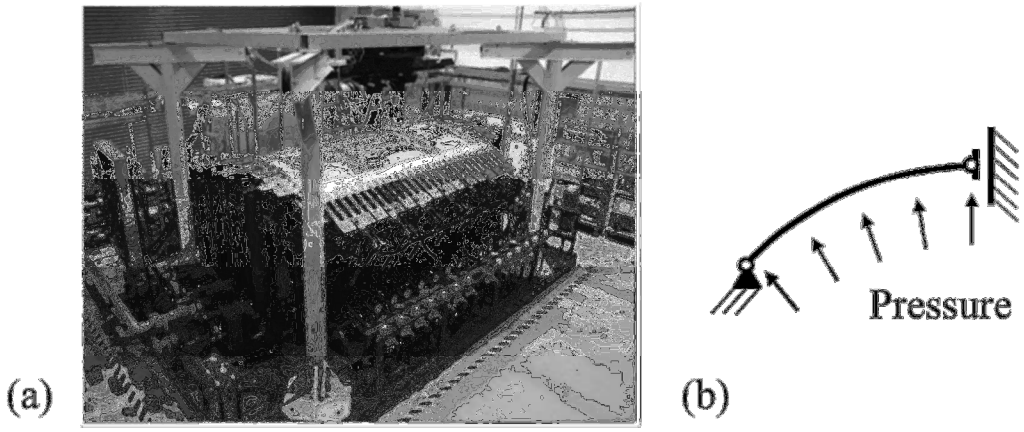

Figure 4.13 –Shell subjected to high cycle fatigue: (a) Experimental set up and loading (AHMED et al., 2007) and (b) representation for the LDM analysis.

According to Ahmed et al. (2007), the fuselage component was subjected to a complex loading history that is shown in Figure 4.14, with pressure given in psi (1.0 psi is equal to 0.0068948 MPa). The stress ratio between minimum and maximum pressure was 0.1.

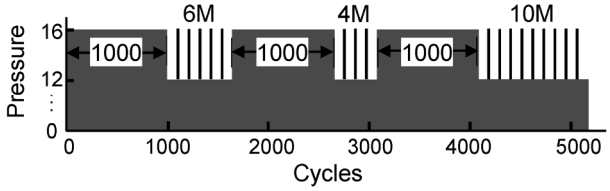

Figure 4.14 – Maximum load spectrum used in the fuselage component fatigue test (AHMED et al., 2007).

In the test, crack appears and propagates along the section AA as represented in Figure 4.15. In such section there is a critical rivet line connection (AHMED et al., 2007), which is responsible for crack nucleation and lead the fuselage component to fatigue collapse.

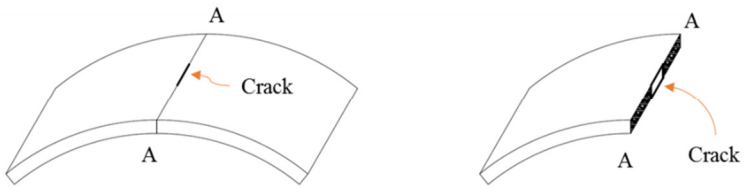

Figure 4.15 – Crack in a fuselage component.

The same model proposed in section 4.2 was used for the numerical simulation. But now, the damage law is that of fatigue and bending damages are neglected as axial damage prevails. Numerical simulation and experimental results are compared in Figure 4.16. Figure 4.16a shows the evolution of the both ends of the crack. Figure 4.16b is a zoom of the last thousand cycles of the loading.

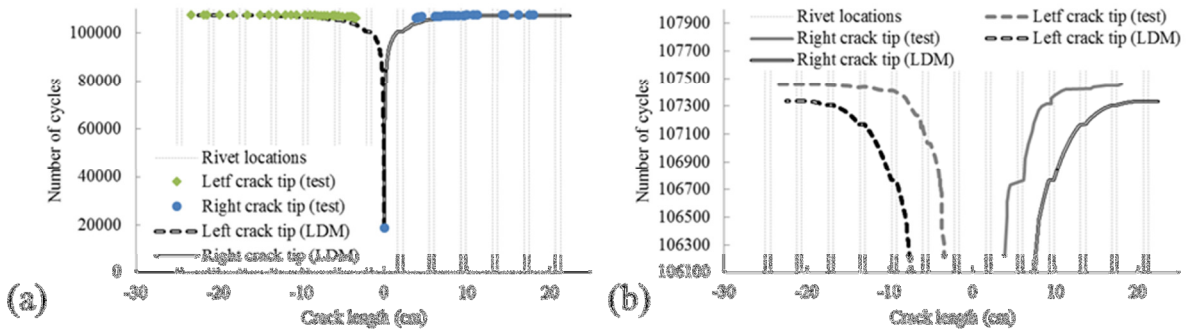

Figure 4.16 – (a) Crack length vs. number of cycles: $C_P = 0.365 \times 10^{-10}$ m/cycle/MPa $\cdot$ m$^{1/2}$, $n_P = 3$; (b) Last 1400 cycles of the loading.

In the LDM analysis, the main result is damage evolution rather than crack length propagation (Figure 4.17). Note that the damage variable starts to increase rapidly between the values of 0.4 and 0.5, where the value of ultimate damage for metals usually lies (LEMAITRE; CHABOCHE, 1985).

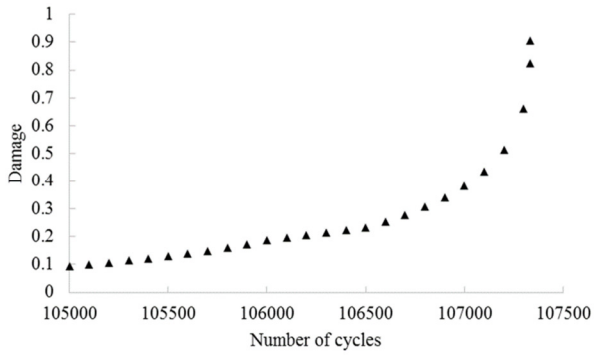

Figure 4.17 – Damage evolution in the last two thousands cycles of the loading.

4.6 Remarks

The examples of this chapter show the reasonable precision that may be attained using the simplified procedure. Note that LDM permits the computation of the structural behaviour, stress intensity factors, stiffness degradation, crack length and COD evolution with a fraction of the human and computational effort. Thus, it is indeed possible the development of a simplified fracture mechanics for complex structural systems.

The material parameters for an LDM analysis can be identified using the standard procedures of the fracture mechanics (coupon tests, three point bending tests and so on). As in any other structural analysis, updating leads to significantly more precise results.

This formulation may be integrated in the protocols for the design, certification and maintenance projects of complex structural systems based on multi-scale analyses. The example on the frame structure shows the significant variation of the local forces on a component subjected to fatigue even if the external forces on the facility or structure are expected to be constant. Thus, LDM incorporation would result in more coherent, safe and effective multi-scale procedures.

The multi-scale procedure may be used in both senses. For instance, in items 4.1.1 and 4.1.2, the fracture mechanics analyses where used to calibrate the correction factors. Thus, a multi-scale scheme with LDM may be as the one illustrated in Figure 4.18. In the multi-scale scheme depicted in Figure 4.18 the analysis starts with a FM stage, where the stress intensity factors for all cracks are calculated. Such values are used to calculate the correction factors for the global stage, where LDM is applied. In the global stage (LDM stage) the damage distribution map and the stress distribution are calculated. Note that using LDM at that stage the stress field can be rearranged, accounting for the cracks. With those results, the loading on components are estimated and then the local analysis is carried out by using classic fracture mechanics (FM stage).

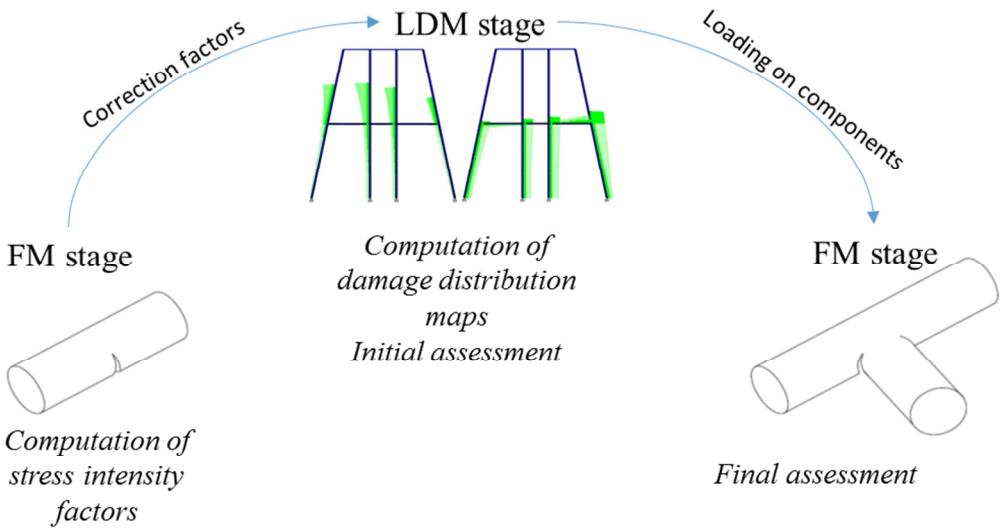

Figure 4.18 – Multi-scale scheme using LDM.

5 EXTENDED LUMPED DAMAGE MECHANICS

5.1 Initial comments

Fracture and damage mechanics are recent theories that characterise inelastic phenomena due to material deterioration. In section 2.3 some concepts of both theories were briefly discussed.

Classic damage mechanics evolved from the theory of plasticity to model material deterioration, initially tertiary creep, and then softening in ductile and brittle materials. As classic damage mechanics derived from the theory of plasticity, the kinematics of damaged solids is based on the concept of strain. Thus, damage evolution laws in classic models relate damage with local strains or plastic strains. The pioneers of the field expected that classic damage mechanics could eventually become an advantageous alternative to fracture mechanics, but this never happened because of the so-called localisation phenomenon.

The term localisation is applied in two different situations. In experimental mechanics, localisation denotes the formation of, for instance, shear bands with strain discontinuities in brittle, ductile or geo-materials, i.e. localisation is an experimental evidence. In structural mechanics, localisation is often used to refer to the mathematical analysis of classic damage models e.g. the loss of ellipticity that leads to ill-posed problems and mesh-dependent numerical algorithms. The failure of the classic damage mechanics describing localisation bands marked the end of this stage of the theory.

Modern damage mechanics was developed to circumvent this issue with two basic ideas: a modification in the damage evolutions laws by weight functions (nonlocal models) and the introduction of suitable kinematics (strain or displacement discontinuities) to take into account the damage localisation. In common, both ideas seek one main objective: the development of models that lead to objective numerical results.

On the other hand, fracture mechanics represents structural deterioration by modifying the geometry of the solids, determining when this modification can occur, and then describing how it happens (see e.g. Shi (2009) for a review). The first works on fracture mechanics, the so-called linear elastic fracture mechanics (LEFM), proposed a two-state description of the process: nothing ensues or crack propagates. It was soon evident that this approach was insufficient for an adequately description of the phenomenon. Describing the inelastic

processes before crack propagation is as important as crack evolution *per se*. As the researchers on the field use geometry modifications as the tool for describing structural deterioration, the dominant approach is the introduction of equivalent cracks longer than the real ones; the inelastic phenomena preceding crack propagation are then assumed to occur in zones of zero volume: the artificial extension of the crack. In the fracture process zone approach (FPZ), a new fracture evolution law is then introduced, but instead of utilising strain as the kinematic variable, this law uses the crack opening displacement concept. So far, the fracture mechanics approach has been much more successful and it is much more frequently used in practical applications than damage mechanics.

LDM is an alternative form of damage mechanics; but as discussed in this thesis, so far, LDM is limited to the analysis of uniaxial cases: beams, columns, frames and arches. In these models, damage as well as plasticity are concentrated in zones of zero length as in the FPZ. However, unlike fracture mechanics, this hypothesis does not modify the geometry of the structure, only the constitutive law as in damage mechanics. LDM does not uses the concept of curvature or strain as in the fibre or beam models but the inelastic rotation of the hinge; a concept that can be considered alike to the crack opening displacement. In general terms, it can be said that classic and modern damage mechanics are closer to plasticity than to fracture mechanics while in LDM is the other way around. LDM was developed to provide a better description of the structural deterioration phenomena in a proper context for civil engineering applications. However, at the same time, these models lead to mathematically objective results (TOI; HASEGAWA, 2011).

In a plate, the inelastic hinges become hinge-lines, in a two-dimensional continuum, they transform in localisation bands, in a three-dimensional solid: localisation surfaces. This chapter shows that LDM is a general framework that can be extended to the analysis of any continuum media and that the resulting formulations may inherit the mesh-independence properties observed in the uniaxial case. In the analysed cases, the proposed LDM procedures present refinement-independence solutions i.e. solutions with no dependence of the size of the elements.

Some finite elements including localisation bands have been presented in the literature (see e.g. Belytschko, Fish and Engelmann (1988) and Borja (2000) for a review). The approach proposed in this Thesis is radically different. The fundamental assumption is that localisation bands are a distinctive phenomenon that needs the introduction of specific state variables with their respective evolution laws for a proper modelling i.e. the continuum

damage variable is not the most adequate tool for describing the phenomena happening in the band.

5.1.1 Mesh-dependence in classic damage mechanics

For the sake of simplicity, the mesh-dependence in classic damage mechanics is here illustrated with a uniaxial example. Consider the following classic elementary problem. A bar of length L and cross section area A is subjected to prescribed displacements at both ends (see Figure 5.1a).

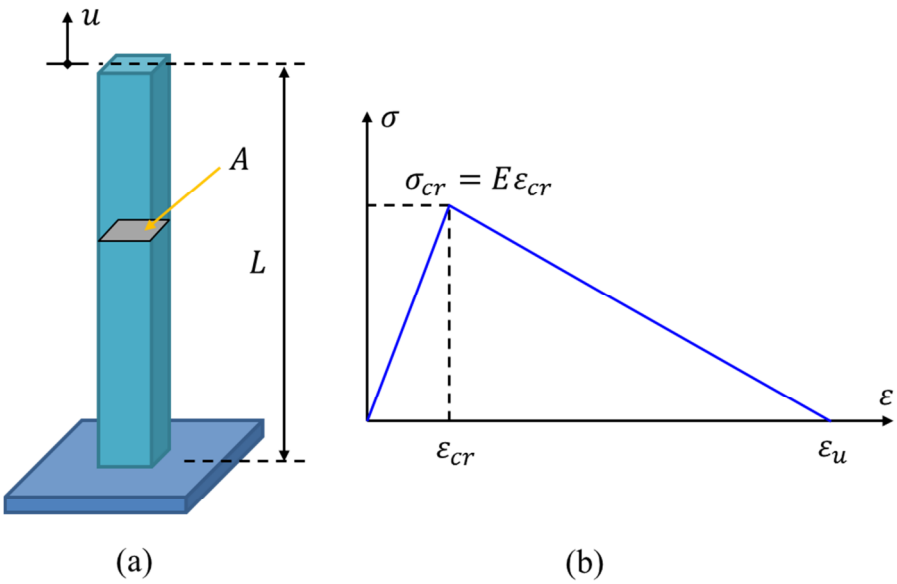

Figure 5.1 – (a) Damageable bar; (b) Stress as a function of strain in the local damage model.

The local damage constitutive equation is defined by:

$$\sigma = (1-\omega)E\varepsilon \tag{5.1}$$

and the damage evolution law is given by:

$$G^{\omega}(\varepsilon) - R^{\omega}(\omega) \leq 0 \quad \therefore \begin{cases} G^{\omega}(\varepsilon) = |\varepsilon| \\ R^{\omega}(\omega) = \dfrac{\varepsilon_{cr}\varepsilon_u}{\varepsilon_u + \omega(\varepsilon_{cr} - \varepsilon_u)} \end{cases} \tag{5.2}$$

where $G^{\omega}(\varepsilon)$ is the adopted energy release rate, $R^{\omega}(\omega)$ is the damage resistance function, ω is the conventional continuum damage variable, σ and ε have the usual meaning, E, ε_{cr} and ε_u are material parameters as indicated in Figure 5.1b.

A two-node finite element with linear displacements can now be developed by the conventional procedures. In the present case, this finite element gives exact solutions. The adopted mesh contains two finite elements, with lengths ℓ_1 and ℓ_2 ($\ell_1 + \ell_2 = L$) (Figure 5.2a). As it is well known, the curve of force as a function of displacement is mesh-dependent when solutions localising in only one element are chosen. Considering the first element (ℓ_1) as that one, the mesh-dependence is illustrated by varying the length ℓ_1 (see Figure 5.2b).

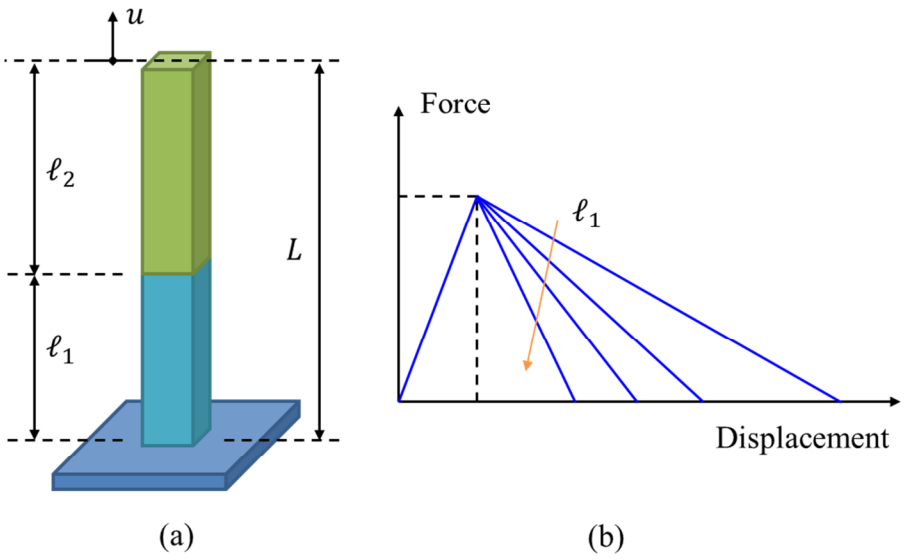

Figure 5.2 – (a) Finite element mesh and (b) force as a function of displacement for two element meshes with different sizes (note that the total length L is constant).

Note that with this simple example the mesh-dependence in classic damage mechanics is easily illustrated.

5.1.2 The hypothesis of strain equivalence revisited

The hypothesis of strain equivalence was previously presented in section 2.3, being the uniaxial relation rewritten just for convenience:

$$\varepsilon - \varepsilon^p = \frac{\sigma}{(1-\omega)E} = \frac{1}{E}\sigma + \frac{\omega}{(1-\omega)E}\sigma \qquad \therefore \begin{cases} \varepsilon^e = \dfrac{1}{E}\sigma \\ \varepsilon^d = \dfrac{\omega}{(1-\omega)E}\sigma \end{cases} \tag{5.3}$$

Neglecting plastic strains, the previous expression is written as follows:

$$\varepsilon = \frac{\sigma}{(1-\omega)E} = \frac{1}{E}\sigma + \frac{\omega}{(1-\omega)E}\sigma \qquad \therefore \begin{cases} \varepsilon^e = \dfrac{1}{E}\sigma \\ \varepsilon^d = \dfrac{\omega}{(1-\omega)E}\sigma \end{cases} \tag{5.4}$$

Thus, according to the hypothesis of strain equivalence, strain can be divided in two terms: an elastic strain (ε^e) and a damage-related one (ε^d). Note that there is an initial compliance given by the inverse of the elasticity modulus; damage induces an additional flexibility term that starts from zero and tends to infinity when the damage tends to one.

For the sake of simplicity, consider only the case of monotonic and positive loadings. Based on the new concept of damage strain, the constitutive equations and the damage evolution law of the model can be rewritten as:

$$\varepsilon = \frac{1}{E}\sigma + \varepsilon^d \tag{5.5}$$

$$\sigma - \sigma_{cr}\left(1 - \frac{\varepsilon^d}{\varepsilon_u}\right) \leq 0 \tag{5.6}$$

The latter is represented in Figure 5.3.

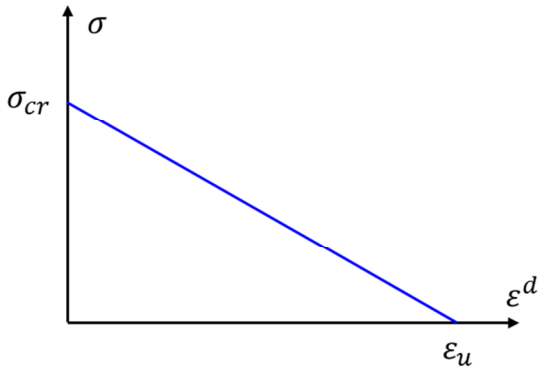

Figure 5.3 – Stress as a function of the damage-related strain.

In the continuation of this chapter, the LDM is formulated to two-dimensional problems of bending plates and tensile plates. Both procedures are presented as extensions

from uniaxial models. This new LDM framework is here called ***ex**tended **l**umped **d**amage **m**echanics* (XLDM).

5.2 Bending plates

This section starts with the formulation presented for mesh-independence in LDM applied to beams. Afterwards, the same procedure is extended to bending plates.

5.2.1 Unicity of the solution in a lumped damage model for bending in beams

Consider now a beam fixed at one end and subjected to imposed deflections at the other one as shown in Figure 5.4a. The beam is divided in two-node finite elements with quadratic displacements. Thus, the matrix of nodal displacements is:

$$\{\mathbf{q}\}_b = \{w_i \quad \theta_i \quad w_j \quad \theta_j\}^T \tag{5.7}$$

Now, a model based on the standard lumped inelasticity model is presented; the element is assumed to be the assemblage of an elastic beam with two inelastic hinges at the ends i and j (see Figure 5.4b). All inelastic effects are lumped at the hinges. The generalised deformation matrix $\{\boldsymbol{\phi}\}_b = \{\phi_i \quad \phi_j\}^T$ (see Figure 5.4c) is adopted as kinematic variable. The variable conjugated with the generalised deformation matrix is denoted as generalised stress matrix: $\{\mathbf{M}\}_b = \{m_i \quad m_j\}^T$ (see Figure 5.4d).

The kinematic equation and the internal forces of the element can be written in the same way as in the case of the frame element:

$$\begin{aligned} &\{\boldsymbol{\phi}\}_b = [\mathbf{B}^0]_b \{\mathbf{q}\}_b \\ &\{\mathbf{Q}\}_b = [\mathbf{B}^0]_b^T \{\mathbf{M}\}_b \\ &\therefore [\mathbf{B}^0]_b = \begin{bmatrix} -\frac{1}{L_b} & 1 & \frac{1}{L_b} & 0 \\ -\frac{1}{L_b} & 0 & \frac{1}{L_b} & 1 \end{bmatrix} \end{aligned} \tag{5.8}$$

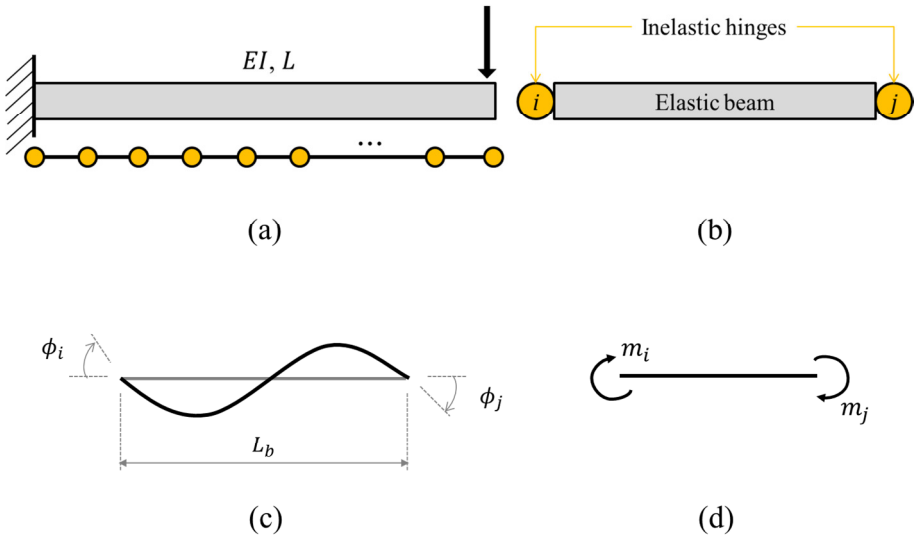

Figure 5.4 – Cantilever beam: (a) geometry and load conditions, (b) lumped inelasticity model, (c) generalised deformations and (d) generalised stresses

Considering the hypothesis of strain equivalence, the generalised deformations can be expressed as:

$$\{\boldsymbol{\phi}\}_b = \{\boldsymbol{\phi}^{\boldsymbol{e}}\}_b + \{\boldsymbol{\phi}^{\boldsymbol{d}}\}_b \tag{5.9}$$

where:

$$\{\boldsymbol{\phi}^{\boldsymbol{e}}\}_b = [\mathbf{F_0}]_b\{\mathbf{M}\}_b = \begin{bmatrix} \frac{L_b}{3EI} & -\frac{L_b}{6EI} \\ -\frac{L_b}{6EI} & \frac{L_b}{3EI} \end{bmatrix}\{\mathbf{M}\}_b \tag{5.10}$$

$$\{\boldsymbol{\phi}^{\boldsymbol{d}}\}_b = \{\phi_i^d \quad \phi_j^d\}^T$$

The damage laws for the inelastic hinges and under monotonic loadings are similar to the one used in (5.17):

$$\begin{aligned} |m_i| - m_{cr}\left(1 - \frac{|\phi_i^d|}{\phi_u}\right) \leq 0 \\ |m_j| - m_{cr}\left(1 - \frac{|\phi_j^d|}{\phi_u}\right) \leq 0 \end{aligned} \tag{5.11}$$

where m_{cr} and ϕ_u are material parameters (see Figure 5.5a).

Consider again the problem of Figure 5.4a. In a first stage, the behavior of the beam is elastic while the imposed displacement generates moments on the fixed end that are less than the critical moment m_{cr}. Next, the inelastic hinge appears; the softening phase develops until the moment on the hinge is equal to zero. At this point, deformations on all the elements are zero and the rotation of the inelastic hinge is equal to ϕ_u. Thus, the final deflection is always equal to the ultimate rotation ϕ_u times the length of the beam no matter how many elements are used; consequently, the curve of force vs. deflection is mesh-independent (see Figure 5.5b).

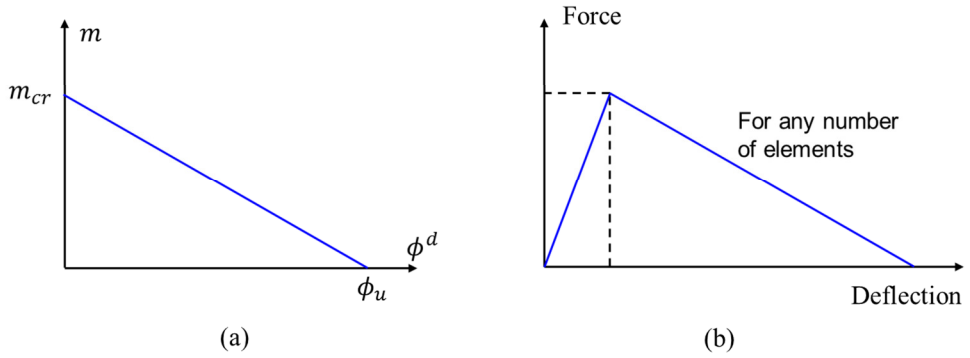

Figure 5.5 – Lumped inelasticity model for beams: (a) inelastic material response and (b) cantilever solution.

5.2.2 The constant moment triangle

5.2.2.1 Kinematic relations

Consider the simplest of the finite elements for elastic plates. Morley (1971) proposed a non-conforming element for slender plates in bending, so-called constant moment triangle (CMT). The CMT element was chosen due to its constant moment approximation. Such characteristic enable a simple modelling of the XLDM.

The CMT element consists in a triangle with six generalised displacements or degrees of freedom:

$$\{\mathbf{q}\}_t = \{w_i \quad w_j \quad w_k \quad \theta_a \quad \theta_b \quad \theta_c\}^T \tag{5.12}$$

where w_i, w_j and w_k are the deflections of the nodes i, j and k of coordinates (x_i, y_i), (x_j, y_j) and (x_k, y_k); θ_a, θ_b, and θ_c are the normal slopes at the middle of, respectively, the sides ij, jk and ki (see Figure 5.6).

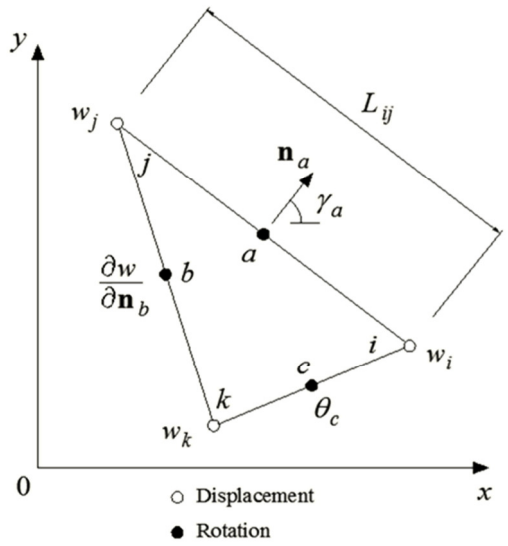

Figure 5.6 – Non-conforming plate-bending element with six degrees of freedom (Morley, 1971).

The deflection $w(x, y)$ in the CMT element is given by a second-degree polynomial. This field can be decomposed in a rigid-body displacement $z(x, y)$ and a relative deflection $w^r(x, y)$:

$$w(x, y) = z(x, y) + w^r(x, y) \tag{5.13}$$

The rigid-body deflection $z(x, y)$ is given by the plane that passes through the points (x_i, y_i, w_i), (x_j, y_j, w_j) and (x_k, y_k, w_k). Let's introduce now the matrix of generalised deformations $\{\boldsymbol{\phi}\}_t$ that is defined as:

$$\{\boldsymbol{\phi}\}_t = \{\phi_a \quad \phi_b \quad \phi_c\}^T$$
$$\phi_a = \left.\frac{\partial w^r}{\partial \mathbf{n}_a}\right|_{(x_a,y_a)} = \theta_a - \left.\frac{\partial z}{\partial \mathbf{n}_a}\right|_{(x_a,y_a)}$$
$$\phi_b = \left.\frac{\partial w^r}{\partial \mathbf{n}_b}\right|_{(x_b,y_b)} = \theta_b - \left.\frac{\partial z}{\partial \mathbf{n}_b}\right|_{(x_b,y_b)} \tag{5.14}$$
$$\phi_c = \left.\frac{\partial w^r}{\partial \mathbf{n}_c}\right|_{(x_c,y_c)} = \theta_c - \left.\frac{\partial z}{\partial \mathbf{n}_c}\right|_{(x_c,y_c)}$$

i.e. the generalised deformation matrix gathers the normal rotations relative to the plane of the element. The kinematic equation relating generalised displacements and deformations is:

$$\{\boldsymbol{\phi}\}_t = [\mathbf{B}^0]_t \{\mathbf{q}\}_t \tag{5.15}$$

where $[\mathbf{B}^0]_t$ is the kinematic matrix, expressed as:

$$\left[\mathbf{B}^0\right]_t = $$
$$= \begin{bmatrix} \frac{c_a(y_k - y_j) + s_a(x_j - x_k)}{2A} & \frac{c_a(y_i - y_k) + s_a(x_k - x_i)}{2A} & \frac{L_{ij}}{2A} & 1 & 0 & 0 \\ \frac{L_{jk}}{2A} & \frac{c_b(y_i - y_k) + s_b(x_k - x_i)}{2A} & \frac{c_b(y_j - y_i) + s_b(x_i - x_j)}{2A} & 0 & 1 & 0 \\ \frac{c_c(y_k - y_j) + s_c(x_j - x_k)}{2A} & \frac{L_{ki}}{2A} & \frac{c_c(y_j - y_i) + s_c(x_i - x_j)}{2A} & 0 & 0 & 1 \end{bmatrix} \tag{5.16}$$

being A the area of the element; L_{ij}, L_{jk}, L_{ki}, the lengths of the sides ij, jk, and ki, respectively; and: $c_a = \cos(\gamma_a)$, $s_a = \sin(\gamma_a)$, $c_b = \cos(\gamma_b)$, $s_b = \sin(\gamma_b)$, $c_c = \cos(\gamma_c)$, $s_c = \sin(\gamma_c)$.

It is noteworthy that the matrix of curvatures can be expressed by the generalised deformations i.e.

$$\{\boldsymbol{\chi}\}_t = \left\{-\frac{\partial^2 w^r}{\partial x^2} \quad -\frac{\partial^2 w^r}{\partial y^2} \quad -2\frac{\partial^2 w^r}{\partial x \partial y}\right\}^T = \frac{1}{A}[\mathbf{T}]_t^T \{\boldsymbol{\phi}\}_t \tag{5.17}$$

where $[\mathbf{T}]_t$ is a transformation matrix, expressed as:

$$[\mathbf{T}]_t = \begin{bmatrix} -L_{ij}c_a^2 & -L_{ij}s_a^2 & -2L_{ij}c_a s_a \\ -L_{jk}c_b^2 & -L_{jk}s_b^2 & -2L_{jk}c_b s_b \\ -L_{ki}c_c^2 & -L_{ki}s_c^2 & -2L_{ki}c_c s_c \end{bmatrix} \tag{5.18}$$

5.2.2.2 Static relations

The specific bending moments (moments per unit length) m_{xx}, m_{yy}, m_{xy} are constant in the CMT element. Such quantities are gathered in the specific bending moment matrix:

$$\{\boldsymbol{\beta}\}_t = \{m_{xx} \quad m_{yy} \quad m_{xy}\}^T \tag{5.19}$$

The specific bending moments m_a, m_b, m_c are defined as the normal specific bending moments at the sides ij, jk, ki as shown in Figure 5.7. Such specific bending moments can be expressed in terms of m_{xx}, m_{yy}, m_{xy}, as follows:

$$\begin{aligned} m_a &= -m_{xx}c_a^2 - m_{yy}s_a^2 - 2m_{xy}c_a s_a \\ m_b &= -m_{xx}c_b^2 - m_{yy}s_b^2 - 2m_{xy}c_b s_b \\ m_c &= -m_{xx}c_c^2 - m_{yy}s_c^2 - 2m_{xy}c_c s_c \end{aligned} \tag{5.20}$$

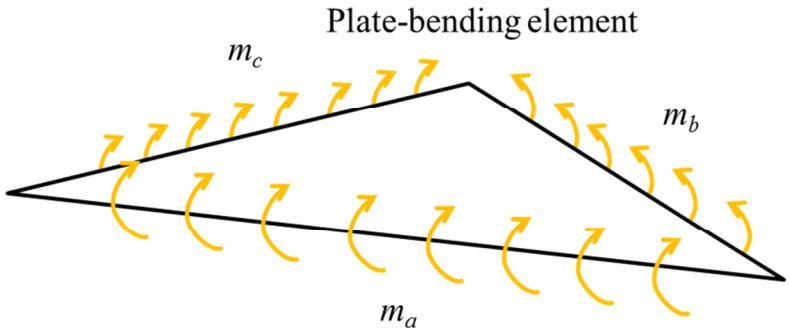

Figure 5.7 – Normal specific bending moments at the sides of the CMT element.

Now, let's define the generalised stress matrix as:

$$\{\mathbf{M}\}_t = \{M_{ij} \quad M_{jk} \quad M_{ki}\}^T = \{L_{ij}m_a \quad L_{jk}m_b \quad L_{ki}m_c\}^T = [\mathbf{T}]_t\{\boldsymbol{\beta}\}_t \tag{5.21}$$

Notice that the quantities M_{ij}, M_{jk}, M_{ki} present units of bending moments.

The nodal forces $\{\mathbf{Q}\}_t$ (vertical forces at the vertices and normal moments at the mid-sides, as presented in Figure 5.8) are defined as follows:

$$\{\mathbf{Q}\}_t^T = \{Q_{wi} \quad Q_{wj} \quad Q_{wk} \quad Q_{\theta a} \quad Q_{\theta b} \quad Q_{\theta c}\} \tag{5.22}$$

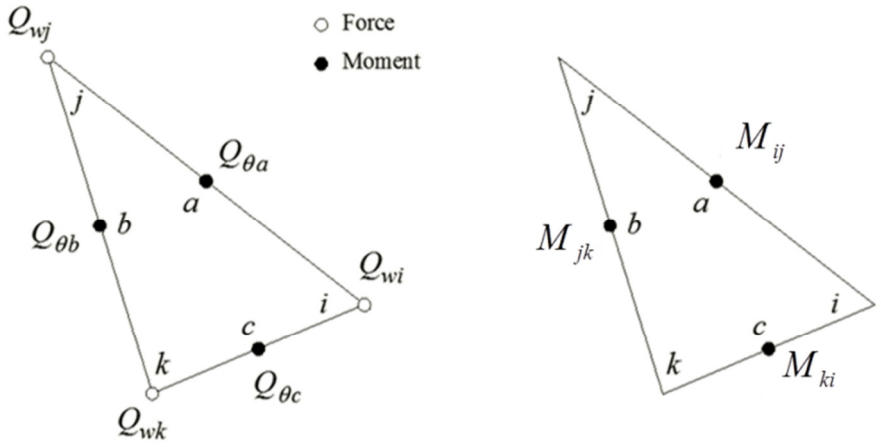

Figure 5.8 – Nodal forces (left) and generalized stresses (right).

The virtual work principle for the CMT element lies:

$$\iint_A \{\boldsymbol{\chi}^*\}_t^T \{\boldsymbol{\beta}\}_t \, dA = \{\mathbf{q}^*\}_t^T \{\mathbf{Q}\}_t \tag{5.23}$$
$$A\{\boldsymbol{\chi}^*\}_t^T \{\boldsymbol{\beta}\}_t = \{\mathbf{q}^*\}_t^T \{\mathbf{Q}\}_t$$

where the superscript $*$ means virtual field. The substitution of (5.17) and (5.21) in (5.23) results:

$$\{\boldsymbol{\phi}^*\}_t^T \{\mathbf{M}\}_t = \{\mathbf{q}^*\}_t^T \{\mathbf{Q}\}_t \tag{5.24}$$

and the substitution of (5.15) in (5.24) lies:

$$\{\mathbf{q}^*\}_t^T [\mathbf{B}^0]_t^T \{\mathbf{M}\}_t = \{\mathbf{q}^*\}_t^T \{\mathbf{Q}\}_t \qquad \forall \{\mathbf{q}^*\}_t \tag{5.25}$$

Finally, the nodal forces are now expressed in terms of generalised stresses, as follows:

$$\{\mathbf{Q}\}_t = [\mathbf{B}^0]_t^T \{\mathbf{M}\}_t \tag{5.26}$$

5.2.2.3 Elasticity

The relationship between the specific bending moments and curvatures of the CMT element can be expressed as follows:

$$\{\boldsymbol{\beta}\}_t = [\mathbf{D}]_t \{\boldsymbol{\chi}\}_t \tag{5.27}$$

where $[\mathbf{D}]_t$ is the flexural rigidity matrix, defined as:

$$[\mathbf{D}] = D \begin{bmatrix} 1 & \nu & 0 \\ \nu & 1 & 0 \\ 0 & 0 & \dfrac{1-\nu}{2} \end{bmatrix} \tag{5.28}$$

being D the bending stiffness of the plate, which is expressed in terms of the Young's modulus E, the Poisson's ratio ν and the thickness of the plate:

$$D = \frac{Eh^3}{12(1-\nu^2)} \tag{5.29}$$

The strain energy U_f of the CMT element can be written as:

$$\begin{aligned} U_f &= \frac{1}{2} \iint_A \{\boldsymbol{\chi}\}_t^T \{\boldsymbol{\beta}\}_t \, dA = \frac{A}{2} \{\boldsymbol{\chi}\}_t^T \{\boldsymbol{\beta}\}_t = \frac{A}{2} \{\boldsymbol{\beta}\}_t^T [\mathbf{D}]^{-1} \{\boldsymbol{\beta}\}_t \\ &= \frac{A}{2} \{\mathbf{M}\}_t^T ([\mathbf{T}]_t^T)^{-1} [\mathbf{D}]^{-1} [\mathbf{T}]_t^{-1} \{\mathbf{M}\}_t \end{aligned} \tag{5.30}$$

Therefore, the generalised deformations are now expressed in terms of generalised stresses:

$$\{\boldsymbol{\phi}\}_t = \frac{\partial U_f}{\partial \{\mathbf{M}\}_t} = A([\mathbf{T}]_t^T)^{-1}[\mathbf{D}]^{-1}[\mathbf{T}]_t^{-1}\{\mathbf{M}\}_t \tag{5.31}$$

where the elastic flexibility matrix is given by:

$$[\mathbf{F_0}]_t = A([\mathbf{T}]_t^T)^{-1}[\mathbf{D}]^{-1}[\mathbf{T}]_t^{-1} \tag{5.32}$$

Then, the elastic constitutive relation is expressed as:

$$\{\boldsymbol{\phi}\}_t = [\mathbf{F_0}]_t\{\mathbf{M}\}_t \tag{5.33}$$

5.2.2.4 Numerical test: linear elasticity

In order to analyse the validity of the formulation presented so far and also evaluate the accuracy of the CMT element, a set of numerical examples is now presented. All examples are addressed to an isotropic square plate (Figure 5.9a) with Poisson's ration taken as 0.3. This plate is loaded either by a central concentrated force P or a uniformly distributed load p, applied on the plate surface. The edges are either all clamped or all simply supported. Figure 5.9b-f presents the finite element meshes adopted to perform the numerical analysis. The results are shown in Table 5.1.

Note that, as finer as the mesh becomes, the numerical solution gets closer to the analytic solution. It is also noteworthy that the displacement decreases with the mesh refinement. This numerical behaviour is due to intrinsic over-flexible characteristics of the CMT element i.e. the CMT element "gives a strict upper bound to the bending energy of a plate" (ALLMAN; MORLEY, 2000, p. 739), which is directly related to the displacement presented in this elastic problem.

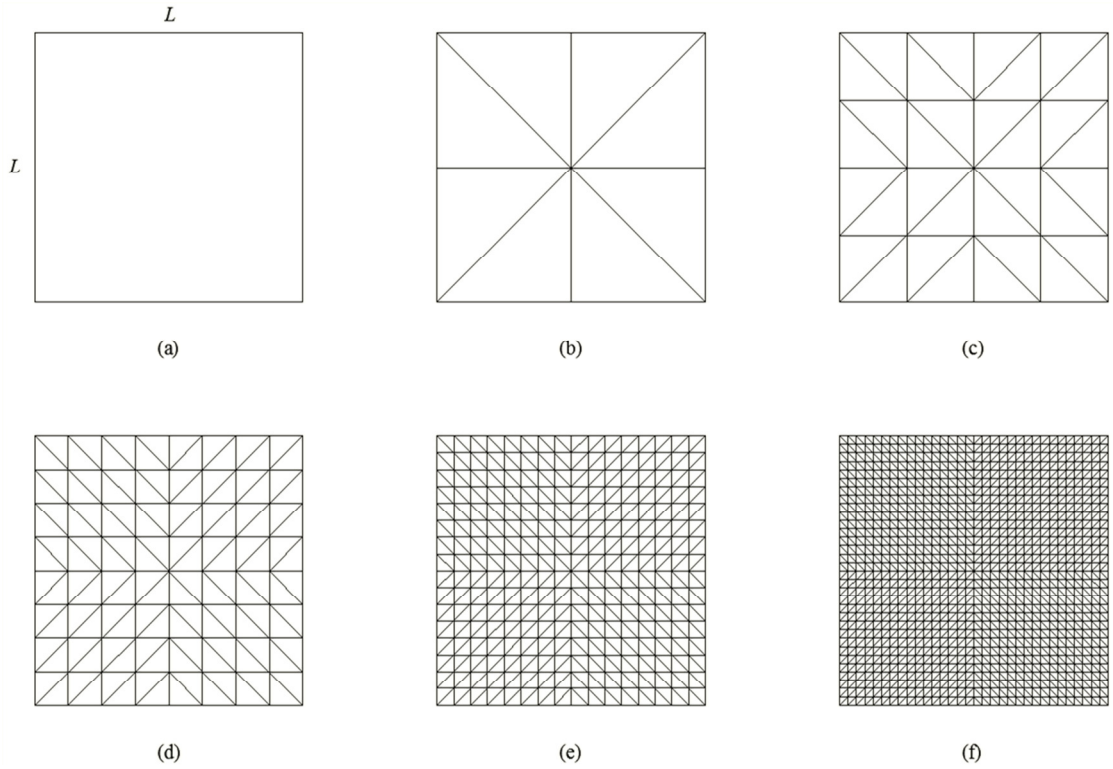

Figure 5.9 – Isotropic square plate: (a) geometry, (b) mesh 2×2, (c) mesh 4×4, (d) mesh 8×8, (e) mesh 16×16 and (f) mesh 32×32.

Table 5.1 – Central deflection of an isotropic square plate.

Mesh	Central point force P		Uniform pressure p	
	Simply supported	Clamped	Simply supported	Clamped
2×2	0.02706	0.02232	0.00902	0.00744
4×4	0.01741	0.01202	0.00513	0.00285
8×8	0.01351	0.00776	0.00432	0.00170
16×16	0.01219	0.00628	0.00413	0.00138
32×32	0.01178	0.00581	0.00408	0.00129
Analytic	0.01160	0.00560	0.00406	0.00126
Multiplier	PL^2/D		pL^4/D	

5.2.3 A lumped damage model for bending plates

5.2.3.1 Model idealisation

Now, consider that the bending plate element is an assemblage of the elastic CMT element with damage hinge-lines, as depicted in Figure 5.10. This assumption is clearly based on the beam element previously presented in this chapter. Therefore, the matrix of generalised damage deformations is introduced as follows:

$$\{\boldsymbol{\phi}^{\boldsymbol{d}}\}_t = \{\phi_a^d \quad \phi_b^d \quad \phi_c^d\}^T \tag{5.34}$$

which contains the damage rotations of the hinge-lines at sides ij, jk and ki, respectively.

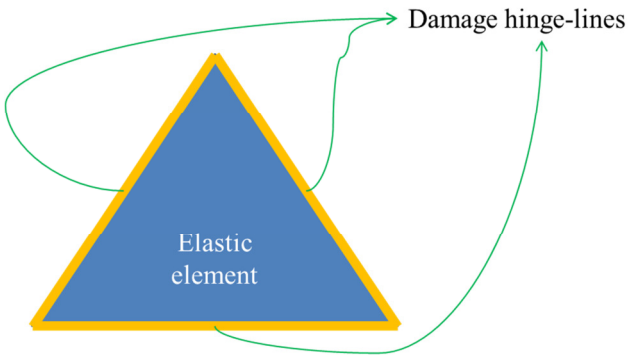

Figure 5.10 – Lumped damage model idealisation.

Considering the hypothesis of strain equivalence, the total generalised deformations are decomposed in an elastic part $\{\boldsymbol{\phi}^{\boldsymbol{e}}\}_t$ and the damage rotations $\{\boldsymbol{\phi}^{\boldsymbol{d}}\}_t$ of the hinge-lines:

$$\{\boldsymbol{\phi}\}_t = \{\boldsymbol{\phi}^{\boldsymbol{e}}\}_t + \{\boldsymbol{\phi}^{\boldsymbol{d}}\}_t \tag{5.35}$$

The generalised elastic deformations are computed by the Morley (1971) element and the generalised damage deformations obey the following evolution laws (Figure 5.11):

$$\left|\frac{M_{ij}}{L_{ij}}\right| - m_{cr}\left(1 - \frac{|\phi_a^d|}{\phi_u}\right) \leq 0$$
$$\left|\frac{M_{jk}}{L_{jk}}\right| - m_{cr}\left(1 - \frac{|\phi_b^d|}{\phi_u}\right) \leq 0 \tag{5.36}$$
$$\left|\frac{M_{ki}}{L_{ki}}\right| - m_{cr}\left(1 - \frac{|\phi_c^d|}{\phi_u}\right) \leq 0$$

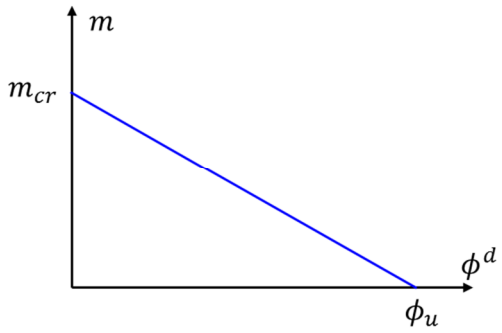

Figure 5.11 – Inelastic response.

Note that if $\phi_u \to \infty$ a curve with constant value m_{cr} represents the inelastic behaviour. Therefore, it can be considered that the lumped damage model reduces to a lumped plasticity model. Such particular case is presented in Appendix B, where the plastic collapse of RC slabs is modelled.

5.2.3.2 Application example

A simple square bending plate $L \times L$ with thickness h is analysed in order to illustrate the potentiality of the proposed model. Such plate is simply supported on the sides and loaded by a concentrated force at the centre. Note that the corners of the plate cannot lift.

In the modelling, three meshes were used to analyse the objectivity of the proposed model. Note that the element size varies from one mesh another (Figure 5.12). The collapse mechanisms obtained with the three meshes are equal (Figure 5.12), and the all damage rotations at the end of the analysis present values equal to the ultimate rotation (ϕ_u). Finally, note also that the model present objectivity in the studied problem, as depicted in the graph of Figure 5.12.

Regarding all results presented in Figure 5.12, it can be affirmed that the proposed model present objectivity i.e. the solution is size-independent. In the end of this chapter the limitations of this procedure are highlighted.

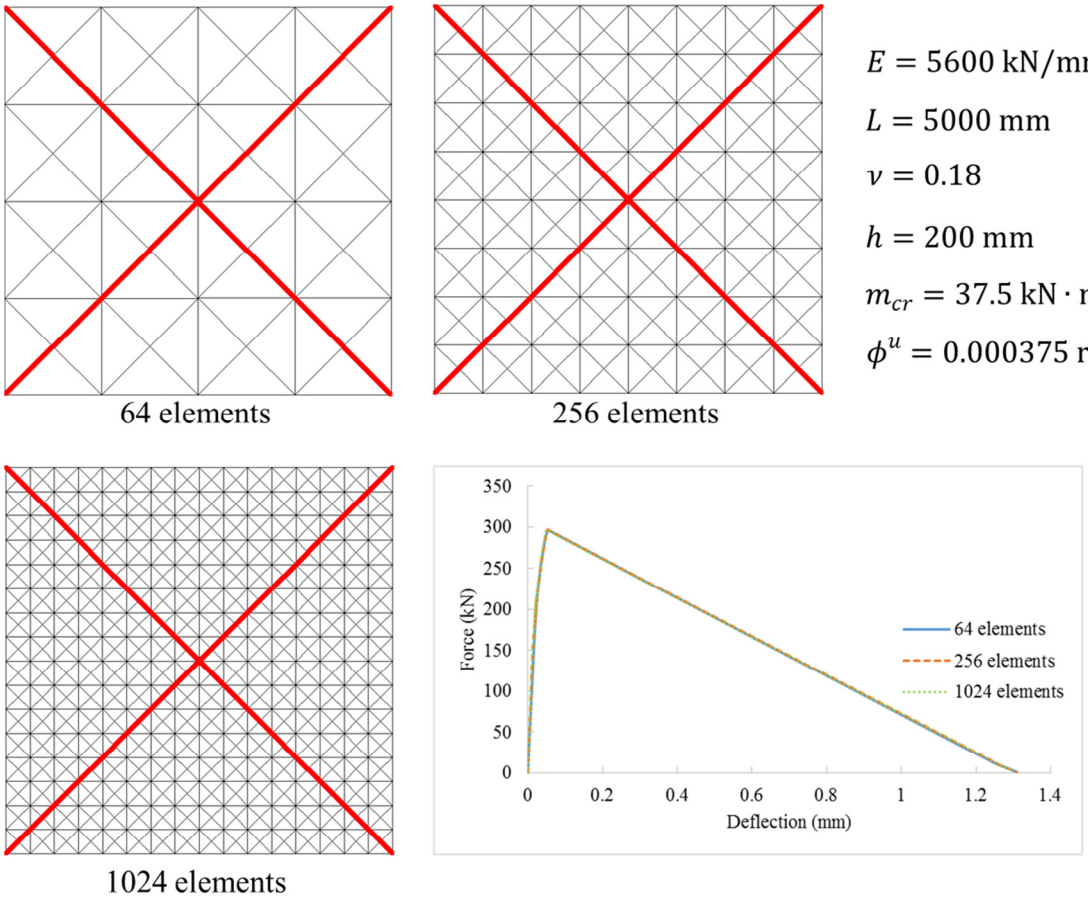

Figure 5.12 – Problem solution with the proposed lumped damage model.

5.3 Tensile plates

In this section, the main ideas of lumped damage mechanics proposed to bending plates are applied to tensile plates. Note that for bending problems the damage variable describes inelastic phenomena lumped on hinges (or hinge-lines). Now, the inelastic phenomena are lumped on localisation bands.

The procedure proposed in this section is firstly illustrated with a bar in tension, and then its application in tensile plates is broached.

5.3.1 A lumped damage model for a bar in tension

Consider again the uniaxial problem presented in subsection 5.1.1. This time, it will be solved using a new two-node finite element inspired on the one described in item 5.2.1. The matrix of nodal displacements is denoted by:

$$\{\mathbf{q}\}_b = \{u_i \quad u_j\}^T \tag{5.37}$$

This time, damage is concentrated in a localisation band while the rest of the element remains elastic. This band has a nil initial thickness (see Figure 5.13). This idea is similar to the concept of inelastic hinge or the FPZ in fracture mechanics.

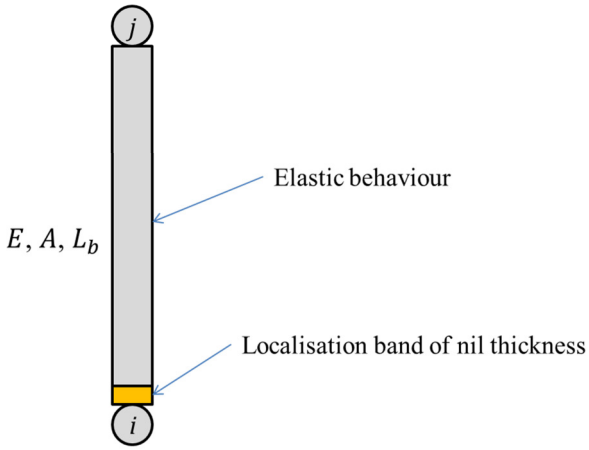

Figure 5.13 – Lumped damage finite element for a uniaxial bar.

In this element, the elongation δ of the element is used as kinematic variable instead of ε. The kinematic equation relating displacements and deformations is:

$$\delta = [\mathbf{B}^0]_b\{\mathbf{q}\}_b \qquad \therefore [\mathbf{B}^0]_b = [-1 \quad 1] \tag{5.38}$$

The matrix of internal forces $\{\mathbf{Q}\}_b$ of the element is:

$$\{\mathbf{Q}\}_b = A[\mathbf{B}^0]_b^T\sigma \tag{5.39}$$

where σ is the conventional Cauchy stress. Now, a deformation equivalence hypothesis is introduced, instead of the strain equivalence one:

$$\delta = \delta^e + \delta^d = \frac{L_b}{E}\sigma + \delta^d \tag{5.40}$$

In the present context, δ^e is the elongation of the elastic part of the element and δ^d represents the elongation of the localisation band. Consider again the particular case of monotonic positive displacements, a damage evolution law similar to (5.17) is chosen, but this time in terms of the damage deformation instead of damage strain:

$$\sigma - \sigma_{cr}\left(1 - \frac{\delta^d}{\delta_u}\right) \leq 0 \tag{5.41}$$

where σ_{cr} and δ_u are material parameters (Figure 5.14a). Note that (5.41) is comparable to a tension-softening law in the FPZ of fracture mechanics, with the damage-related elongation δ^d playing the role of the crack-opening displacement. This finite element generates displacement vs. force curves that are mesh-independent (Figure 5.14b).

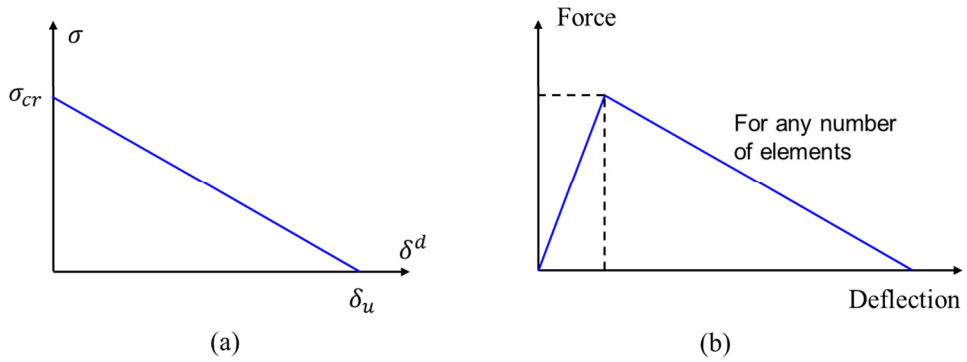

Figure 5.14 – Lumped inelasticity model for bars in tension: (a) inelastic material response and (b) numerical solution for a simple bar in tension.

It is easy to understand why this new element leads to stable results while the conventional one does not. In the conventional damage model, stress is zero when damage is equal to one (see the elasticity law of subsection 5.1.1), thus the elastic strain is also zero and only the damage-related strain may be no nil (see the elasticity law of subsection 5.1.2). According to the damage law, for σ equal to zero, the damage-related strain ε^d is equal to the ultimate strain ε_u. Therefore, the ultimate displacement is equal to the ultimate strain times the length of the element i.e. $\varepsilon_u L_b$. Consequently, the curve of displacement vs. force is mesh-dependent.

On the other hand, in the lumped damage model, the elongation of the localisation band is equal to the ultimate elongation δ_u when damage reaches the value of one and the stress is equal to zero. The rest of the bar is un-deformed; therefore, the ultimate displacement

does not depend on the length of the element and the resulting curve is, of course, mesh-independent.

In the simulations, one defect was introduced in the first element of all the meshes in order to impose damage localisation always at the same location. This feature may be compared with the introduction of an initial crack in fracture mechanics problems.

5.3.2 A lumped damage model for tensile plates

5.3.2.1 The elastic four-node element revisited

Consider now a two-dimensional continuum. The classic four-node element (see Figure 5.15a) is defined by the following displacement matrix:

$$\{\mathbf{q}\}_b = \{u_i \quad v_i \quad u_j \quad v_j \quad u_k \quad v_k \quad u_l \quad v_l\}^T \tag{5.42}$$

The conventional shape functions leads to expressions for strains $\{\boldsymbol{\varepsilon}\}_b$, stresses $\{\boldsymbol{\sigma}\}_b$, nodal forces $\{\mathbf{Q}\}_b$ and stiffness matrix $[\mathbf{K}]_b$ that can be written as follows:

$$\begin{aligned}
&\{\boldsymbol{\varepsilon}\}_b = [\mathbf{b}]_b\{\mathbf{q}\}_b \\
&\{\boldsymbol{\sigma}\}_b = [\mathbf{H}]\{\boldsymbol{\varepsilon}\}_b = [\mathbf{H}][\mathbf{b}]_b\{\mathbf{q}\}_b \\
&\{\mathbf{Q}\}_b = \iiint [\mathbf{b}]_b^T \{\boldsymbol{\sigma}\} dV \\
&[\mathbf{K}]_b = \iiint [\mathbf{b}]_b^T [\mathbf{H}][\mathbf{b}]_b dV
\end{aligned} \tag{5.43}$$

where $[\mathbf{b}]_b$ is the conventional kinematic matrix and $[\mathbf{H}]$ represents the matrix of elastic coefficients.

Exactly the same element can be rewritten using a notation that will allow for the formulation of two-dimensional LDM element in a simpler way. Introduce now an equivalent five-bar truss as shown in Figure 5.15b. The total elongations of the bars are included in the matrix of generalised deformations:

$$\{\boldsymbol{\delta}\}_b = \{\delta_{ij} \quad \delta_{ik} \quad \delta_{il} \quad \delta_{jk} \quad \delta_{kl}\}^T \tag{5.44}$$

Where the subscript at each term of $\{\boldsymbol{\delta}\}_b$ represents the nodes that contains the truss bar, e.g. δ_{ij} represents the elongation of the bar between nodes i and j and so on.

The kinematic equation between the nodal displacements and generalised deformations can, of course, be written as:

$$\{\boldsymbol{\delta}\}_b = [\mathbf{B}]_b\{\mathbf{q}\}_b \tag{5.45}$$

being $[\mathbf{B}]_b$ the kinematic transformation matrix given in the Cartesian system (Appendix C) and

$$[\mathbf{B}']_b = \begin{bmatrix} -1 & 0 & 1 & 0 & 0 & 0 & 0 & 0 \\ -\frac{\sqrt{2}}{2} & -\frac{\sqrt{2}}{2} & 0 & 0 & -\frac{\sqrt{2}}{2} & -\frac{\sqrt{2}}{2} & 0 & 0 \\ 0 & -1 & 0 & 0 & 0 & 0 & 0 & 1 \\ 0 & 0 & 0 & -1 & 0 & 1 & 0 & 0 \\ 0 & 0 & 0 & 0 & 1 & 0 & -1 & 0 \end{bmatrix} \tag{5.46}$$

the kinematic transformation matrix given in the reference space (Figure 5.15c).

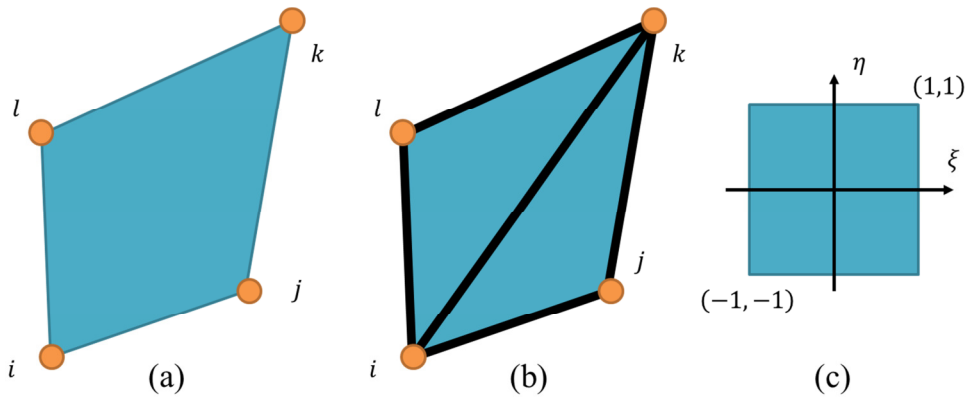

Figure 5.15 – (a) Conventional four-node quadrilateral element; (b) equivalent truss; (c) reference space.

The strain tensor in any point of the conventional element depends on five constants; therefore it can also be expressed as a function of the generalized deformations:

$$\{\boldsymbol{\varepsilon}\}_b = [\mathbf{T}]_b\{\boldsymbol{\delta}\}_b \tag{5.47}$$

being $[\mathbf{b}]_b = [\mathbf{T}]_b[\mathbf{B}]_b$, where $[\mathbf{T}]_b$ is the transformation matrix in Cartesian coordinates (Appendix C) and

$$[\mathbf{T}']_b = \frac{1}{4}\begin{bmatrix} 1-\xi & 0 & 0 & 0 & 1+\xi \\ 0 & 0 & 1-\eta & 1+\eta & 0 \\ -(1+\eta) & \sqrt{2}/_2 & -(1+\xi) & \xi-1 & \eta-1 \end{bmatrix} \tag{5.48}$$

is the transformation matrix expressed in the usual reference space of coordinates ξ and η. The stress matrix is now given by:

$$\{\boldsymbol{\sigma}\}_b = [\mathbf{H}][\mathbf{T}]_b\{\boldsymbol{\delta}\}_b \tag{5.49}$$

Finally, the nodal forces and stiffness matrix are rewritten as:

$$\begin{aligned} \{\mathbf{Q}\}_b &= \iiint [\mathbf{b}]_b^T \{\boldsymbol{\sigma}\}_b dV = [\mathbf{B}]_b^T \iiint [\mathbf{T}]_b^T \{\boldsymbol{\sigma}\}_b dV \\ [\mathbf{K}]_b &= \iiint [\mathbf{b}]_b^T [\mathbf{H}][\mathbf{b}]_b dV = [\mathbf{B}]_b^T \left(\iiint [\mathbf{T}]_b^T [\mathbf{H}][\mathbf{T}]_b dV \right) [\mathbf{B}]_b \end{aligned} \tag{5.50}$$

5.3.2.2 The LDM four-node element

In the beam element only two inelastic hinges at its extremes were considered. This, of course, is an arbitrary choice for the sake of simplicity. Other elements with more than two hinges with variable location, that can be a function of the nodal displacements, can be imagined. In this section, keeping the same spirit, an element that is the result of the assemblage of an elastic part with four fixed localisation bands at the sides of the element is proposed (see Figure 5.16a).

Given the nature of the shape functions of the element, it is assumed a linear variation in the thickness of the band (see Figure 5.16b). When a localisation band crosses any of the equivalent bars, it generates elongations $\{\boldsymbol{\delta}^{\boldsymbol{d}}\}_b$. In the reference space, this damage related elongations have the following simple expression:

$$\{\boldsymbol{\delta}^{\boldsymbol{d}}\}_b = \begin{Bmatrix} 0 \\ \epsilon_{i\eta}\,\sqrt{2}/2 \\ \epsilon_{i\eta} \\ \epsilon_{j\eta} \\ 0 \end{Bmatrix} + \begin{Bmatrix} \epsilon_{j\xi} \\ \epsilon_{k\xi}\,\sqrt{2}/2 \\ 0 \\ 0 \\ \epsilon_{k\xi} \end{Bmatrix} + \begin{Bmatrix} 0 \\ \epsilon_{k\eta}\,\sqrt{2}/2 \\ \epsilon_{l\eta} \\ \epsilon_{k\eta} \\ 0 \end{Bmatrix} + \begin{Bmatrix} \epsilon_{i\xi} \\ \epsilon_{i\xi}\,\sqrt{2}/2 \\ 0 \\ 0 \\ \epsilon_{l\xi} \end{Bmatrix} \tag{5.51}$$

where $\epsilon_{i\eta}$ is the thickness of the band at the node i on the side ij (see Figure 5.16b), $\epsilon_{j\xi}$ corresponds to the node j in the band jk and so on. The matrix $\{\boldsymbol{\delta}^{\boldsymbol{d}}\}_b$ in the Cartesian system is presented in Appendix C.

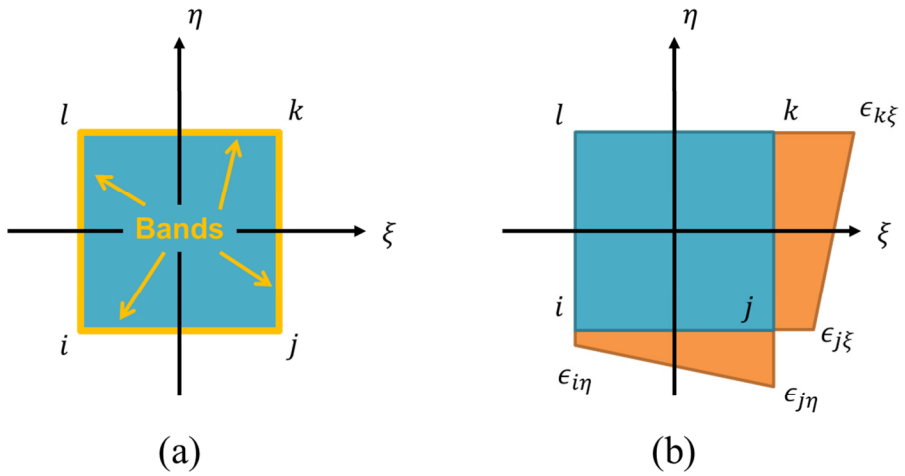

Figure 5.16 – (a) Localisation bands in a four-node element; (b) thickness of the bands ij and jk.

The deformation equivalence hypothesis establishes now that the total elongations are equal to the elongations of the elastic element plus those due to the localisation bands:

$$\{\boldsymbol{\delta}\}_b = \{\boldsymbol{\delta}^{\boldsymbol{e}}\}_b + \{\boldsymbol{\delta}^{\boldsymbol{d}}\}_b \tag{5.52}$$

Therefore, the elasticity law is:

$$\{\boldsymbol{\sigma}\}_b = [\mathbf{H}][\mathbf{T}]_b\{\boldsymbol{\delta} - \boldsymbol{\delta}^{\boldsymbol{d}}\}_b \tag{5.53}$$

The constitutive equations are completed with the following damage laws in the reference element:

$$\begin{aligned}
&\sigma_\eta(\xi_i,\eta_i)-\sigma_{cr}\left(1-\frac{\epsilon_{i\eta}}{\delta_u}\right)\le 0 \qquad && \sigma_\eta(\xi_j,\eta_j)-\sigma_{cr}\left(1-\frac{\epsilon_{j\eta}}{\delta_u}\right)\le 0\\
&\sigma_\xi(\xi_j,\eta_j)-\sigma_{cr}\left(1-\frac{\epsilon_{j\xi}}{\delta_u}\right)\le 0 \qquad && \sigma_\xi(\xi_k,\eta_k)-\sigma_{cr}\left(1-\frac{\epsilon_{k\xi}}{\delta_u}\right)\le 0\\
&\sigma_\eta(\xi_k,\eta_k)-\sigma_{cr}\left(1-\frac{\epsilon_{k\eta}}{\delta_u}\right)\le 0 \qquad && \sigma_\eta(\xi_l,\eta_l)-\sigma_{cr}\left(1-\frac{\epsilon_{l\eta}}{\delta_u}\right)\le 0\\
&\sigma_\xi(\xi_l,\eta_l)-\sigma_{cr}\left(1-\frac{\epsilon_{l\xi}}{\delta_u}\right)\le 0 \qquad && \sigma_\xi(\xi_i,\eta_i)-\sigma_{cr}\left(1-\frac{\epsilon_{i\xi}}{\delta_u}\right)\le 0
\end{aligned} \tag{5.54}$$

Finally, the same kinematic and equilibrium equations of item 5.3.2.1 may be used:

$$\begin{aligned}
&\{\boldsymbol{\delta}\}_b=[\mathbf{B}]_b\{\mathbf{q}\}_b\\
&\{\mathbf{Q}\}_b=[\mathbf{B}]_b^T\iiint[\mathbf{T}]^T\{\boldsymbol{\sigma}\}dV
\end{aligned} \tag{5.55}$$

5.3.2.3 Application example

The proposed finite element was implemented in an academic structural analysis programme (UZCATEGUI, 2012). The example presented in Figure 5.17 is used to show the convergence of the numerical solution with respect to the element size. This L-shaped plate is fixed at the bottom side and was subjected to a monotonically increasing displacement at the lower right corner designated as point A. The analysis ends when the ultimate elongation of the band is achieved at the interior corner of the plate. The material properties and the dimensions of the plate are indicated in Figure 5.17.

Six meshes were used in the analysis. Such meshes present 12, 48, 108, 192, 300, 432 elements. In this analysis, the finite elements present square shape, dividing the problem area equally e.g. for the mesh with 12 elements, the problem area is divided in 12 equal squares.

Figure 5.18 shows the curves of displacement vs. reaction-force at point A. The last two curves, i.e. those corresponding to the meshes with 300 and 432 elements, are presented in Figure 5.19. These figures show the convergence of the analysis for this example. Finally, Figure 5.20 shows the final configuration for the meshes with 108, 192, 300 and 432 elements, presenting also the localisation bands distribution.

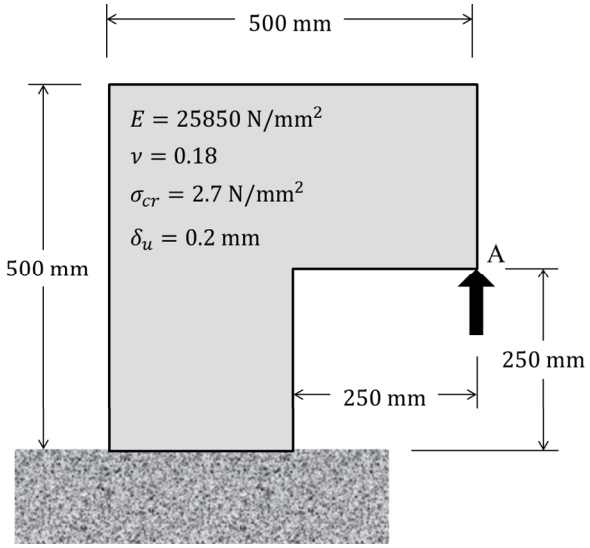

Figure 5.17 – L-shaped plate: geometry, material properties and boundary conditions.

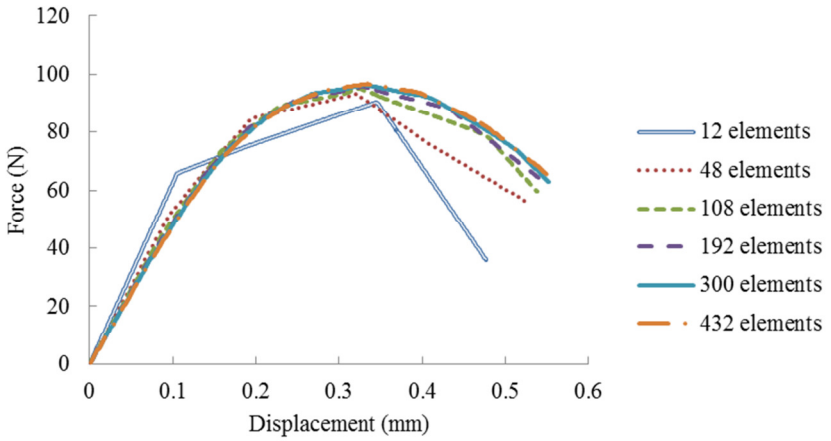

Figure 5.18 – Displacement vs. force for the adopted meshes.

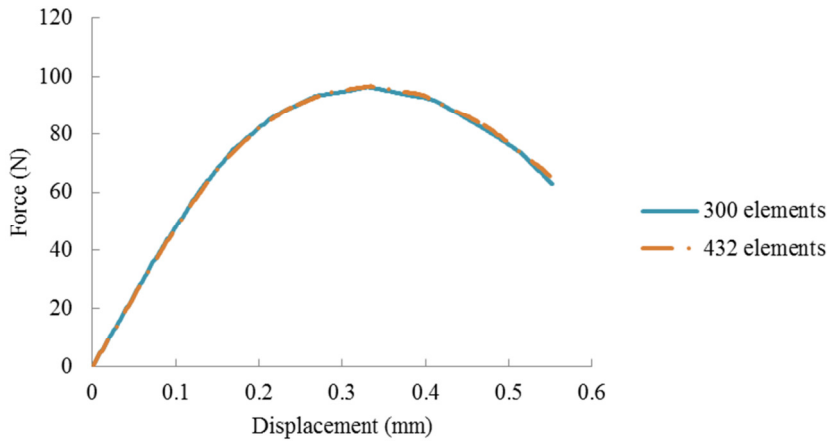

Figure 5.19 – Displacement vs. force for meshes with 300 and 432 elements.

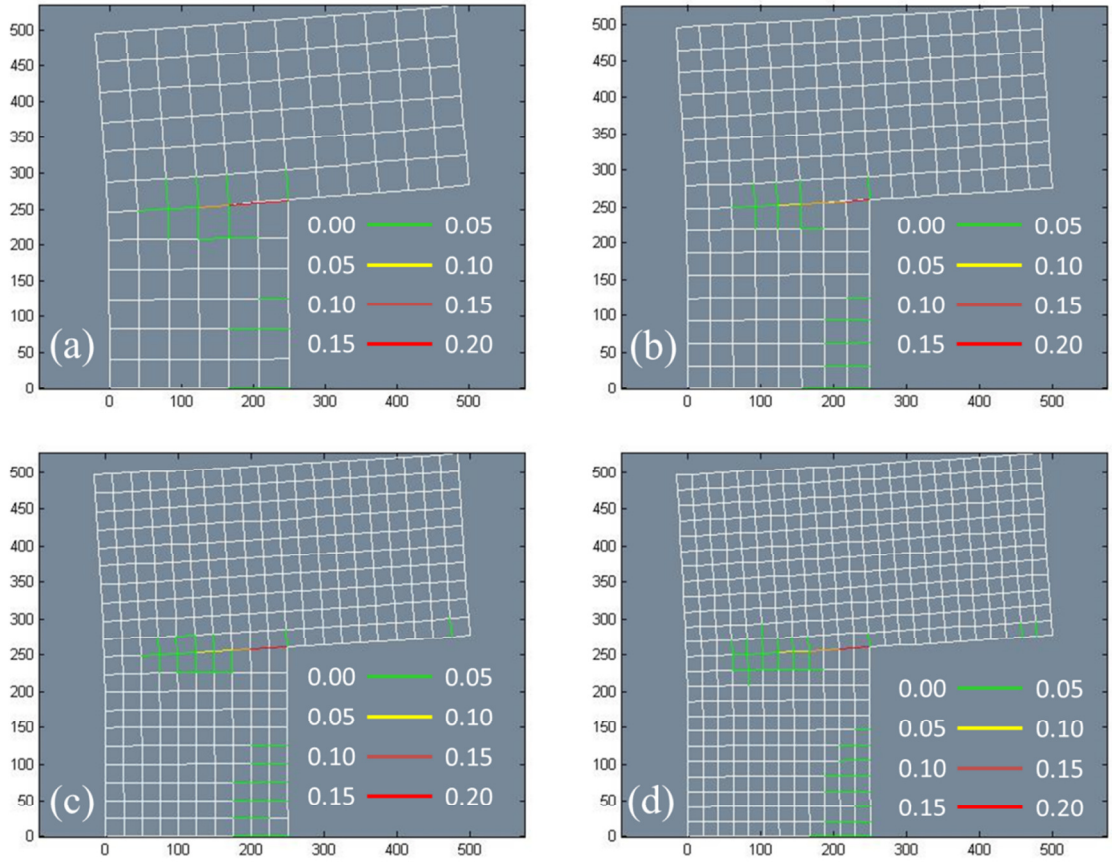

Figure 5.20 – L-shaped plate: deformed shape and localisation bands for meshes with (a) 108, (b) 192, (c) 300 and (d) 432 elements.

Considering this numerical example, it can be affirmed that the proposed lumped damage model presents objectivity i.e. the model is refinement- or size-independent. Note that, in Figure 5.18, as finer meshes are used, the numerical modelling appears to reach a unique solution. In Figure 5.20 the localisation bands in the four finer meshes simulations present a similar pattern. The critical bands appear near to the inner corner. However, some diffuse bands nucleate especially near to the base of the specimen. These bands present small thickness (from 10^{-6} to 10^{-3} at the end of the analysis), being negligible to the specimen collapse. The limitations of the proposed model are discussed in the next section.

5.4 Limitations of the proposed models and perspective for future works

Both lumped damage models for bending and tensile plates show great potentiality, leading to size-independent solutions. Although the simplicity of the examples, the results

presented in this chapter already prove the feasibility of the approach and justifies further efforts in this direction. The advantages with respect to other approaches in terms of simplicity and physical correctness might be important. However, some limitations must be highlighted in order to suggest improvements for further works.

Considering the lumped damage model for bending plates, the collapse mechanism coincides with the sides of the elements. Once the hinge-lines can appear only at the sides of the elements, the mesh was deliberately chosen to ensure such coincidence. Obviously, another mesh with distorted elements could force the model to find another solution close to the expected one. However, such modelling would only present some kind of distortion limit for the mesh, which would be only applicable to the analysed meshes. Therefore, instead of this simplistic observation, it is preferable to suggest the modelling of arbitrary hinge-lines, allowing their appearance inside the finite element. The use of other finite elements is also suggested.

Regarding the lumped damage model for tensile plates, the abovementioned observations about hinge-lines are applicable to the localisation bands, as well as the ones about element types. The formulation and implementation of other damage laws are also suggested, in order to reproduce, numerically, experimental observations.

6 CONCLUSIONS

This thesis presents some original contributions on the Lumped Damage Mechanics (LDM) framework. These contributions are here characterised in four categories, being three advances in frame structures and one for continuum media:

i. LDM for reinforced concrete arches;
ii. LDM for unreinforced concrete structures;
iii. LDM for high cycle fatigue analysis;
iv. LDM for continuum media (or extended LDM).

Note that, before this work, the great majority of models based on LDM presented solutions for reinforced concrete (RC) frames and just a few studies introduced LDM models to analyse local buckling in steel frames. As discussed in the main body of the text, the modelling of structures using LDM associates an internal variable for each inelastic phenomenon. Regarding RC structures, the main inelastic phenomena are concrete cracking and steel yielding; then, respectively, damage variables and plastic deformations account for those inelastic phenomena.

So far, the application of LDM models was limited to straight frames. Therefore, the first original development of this thesis was the modelling of RC arches using LDM. The main objective was the analysis of circular RC structures, such as arch bridges and tunnels. The comparison between the proposed formulation and experimental results showed the accuracy of the LDM for RC arches. In such comparisons, the main observations are the use of the classic theory of reinforced concrete and the damage localisation. The classic theory of reinforced concrete is used to calculate the model parameters, which is preferable for practical applications. In an analysed case, the model correctly represented the softening phase, which was due to localisation of inelastic phenomena. Such important observation depicts the capability of the proposed procedure. Still, it is noteworthy that this first development also illustrates how to introduce finite elements with complex geometries in the LDM framework.

The second original contribution is the LDM model for unreinforced concrete structures, or any kind of quasi-brittle materials. Once there is no reinforcement, the main inelastic phenomenon is the concrete cracking, which is modelled by damage variables. The quasi-brittle behaviour is reproduced by the damage evolution law. A special logarithm, known as Lambert W function, is used in the damage evolution law. Such LDM model

accurately represents the quasi-brittle behaviour of unreinforced concrete structures. As a main crack leads the cross section collapse, the damage variable is directly related to the Crack Opening Displacement (COD). Therefore, the COD estimated via LDM presents suitable results in comparison with experimental responses and fracture mechanics analyses. Despite the good accuracy, the model parameter has not a well-defined physical meaning. Therefore, further theoretical and experimental studies should be carried out in order to present a better physical meaning of the model parameter, or, at least, any kind of relation with the material properties.

It is noteworthy that the LDM model for unreinforced concrete structures were also utilised to analyse masonry arches. Such particular type of structure is standard for historic construction in the western civilisation. Therefore, the analysis and behaviour prediction is extremely important. The main assumption to apply the aforementioned LDM model is that the only inelastic phenomenon is mortar cracking. This is not entirely true, but the numerical modelling showed that this is a reasonable approximation for the analysed problems. Further developments on LDM to analyse historic constructions are here suggested as a research frontier.

The third original contribution is the modelling of structures under high cycle fatigue using LDM. Such contribution concludes the development of LDM models for frame structures. The objective was the simplified modelling of high cycle fatigue in complex structures, such as offshore platforms and aeroplanes. This LDM model was formulated to analyse single crack propagation by a damage variable, as the one for unreinforced concrete. However, instead of propose a new damage evolution law any classic fatigue law could be used. Note that the damage variable is easily related to the stress intensity factors through fracture mechanics concepts. Both bending and axial damage models were proposed, achieving accurate results.

It is noteworthy that the original developments in LDM for frame analysis are based in the same principles of fracture and damage mechanics. As discussed in the text, in a structural analysis, data input and transformation of numerical results into engineering decisions are human activities. LDM simplifies both jobs considerably. The evaluation of damage distribution maps, as the one presented in Figure 4.10, becomes an easy and straightforward task, therefore reducing the possibility of human errors. All proposed frame models can be incorporated in conventional nonlinear structural analysis programmes simply as new finite elements.

In this thesis, the LDM formulation for frame structures was applied to the analysis of beams, plane frames, arches and rings subjected to monotonic loadings or fatigue. The generalisation to the tri-dimensional case is very important in the context of the potential applications of the theory. This task has been carried out successfully in the case of reinforced concrete structures subjected to monotonic loadings or ultra-low cycle fatigue (BAI et al., 2016). Basically, the idea consists in introducing vector measures of damage in the hinges with the corresponding generalisation of the damage evolution laws. The components of these vectors are the damage parameters in the two principal directions of the cross section. The analysis of tri-dimensional structures under high cycle fatigue may be accomplished adopting the same ideas; however, the experimental validation and the evaluation of the precision of such a procedure must be done.

Once LDM models for frame structures are based on the same general ideas, it is therefore possible to simulate the effect that high cycle fatigue has on the structural behaviour under an extreme event such as an earthquake, impact or explosion; and this analysis can be carried out for the entire industrial facility, airframe or bridge. Taken into account the inherently random character of the phenomenon, the use of probabilistic technics is indispensable; LDM appears to be an ideal approach for this kind of procedures.

The coupling with other, non-structural, degrading phenomena, such as corrosion would also be very important for practical applications. Even if this subjected remains an open problem in the framework of LDM, it can be expected that the already established procedures may be successfully adapted to the theory. Therefore, LDM may become a useful tool for the assessment and retrofitting projects of ageing infrastructures. In general terms, the number and significance of the practical applications of LDM can be important.

Finally, the fourth original contribution is the modelling of continuum media with LDM. This new branch of LDM framework was here named as extended lumped damage mechanics (XLDM). In this thesis, the modelling of continuum media through XLDM was limited to bi-dimensional problems, where models for bending and tensile plates were proposed. Regarding bending plates, the XLDM model was clearly inspired in LDM models for beams. In this case, inelastic hinges became inelastic hinge-lines. Therefore, the XLDM finite element was considered as an assemblage of an elastic plate-bending element with inelastic hinge-lines at its sides. Analogously, for tensile plates the XLDM finite element is an assemblage of an elastic plate element with localisation bands at its sides.

The examples (presented chapter 5) show that the XLDM leads to size-independent finite element analysis in plates subjected to plane strain or bending. The formulation is

remarkable for its simplicity, which may also present drawbacks. The element is not very efficient in some cases, especially when a band (or hinge-line) tends to cross diagonally the elements. However, the room for improvements is also significant. Bands do not need to match the sides of the elements and other elements with bands of arbitrary orientation may be imagined. Additionally, the element does not need to have exclusively an elastic behaviour. It can be elastic-plastic and/or it can even exhibit continuum damage. Of course, after detection of localisation, damage should be made to concentrate exclusively in the bands as in the presented formulation.

In the XLDM element for tensile plates presented in this thesis, bands are loaded on mode I. But, this does not need to be a limitation of the formulation neither. A more complex formulation involving mode II could also be considered.

Lastly, the extension to the tri-dimensional case could be remarkably simple, opening a significant number of new applications. The results presented in this thesis already prove the feasibility of the approach and justifies further efforts in this direction. The advantages with respect to other approaches in terms of simplicity and physical correctness might be important.

Despite the limitations of XLDM models proposed here, a significant step into the characterisation of LDM as a general theory, such as fracture and damage mechanics, was given in this thesis.

REFERENCES

AHMED, A.; BAKUCKAS Jr., J. G.; AWERBUCH, J.; LAU, A. C.; TAN, T.-T. Fatigue Testing of a Stiffened Lap Joint Curved Fuselage Structure. **Journal of Aircraft**, v. 44, n. 03, p. 750-757, 2007.

ALLMAN, D. J.; MORLEY, L.S.D. The 'constant' bending moment three-noded triangle. **Comunications in Numerical Methods in Engineering**, v. 16, p. 733-741, 2000.

ALVA, G. M. S. **Estudo teórico-experimental do comportamento de nós de pórtico de concreto armado submetidos a ações cíclicas**. 2004. 218 p. Thesis (Doctorate) – São Carlos School of Engineering, University of São Paulo, São Carlos, 2004.

ALVA, G. M. S.; EL DEBS, A. L. H. C. Application of lumped dissipation model in nonlinear analysis of reinforced concrete structures. **Engineering Structures**, v. 32, p. 974-981, 2010.

ÁLVARES, M. S. **Contribuição ao estudo e emprego de modelos simplificados de dano e plasticidade para a análise de estruturas de barras em concreto armado**. 1999. 123 p. Thesis (Doctorate) – São Carlos School of Engineering, University of São Paulo, São Carlos, 1999.

AMORIM, D. L. N. F.; PROENÇA, S. P. B.; FLÓREZ-LÓPEZ, J. A model of fracture in reinforced concrete arches based on lumped damage mechanics. **International Journal of Solids and Structures**, v. 50, n. 24, p. 4070-4079, 2013.

AMORIM, D. L. N. F.; PROENÇA, S. P. B.; FLÓREZ-LÓPEZ, J. Simplified modeling of cracking in concrete: application in tunnel linings. **Engineering Structures**, v. 70, p. 23-35, 2014a.

AMORIM, D. L. N. F.; PROENÇA, S. P. B.; FLÓREZ-LÓPEZ, J. Lumped damage mechanics as an alternative to analyse masonry arches. In: International Workshop by Young Researchers for 'Application of Structural Engineering and Structural Health Monitoring to Historic Buildings', 2014, Kyoto. **Proceedings…** Uji: Kyoto University, 2014b. p. 19-25.

ANDERSON, T. L. **Fracture Mechanics**: Fundamentals and Applications. CRC Press, Boca Raton, 2005.

ANDREAUS, U.; BARAGATTI, P. Fatigue crack growth, free vibrations, and breathing crack detection of aluminium alloy and steel beams. **Journal of Strain Analysis**, v. 44, p. 595-608, 2009.

ARAÚJO, F. A. **Formulação de um modelo de dissipação concentrada para a análise não linear de estruturas reticuladas planas em concreto armado**. 2007. 232 p. Thesis (Doctorate) – São Carlos School of Engineering, University of São Paulo, São Carlos, 2007.

ARAUJO, F., PROENÇA, S.P.B. Application of a lumped dissipation model to reinforced concrete structures with the consideration of residual strains and cycles of hysteresis. **Journal of Mechanics of Materials and Structures**, v. 03, p. 1011-1031, 2008.

ARMERO, F.; Ehrlich, D. Finite element methods for the multi-scale modeling of softening hinge lines in plates at failure. **Computer Methods in Applied Mechanics and Engineering**, v. 195, p. 1283-1324, 2006.

AVÓN, D. T. **Un algoritmo para mejorar la convergencia de problemas no lineales en mecánica de sólidos**. 2002. 139 p. Dissertation (Master) – University of Los Andes, Mérida, 2002.

BAI Y., KURATA M., FLÓREZ-LÓPEZ J., Nakashima M. Model for fatigue crack propagation and closure in steel beams subjected to non-stationary loading. **Journal of Structural Engineering (ASCE)**, Forthcoming, 2016.

BASILIO SÁNCHEZ, I. **Strengthening of arched masonry structures with composite materials**. 2007. 232 p. Thesis (Doctorate) – Department of Civil Engineering, University of Minho, Guimarães, 2007.

BAŽANT, Z. P.; JIRÁSEK, M. Nonlocal integral formulations of plasticity and damage: survey of progress. **Journal of Engineering Mechanics (ASCE)**, v. 128, n. 11, p. 1119-1149, 2002.

BAŽANT, Z. P.; LIN, F.-B. Nonlocal smeared cracking model for concrete fracture. **Journal of Structural Engineering**, v. 114, n. 11, p. 2493-2510, 1988.

BELYTSCHKO, T.; Fish, J.; Engelmann, B. A finite element with embedded localization zones. **Computer Methods in Applied Mechanics and Engineering**, v. 70, p. 59-89, 1988.

BORJA, R. A finite element model for strain localization analysis of strongly discontinuous fields based on standard Galerkin approximation. **Computer Methods in Applied Mechanics and Engineering**, v. 190, p. 1529-1549, 2000.

BROEK, D. **Elementary engineering fracture mechanics**. Martinus Nijhoff Publishers, Dordrecht. 1984.

CIPOLLINA, A.; LÓPEZ-INOJOSA, A.; FLÓREZ-LÓPEZ, J. A simplified damage mechanics approach to nonlinear analysis of frames. **Computers & Structures**, v. 54, n. 6, p. 1113-1126, 1995.

CLOUGH, R. W.; BENUSKA, K. L.; WILSON, E. L. Inelastic earthquake response of tall buildings. In: THIRD WORLD CONFERENCE ON EARTHQUAKE ENGINEERING, 1965, New Zealand. **Proceedings…** New Zealand National Committee on Earthquake Engineering: v. 11, 1965.

COMI, C.; PEREGO, U. On visco-damage models for concrete at high strain rates. In: COMPLAS 5, 1997, Barcelona, Spain, **Proceedings…** Barcelona: IACM, 1997. p. 17-20.

COMI, C.; RIZZI, E. On bifurcation in local and nonlocal materials with tension and compression damage. In: ECCOMAS, 2000, Barcelona, Spain, **Proceedings…** Barcelona: ECCOMAS, 2000. p. 1-20.

COMI, C.; PEREGO, U. Fracture energy based bi-dissipative damage model for concrete. **International Journal of Solids and Structures**, v. 38, p. 6427-6454, 2001.

CORLESS, R. M.; GONNET, G. H.; HARE, D.E.G.; JEFFREY, D.J.; KNUTH, D.E. On the Lambert W function. **Advances in Computational Mathematics**, v. 05, p. 329-359, 1996.

DESMORAT, R.; GATUINGT, F.; RAGUENEAU, F. Nonlocal anisotropic damage model and related computational aspects for quasi-brittle materials. **Engineering Fracture Mechanics**, v. 74, n. 10, p. 1539-1560, 2007.

FALEIRO, J.; OLLER, S.; BARBAT, A.H. Plastic-damage analysis of reinforced concrete frames. **Engineering Computations**, v. 27, p. 57-83, 2010.

FERREIRA, C. C. **Inspeção de equipamentos: estudo de casos:** Caso 050: Fratura Frágil dos Navios Classe LIBERTY (1941/1945). [S.I.]: 2013. Available in: <http://inspecaoequipto.blogspot.com.br/2013/11/caso-050-fratura-fragil-dos-navios.html> Accessed in: Dec. 17th, 2015.

FLÓREZ-LÓPEZ, J. Modelos de daño concentrado para la simulación numérica del colapso de pórticos planos. **Revista Internacional de Métodos Numéricos para Cálculo y Diseño en Ingeniería**, v. 09, n. 02, p. 123-139, 1993.

FLÓREZ-LÓPEZ, J. Simplified Model of Unilateral Damage for RC Frames. **Journal of Structural Engineering**, v. 121, n. 12, p. 1765-1772, 1995.

FLÓREZ-LÓPEZ, J.; MARANTE, M. E; PICÓN, R. A. **Fracture and Damage Mechanics for Structural Engineering of Frames**: State-of-the-Art Industrial Applications. IGI Global, Hershey. 2015.

FLÓREZ-LÓPEZ, J.; PROENÇA, S. P. B. A curvilinear frame element with plastic hinges. In: INTERNATIONAL SYMPOSIUM ON SOLID MECHANICS, 2013, Porto Alegre. **Proceedings**… Porto Alegre: 2013. p. 1-11.

GDOUTOS, E. E. **Fracture Mechanics**: An Introduction. Springer, Norwell. 2005.

GRIFFITH, A. A. The phenomena of rupture and flow in solids. **Philosophical Transactions of the Royal Society of London A**, v. 221, p. 163-198, 1921.

GRIFFITH, A. A. The theory of rupture. In: FIRST INTERNATIONAL CONGRESS OF APPLIED MECHANICS, 1924, Delft. **Proceedings**… Delft: 1924, p. 55-63.

INGLIS, C. E. Stress in a plate due to the presence of cracks and sharp corners. **Transactions of the Institute of Naval Architects**, v. 55, p. 219-230, 1913.

IRWIN, G. R. Analysis of Stresses and Strains Near the End of a Crack Traversing a Plate. **Journal of Applied Mechanics**, n. 24, p. 361-364, 1957.

KACHANOV, L. M. Time of the rupture process of nonlinear solid mechanics. **Otdeleniye Technicheskikh Nauk**, v. 08, p. 28-31, 1958.

KAEWKULCHAI, G.; WILLIAMSON, E. B. Beam element formulation and solution procedure for dynamic progressive collapse analysis. **Computers and Structures**, v. 82, p. 639-651, 2004.

KIM, K. D. **Development of analytical models for earthquake analysis of steel moment frames**. 2007. 216 p. Thesis (Doctorate) – University of Texas at Austin, Austin, 2007.

KIRSCH, G. Die Theorie der Elastizitat and die Bediirfnisse der Festigkeitslehre. **Z. Vereines Deutscher Ing.**, v. 42, p. 797-807, 1898.

KOSOLOV, G. V. On the application of complex function theory to a plane problem of the mathematical theory of elasticity. **Yuriev Publ. Co.**, 1909.

LEMAITRE, J.; CHABOCHE, J.-L. **Mécaniques des matériaux solides**. Dunod, Paris. 1985.

LIU, Y.-B., LIU, J.-B. A damage beam element model for nonlinear analysis of reinforced concrete member. **Journal of Earthquake Engineering and Engineering Vibration**, v. 24, n. 02, p. 95-100, 2004.

MARANTE, M. E.; FLÓREZ-LÓPEZ, J. Three-Dimensional Analysis of Reinforced Concrete Frames Based on Lumped Damage Mechanics. **International Journal of Solids and Structures**, v. 40, n. 19, p. 5109-5123, 2003.

MARIGO, J. J. Modelling of brittle and fatigue damage for elastic material by growth of microvoids. **Engineering Fracture Mechanics**, v. 21, n. 4, p. 861-874, 1985.

MANZOLI, O.; OLIVER, X.; CERVERA, M. **Localización de Deformaciones: Análisis y Simulación Numérica de Discontinuidades en Mecánica de Sólidos**. CIMNE, Barcelona. 1998.

MORLEY, L. S. D. The constant-moment plate-bending element. **Journal of Strain Analysis**, v. 06, n. 01, p. 20-24, 1971.

MULAS, M. G.; FILIPPOU, F. C. Analytical Procedures in the Study of Seismic Response of Reinforced Concrete Frames. **Engineering Structures**, v. 12, p. 37-48, 1990.

PALANINATHAN, J. R.; CHANDRASEKHARAN, P. S. Curved beam element stiffness matrix formulation. **Computers and Structures**, v. 21, p. 663-669, 1985.

PARIS, P. C.; GOMEZ, M. P.; ANDERSON, W. P. A rational analytic theory of fatigue. **The Trend in Engineering**, v. 13, p. 9-14, 1961.

PARIS, P. C.; ERDOGAN, F. A critical analysis of crack propagation laws. **Journal of Basic Engineering**, v. 85, p. 528-534, 1963.

PEERLINGS, R. H. J.; de BORST, R.; BREKELMANS, W. A. M.; de VREE, J. H. P.; SPEE, I. Some observations on localisation in non-local and gradient damage models. **European Journal of Mechanics: A/solids**, v. 15, n. 06, p. 937-953, 1996.

PERDOMO, M. E.; RAMÍREZ, A.; FLÓREZ-LÓPEZ, J. Simulation of damage in RC frames with variable axial force. **Earthquake Engineering and Structural Dynamics**, v. 28, p. 311-328, 1999.

PERDOMO, M. E.; PICÓN, R.; MARANTE, M. E.; HILD, F.; ROUX, S.; FLÓREZ-LÓPEZ, J. Experimental analysis and mathematical modeling of fracture in RC elements with any aspect ratio. **Engineering Structures**, v. 46, p. 407-416, 2013.

PERERA, R.; CARNICERO, A.; ALARCON, E.; GOMEZ, S. A fatigue damage model for seismic response of RC structures. **Computers and Structures**, v. 78, p. 293-302, 2000.

POWELL, H.G. Theory for nonlinear elastic structures. **Journal of the Structural Division**, ASCE, v. 95, ST12, p. 2687-2701, 1969.

RABOTNOV, Y. N. Creep rupture, In: Hetényi, M.; Vincenti, W. G. Proceedings of the Twelfth International Congress of Applied Mechanics, 1968, Berlin. **Proceedings**… Berlin: Springer-Verlag, 1968, p. 342–349.

RICHARD, B.; RAGUENEAU, F. Continuum damage mechanics based model for quasi-brittle materials subjected to cyclic loadings: formulation, numerical implementation and applications. **Engineering Fracture Mechanics**, v. 98, p. 383-406, 2013.

RIVA, P.; COHN, M. Z. Engineering approach to nonlinear analysis of concrete structures. **Journal of Structural Engineering ASCE**, v. 116, p. 2162-2186, 1990.

SANTORO, M.; KUNNATH, S. Damage-based RC beam element for nonlinear structural analysis. **Engineering Structures**, v. 49, 2013, p. 733-742.

SILVA J. L. **Análise de tubos circulares de concreto armado para o ensaio de compressão diametral com base na teoria de confiabilidade**. 2011. 154 p. Thesis (Doctorate) – São Carlos School of Engineering, University of São Paulo, São Carlos, 2011.

TAKEDA, T.; SOZEN, M. A.; Nielsen, N. N. Reinforced concrete response to simulated earthquakes. **Journal of the Structural Division**, ASCE, v. 96, ST12, p. 2557-2573, 1970.

TECHCON. **Estruturas Metálicas**. [S.I.]: 2015. Available in: <http://idcomercial.com.br/sites/admin/000339/arquivos/images/Estrutura%20Offshore.jpg> Accessed in: Sep. 26th, 2015.

TOI, Y.; HASEGAWA, K.H. Element-size independent, elasto-plastic damage analysis of framed structures using the adaptively shifted integration technique. **Computers and Structures**, v. 89, p. 2162-2168, 2011.

TWI-GLOBAL. **Static strength of cracked tubular joints**: Case study 112. [S.I.]: 2013. Available in: <http://www.twi-global.com/EasysiteWeb/getresource.axd?AssetID=11536&type=full&servicetype=Inline> Accessed in: Sep. 26th, 2015.

UZCATEGUI, M., 2012. **Desarrollo de un programa de elementos finitos tridimensional basado en la web**. 2012. 250 p. Thesis (Doctorate) – University of Los Andes, Mérida, 2012.

APPENDIX A - Interaction diagrams for reinforced concrete

The main objective of this appendix is to introduce the interaction diagrams for reinforced concrete (RC). Since this theme is used in the modelling of RC frame structures (FLÓREZ-LÓPEZ; MARANTE; PICÓN, 2015), initially the main concepts regarding plastic hinges are briefly presented.

The plastic hinge

Consider a simply supported beam constituted by a homogeneous material and bi-symmetric cross section (Figure A.1a). As the applied force increases, at some point the maximum bending moment m exceeds the plastic threshold, or plastic moment, M_p although m still smaller than the collapse limit, or ultimate moment, M_u (Figure A.1b). As a result, plastic strains occur where the bending moment exceeded M_p (Figure A.1a). The resulting curvature distribution is depicted in Figure A.1c. Note that, at the mid-section, $\chi \to \infty$ while $m \to M_u$ (Figure A.1c). The exact moment-curvature response for this structure is given in Figure A.2.

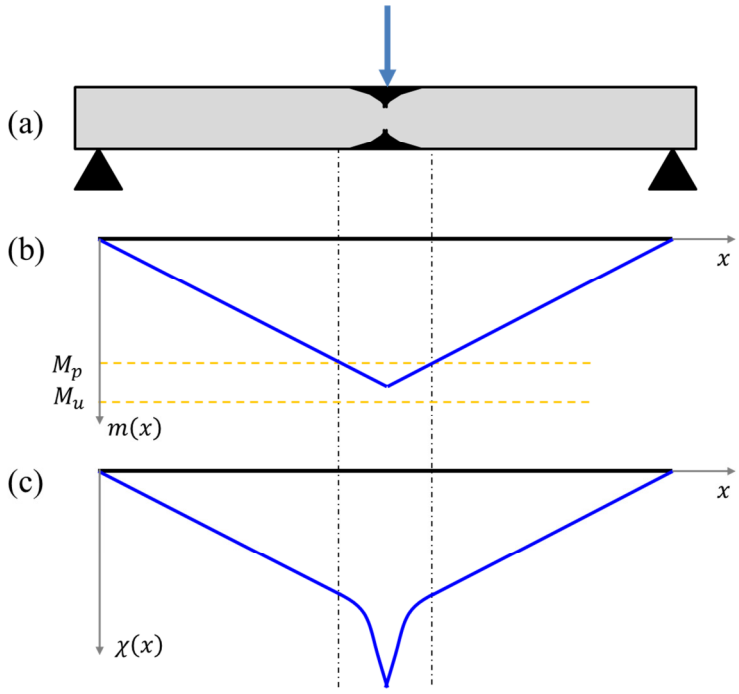

Figure A.1 – Simply supported beam: (a) plastic zone distribution in the beam; (b) bending moment distribution across the beam; (c) curvature distribution across the beam.

The exact response of this problem can be simplified by considering a plastic hinge located at the mid-span of the beam. For the sake of simplicity, the elastic-plastic moment-curvature relationship is considered elastic-perfectly plastic. Then, for a given cross section, if the yield threshold M_y is reached, the cross section yields entirely. Therefore, M_y is usually taken as M_p or M_u (Figure A.2). For a detailed discussion about plastic hinges, see Flórez-López, Marante and Picón (2015).

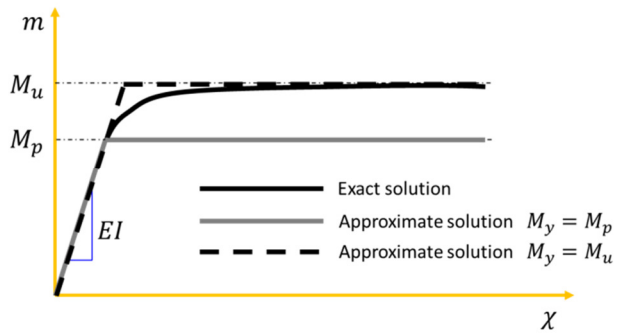

Figure A.2 – Moment-curvature at the mid-section of the beam.

Now, an academic example is presented in order to apply the plastic hinge concept. Consider the beam depicted in Figure A.3a, where L is its total length and P is the applied load. The deflection along the beam is represented by $w(x)$ and:

$$\begin{aligned} \theta(x) &= -\frac{dw}{dx} \\ m(x) &= EI\chi(x) = EI\frac{d^2w}{dx^2} \\ V(x) &= \frac{dm}{dx} = EI\frac{d^3w}{dx^3} \\ p_0(x) &= \frac{dV}{dx} = EI\frac{d^4w}{dx^4} \end{aligned} \tag{A.1}$$

being EI the flexural stiffness, $\theta(x)$ the total rotation of the cross section, $m(x)$ the bending moment, $\chi(x)$ is the curvature distribution, $V(x)$ is the shear force and $p_0(x)$ is the load distribution along the beam.

Since the only external force is P the load distribution is given by:

$$p_0(x) = -\delta_D\left(x - \frac{L}{4}\right)P \tag{A.2}$$

where $\delta_D(\quad)$ is the Dirac delta function.

The deflection along the beam $w(x)$ is obtained by the solution of an ordinary differential equation, where the boundary and initial conditions are:

$$w(0) = 0 \quad \theta(0) = 0 \quad w(L) = 0 \quad m(L) = 0 \quad w(L/2) = 0 \tag{A.3}$$

In the analysis, the elastic limit is reached in the first step (Figure A.3b) i.e. the absolute value of $m(0)$ reached the adopted yield moment M_y (Figure A.3d). At this point the first plastic hinge is activated and the beam presents elastic behaviour. Note that the graphs of the bending moment distributions (Figure A.3d) follow the tensioned fibres of the cross sections along the beam.

Another plastic hinge is activated in the second step (Figure A.3b). As the analysis reach the second step, the plastic rotation of the first hinge evolves (Figure A.3c). The difference between both responses (black and blue curves in Figure A.3c-d) is still small.

The next step of the analysis consists in the activation of the third hinge. Since the beam is two times hyperstatic, the evolution of plastic rotations at the third hinge will turn the beam in a mechanism. Therefore, the maximum value of P is then reached. Note that the plastic rotations of hinges 1 and 2 just reached their maximum value (Figure A.3c). From now on, while the deflection w_P increases (point 4 in Figure A.3b), P remains constant and the plastic rotation of the third hinge $\theta^p(L/2)$ evolves. If $\theta^p(L/2)$ reaches its maximum value, the structure turns into a hypostatic system.

Note that, at the end of the analysis the total rotation along the beam $\theta(x)$ presents discontinuities characterised by the plastic rotations at the hinges.

This example was solved using directly the differential relations for this beam. However, a finite element analysis with plastic hinges could be carried out. Then, the yield function is:

$$f(m) = |m| - M_y \leq 0 \tag{A.4}$$

and the elastic domain is given for $f(m) < 0$ i.e. $-M_y < m < M_y$.

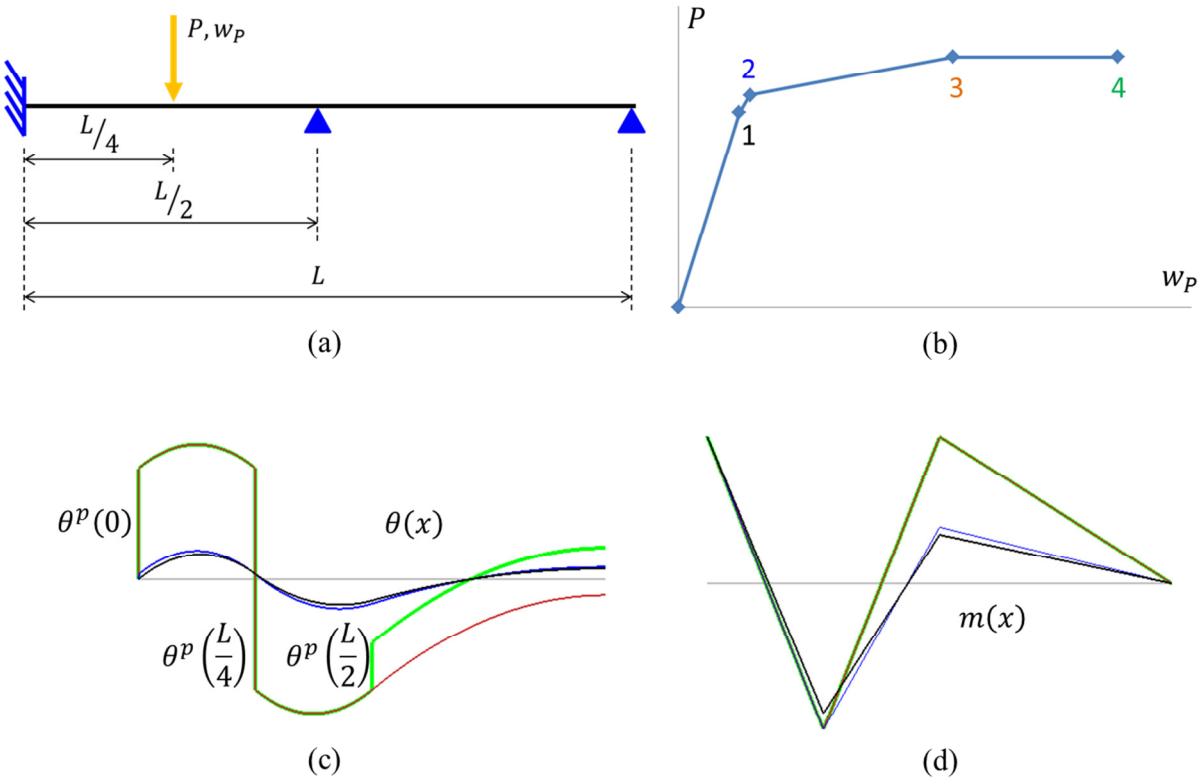

Figure A.3 – Academic problem: (a) geometry; (b) load-deflection response; (c) total rotation distribution; (d) bending moment distribution.

On the other hand, for frame structures the plastic hinge may present plastic rotations and plastic elongations. Considering a rectangular cross section and linear stress and strain distribution, the yield function results (FLÓREZ-LÓPEZ; MARANTE; PICÓN, 2015):

$$f(m,n) = \frac{|m|}{M_y} + \left(\frac{n}{N_y}\right)^2 - 1 \leq 0 \tag{A.5}$$

where n is the axial force in the cross section and N_y is the axial force that produces the total plasticisation of the cross section.

Now, the elastic domain and the yield surface are presented in Figure A.4. Note that the evolution of the internal variables, plastic rotation (θ^p) and plastic elongation (Δ^p), is

given by a normality rule (Figure A.4). If other type of cross section is considered, the yield function changes, which leads to a modification on the shape of the yield surface.

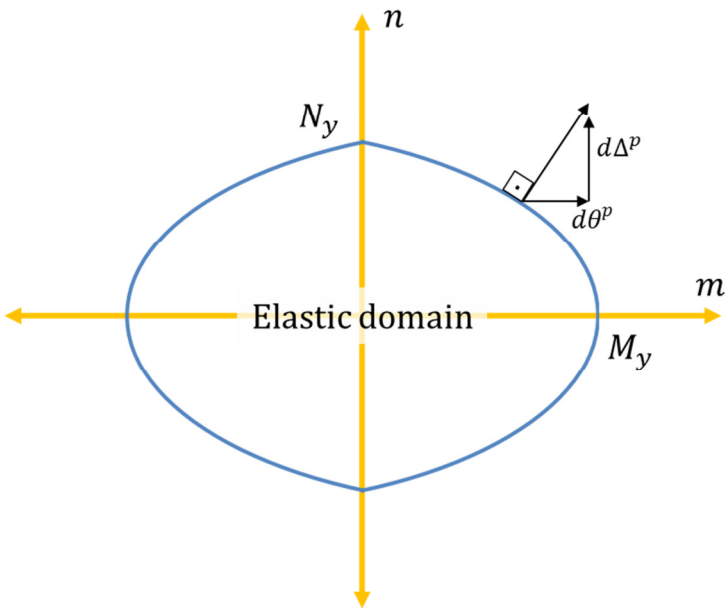

Figure A.4 – Yield surface, elastic domain and normality rule for a rectangular cross section.

So far, a perfectly plastic behaviour was assumed to analyse structures composed by a homogenous material. If an isotropic or a kinematic yield function is adopted, the modelling of steel structures is possible with accurate results. However, RC structures are composed by two materials: steel bars and concrete.

Reinforced concrete: behaviour of the materials

In conventional buildings, the RC beams and columns usually present rectangular cross sections. Then, consider a rectangular concrete cross section $\mathrm{b} \times \mathrm{h}$ (Figure A.5) reinforced by longitudinal and transversal steel. Internal forces are equilibrated by stresses in the cross section. Most of compression stresses are supported by the concrete; longitudinal and transversal reinforcements mainly support, respectively, tension and shear forces.

Since tension stresses in RC structures usually occur due to bending, the longitudinal reinforcement is positioned near to the faces of the cross section (Figure A.5). The longitudinal reinforcement areas $\mathrm{A_s}$ and $\mathrm{A'_s}$ support tension and compression (in part) stresses, respectively. The values d and $\mathrm{d'}$ are distances of tensioned ($\mathrm{A_s}$) and compressed

(A'_s) reinforcements to the most compressed fibre. The transversal reinforcement, usually constituted by stirrups, support shear forces and keep the longitudinal steel in place during the construction. For rectangular cross sections, stirrups usually present hoop shapes.

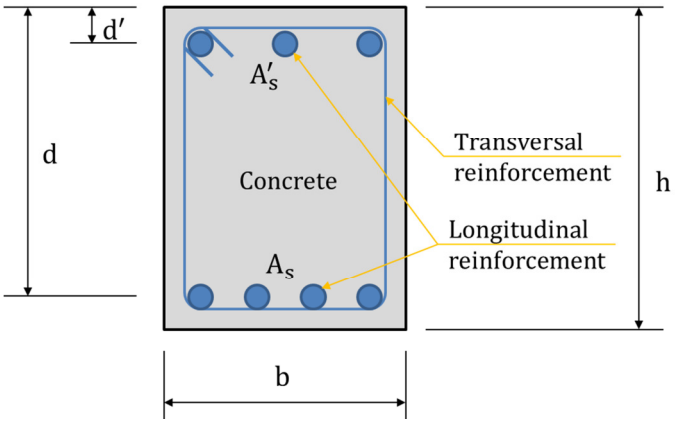

Figure A.5 – Typical cross section of a reinforced concrete element.

The concrete compressive strength (f'_c) is measured by the standard compression test, where concrete cylinders at the age of 28 days are subjected to axial loads up to collapse in a compression-test machine. Then, the compressive strength of the specimen is the ratio between the failure load and the circular cross section. All steps of this test are standardised in code regulations.

The concrete compressive behaviour is precisely measured by nonlinear elastic models. One of the most cited and accurate model was proposed by Hognestad (1951). In such model (Figure A.6), $f_c = -\sigma$ is the compression stress and $\varepsilon_c = -\varepsilon$ is the compression strain. Note that, in the Hognestad (1951) model, the maximum compression stress f''_c is different from cylinder strength f'_c due to the specimen geometry and the strain rate applied during the test. Generally the maximum compression stress f''_c is taken as $0.85f'_c$ for usual concretes in practical applications. Up to $0.5f''_c$ the compressive behaviour is almost linear. From $0.5f''_c$ to f''_c a parabolic behaviour is assumed. At the maximum compression stress f''_c the concrete presents a strain value ε_0 which is almost constant ($2‰$) for usual concretes. The failure deformation ε_{cu} usually takes value from $3‰$ to $4‰$ depending on the concrete resistance.

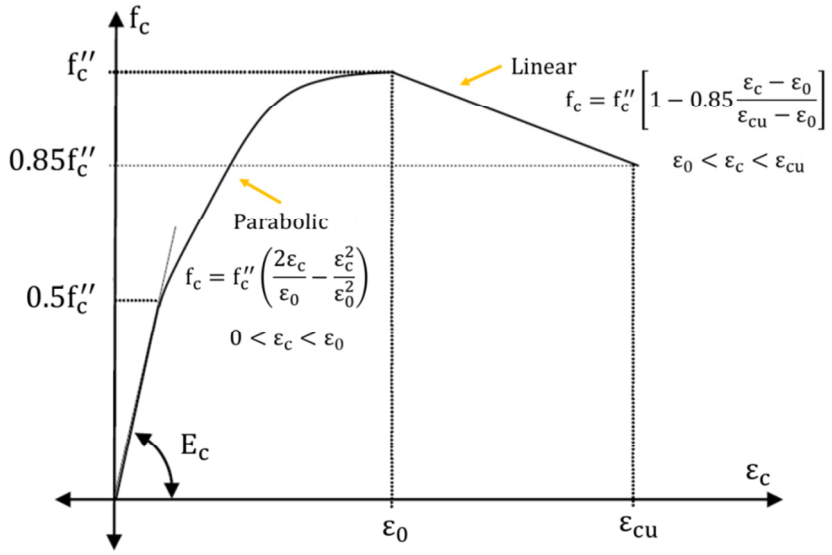

Figure A.6 – Stress-strain curve proposed by Hognestad (1951).

The elasticity modulus E_c is usually calculated by empirical equations given in code regulations, such as the ACI 318-05 (ACI, 2005) and the NBR 6118:2014 (ABNT, 2014). In these calculations, E_c is estimated by the cylinder strength (f_c'), which is given in MPa in codes that use SI units (ABNT, 2014) or in psi in those that still use the Imperial System (ACI, 2005).

In practice, the transversal reinforcement may confine the concrete core in the cross section (Figure A.5). For confined concretes, many studies proposed modifications in Hognestad (1951) model, being the Kent and Park (1971) model one of the most used (Figure A.7).

Even neglected during the design, the concrete tension strength is important to determine the cracking process. The concrete tension strength (f_t) is directly measured by a standard direct tension test. However, this test might present execution issues, being susceptible to errors. An alternative is the Brazilian test, where the tension strength is estimated by a diameter compression in standard cylinders. The Brazilian test is simple to execute, once the same materials of the compression test are used, being less susceptible to errors.

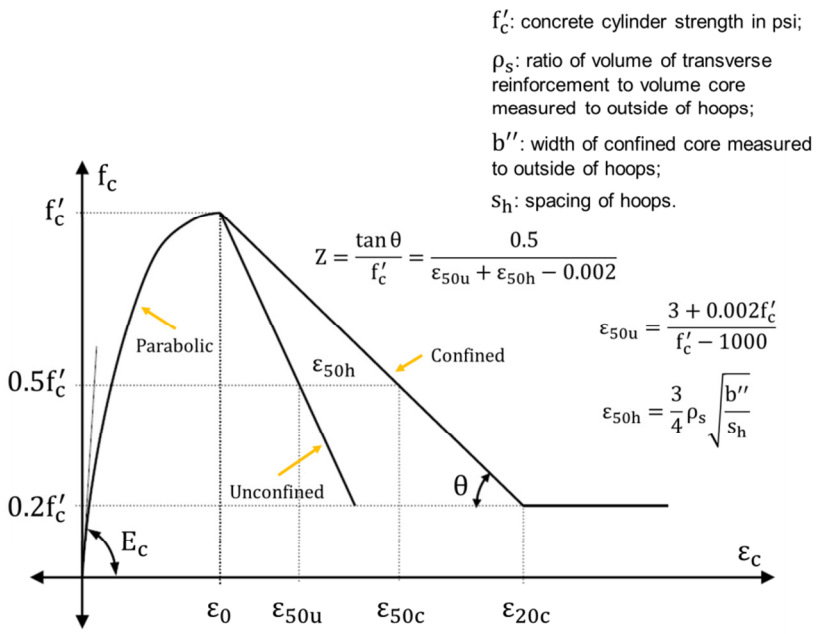

Figure A.7 – Stress-strain curve proposed by Kent and Park (1971).

The steel bars used in reinforced concrete structures present a nonlinear behaviour as shown in Figure A.8. Commonly in the RC theory, the important information from the steel behaviour curve is: yield stress (f_y), yield strain (ε_y), and the ultimate stress (f_{su}).

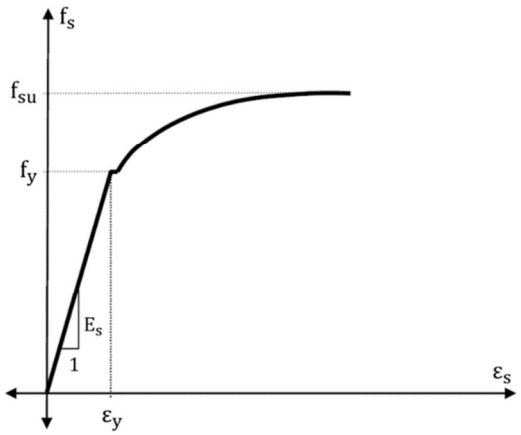

Figure A.8 – Behaviour curve of steel bar.

Computation of the interaction diagrams

The concept of plastic hinge can be applied in RC elements. In the plastic hinge concepts introduced in this appendix only a yield moment was needed to describe the nonlinear behaviour of a structural element, as the beam in the academic example. For elements subjected to bending moment and axial force, the concept of yield surface (Figure

A.4) was briefly introduced. This leads to a moment-curvature relation that depends on the axial force. However, an accurate description of RC elements require a more sophisticated moment-curvature (-rotation) relation. A possibility is presented in Figure A.9. Such curve is described by four properties of an RC cross section: first cracking moment (M_{cr}), plastic moment (M_p), ultimate moment (M_u) and ultimate plastic rotation (ϕ_u^p). Such quantities depend on the axial force, being presented then by interaction diagrams (Figure A.10).

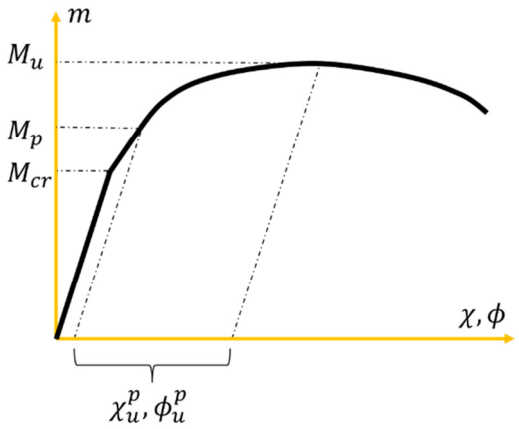

Figure A.9 – Constitutive model for RC elements.

For a cross section, an interaction diagram is constructed using at least four conditions: pure compression, pure tension, pure bending and maximum bending resistance (balanced conditions). Note that the interaction diagrams can present more points if the analyst considers necessary, and these points should be joined by straight lines as presented in Figure A.10.

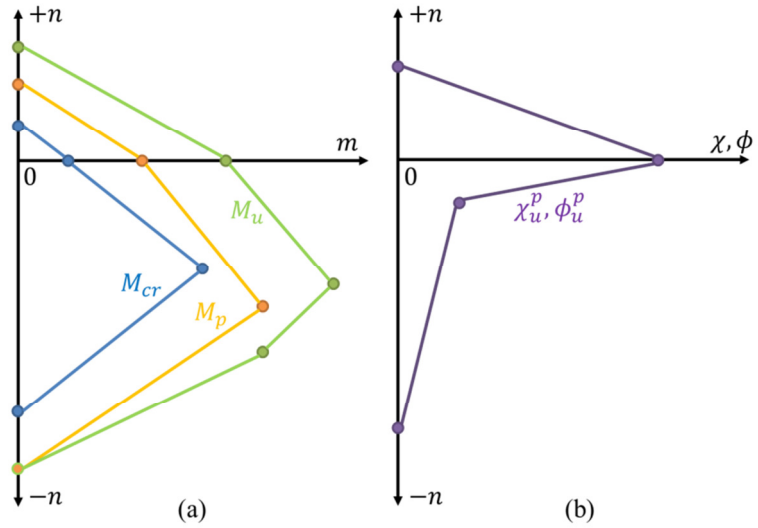

Figure A.10 – Interaction diagrams.

Initially, the *first cracking condition* is analysed. For such condition, the transformed section concept is applied in the cross section (see e.g. Figure A.11), where A_{TS} and I_{TS} are the area and inertia moment of the transformed cross section, respectively.

In the pure compression point (Figure A.11) the strain and stress distributions are assumed constant in the cross section. Assuming a linear behaviour of concrete up to almost half of the total resistance, the axial compression force at the concrete cracking threshold is:

$$N_{cr} = -A_{TS}0.45f_c' \tag{A.6}$$

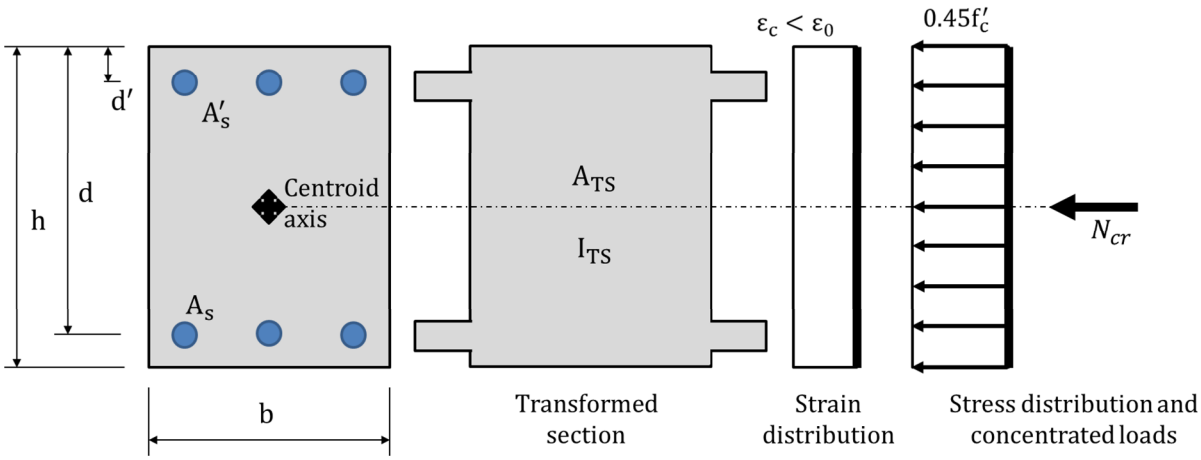

Figure A.11 – Transformed section, strain and stress distributions in pure compression for first cracking.

In the pure tension point (Figure A.12) the strain and stresses are also constant in the cross section. If the stresses reach the tension strength f_t then cracks nucleate, therefore the corresponding axial force is:

$$N_{cr} = A_{TS} f_t \tag{A.7}$$

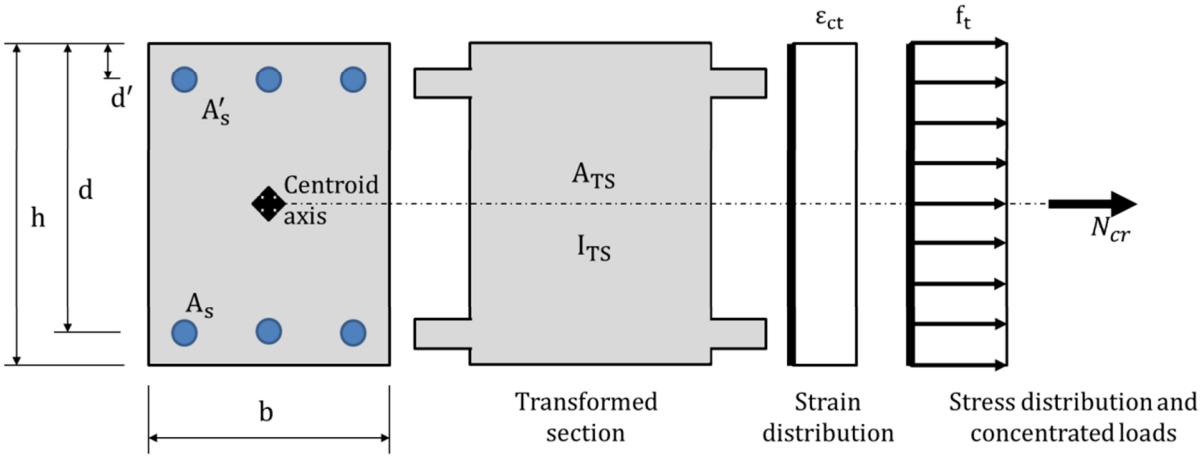

Figure A.12 – Transformed section, strain and stress distributions in pure tension for first cracking.

The pure bending consists, evidently, in a condition where there is no axial force. Since the Euler-Bernoulli beam theory is adopted (see chapter 2), the stress and strain distributions are assumed linear (Figure A.13). Then, considering that the maximum tension stress is equal to f_t the first cracking moment is:

$$f_t = \frac{M_{cr} z_{CA}}{I_{TS}} \quad \Rightarrow \quad M_{cr} = \frac{f_t I_{TS}}{z_{CA}} \tag{A.8}$$

where z_{CA} is the distance between the extreme tension fibre and the centroid axis (Figure A.13).

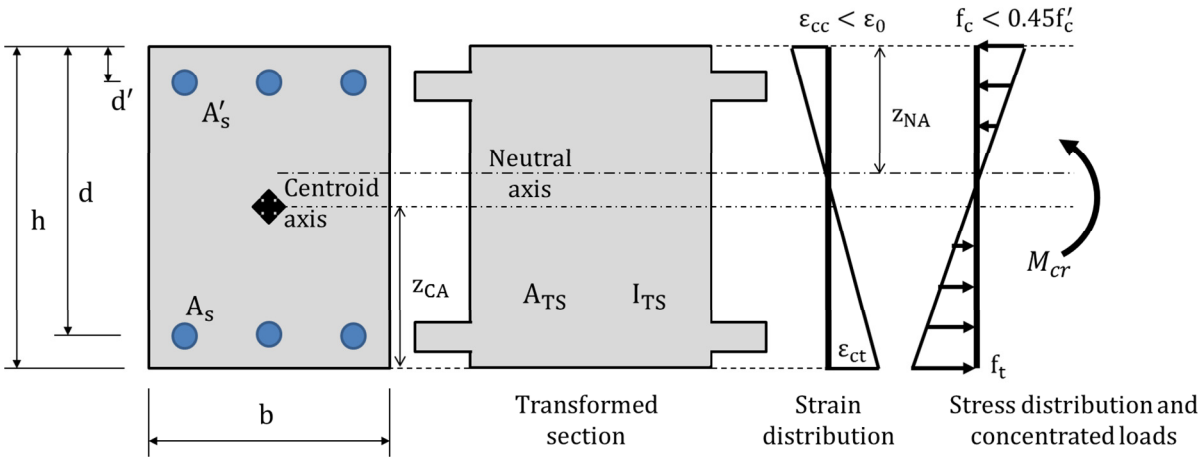

Figure A.13 – Transformed section, strain and stress distributions in pure bending for first cracking.

The main assumption in the balanced condition point is that the maximum compression and tension stresses are, respectively, $0.45f'_c$ and f_t i.e. both simultaneously reach the adopted limits (Figure A.14).

The stress distribution (f) is linearly described by the following equation:

$$f = \frac{M_{cr} z}{I_{TS}} + \frac{N_{cr}}{A_{TS}} \tag{A.9}$$

where z is the distance between the centroid axis and the considered fibre (Figure A.14).

The bending moment and the axial force are calculated considering f'_c and f_t as the maximum compressive stress and maximum tension stress, respectively.

$$\begin{cases} 0.45f'_c = \dfrac{M_{cr}(h - z_{CA})}{I_{TS}} + \dfrac{N_{cr}}{A_{TS}} \\ f_t = \dfrac{M_{cr} z_{CA}}{I_{TS}} - \dfrac{N_{cr}}{A_{TS}} \end{cases} \Rightarrow \begin{cases} N_{cr} = \dfrac{z_{CA}(0.45f'_c + f_t) - hf_t}{h} A_{TS} \\ M_{cr} = \dfrac{0.45f'_c + f_t}{h} I_{TS} \end{cases} \tag{A.10}$$

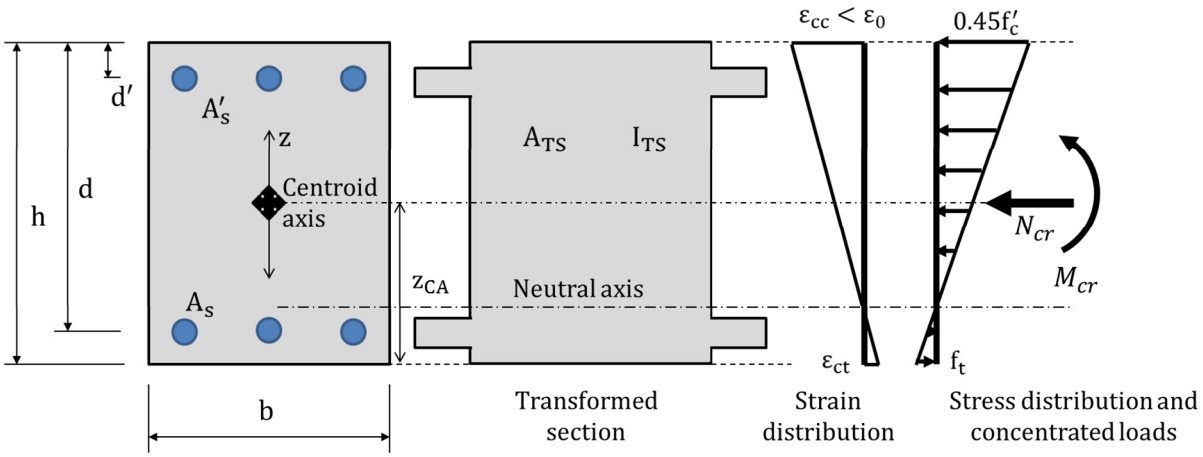

Figure A.14 – Transformed section, strain and stress distributions in the balanced condition point for first cracking.

In the *plastic condition*, concrete presents no resistance to tension stresses due to cracks. Therefore, the longitudinal reinforcement is responsible to resist to tension stresses up to plastic limit.

In the pure compression point, the strain distribution in the cross section is constant and equal to the yield strain (ε_y), leading to the following axial force:

$$N_p \cong C'_s + C_c + C_s = -f_y A'_s - f_c(bh - A'_s - A_s) - f_y A_s \quad (A.11)$$

where f_c is the maximum stress in the concrete. The main assumption in this point is that the reinforcement yields in compression while concrete reaches compression maximum strength.

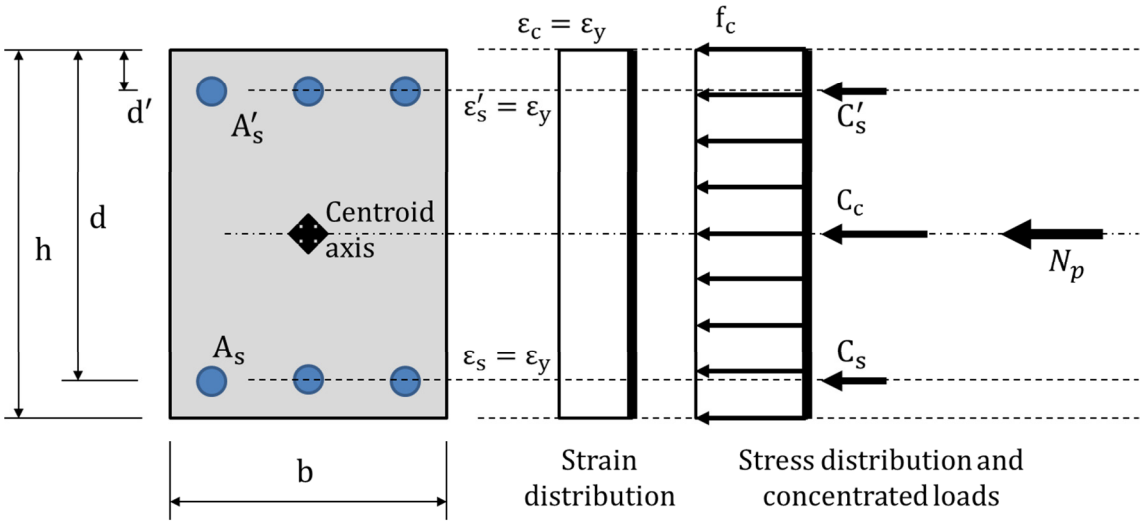

Figure A.15 – Concentrated loads, strain and stresses distributions in the pure compression point for plastic condition.

For the pure tension point the concrete resistance is neglected (Figure A.16) and the strain at the reinforcement bars is equal to the yield strain (ε_y) resulting the following expression to the axial force:

$$N_p \cong T'_s + T_s = f_y A'_s + f_y A_s \tag{A.12}$$

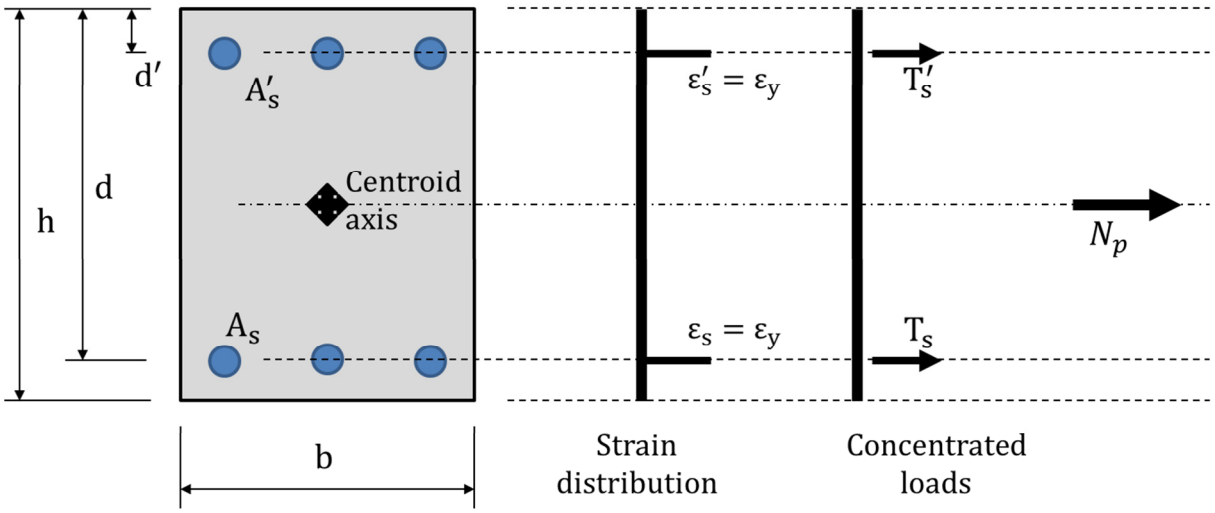

Figure A.16 – Concentrated loads, strain and stresses distributions in the pure compression point for plastic condition.

As the classic RC theory for bending elements is based on the Euler-Bernoulli theory, the strain presents linear distribution.

Considering the pure bending point (Figure A.17), the main assumption is that the tensioned reinforcement starts yielding. In the following equation the location of the neutral axis z_{NA} is determined:

$$N_p = C'_s + C_c + T_s = -f_s A'_s - b\int_0^{z_{NA}} f_c\, dz + f_y A_s = 0 \tag{A.13}$$

Then, the plastic moment M_p is:

$$M_p = C'_s\left(\frac{h}{2} - d'\right) + C_c\left[\frac{h}{2} - \left(z_{NA} - z_{C_c}\right)\right] + T_s\left(d - \frac{h}{2}\right) \tag{A.14}$$

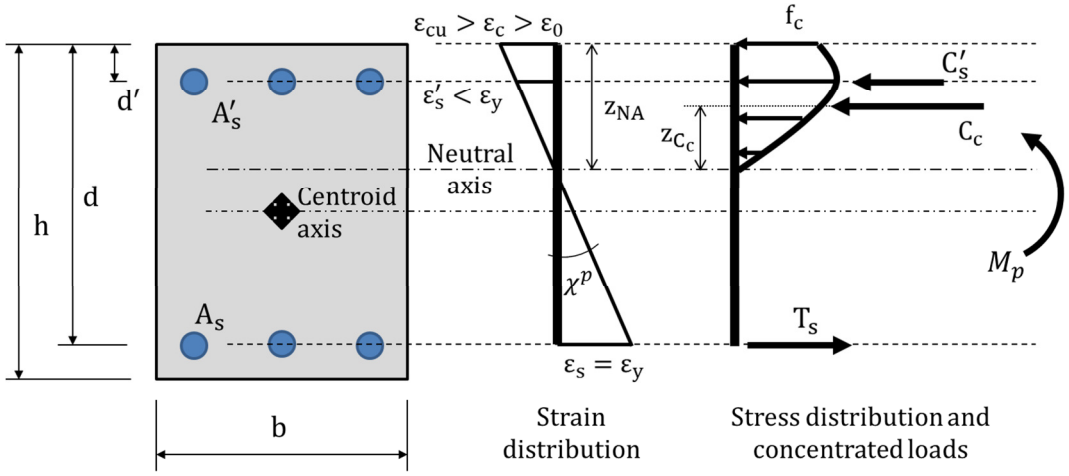

Figure A.17 – Concentrated loads, strain and stresses distributions in the pure bending point for plastic condition.

In the maximum bending resistance point (Figure A.18), the tensioned and compressed reinforcements are assumed to yield simultaneously. Thus, the neutral axis location is:

$$z_{NA} = \frac{d + d'}{2} \tag{A.15}$$

Then, the strain at the extreme compression fibre is determined and the plastic load N_p and the plastic moment M_p are obtained:

$$\begin{cases} N_p = C'_s + C_c + T_s = -f_s A'_s - b\int_0^{z_{NA}} f_c\, dz + f_y A_s \\ M_p = C'_s\left(\frac{h}{2} - d'\right) + C_c\left[\frac{h}{2} - \left(z_{NA} - z_{C_c}\right)\right] + T_s\left(d - \frac{h}{2}\right) \end{cases} \tag{A.16}$$

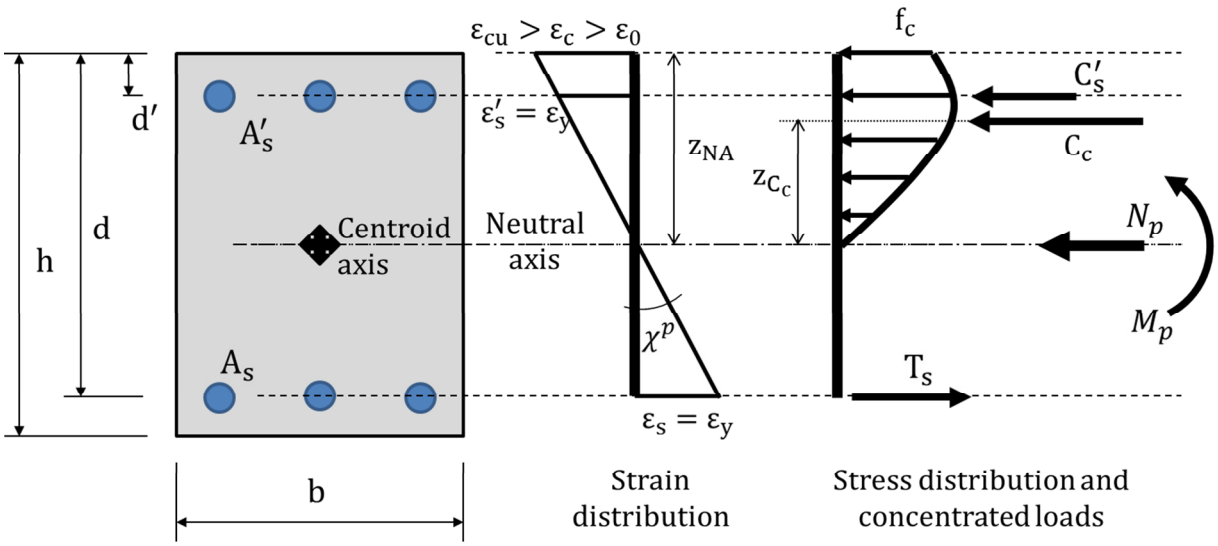

Figure A.18 - Concentrated loads, strain and stresses distributions in the balanced condition point for plastic condition.

Finally, in the *ultimate condition* the cross section presents maximum load capacity. In the pure compression (Figure A.19) point the ultimate axial force is assumed approximately equal to the plastic axial force i.e.

$$N_u \cong N_p \cong C'_s + C_c + C_s = -f_y A'_s - f_c(bh - A'_s - A_s) - f_y A_s \tag{A.17}$$

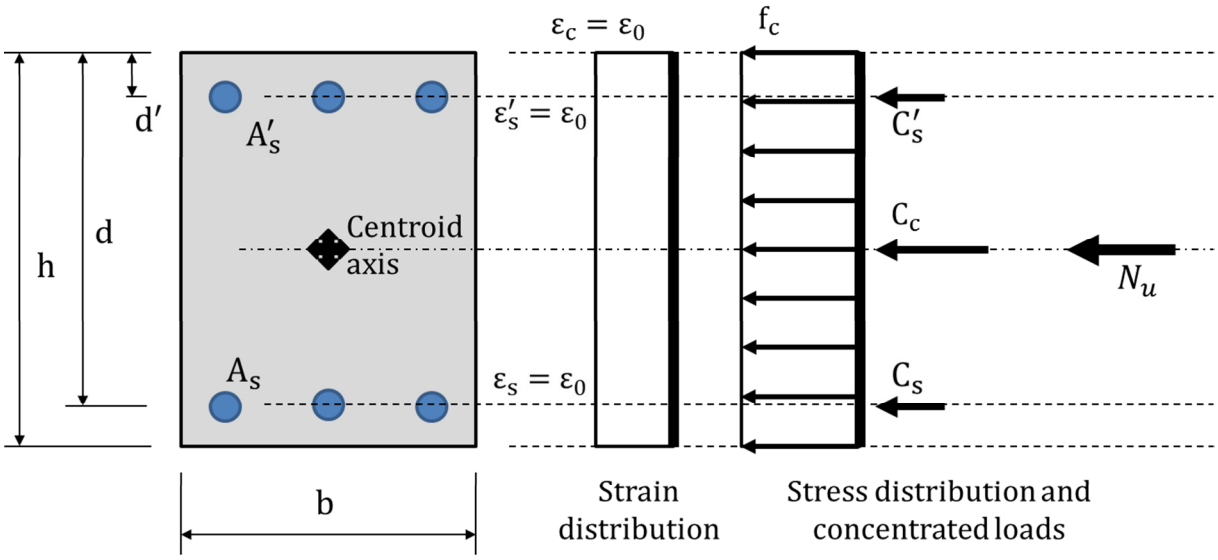

Figure A.19 – Concentrated loads, strain and stresses distributions in the pure compression point for ultimate condition.

In the pure tension point (Figure A.20) the hardening of the steel is considered, which leads to the following axial force:

$$N_u \cong T'_s + T_s = f_{su}A'_s + f_{su}A_s \tag{A.18}$$

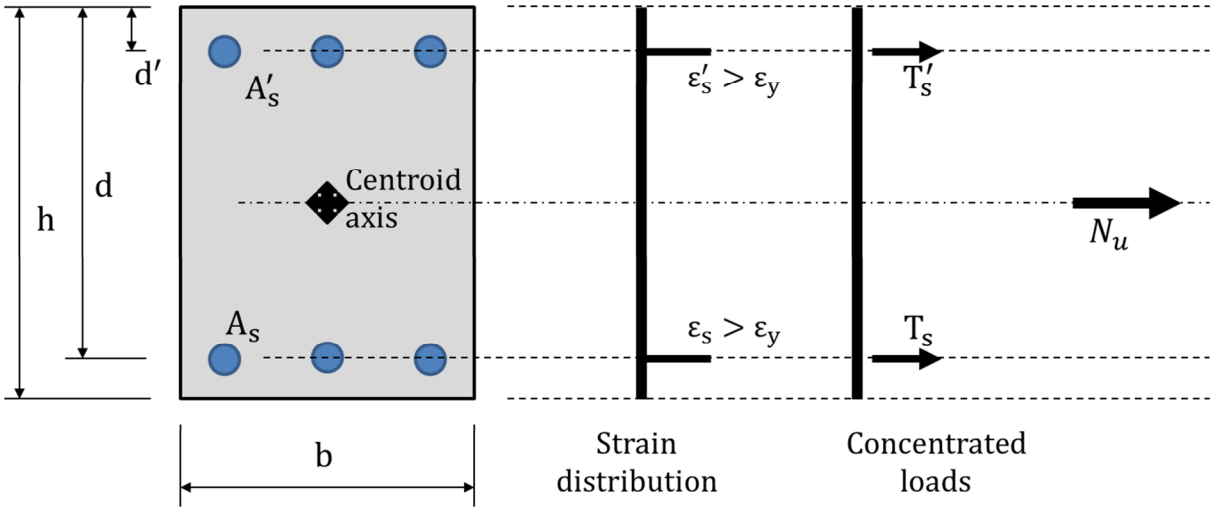

Figure A.20 – Concentrated loads, strain and stresses distributions in the pure tension point for ultimate condition.

The pure bending point (Figure A.21) is characterised by the assumption that the extreme compression fibre reaches the ultimate value (ε_{cu}). The axial equilibrium leads to the location of the neutral axis z_{NA} i.e.

$$N_u = C'_s + C_c + T_s = -f_s A'_s - b\int_0^{z_{NA}} f_c\, dz + f_y A_s = 0 \tag{A.19}$$

Then, the bending moment results:

$$M_u = C'_s\left(\frac{h}{2} - d'\right) + C_c\left[\frac{h}{2} - \left(z_{NA} - z_{C_c}\right)\right] + T_s\left(d - \frac{h}{2}\right) \tag{A.20}$$

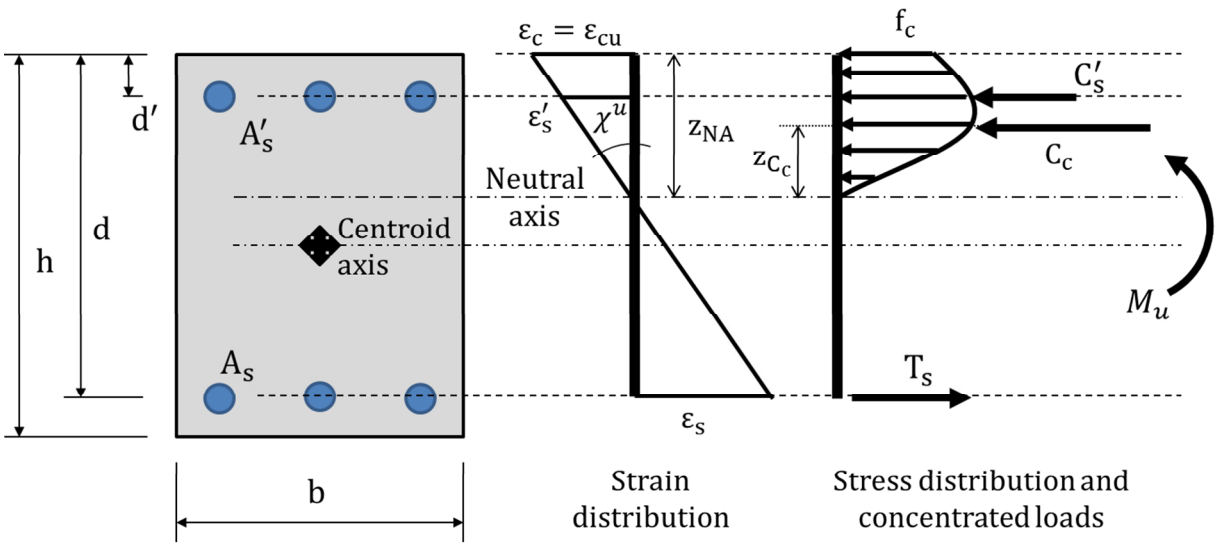

Figure A.21 – Concentrated loads, strain and stresses distributions in the pure bending point for ultimate condition.

To reach the maximum bending resistance point (Figure A.22), the strain in the maximum compressive fibre and the strain in the tensioned reinforcement are assumed with their maximum values i.e. ε_{cu} and ε_y respectively. Then, the neutral axis location is given by:

$$z_{NA} = \frac{\varepsilon_{cu}}{\varepsilon_{cu} + \varepsilon_y} d \tag{A.21}$$

Thus, the axial force and the bending moment are:

$$\begin{cases} N_u = \mathrm{C_s'} + \mathrm{C_c} + \mathrm{T_s} = -\mathrm{f_s A_s'} - \mathrm{b}\int_0^{\mathrm{z_{NA}}} \mathrm{f_c}\, dz + \mathrm{f_y A_s} \\ M_u = \mathrm{C_s'}\left(\frac{\mathrm{h}}{2} - \mathrm{d'}\right) + \mathrm{C_c}\left[\frac{\mathrm{h}}{2} - \left(\mathrm{z_{NA}} - \mathrm{z_{C_c}}\right)\right] + \mathrm{T_s}\left(\mathrm{d} - \frac{\mathrm{h}}{2}\right) \end{cases} \tag{A.22}$$

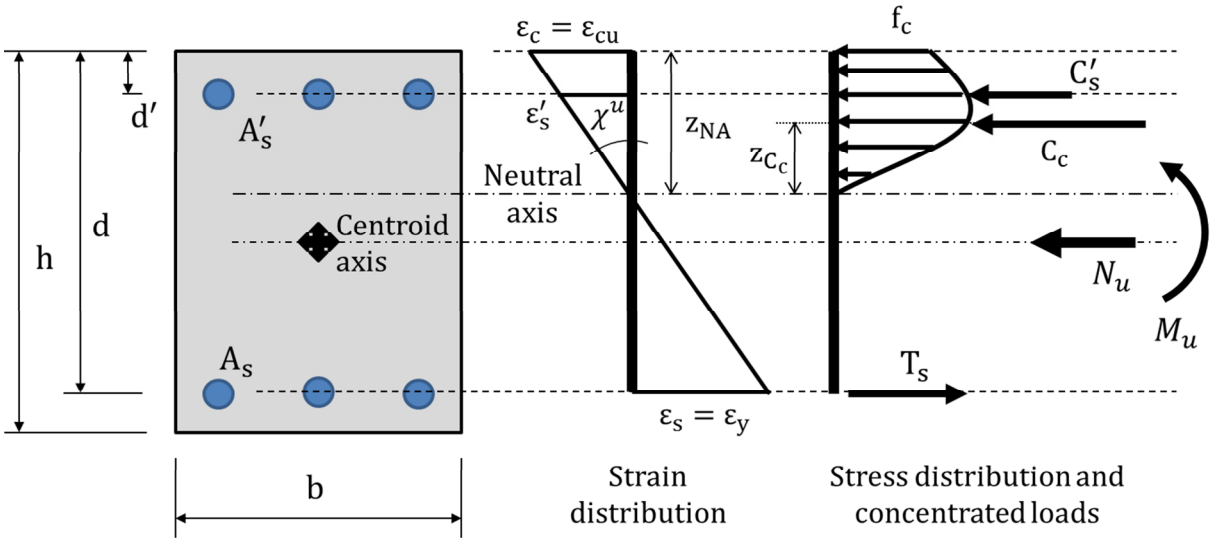

Figure A.22 – Concentrated loads, strain and stresses distributions in the balanced condition point for ultimate condition.

In the plastic and ultimate conditions, two quantities were presented in strain distributions in bending: plastic χ^p and ultimate χ^u curvatures. The difference between such quantities characterise the ultimate plastic curvature:

$$\begin{cases} \chi^p = \dfrac{\varepsilon_y}{\mathrm{d} - \mathrm{z_{NA}}} \\ \chi^u = \dfrac{\varepsilon_{cu}}{\mathrm{z_{NA}}} \end{cases} \quad \therefore \chi_u^p = \chi^u - \chi^p \tag{A.23}$$

The ultimate plastic rotation ϕ_u^p is defined as:

$$\phi_u^p = \chi_u^p l_p \tag{A.24}$$

where l_p is called plastic hinge length in RC literature and it represents the zone where the reinforcement bars underwent plastic deformations. Note that l_p is usually computed using empirical expressions, such as (FLÓREZ-LÓPEZ; MARANTE; PICÓN, 2015):

$$l_p = 0.5\mathrm{d} + 0.05\mathrm{x_{cs}} \tag{A.25}$$

being $\mathrm{x_{cs}}$ the distance from the critical section to the point of inflection.

The interaction diagram for the ultimate plastic rotation/curvature is computed as the previous ones. In the pure tension and pure compression points the plastic rotations/curvatures are zero; and in pure bending and maximum bending resistance points χ_u^p and ϕ_u^p are calculated using equations (A.23) and (A.24).

Therefore, with the interaction diagrams presented here, the modelling of RC structures with plastic hinges (chapter 2) is then based on the classic RC theory.

References

AMERICAN CONCRETE INSTITUTE. **ACI 318-05**: Building code requirements for structural concrete. Farmington Hills, 2005.

ASSOCIAÇÃO BRASILEIRA DE NORMAS TÉCNICAS. **NBR 6118**: Projeto de estruturas de concreto – procedimento. Rio de Janeiro, 2014.

FLÓREZ-LÓPEZ, J.; MARANTE, M. E.; PICÓN, R. A. **Fracture and Damage Mechanics for Structural Engineering of Frames**: State-of-the-Art Industrial Applications. IGI Global, Hershey. 2015.

HOGNESTAD, E. A study of combined bending and axial load in reinforced concrete members. **University of Illinois Engineering Experiment Station**, University of Illinois at Urbana-Champaign, Urbana, p. 43-46, 1951.

KENT, D. C.; PARK, R. Flexural members with confined concrete. **Journal of the Structural Division**, 97, p. 1960-1990, 1971.

APPENDIX B – A lumped plasticity model for RC slabs

Introduction

In the beginning of the 20th century there were many nonlinear studies using the theory of plasticity. The most common developments were made using limit analysis (see e.g. Save and Massonet (1972) for a review). Using this idea, some studies appeared in order to account for the collapse of plates. The research frontier that treated the reinforced concrete (RC) plates is usually known as *yield-line theory* (or *fracture-line theory*).

The yield-line theory was fundamentally conceptualised in Bach (1890) process. Despite its significance, such process could be applied only for a few problems. Later, Inglerslev (1923) formulated rupture criteria for clamped and simply supported rectangular RC slabs, assuming the collapse by yielding of the reinforcement. However, some hypotheses assumed by Inglerslev (1923) were corrected solely a few years later by Johansen (1932). In Johansen (1932) the yield-line theory was presented in a very formal way. Based on Johansen (1932), there were many developments of this theory in the following decades, where here the work of Chamecki (1948) is emphasised. Among great developments around the world, the most significant were presented by Jones and Wodd (1967) and van Langendonck (1970, 1975).

Despite the significance of the aforementioned works, the yield-line theory requires an assumption of the collapse mechanism that the RC slab will suffer. For usual problems, this issue is well-solved. However, for slabs with complex geometries, this can be a real problem.

On the other hand, models based on lumped plasticity concepts, i.e. the idealisation of plastic hinges, are quite useful to analyse RC frames (see e.g. Park and Paulay (1975) and Inel and Ozmen (2006) for a review). In fact, these concepts were expanded by additional concepts of fracture and damage mechanics in order to represent a more realistic behaviour of RC frames (for a review, see Flórez-López, Marante and Picón (2015) and the references therein). This is achieved by the consideration of a damage variable that characterises the concrete cracking. Therefore, after those studies, the lumped plasticity models became lumped damage models and, consequently, the plastic hinges became inelastic hinges.

In the light of the foregoing, in this appendix a lumped plasticity model is presented in order to study the plastic collapse of RC slabs. This lumped plasticity model is a simple

reduction of the lumped damage model proposed in chapter 5. Comparisons with experimental and theoretical results show the good accuracy of the model.

It is noteworthy that a previous model considering plastic collapse of plates was presented by Armero and Ehrlich (2006). Such model is also based on lumped plasticity concepts. However, Armero and Ehrlich (2006) have focused only on numerical studies for thick plates, presenting notorious results on that approach. Then, the research frontier presented here also aims for a model that characterises the behaviour of RC slabs in a realistic way. Therefore, now only the lumped plasticity model is presented. Note that the procedure presented here is applied for thin plates.

In future works, the main objective must be a generalisation of the lumped damage model proposed in chapter 5 that accounts for concrete cracking and yielding of reinforcement. Such generalisation may present a more realistic behaviour of collapsed RC slabs.

Brief review on the yield-line theory for RC slabs

The yield-line theory is still used in engineering design of RC slabs. Usually, this theory is simplified for usual geometries and applied to RC buildings and bridges. The yield-line theory consists in an application of the upper bound limit theorem of plasticity limit analysis.

In conventional RC slabs undergoing proportional loads there are three different phases of behaviour (PINHEIRO, 1988): elastic phase (OA), cracking phase (AC), and plastic phase (CD).

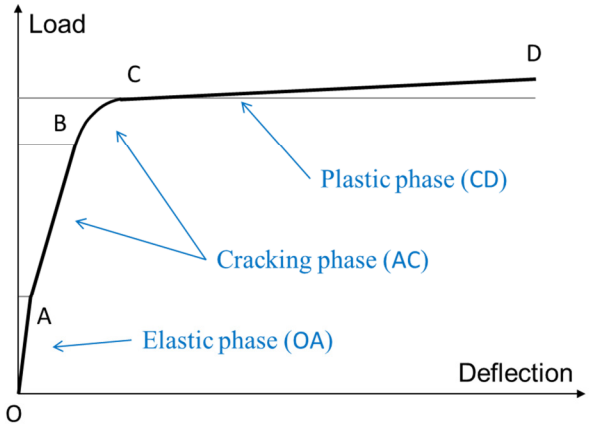

Figure B.1 – Phases of behaviour for an RC slab. [After Pinheiro (1988)]

For small loads the RC slab presents an elastic behaviour (OA) i.e. there are no cracks and the concrete resists to tension. The cracking threshold (point A) is trespassed by increasing the load, resulting in nucleation and propagation of cracks at the most loaded sections. Bending moments, at the non-cracked sections, increase due to such cracks. This process results in nucleation and propagation of new cracks (AB). Once the reinforcement trespasses the elastic threshold (BC) the deflection increases rapidly. Finally, the plastic phase (CD) occurs when the reinforcement yields in the most loaded sections. Analogously, bending moments at non-yielded sections increase due to such process. This results into reinforcement yielding at such sections and, as a consequence, the propagation of the yield-lines in the RC slab. Therefore, The RC slab is assumed as collapsed when the yield-lines complete the propagation process. At this point, the load level that ensures such condition is called as ultimate load or collapse load.

The yield-line theory is an upper bound limit analysis approach. Thus, it is considered that the RC slab is rigid for loads smaller than the collapse load and immediately collapses when the collapse load is achieved (Figure B.2). In other words, the RC slab is considered as a rigid-plastic material (Figure B.2) in the yield-line theory (see e.g. Johansen (1932), Jones and Wodd (1967) and van Langendonck (1970, 1975) for a detailed review).

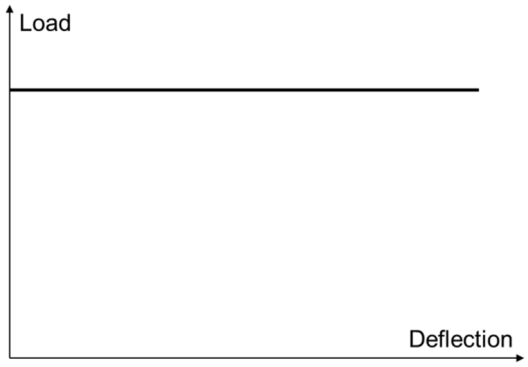

Figure B.2 – Rigid-plastic material.

The reduced lumped damage model

The numerical modelling of plastic collapse of RC slabs based on the yield-line theory must fulfil some conditions in order to reproduce the aforementioned theoretical behaviour. Considering a finite element analysis, for instance, the rigid-plastic behaviour is modelled using an elastic-plastic curve. Note that an elastic-perfectly plastic curve is suitable due to

the behaviour hypothesis of the yield-line theory (Figure B.2). Therefore, the lumped damage model for bending plates proposed in chapter 5 degenerates in an elastic-perfectly plastic model if $\phi_u \to \infty$ (Figure B.3).

According to Chamecki (1948), the yield-line theory presents three main hypotheses:

- The rupture lines are considered straight;
- The slab parts, which are limited by the yield lines and the slab borders, are considered plains;
- Along and in the neighbourhood of each yield line, the specific bending moment (moment per length unit) is considered constant and equal to the maximum bending moment that the slab can resist in this direction.

Considering the first hypothesis, in the lumped damage model applied to the finite element known as the constant moment triangle (CMT), proposed by Morley (1971) and presented in chapter 5, the damage rotations occur only in the element sides, which are straight lines. The CMT element is an acceptable approximation for the second hypothesis, once the element presents constant curvature. The third hypothesis is fulfilled once the collapse mechanism is completed, once the CMT element presents constant bending moments. Thus, the degenerated (Figure B.3) lumped damage model for bending plates proposed in chapter 5 is a reasonable approximation to analyse plastic collapse of RC slabs.

Regarding the model degeneration, the finite element is now considered as a result of the assemblage of an elastic CMT element with three plastic hinge-lines located at its sides (Figure B.4). Note that the damage deformations originally proposed (chapter 5) become now plastic deformations:

$$\{\boldsymbol{\phi}^{\boldsymbol{p}}\}_t = \left\{\phi_a^p \quad \phi_b^p \quad \phi_c^p\right\}^T \tag{B.1}$$

which contains the plastic rotations of the hinge-lines at the sides ij, jk and ki, respectively.

Then, the hypothesis of strain equivalence is rewritten as:

$$\{\boldsymbol{\phi}\}_t = \{\boldsymbol{\phi}^{\boldsymbol{e}}\}_t + \{\boldsymbol{\phi}^{\boldsymbol{p}}\}_t \tag{B.2}$$

and the model formulation is rewritten as:

$$\{\boldsymbol{\phi}\}_t = [\mathbf{B}^0]_t\{\mathbf{q}\}_t$$
$$\{\mathbf{Q}\}_t = [\mathbf{B}^0]_t^T\{\mathbf{M}\}_t \quad \text{(B.3)}$$
$$\{\boldsymbol{\phi} - \boldsymbol{\phi}^{\boldsymbol{p}}\}_t = [\mathbf{F_0}]_t\{\mathbf{M}\}_t$$

where the definition of such variables is found in chapter 5.

According to the model degeneration (Figure B.4), m_{cr} takes the value of the plastic bending moment m_p ($m_{cr} \leftarrow m_p$), calculated from the yield-line theory. Then, the plastic evolution law results:

$$\left|\frac{M_{ij}}{L_{ij}}\right| - m_p \leq 0$$
$$\left|\frac{M_{jk}}{L_{jk}}\right| - m_p \leq 0 \quad \text{(B.4)}$$
$$\left|\frac{M_{ki}}{L_{ki}}\right| - m_p \leq 0$$

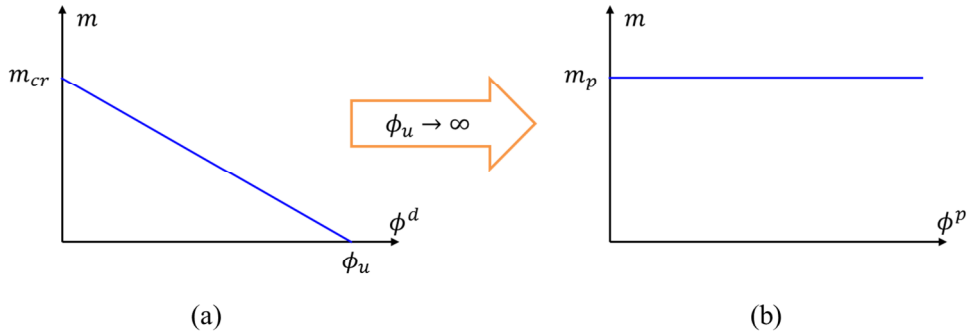

Figure B.3 – Lumped damage model: (a) original model; (b) model reduction to lumped plasticity.

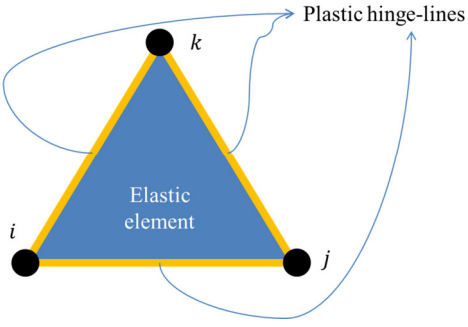

Figure B.4 – Lumped plasticity model.

Practical applications in RC slabs

In order to evaluate possible practical applications of the aforementioned reduced lumped damage model, two RC slabs where analysed (SAWCZUK; JAEGER, 1963). Despite the simplicity of the examples, the potentialities and limitations of the proposed model are highlighted. It is noteworthy that, according to Sawczuk and Jaeger (1963), the Poisson's ratio is 0.3 in both examples. Once the Young's modulus is not given and the proposed lumped plasticity model intends to reproduce the theoretical solutions given by the yield-line theory, such parameter is taken as a very large value.

The first example addresses to a four-sided simply supported square isotropic RC slab tested by Sawczuk and Jaeger (1963). Such RC slab presents side length of 150 cm, thickness of 6 cm (Figure B.5a) and an isotropic yield moment equal to 464 kgf. If plastic hardening is neglected, this example has a well-known analytical solution obtained with the yield-line theory (Figure B.5a). Figure B.5b shows the fracture pattern of the tested plate, which was loaded up to a center deflection of 5.4 cm. Figure B.5c-e shows the numerical hinge-line pattern, obtained through the proposed hinge-line procedure. Figure B.6 presents graph representations of load-displacement responses for the simulated meshes.

Note the good agreement of the numerical analyses with the theoretical plastic hinge-lines. Regarding the numerical responses, there are two patterns of hinge-lines: an X-shaped mechanism, in red, and a cross-shaped mechanism, in green. Notice that the X-shaped mechanism is equal to the theoretical collapse mechanism and also presents plastic rotations with $0.10 - 0.13$ rad of magnitude; the cross-shaped mechanism extends itself only in the central region of the slab and presents plastic rotations with $0.0001 - 0.0012$ rad of magnitude. Therefore, it can be stated that only the X-shaped mechanism leads the structure to collapse. It is noteworthy that the theoretical calculation and the numerical analyses achieved a collapse load P of 3712 kgf while the test carried out by Sawczuk and Jaeger (1963) reached 3900 kgf (this is probably an approximated value).

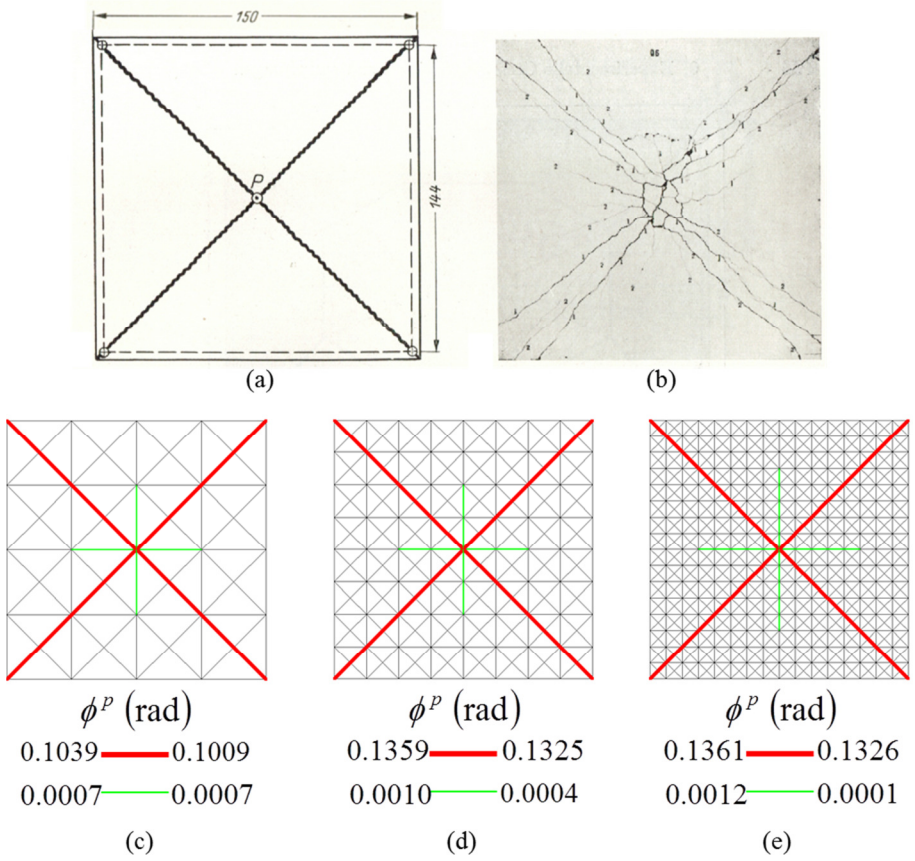

Figure B.5 – Four-sided simply supported square RC slab: (a) geometry and theoretical collapse mechanism (Sawczuk and Jaeger, 1963); (b) actual collapse mechanism (Sawczuk and Jaeger, 1963); and numerical solutions for (c) 64 (4×4), (d) 256 (8×8) and (e) 1024 (16×16) elements.

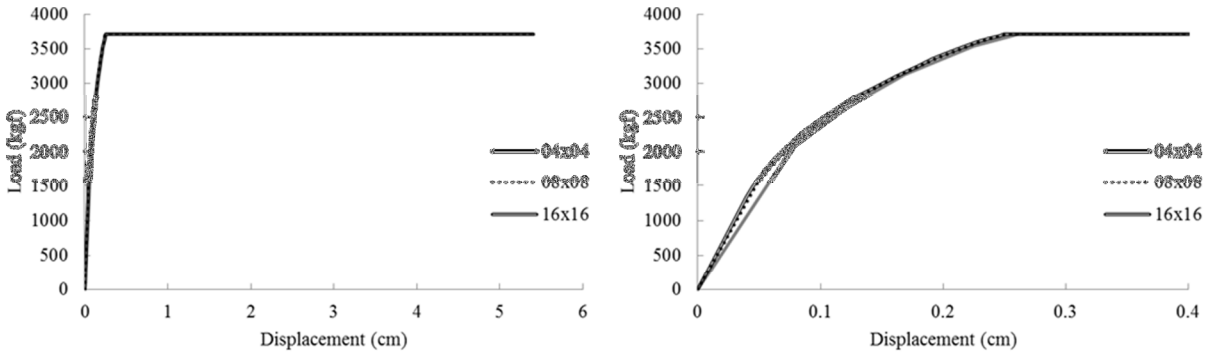

Figure B.6 – Load-displacement responses for numerical analyses.

The second example addresses to a four-sided simply supported rectangular RC slab (224 cm × 150 cm × 6 cm) tested by Sawczuk and Jaeger (1963). Such RC slab presents orthotropic index about 0.92 i.e. $m_{px} = 455$ kgf and $m_{py} = 417$ kgf (SAWCZUK; JAEGER, 1963). Figure B.7a presents the geometry of the problem and also the adopted theoretical

collapse mechanism, and Figure B.7b shows the actual crack pattern experimentally observed (Sawczuk and Jaeger, 1963). Figure B.7c-e depicts the numerical collapse mechanisms obtained with different meshes and Figure B.7f shows the magnitude of the numerical plastic rotations. Figure B.8 presents graph representations of load-displacement responses for the simulated meshes.

In the numerical procedure, since this slab is orthotropic, for each side of an element a yield bending moment is calculated based on its direction and the theoretical yield bending moments i.e. m_{px} and m_{py}. As observed in the previous example, notice the good agreement of the numerical analyses with the theoretical plastic hinge-lines. Again, there are two numerical patterns of hinge-lines: an X-shaped mechanism, in red, and a cross-shaped mechanism, in green (Figure B.7c-e). Analogously as discussed in the previous example, only the X-shaped mechanism leads the structure to collapse (see plastic rotations magnitude in Figure B.7f). It is noteworthy that the theoretical calculation and the numerical analyses achieved a collapse load P of $3982\ \mathrm{kgf}$ while the test carried out by Sawczuk and Jaeger (1963) reached $4200\ \mathrm{kgf}$ (this is probably an approximated value).

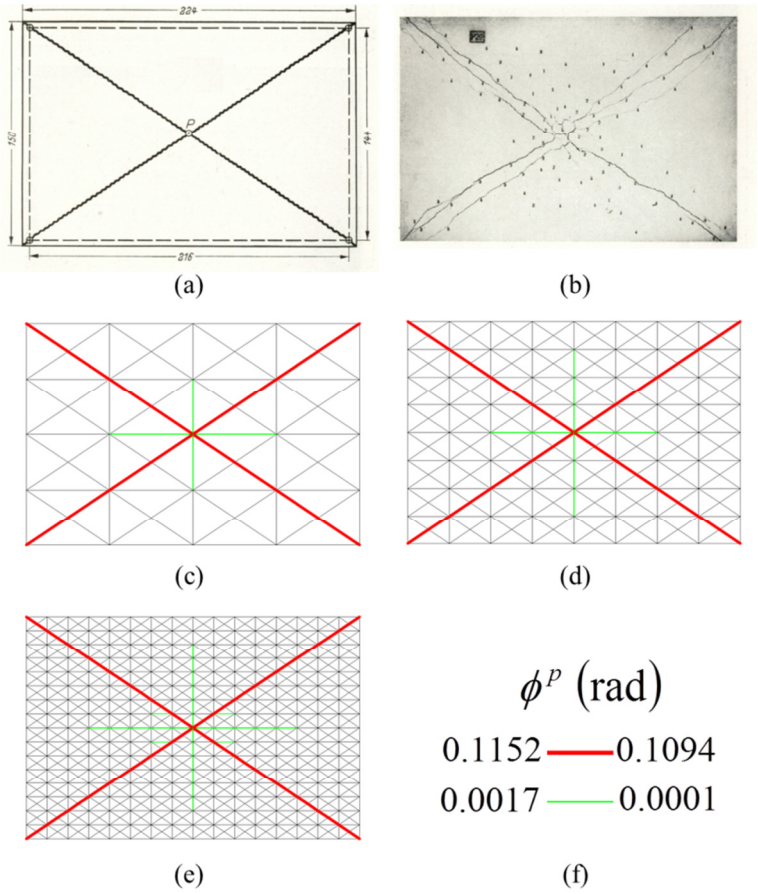

Figure B.7 – Four-sided simply supported rectangular RC slab: (a) geometry and theoretical solution; (b) experimental response; (c-e) numerical responses for meshes (c) 04×04, (d) 08×08 and (e) 16×16; (f) magnitude of the numerical plastic rotations.

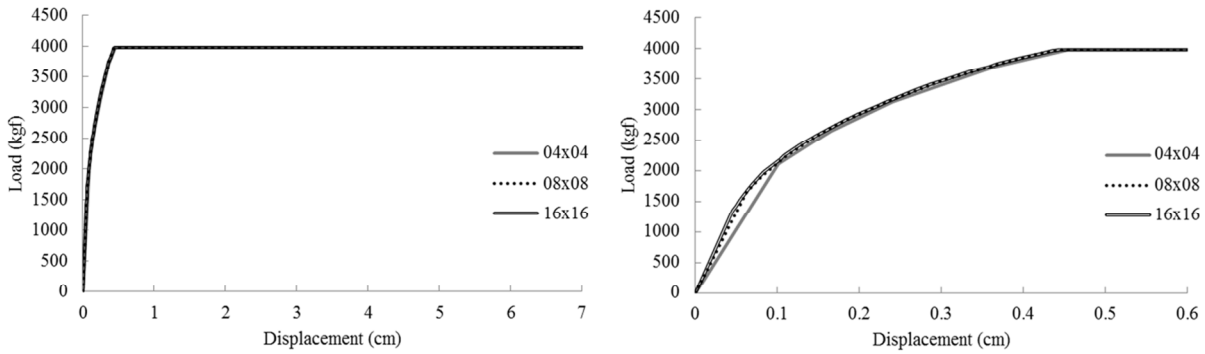

Figure B.8 – Load-displacement responses for numerical analyses.

Concluding remarks and suggestions for future works

Considering the analysed examples, the proposed lumped plasticity model, which is a particular case of the lumped damage model presented in chapter 5, presents good accuracy. It is emphasised that, unlike the limit analysis procedure (yield-line theory), no

mechanism is *a priori* imposed as input i.e. the collapse mechanism is a result of the computation. On the other hand, choosing meshes that include the actual mechanism allows for very good results even with coarse meshes (Figure B.5c and Figure B.7c). For meshes that do not include the collapse mechanism, the simulation will probably need finer meshes in order to achieve acceptable results.

For future works, the first objective should be a formulation that allows the hinge-lines to appear inside the finite element. This update may imply in good results even for coarse meshes that do not contain the collapse mechanism. Another suggestion is the development of a lumped damage model for RC slabs similar to the one presented for RC frames (see chapter 2). Such new model may be able to reproduce a more realistic behaviour of RC slabs.

References

BACH, C. **Verusche über die Widerstand Fähigkeit ebener Platten**. Zs. V.D.I., 1890.

CHAMECKI, S. **Cálculo, no regime de ruptura, das lajes de concreto armadas em cruz**. Guaíra ltda., 1948, Curitiba.

FLÓREZ-LÓPEZ, J.; MARANTE, M. E.; PICÓN, R. A. **Fracture and Damage Mechanics for Structural Engineering of Frames**: State-of-the-Art Industrial Applications. IGI Global, Hershey. 2015.

INEL, M.; OZMEN, H. B. Effects of plastic hinge properties in nonlinear analysis of reinforced concrete buildings. **Engineering Structures**, v. 28 n. 11, 2006, p. 1494-1502.

INGLERSLEV, A. The strength of Rectangular Slabs. **The Institution of Structural Engineer's Journal**, Jan., 1923.

JOHANSEN, K. W. **Brudlinieteorier**. Polyteknish Forening, Genoptrykt, 1943.

JONES, L. L.; WODD, R. H. **Yield-Line Analysis of Slabs**. Thames and Hudson, London, 1967.

VAN LANGENDONCK, T. **Teoria Elementar das Charneiras Plásticas** – Volume I. ABCP, São Paulo, 1970.

VAN LANGENDONCK, T. **Teoria Elementar das Charneiras Plásticas** – Volume II. ABCP, São Paulo, 1975.

MORLEY, L. S. D. The constant-moment plate-bending element. **Journal of Strain Analysis**, v. 06, n. 01, p. 20-24, 1971.

PINHEIRO, L. M. **Análise elástica e plástica de lajes retangulares de edifícios**. 1988. 303 p. Thesis (Doctorate) – São Carlos School of Engineering, University of São Paulo, São Carlos, 1988.

SAVE, M. A., MASSONET, C. E. **Plastic Analysis and Design of Plates, Shells and Disks**. North-Holland Publishing Company, Amsterdan-London, 1972.

SAWCZUK, A., JAEGER, T. **Grenztragfähigkeits-Theorie der Platten**. Springer-Verlag, Berlin, 1963.

APPENDIX C - Matrices of the LDM four-node element

In this appendix, some of the matrices of the LDM four-node element b are presented in the global Cartesian system. Note that in the main body of the thesis, such matrices were presented in the reference system. This was made due to a simple presentation of the new concepts proposed in this thesis.

The kinematic transformation matrix $[\mathbf{B}]_b$ in Cartesian coordinates is given by:

$$[\mathbf{B}]_b = \begin{bmatrix} B_{11} & B_{12} & B_{13} & B_{14} & 0 & 0 & 0 & 0 \\ B_{21} & B_{22} & 0 & 0 & B_{25} & B_{26} & 0 & 0 \\ B_{31} & B_{32} & 0 & 0 & 0 & 0 & B_{37} & B_{38} \\ 0 & 0 & B_{43} & B_{44} & B_{45} & B_{46} & 0 & 0 \\ 0 & 0 & 0 & 0 & B_{55} & B_{56} & B_{57} & B_{58} \end{bmatrix} \tag{C.1}$$

where

$$B_{11} = \frac{x_i - x_j}{\sqrt{\left(x_j - x_i\right)^2 + \left(y_j - y_i\right)^2}} \tag{C.2}$$

$$B_{12} = \frac{y_i - y_j}{\sqrt{\left(x_j - x_i\right)^2 + \left(y_j - y_i\right)^2}} \tag{C.3}$$

$$B_{13} = \frac{x_j - x_i}{\sqrt{\left(x_j - x_i\right)^2 + \left(y_j - y_i\right)^2}} \tag{C.4}$$

$$B_{14} = \frac{y_j - y_i}{\sqrt{\left(x_j - x_i\right)^2 + \left(y_j - y_i\right)^2}} \tag{C.5}$$

$$B_{21} = \frac{x_i - x_k}{\sqrt{(x_k - x_i)^2 + (y_k - y_i)^2}} \tag{C.6}$$

$$B_{22} = \frac{y_i - y_k}{\sqrt{(x_k - x_i)^2 + (y_k - y_i)^2}} \tag{C.7}$$

$$B_{25} = \frac{x_k - x_i}{\sqrt{(x_k - x_i)^2 + (y_k - y_i)^2}} \tag{C.8}$$

$$B_{26} = \frac{y_k - y_i}{\sqrt{(x_k - x_i)^2 + (y_k - y_i)^2}} \tag{C.9}$$

$$B_{31} = \frac{x_i - x_l}{\sqrt{(x_l - x_i)^2 + (y_l - y_i)^2}} \tag{C.10}$$

$$B_{32} = \frac{y_i - y_l}{\sqrt{(x_l - x_i)^2 + (y_l - y_i)^2}} \tag{C.11}$$

$$B_{37} = \frac{x_l - x_i}{\sqrt{(x_l - x_i)^2 + (y_l - y_i)^2}} \tag{C.12}$$

$$B_{38} = \frac{y_l - y_i}{\sqrt{(x_l - x_i)^2 + (y_l - y_i)^2}} \tag{C.13}$$

$$B_{43} = \frac{x_j - x_k}{\sqrt{\left(x_k - x_j\right)^2 + \left(y_k - y_j\right)^2}} \tag{C.14}$$

$$B_{44} = \frac{y_j - y_k}{\sqrt{\left(x_k - x_j\right)^2 + \left(y_k - y_j\right)^2}} \tag{C.15}$$

$$B_{45} = \frac{x_k - x_j}{\sqrt{\left(x_k - x_j\right)^2 + \left(y_k - y_j\right)^2}} \tag{C.16}$$

$$B_{46} = \frac{y_k - y_j}{\sqrt{\left(x_k - x_j\right)^2 + \left(y_k - y_j\right)^2}} \tag{C.17}$$

$$B_{55} = \frac{x_k - x_l}{\sqrt{(x_l - x_k)^2 + (y_l - y_k)^2}} \tag{C.18}$$

$$B_{56} = \frac{y_k - y_l}{\sqrt{(x_l - x_k)^2 + (y_l - y_k)^2}} \tag{C.19}$$

$$B_{57} = \frac{x_l - x_k}{\sqrt{(x_l - x_k)^2 + (y_l - y_k)^2}} \tag{C.20}$$

$$B_{58} = \frac{y_l - y_k}{\sqrt{(x_l - x_k)^2 + (y_l - y_k)^2}} \tag{C.21}$$

The matrix $[\mathbf{T}]_b$ is obtained through a simple matrix manipulation. For this purpose, the first relation of (5.43), and the equations (5.45) and (5.47) are rewritten here just for convenience:

$$\begin{aligned} \{\boldsymbol{\varepsilon}\}_b &= [\mathbf{b}]_b\{\mathbf{q}\}_b \\ \{\boldsymbol{\delta}\}_b &= [\mathbf{B}]_b\{\mathbf{q}\}_b \\ \{\boldsymbol{\varepsilon}\}_b &= [\mathbf{T}]_b\{\boldsymbol{\delta}\}_b \end{aligned} \tag{C.22}$$

The following relation is a result of some matrix manipulation:

$$[\mathbf{b}]_b\{\mathbf{q}\}_b = [\mathbf{T}]_b[\mathbf{B}]_b\{\mathbf{q}\}_b \tag{C.23}$$

where $\{\mathbf{q}\}_b$ contains the degrees of freedom of the four-node element b. Note that $[\mathbf{b}]_b$ is the well-known transformation matrix from the classic four-node finite element and $[\mathbf{B}]_b$ was already presented in this appendix. Therefore, the terms of the matrix $[\mathbf{T}]_b$ are easily obtained by the following equation:

$$[\mathbf{b}]_b = [\mathbf{T}]_b[\mathbf{B}]_b \tag{C.24}$$

Finally, the matrix of generalised deformations $\{\boldsymbol{\delta}\}_b$ is also presented in Cartesian coordinates on what follows (see also Figure C.1).

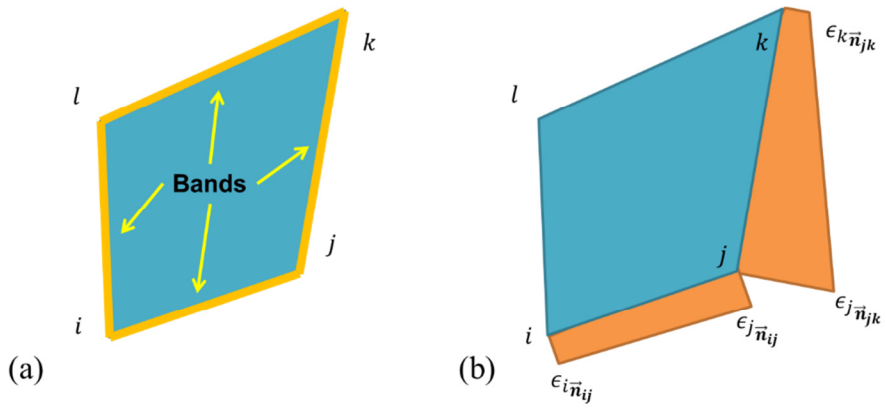

Figure C.1 – (a) Localisation bands in a four-node element; (b) thickness of the bands ij and jk.

$$\left\{\boldsymbol{\delta}^{\boldsymbol{d}}\right\}_b = \begin{Bmatrix} 0 \\ \epsilon_{i\vec{\boldsymbol{n}}_{\boldsymbol{ij}}} \dfrac{x_i y_j - x_i y_k - x_j y_i + x_j y_k + x_k y_i - x_k y_j}{\sqrt{(x_i - x_k)^2 + (y_i - y_k)^2}\sqrt{\left(x_i - x_j\right)^2 + \left(y_i - y_j\right)^2}} \\ \epsilon_{i\vec{\boldsymbol{n}}_{\boldsymbol{ij}}} \dfrac{x_i y_j - x_i y_l - x_j y_i + x_j y_l + x_l y_i - x_l y_j}{\sqrt{(x_i - x_l)^2 + (y_i - y_l)^2}\sqrt{\left(x_i - x_j\right)^2 + \left(y_i - y_j\right)^2}} \\ \epsilon_{j\vec{\boldsymbol{n}}_{\boldsymbol{ij}}} \dfrac{x_i y_j - x_i y_k - x_j y_i + x_j y_k + x_k y_i - x_k y_j}{\sqrt{\left(x_j - x_k\right)^2 + \left(y_j - y_k\right)^2}\sqrt{\left(x_i - x_j\right)^2 + \left(y_i - y_j\right)^2}} \\ 0 \end{Bmatrix}$$

$$+ \begin{Bmatrix} \epsilon_{j\vec{\boldsymbol{n}}_{\boldsymbol{jk}}} \dfrac{x_i y_j - x_i y_k - x_j y_i + x_j y_k + x_k y_i - x_k y_j}{\sqrt{\left(x_i - x_j\right)^2 + \left(y_i - y_j\right)^2}\sqrt{\left(x_j - x_k\right)^2 + \left(y_j - y_k\right)^2}} \\ \epsilon_{k\vec{\boldsymbol{n}}_{\boldsymbol{jk}}} \dfrac{x_i y_j - x_i y_k - x_j y_i + x_j y_k + x_k y_i - x_k y_j}{\sqrt{(x_i - x_k)^2 + (y_i - y_k)^2}\sqrt{\left(x_j - x_k\right)^2 + \left(y_j - y_k\right)^2}} \\ 0 \\ 0 \\ \epsilon_{k\vec{\boldsymbol{n}}_{\boldsymbol{jk}}} \dfrac{x_j y_k - x_j y_l - x_k y_j + x_k y_l + x_l y_j - x_l y_k}{\sqrt{(x_k - x_l)^2 + (y_k - y_l)^2}\sqrt{\left(x_j - x_k\right)^2 + \left(y_j - y_k\right)^2}} \end{Bmatrix} \quad \text{(C.25)}$$

$$+ \begin{Bmatrix} 0 \\ \epsilon_{k\vec{\boldsymbol{n}}_{\boldsymbol{kl}}} \dfrac{x_i y_k - x_i y_l - x_k y_i + x_k y_l + x_l y_i - x_l y_k}{\sqrt{(x_i - x_k)^2 + (y_i - y_k)^2}\sqrt{(x_k - x_l)^2 + (y_k - y_l)^2}} \\ \epsilon_{l\vec{\boldsymbol{n}}_{\boldsymbol{kl}}} \dfrac{x_i y_k - x_i y_l - x_k y_i + x_k y_l + x_l y_i - x_l y_k}{\sqrt{(x_i - x_l)^2 + (y_i - y_l)^2}\sqrt{(x_k - x_l)^2 + (y_k - y_l)^2}} \\ \epsilon_{k\vec{\boldsymbol{n}}_{\boldsymbol{kl}}} \dfrac{x_j y_k - x_j y_l - x_k y_j + x_k y_l + x_l y_j - x_l y_k}{\sqrt{\left(x_j - x_k\right)^2 + \left(y_j - y_k\right)^2}\sqrt{(x_k - x_l)^2 + (y_k - y_l)^2}} \\ 0 \end{Bmatrix}$$

$$+ \begin{Bmatrix} \epsilon_{i\vec{\boldsymbol{n}}_{\boldsymbol{li}}} \dfrac{x_i y_j - x_i y_l - x_j y_i + x_j y_l + x_l y_i - x_l y_j}{\sqrt{\left(x_i - x_j\right)^2 + \left(y_i - y_j\right)^2}\sqrt{(x_i - x_l)^2 + (y_i - y_l)^2}} \\ \epsilon_{i\vec{\boldsymbol{n}}_{\boldsymbol{li}}} \dfrac{x_i y_k - x_k y_l - x_k y_i + x_k y_l + x_l y_i - x_l y_k}{\sqrt{(x_i - x_k)^2 + (y_i - y_k)^2}\sqrt{(x_i - x_l)^2 + (y_i - y_l)^2}} \\ 0 \\ 0 \\ \epsilon_{l\vec{\boldsymbol{n}}_{\boldsymbol{li}}} \dfrac{x_i y_k - x_k y_l - x_k y_i + x_k y_l + x_l y_i - x_l y_k}{\sqrt{(x_k - x_l)^2 + (y_k - y_l)^2}\sqrt{(x_i - x_l)^2 + (y_i - y_l)^2}} \end{Bmatrix}$$